Bidirektionale Reflektanz von städtischen Oberflächen

(Bidirectional Reflectance of Urban Surfaces)

Dissertation
zur Erlangung des Doktorgrades
des Fachbereichs Physik
der Universität Hamburg

vorgelegt von
Gerhard Meister
aus Hamburg

Hamburg
2000

Abstract

The reflectance of a surface usually depends on the angles, at which the surface is illuminated and viewed. The dependence can be described by the *Bidirectional Reflectance Distribution Function* BRDF. In this study, the BRDFs of several samples typically found in urban areas (roof tiles, asphalt, etc.) were measured at the *European Goniometric Facility* EGO in Ispra, Italy with hyperspectral sensors. The basic characteristics of the measured BRDFs are a specular peak, an increase in backscattering direction for the roughest surfaces and a constant diffuse component for the surfaces of moderate roughness. Surfaces of moderate roughness can be well described by the BRDF model for specular reflection of rough surfaces by (Torrance & Sparrow 1967), whereas for very rough surfaces the model by (Oren & Nayar 1995) is more appropriate. Surface topography measurements suggest that the size of the scattering structure is in the 20 μm range.

In reflectance terminology, the *principal plane* is the plane formed by the surface normal and the illuminating light ray. We found that the angular width of the specular peak of rough surfaces perpendicular to the principal plane decreases proportionally to the cosine of the illumination zenith angle. This result is important in computer vision applications, but it is also of theoretical interest.

The BRDF measurements were also used to develop a BRDF model for urban areas remotely sensed from spaceborne sensors with pixel-sizes above 500 m. The model is built on the street structure of urban areas. It shows a strong increase of reflectance in backscattering direction. Model predictions and simulated data derived from multispectral imagery of an airborne scanner agree well. The major areas of application are albedo calculation and landcover identification in global image data.

Kurzfassung

Die Reflektanz einer Oberfläche ist im Allgemeinen eine Funktion der Ein- und Ausfallswinkel, der sogenannten *Bidirectional Reflectance Distribution Function* BRDF. In dieser Arbeit wurden die BRDFs von Proben gemessen, die für die Fernerkundung von städtischen Gebieten wichtig sind (Dachziegel, Asphalt, etc.). Die Messungen wurden im Labor der *European Goniometric Facility* in Ispra, Italien unter Verwendung hyperspektraler Sensoren durchgeführt. Die grundlegenden Merkmale der gemessen BRDF's sind das Spiegelungsmaximum, ein Anstieg in der Rückstreurichtung für die rauhesten Oberflächen und eine konstante diffuse Komponente für Flächen mittlerer Rauhigkeit. Letztere Flächen werden durch das BRDF Modell von (Torrance & Sparrow 1967) gut beschrieben, während für sehr rauhe Oberflächen das BRDF Modell von (Oren & Nayar 1995) bessere Ergebnisse liefert. Oberflächentopographiemessungen deuten an, dass die Grösse der Strukturen, an denen das Licht gestreut wird, im Bereich um 20 μm liegt.

Bei Reflektanzmessungen bezieht sich der Ausdruck *Hauptebene* auf die Ebene, die durch die Oberflächennormale und den einfallenden Lichtstrahl aufgespannt wird. In dieser Arbeit wird gezeigt, dass die Winkelbreite des Spiegelungsmaximums rechtwinklig zur Hauptebene proportional mit dem Kosinus des Einfallszenitwinkels abfällt. Dieses Ergebnis ist wichtig für Anwendungen in der computergestützten Bilderkennung und Bilderzeugung, es ist aber auch von theoretischem Interesse.

Des weiteren wurden die BRDF Messungen benutzt, um ein BRDF Modell für städtische Gebiete zu erstellen für die Auswertung von Daten von satellitengeststützten Sensoren mit Pixelgrössen von mehr als 500 m. Das Modell basiert auf der Strassenstruktur städtischer Gebiete. Ein starker Anstieg der Reflektanz in Rückstreurichtung wird vorhergesagt. Modellergebnisse stimmen gut mit simulierten Daten überein, die aus Bilddaten eines multispektralen, flugzeuggestützten Sensors abgeleitet wurden. Hauptanwendungsgebiete sind Albedobestimmung und Landklassenidentifikation in globalen Bilddaten.

Contents

Nomenclature

Symbols and abbreviations used throughout this thesis are defined here. Symbols that only have a local meaning, and are defined close to where they are used, are not included here. The list is alphabetical, with the following precedences: lower case before upper case, quantities before abbreviations, Roman before Greek.

Symbol	**Description**	**Page**
a	width of the street of a street structure	113
b	height of the buildings of a street structure	113
c	width of the buildings of a street structure	113
d_f	degrees of freedom	81
f_r	Bidirectional Reflectance Distribution Function	14
g	relative angle between viewing and illumination direction	124
h	area hidden from the detector of a street structure	117
i (subscript)	incident	
k	index of absorption	43
k_d	diffuse albedo in the ON model	47
k_s	specular intensity in the ON model	47
k_w	roughness parameter in the ON model	46
n	index of refraction	43
p_i	parameters in the approximation to the urban BRDF model	137
r (subscript)	reflected	
s	shadowed area of a street structure	117
t_0	Lambertian component in the TS model	43
t_1	intensity parameter in the TS model	43
w	specular peak width parameter in the TS model	43
A	area	
ASF	Angular Sensitivity Function	103
BRDF	Bidirectional Reflectance Distribution Function	14
BRF	Biconical Reflectance Factor	14
F	Fresnel reflectance	43
G	Geometric Attenuation Factor	45
L	radiance	13
$P(\alpha)$	probability distribution of α	45
E	irradiance	14
R	Biconical Reflectance Factor	14
spec (superscript)	specular	
ASD	spectrometer ASDFieldspec	33
AVG	average	
Cadr.	Cadrezzate, Italy	7
EGO	European Goniometric Facility	16
IR	wavelength range for infrared light	

JRC	Joint Research Center, Ispra, Italy	
FOV	field of view	
FWHM	full width half maximum	
NIR	wavelength range for near infrared light	
ON	Oren-Nayar	45
RM600	optical profiler	91
SE590	spectrometer SE590	15
TS	Torrance-Sparrow	43
V	vertical	
VIS	wavelength range for visible light	
α	inclination of a surface facet	45
γ	bin size for spatial averaging	98
θ	zenith angle	87
θ_i'	local incidence angle on a surface facet	45
λ	wavelength	
ρ	albedo	14
ρ_s	specular albedo	49
σ	error or standard deviation	
$\sigma_{\Delta_{\text{ind,j}}}$	standard deviation of $\Delta_{\text{ind,j}}$	20
$\sigma_{\Delta_{\text{norm,j}}}$	normalized $\sigma_{\Delta_{\text{ind,j}}}$	20
φ	relative azimuth angle	120
$\varphi_{i/r}$	azimuth angle of incidence/reflection	113
χ^2	sum of the square of deviations divided by square of error	81
ω	solid angle	13
Δ	difference	
Ω	projected solid angle	13

Chapter 1

Introduction

The reflection of light from rough surfaces is a subject of importance in remote sensing as well as computer vision. A key factor in the evaluation of reflected light is the composition of the illumination, see (Wiemker et al. 1998) for a comprehensive investigation of this topic. In this study, the incoming light is a known quantity, the focus is on the *surface intrinsic* reflection properties.

It is a common assumption (Horn 1986) that a surface is either specular (like a mirror) or Lambertian (Lambert 1760), i.e. the incoming light is reflected isotropically into every direction, or a combination of both. This is illustrated in fig. 1.1.

However, the need for a more accurate description of the variation of reflectance with changing viewing or illumination geometry has been clearly recognized, for remote sensing applications by (Kimes 1983), (Roujean et al. 1992), (Rahman et al. 1993), (Wanner et al. 1997), (Strahler 1997), (Diner et al. 1999), as well as for computer vision (Nayar et al. 1991), (Schlick 1994), (Oren & Nayar 1995), (Wolff 1996). We will use the *Bidirectional Reflectance Distribution Function* BRDF as defined by (Nicodemus 1970) to describe the directional reflectance properties.

Smooth surfaces can be considered specular, i.e. the incident light is reflected into one direction only. Most surfaces are not smooth but rough. If the surface height function $h(x, y)$, where x and y are the horizontal location parameters, satisfies the restrictions $|h(x, y)|/\lambda \ll 1$ and $|\bigtriangledown h(x, y)| \ll 1$, i.e. if the surface roughness is small compared to the wavelength of the incident light λ and the inclination of the local slopes of the surface is small as well, *perturbation theory* can be used to analyze the specular peak (Ogilvy 1992) by assuming that the scatterer satisfies certain boundary. The wave character of light becomes apparent for such surfaces.

According to (Ogilvy 1992), the most quoted book on wave scattering from rough surfaces is that of (Beckmann & Spizzichino 1963). In this book, the radiation fields are analyzed for surfaces using Kirchhoff theory, also known as tangent plane or physical optics theory. The basic assumption is that the surface does not have any sharp edges compared to the wavelength of the incident light. Thus this theory is applicable to a much wider range of surfaces than perturbation theory.

This study focuses on man-made surfaces, most of which are characterized by a strong roughness in the μm scale, such that the assumptions of perturbation theory or physical optics become invalid. The BRDF of man-made surfaces has recently received widespread attention ((Stavridi et al. 1997), (Ginneken et al. 1998), (Oren & Nayar 1994)). An extensive BRDF database for man-made-surfaces is easily accessible via Internet (CUReT 1996) and well documented (Dana et al. 1999), (Dana et al. 1996). Unfortunately, this database does not include some surface types important for remote sensing of urban areas, like e.g. asphalt, and only one type of roof cover. Furthermore, it is restricted to 3 spectral channels (red, green and blue). In our research group, a systematic measurement campaign to determine the BRDF of surfaces typical for urban areas has been conducted at the European Joint Research Center at Ispra, Italy, using the EGO (*European Goniometric Facility* (Solheim et al. 1996)) and 2 hyperspectral sensors. Our campaign at the EGO has been the first

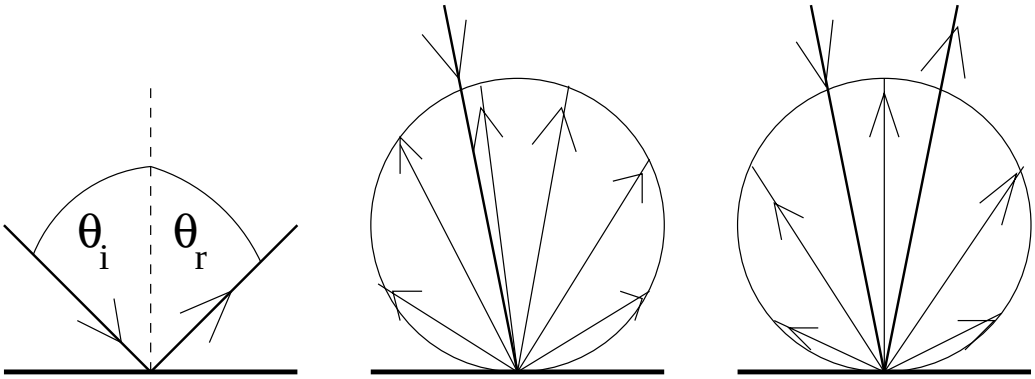

Figure 1.1: Specular and Lambertian reflection. Plot on the left: specular reflection, incoming light from zenith angle θ_i is reflected into direction $\theta_r = \theta_i$ only. Center plot: Lambertian reflection, incoming light is reflected into all directions of the upper hemisphere proportional to the cosine of the reflection zenith angle θ_r, indicated by the length of the arrows. Plot on the right: mixture of specular and Lambertian reflection. The area viewed by a radiance measuring sensor is inversely proportional to $\cos\theta_r$, thus the radiance measured by the sensor is independent of the viewing angle for a Lambertian surface. But the reflected radiance does depend on the illumination angle, for a Lambertian surface it is proportional to $\cos\theta_i$.

extensive study of urban surfaces at this laboratory. We fully exploited the bidirectional capabilities of the EGO by performing extensive measurements covering all azimuth angles, with especially dense angular grids around the specular direction.

We found that many man-made rough surfaces show a broadened specular peak, whose shape can be well described by the BRDF model of (Torrance & Sparrow 1967). This model assumes that the surface consists of a superposition of symmetric V-cavities of indefinite length (see fig. 1.2) heading into all horizontal directions. 'Crossings' between V-cavities are ignored. The facets reflect the incoming light like mirrors (with an adjustable dampening coefficient). The angular distribution of facet slopes determines the width of the specular peak.

We discovered that the width of the specular peak perpendicular to the plane of incidence decreases proportionally to the cosine of the illumination angle. This is a very important result for image rendering [1] applications, where the Phong-model (Phong 1975) is often used, which predicts a constant width of the specular peak. We also found that shape and intensity of the specular peak do not vary strongly with wavelength, less than 10 % from 450 nm to 700 nm, even with the diffuse component varying strongly with wavelength. The diffuse component of the BRDF is often Lambertian. Only for very rough surfaces (like e.g. asphalt) it is necessary to model masking and shadowing effects, the BRDF model of (Oren & Nayar 1995) predicts the observed increase in backscattering direction very well. This model is similar to the TS model, but it assumes that the facets reflect the incoming light diffuse.

We compared results on the width of the specular peak to surface topography data with a horizontal resolution of 1 μm and a vertical resolution of 0.16 μm. Unfortunately, the results from this section are not conclusive.

[1] i.e. creating images with a computer that appear as realistic as possible

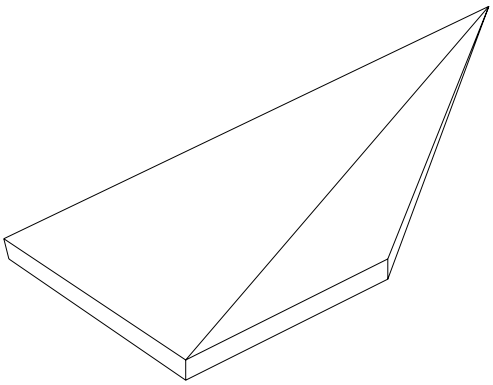

Figure 1.2: A symmetric cavity of the Torrance-Sparrow model. It is impossible to physically realize the superposition of these cavities heading into different directions, thus we can only present one cavity here.

The results of the BRDF measurement campaign for samples with areas in the cm range were used in the development of a BRDF model for remote sensing of urban areas at pixel-sizes in the km range. In recent years, remotely sensed, multiangular global data sets have become available, in particular from AVHRR (James & Kalluri 1994) and POLDER (Leroy et al. 1997). With the upcoming operation of multiangular sensors like MODIS/MISR (Wanner et al. 1997) and MERIS (Bezy & Gourmelon 1999) the availability and potential of such imagery will be largely enhanced. The prime dedication of the sensors is albedo determination (e.g. for global climate models) and global land cover monitoring at relatively coarse pixel sizes between 0.3 and 8.0 km. Land cover classification often focuses on vegetation and bare soil areas, but for a detailed approach to this kind of data it is necessary to identify the urban areas as a landcover class as well. The BRDF must be determined for each landcover class in order to derive albedo or to support multiangular and multitemporal monitoring. There have been numerous studies for vegetated surfaces (e.g. reviewed in (Myneni et al. 1995), (Qin & Goel 1995)), as well as for bare surfaces ((Hapke 1993), (Jacquemoud et al. 1992), (Liang & Townshend 1996b), (Staylor & Suttles 1986), (Li et al. 1996), (Gibbs et al. 1993), (Deering et al. 1990)). There have been studies determining the BRDF of man made surfaces for sizes about 10 cm $\times$ 10 cm (Torrance & Sparrow 1967), (Oren & Nayar 1995), (Wolff 1996), (Ginneken et al. 1998), (Stavridi et al. 1997), (Schlick 1994), (Dana et al. 1999), (Meister et al. 1996a), (Meister et al. 1999c). But the bidirectional reflectance of urban areas has not been investigated before for data with a pixel-diameter of about 1 km.

In fact, there are several problems associated with the design of an urban BRDF model on this scale. The biggest one is the large heterogeneity within an urban area: the homogeneity needed to properly define a BRDF (Nicodemus et al. 1977) is very often interrupted by large scale structures like rivers, airports, train stations, etc. Furthermore cities like Cairo, New York City and Geneva are so different that it is quite challenging to design a BRDF model that covers them all. Even within a single city, different BRDFs are expected for different parts of the city, consider e.g. a downtown area with high-rise buildings and a suburban area with one storeyed houses. However, all cities have a common property that can be exploited for the design of a BRDF model: every urban area contains a street structure, whose BRDF effect can be relatively simply modeled by geometrical optics. Although in each city there may be many different street structures (e.g. low buildings at a wide street and high buildings at a narrow street), we will show that it is sufficient to use the average street dimensions to achieve a good approximation to the overall BRDF.

We readily admit that the proposed BRDF model may be insufficient to *accurately* describe the BRDF of urban areas in general. However, airborne data measured by us show strong deviations (factor of 2) from the commonly assumed Lambertian behavior. Therefore our model is a useful first approximation with an anticipated accuracy in the 20 % range.

There are several possible *areas of application*: 1) Albedo calculation can be improved by including BRDF effects. 2) The *atmospheric correction* of measured radiances is strongly intertwined with the BRDF of the respective pixel (Wanner et al. 1997), (Vermote et al. 1997a). 3) Common *change detection* algorithms do not consider BRDF effects and will most likely give wrong results if the BRDF effect is as strong as shown here. 4) *Classification* algorithms can benefit from an improved knowledge about the BRDF of the underlying classes. 5) A global map of *simulated reflected radiances* necessarily includes BRDF information from all landcover classes.

This thesis consists of the following chapters: in chapter 2, the investigated samples are briefly described. Then the radiometric quantities are defined, following the notation of (Nicodemus 1970). Chapter 4 presents the error determination for the laboratory BRDF measurements. The next chapter describes the measurement results and evaluates the performance of the BRDF models by (Torrance & Sparrow 1967) and (Oren & Nayar 1995). The findings on the width of the specular peak perpendicular to the plane of incidence are presented in chapter 6. The topography measurements are discussed in chapter 7. Chapter 8 describes a post-flight angular calibration method for airborne scanner data. This method was applied to DAEDALUS data, to obtain the large scale BRDF data needed in chapter 9, where a BRDF model for large scale urban areas is developed. A summary concludes the main part of this thesis.

Chapter 2

Description of the Samples

2.1 Overview

In this chapter, the samples are described that have been used in this study. We give a qualitative description and show which kinds of measurements were performed on each sample. The goal is to investigate the BRDF of man-made materials important for remote sensing of urban areas. We chose several materials that represent roof coverings as well as street coverings. We restricted ourselves to surfaces that looked rotationally symmetric, in order to be able to describe the BRDFs only with a relative azimuth φ. BRDFs depending on both the incident and viewing azimuth are much more tedious to measure. We also included a few materials (wall paper, plastic, red painted aluminum) that are relatively unimportant in remote sensing imagery, but help to explore the range of BRDFs of urban areas and are more useful e.g. in computer vision or image rendering. Two reference panels were used for calibration purposes.

Table 2.1 gives an overview of the measurements performed for each sample. Two sensors were used for the radiometric BRDF measurements: SE590 and ASDFieldspec. The details are given in chapter 4, the basic difference between the two sensors are

- wavelength range: the SE590 covers 425 nm to 925 nm, the ASDFieldspec covers 450nm to 2280 nm
- angular coverage: for the ASDFieldspec, we measured only in forward scattering direction ($\varphi = 180^\circ$), whereas with the SE590 we varied the relative azimuth angle continously from 0° to 180°
- reliability: the ASDFieldspec turned out to be less stable than the SE590, and some of the measurements in the specular direction have overflows.

Furthermore surface profiles were taken for several samples. Results from the topography measurements are presented in chapter 7.

2.2 Qualitative Description

Pictures of the samples taken with a digital camera are shown in figures 2.1 to 2.4. For some samples, we also provide close-up photographs. All pictures include an ordinary pen serving as a size reference. The pictures are shown in the same order as in table 2.1.

Unless otherwise noted, all the samples are new, i.e. they were not exposed to field conditions for extended periods of time. We focused our study on 'new' samples because the dirt that accumulates on surfaces exposed to exterior influence can be distributed inhomogeneously over the surface, thus preventing rotational symmetry.

Sample	SE590	ASD	Topography
Spectralon 0.5	X	X	
Spectralon 1.0	X	X	
Red concrete	X	X	X
Blue concrete	X	X	X
Black concrete		X	
Red roof tile	X	X	X
Roof tile (Opal)		X	X
Sanded roof paper	X	X	(X)
Green roof paper		X	(X)
Red roof paper		X	
Wall paper		X	(X)
Brown slate		X	X
Green slate		X	
Red slate		X	X
Dirty roof tile		X	
Asphalt (Cadr.)	X		
Asphalt (Ispra)		X	(X)
Walkway slab		X	
Plastic		(X)	X
Red aluminum	X	X	X

Table 2.1: Overview of the measurements performed for each sample. X indicates a successful measurement series, (X) indicates that the measurements series was discarded because of too many overflows.

- The two Spectralon panels were produced by Labsphere, Inc.,Boulder, Colorado (USA). The '**Spectralon 1.0**' panel has an albedo of almost 1.0, the exact numbers are wavelength dependent. It belongs to the TDP unit of the JRC, Space Applications Institute in Ispra, Italy. Its internal reference number is WT05. The '**Spectralon 0.5**' panel belongs to our group (CENSIS at the Institute of Experimental Physics, University of Hamburg, Germany). Its albedo is about 0.51, see (Meister 1995) for a table of the albedos as a function of wavelength.

- '**Red concrete**', '**blue concrete**' and '**black concrete**' refer to three concrete tiles produced by Braas GmbH, Hamburg. All the tiles have a very similar surface structure, the only difference between these tiles is the color pigments added during production. The tiles are very homogeneous, rotational symmetry is given. Their surface area is 40 cm x 29 cm, thus the positioning of the sample in the center of the field of view (FOV) is easy. The concrete tiles were produced by *Braas Dachsysteme GmbH, Germany*.

- '**Red roof tile**' is a tile made of baked clay whose color is between red and orange. This type of roof tile is called 'Biberschwanz' in German, literally translated to English: 'beaver's tail'. The reason is its flat shape. This is a very important feature, because many roof tiles have a sinusoidal shape, which makes them unsuitable for laboratory BRDF measurements [1]. The area of one tile is 15 cm x 30 cm. In order to obtain a surface big enough to cover the FOV of the sensor even for large zenith angles, we put 3 tiles next to each other. Although the edges violate rotational symmetry, the effect of the edges is so small that it can easily be ignored.

[1] These measurements are presented in (Meister et al. 1996a), (Meister et al. 1999c)

- '**Roof tile (Opal)**' is another roof tile made of baked clay very similar to the 'Red roof tile' described above, but its size is much smaller, only 19 cm x 18 cm. It is colored red. It is very homogeneous.

- '**Sanded roof paper**' is a roof paper made of bitumen partly covered with quartz (sand) grains with a diameter of about 1 mm to 2 mm. Thus it has a very complicated surface structure: a dark background covered with bright objects. A very non-lambertian BRDF is expected, because the background is strongly recognizable from nadir viewing, but it is hidden from sight for oblique viewing. The distribution of quartz grains is random, but very homogeneous over areas larger than 2 cm x 2 cm, thus we expect rotational symmetry despite the complicated structure. The total area is larger than 40 cm x 40 cm.

- '**Green roof paper**' and '**red roof paper**' are bitumen roof papers that are partly covered by patches that are black or green resp. red. The shape of the patches is ellipsoidal to rectangular, with edges from 0.3 cm to 1.5 cm. Between the patches 'valleys' up to 1 mm deep are possible. The samples appear to be rotationally symmetric to the human observer. The size is 23 cm x 27 cm.

- '**Brown slate**': slate (in German: 'Schiefer') tiles are a common roof cover in the USA, in Germany they are mainly used to cover small sections of the roof, especially if a section of a roof is vertical. Our sample was assembled from two parts to form an area of 27 cm x 26 cm. Again, the effects of the edges are so small that they can easily be ignored concerning rotational symmetry.

- '**Red slate**' and '**green slate**' not only differ in color from 'brown slate', also their surface looks smoother than 'brown slate'. The area of the sample was only 17 cm x 14 cm, thus special care had to be taken to position the samples in the center of the FOV.

- '**Dirty roof tile**' is a roof tile made of baked clay that was actually used as a roof tile for probably more than 50 years. Dirt is distributed inhomogeneously over the surface, rotational symmetry cannot be assumed. The tile is of type 'Biberschwanz'. The size is only 14 cm x 13 cm.

- The sample '**Asphalt (Ispra)**' was taken from a construction site in Ispra, Italy, the sample '**Asphalt (Cadr.)**' was found in Cadrezzate, Italy. Both samples show irregularly colored patches (gravel inclusions) on a grey background. The patches are relatively small (covering about 10 % of the surface) with diameters of about 0.5 cm to 1 cm, thus we expect deviations from rotational symmetry to be small. The size of 'Asphalt (Ispra)' is about 20 cm x 30 cm, the size of 'Asphalt (Cadr.)' is 15 cm x 11 cm. The asphalt samples have the greatest roughness of the samples used in this study (except for 'sanded roof paper'). As both samples were actually used as street coverings before and covered with sand from the construction sites, we rinsed them with water.

- '**Walkway**' is a part (area: 20 cm x 15 cm) of a typical grey concrete walkway slab (original area: 50 cm x 50 cm) used by pedestrians, taken from a construction site in Hamburg, Germany. Its roughness is comparable (probably rather higher) to the roughness of the sample 'red roof tile'. It is very homogeneous. We also rinsed it with water to remove the sand stemming from the construction site.

- '**Wallpaper**' is a piece of rough wallpaper (in German: 'Rauhfasertapete') with an area of 32 cm x 28 cm painted white. Its topography shows large variations (up to 2 mm), still it seems to show rotational symmetry to the human eye.

- '**Plastic**' is a tray of white plastic (made for household use). It is very smooth, has a shiny surface and is extremely homogeneous. Its dimensions are 37 cm x 25 cm.

- ’**Red aluminum**’ is a sheet with a thickness of 5 mm of aluminum with an area of 40 cm x 30 cm. It was painted red by using a spray produced by ’BÜFABaeuerle Farben GmbH’, the color-type is blazing red. The surface is glossy and very homogeneous.

Spectralon 0.5

Red concrete

Blue concrete

Black concrete

Red roof tile

Red roof tile (close-up)

Figure 2.1: Pictures taken with a digital camera of Spectralon 0.5; red, blue and black concrete tiles; and red roof tile.

Roof tile Opal

Roof tile Opal (close-up)

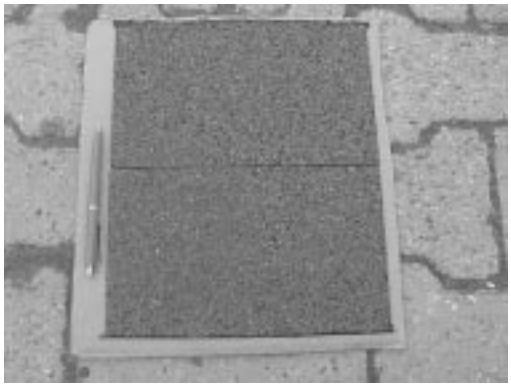

Green roof paper

Green roof paper (close-up)

Red roof paper

Wall paper

Figure 2.2: Pictures taken with a digital camera of roof tile Opal, green roof paper, red roof paper and wall paper.

Brown slate

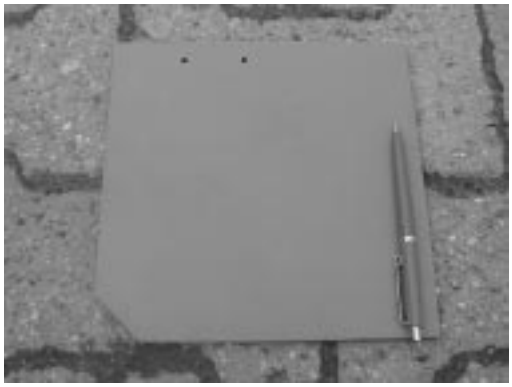

Green slate

Green slate (close-up)

Red slate

Dirty roof tile

Dirty roof tile (close-up)

Figure 2.3: Pictures taken with a digital camera of brown, green and red slate tiles, and dirty roof tile.

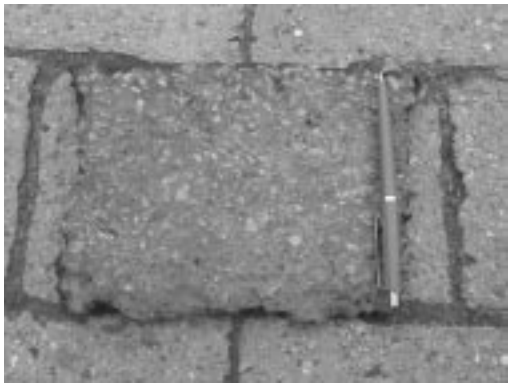

Asphalt (Ispra)

Asphalt (Ispra) (close-up)

Plastic

Plastic (close-up)

Red aluminum

Red aluminum (close-up)

Figure 2.4: Pictures taken with a digital camera of asphalt (Ispra), plastic and red aluminum.

Chapter 3

Radiometric Quantities

3.1 Radiance L

In this study, we use the radiometric notation introduced by (Nicodemus 1970) and (Nicodemus et al. 1977). Electromagnetic radiation can be measured as **radiant flux** Φ [W] (energy of photons per time which pass the aperture of the sensor). **Radiance** L is defined by

$$L \equiv \frac{\partial^2 \Phi}{\cos\theta \cdot \partial A \cdot \partial \omega} \tag{3.1}$$

$\partial\omega = \sin\theta \cdot \partial\theta \cdot \partial\phi$ is the solid angle, θ is the zenith angle and ϕ is the azimuth angle. A is the area considered (either a detector area or a surface area). The radiance is constant along a ray of light if the medium neither absorbs nor scatters. Usually, radiance is defined per wavelength interval, thus the unit becomes $[\mathrm{W} \cdot \mathrm{m}^{-2} \cdot \mathrm{sr}^{-1} \cdot \mu\mathrm{m}^{-1}]$.

3.2 Bidirectional Reflectance Distribution Function BRDF

The *Bidirectional Reflectance Distribution Function* (**BRDF**) has been accepted by the scientific community as the most appropriate way of describing diffuse reflection. The radiant flux $d\Phi_i$, originating from the direction (θ_i, ϕ_i), hitting an infinitesimal surface element $\mathrm{d}A$ is given by

$$\mathrm{d}\Phi_i = L_i(\theta_i, \phi_i) \cdot dA \cdot \mathrm{d}\Omega_i \ \ [\mathrm{W}] \tag{3.2}$$

where $\mathrm{d}\Omega_i$ is the projected solid angle:

$$d\Omega_i \equiv \cos\theta_i \cdot d\omega_i \ \ [\mathrm{sr}]. \tag{3.3}$$

For a diffuse surface, $\mathrm{d}\Phi_i$ will be scattered into all directions of the upper hemisphere. In case the light source is not a true point source (which is especially important for *in situ* measurements), the radiance reflected into the direction (θ_r, ϕ_r) will be a superposition of radiation stemming from different directions:

$$L_r(\theta_r, \phi_r) = \int_{\omega_i} dL_r(\theta_i, \phi_i, \theta_r, \phi_r) \tag{3.4}$$

If a sensor at direction (θ_r, ϕ_r) is pointed at a surface illuminated from (θ_i, ϕ_i) , it would measure

$$\mathrm{d}\Phi_r = \mathrm{d}L_r(\theta_i, \phi_i, \theta_r, \phi_r) \cdot \mathrm{d}A \cdot \mathrm{d}\Omega_r \tag{3.5}$$

where $\mathrm{d}\Omega_r$ is determined by the FOV of the sensor.

It is possible to define a quantity X as

$$X = \frac{d\Phi_r}{d\Phi_i} = \frac{dL_r \cdot d\Omega_r}{L_i \cdot d\Omega_i}. \tag{3.6}$$

X is dimensionless and invariant against L_i and $\mathrm{d}\Omega_i$, because both quantities are directly proportional to $\mathrm{d}L_r$ (doubling the incoming light will double the reflected light). Unfortunately, X is not invariant with respect to $\mathrm{d}\Omega_r$, but proportional to it (a detector with a larger FOV will measure a greater $\mathrm{d}\Phi_r$ reflected from a diffuse surface, because $\mathrm{d}\Omega_r$ increases). Thus (Nicodemus et al. 1977) introduced the Bidirectional Reflectance Distribution Function f_r:

$$f_r(\theta_i, \phi_i, \theta_r, \phi_r) \equiv \frac{dL_r(\theta_i, \phi_i, \theta_r, \phi_r)}{L_i(\theta_i, \phi_i) \cdot d\Omega_i} \ [\mathrm{sr}^{-1}] \tag{3.7}$$

f_r **depends only on properties of the surface and is independent of characteristics of the light source or the detector.**

For a *Lambertian* surface, the BRDF is constant with respect to illumination and viewing angle. For a perfectly specular surface, the BRDF becomes a product of two Dirac delta-functions (Nicodemus et al. 1977):

$$f_r = 2 \cdot \delta(\sin^2\theta_r - \sin^2\theta_i) \cdot \delta(\phi_r - \phi_i \pm \pi) \tag{3.8}$$

3.3 Irradiance, Albedo and BRF

The **irradiance** E_i is a measure for the total radiative energy reaching the surface. It is defined as

$$E_i \equiv \frac{d\Phi_i}{dA} \tag{3.9}$$

Integrating the incoming radiance L_i over the upper hemisphere yields the radiance:

$$E_i \equiv \int_\Omega L_i(\theta_i, \phi_i) \ d\Omega = \int_{\phi_i=0}^{\phi_i=2\pi} \int_{\theta_i=0}^{\theta_i=\frac{\pi}{2}} L_i(\theta_i, \phi_i) \cdot \sin\theta_i \cdot \cos\theta_i \ d\theta_i d\phi_i \tag{3.10}$$

The unit of irradiance is $\mathrm{W{\cdot}m^{-2}}\mu\mathrm{m}^{-1}$. Very often, BRDF is defined as the ratio of reflected radiance and irradiance:

$$f_r \equiv \frac{dL_r(\theta_i, \phi_i, \theta_r, \phi_r)}{dE_i(\theta_i, \phi_i)} \tag{3.11}$$

which is equivalent to the definition of eq. 3.7.

The **albedo** (called '*directional-hemispherical reflectance*' by (Nicodemus 1970)) can be calculated by integrating the reflected radiances L_r over the upper hemisphere and dividing by the irradiance, if the irradiance originates from only one direction:

$$\rho \equiv \frac{\int_\Omega L_r(\theta_r, \phi_r) \ d\Omega}{E_i} \tag{3.12}$$

The albedo can be a function of the incidence angle θ_i.

The *bidirectional reflectance factor* is defined as

$$R(\theta_i, \phi_i, \theta_r, \phi_r) = \pi f_r(\theta_i, \phi_i, \theta_r, \phi_r). \tag{3.13}$$

The *biconical reflectance factor* **BRF** is defined as

$$R(\omega_i, \omega_r) = \frac{\pi}{\Omega_i \Omega_r} \cdot \int_{\omega_i} \int_{\omega_r} f_r(\theta_i, \phi_i, \theta_r, \phi_r) d\Omega_r d\Omega_i \ [\mathrm{dimensionless}] \tag{3.14}$$

where π has the unit [sr]. A difference between these two quantities only emerges if the BRDF varies strongly within either $\mathrm{d}\omega_i$ or $\mathrm{d}\omega_r$, which is rarely the case for diffuse surfaces. We will follow common practice and neglect the distinction.

Chapter 4

Radiometric Calibration of the EGO Sensors

4.1 Overview

The European Goniometric Facility (EGO) at the Space Applications Institute, Joint Research Center, Ispra, Italy, provides the opportunity for laboratory multiangular reflectance measurements. This chapter describes the error analysis for our measurement campaign at the EGO. The errors will be used in the following chapters. The results can also be directly used for future measurement campaigns at the EGO, and the methods presented are useful for any similar experiment setup. The average total error depends strongly on the spectral signature of the sample for the SE590 detector (Spectron Engineering), varying from 4 % to up to 14 %. The spatial illumination heterogeneity is identified as the largest error source. Its effects increase with increasing zenith angles. It is shown that the instrument noise of the detector SE590 is a function of the maximum signal in a measured spectrum. Based on this result, a procedure to define the wavelength range with acceptable measurement errors is presented. Different ways to calculate the irradiance are compared. It is shown that calculating a constant irradiance for each incidence angle is in better agreement with the reciprocity principle than assuming a different irradiance for each illumination and viewing geometry. The measurement error of the ASDFieldspec is found to be dominated by dark current noise. Parts of this chapter have been published in (Meister et al. 1999d).

4.2 Experimental Setup

The goniometer at EGO consists of two quarter arcs with a radius of 2 m, see fig 4.1 for an illustration. A sensor and a light source can be attached to the arcs, their position on the arc determines the zenith angle. The arcs can be moved on a circular rail (radius: 2 m), determining the azimuth angle. The angles can be positioned with an accuracy of 0.1°. Several light sources and sensors are available, we used a 1000 W halogen lamp and a spectroradiometer SE590, Spectron Engineering Inc., Denver, USA. The target samples were man-made surfaces typical of urban areas like e.g roof tiles or asphalt. They are ideal for laboratory measurements because of their homogeneity and temporal invariance, opposed to e.g. vegetation samples, see (Sandmeier et al. 1998). The sections in this chapter discuss the following aspects for the SE590: wavelength considerations, lamp constancy and detector noise, illumination heterogeneity, determination of the irradiance, total measurement error and reciprocity principle. Concerning the ASDFieldspec, wavelength range, BRDF calculation and error determination are discussed. The chapter concludes with a comparison of the SE590 and the ASDFieldspec data.

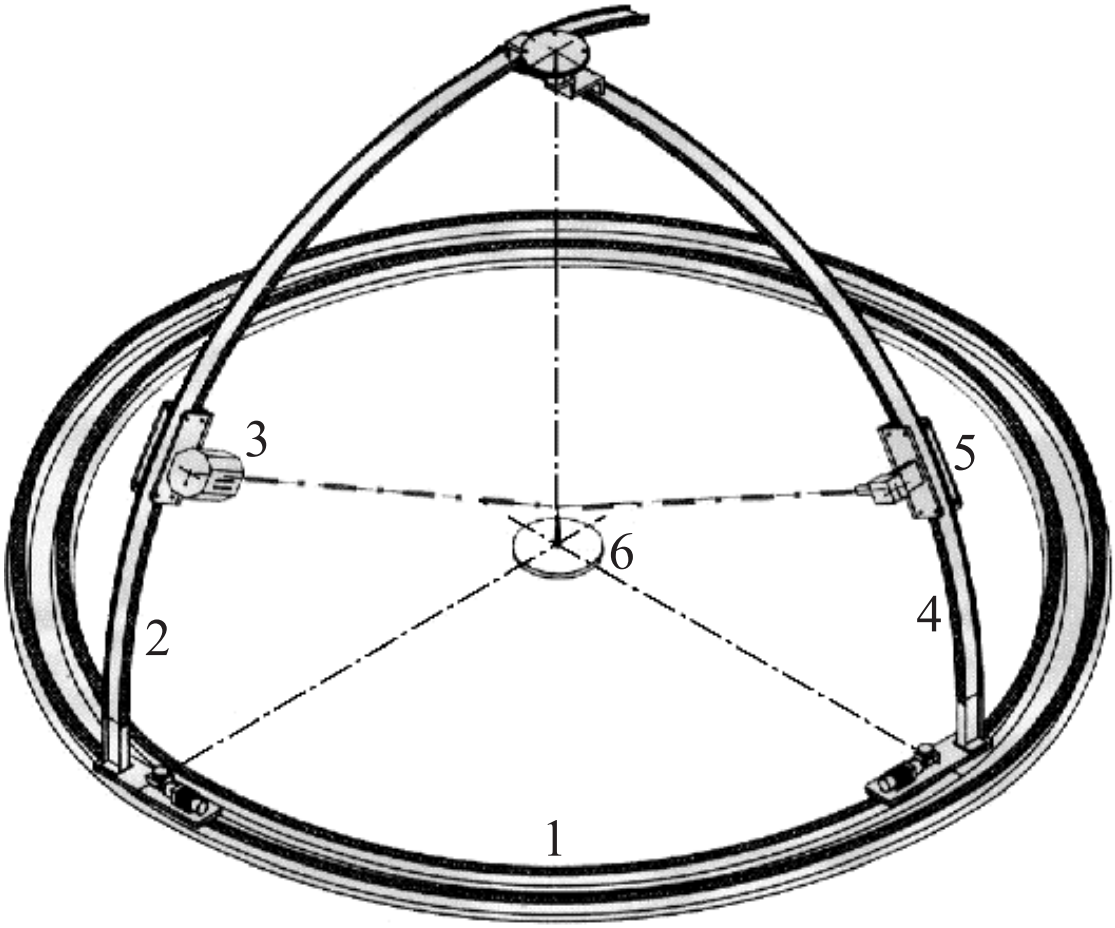

Figure 4.1: Design of the EGO: two quarter arcs (’2’ and ’4’), running on circular rails (’1’). Sleds are attached to the arcs to carry light source (’3’) and sensor (’5’). The sample is placed in the center (’6’). This sketch, originally published by JRC, was edited by André Rothkirch to account for recent changes to the goniometer design.

4.3 Wavelength Characteristics of the SE590

4.3.1 Wavelength Resolution

The wavelength range of the SE590 covers 400 nm to 1100 nm with 252 channels, i.e. a sampling interval of about 3 nm per channel. There is a strong overlap of the spectral sensitivity function between adjacent channels. The full width half maximum (FWHM) spectral resolution is 3 to 4 detector elements, or 10 nm, if no FOV (field of view) optics is used (standard slit aperture), for smaller slit apertures a resolution of 1 to 2 detector elements is possible (all values quoted from the SE590 documentation by Spectron Engineering). We found that the sampling interval increases from 2.6 nm for short wavelengths to 3.1 nm for long wavelengths.

We measured the signal of a green laser at 543 nm after being scattered on white paper with a 1° FOV optics. The FWHM is less than the quoted 10 nm, rather about 5 nm. The small FWHM can be attributed to the 1° FOV optics, after removing this device the FWHM increases to about 15 nm. Similar results were obtained by (Rothkirch et al. 1999). Although we used the 1° FOV optics for our campaign, we chose to average over 5 detector elements. This yields 50 channels with a sampling interval of about 15 nm and ensures that the averaged signals will only be weakly influenced by neighboring pixels. The strong overlap of the spectral sensitivity functions between each detector element (praised in the documentation, because it prevents sensitivity gaps) is rather inconvenient for our purposes, because we need signals not disturbed by neighboring wavelengths. The error stemming from the signal of neighboring wavelengths after averaging is negligible in our case, because our signals do rarely show rapid variations within short wavelength intervals. For outdoor measurements, where sharp atmospheric absorption lines can be seen in the data, e.g. O_2A at 760 nm, an error estimation might be necessary.

4.3.2 Wavelength Calibration

The wavelength calibration of the SE590 using the 1° FOV is not quite exact: the peak in the green laser spectrum is expected to be at 543 nm, the highest measured value is at 544.7 nm, see fig. 4.2. Given the sampling interval of 2.8 nm, i.e. the neighboring detector elements are at 541.9 nm and 547.5 nm, an exact calibration would have yielded the peak value (or peak center in case of an asymmetric peak) at 541.9 nm. For the standard slit aperture, the highest value is at 544.7 nm too, but the peak center is shifted by about 1 detector element towards smaller wavelengths, yielding the expected 541.9 nm. Results from (Rothkirch et al. 1999) also show a very good agreement between wavelength calibration and a red (632.8 nm) laser spectrum for the standard slit aperture. This indicates that the wavelength calibration is optimized for the standard slit aperture. We conclude that for the 1° FOV optics the wavelength calibration has an error about as large as the instrument sampling interval, which is negligible for us as we summarize over 5 detector elements (see section 4.3.1). As the check of wavelength calibration was made for only two wavelengths (534 nm and 633 nm), it is possible that different errors occur at other wavelengths.

4.3.3 Wavelength Range

The wavelength range of the SE590 is 400 nm to 1100 nm according to the SE590 documentation. The data even contains a larger wavelength range, from 368.4 nm to 1113.7 nm. The measured spectrum is the product of the lamp spectrum, the target reflectance and the sensor sensitivity. The measured intensity is always very weak below 400 nm and above 1000 nm. It will be shown in section 4.4 that there is a detector noise of about 0.2 % of the maximum signal. This would give a very high error for those wavelengths with low counts, about 20 % at 1100 nm. We excluded those wavelengths where the average detector noise is expected to be higher than 2 %. Therefore we computed the average spectrum of all samples after normalizing to its maximum value, see fig. 4.3. All the values lower than 0.1 (dashed line) correspond to average detector noise

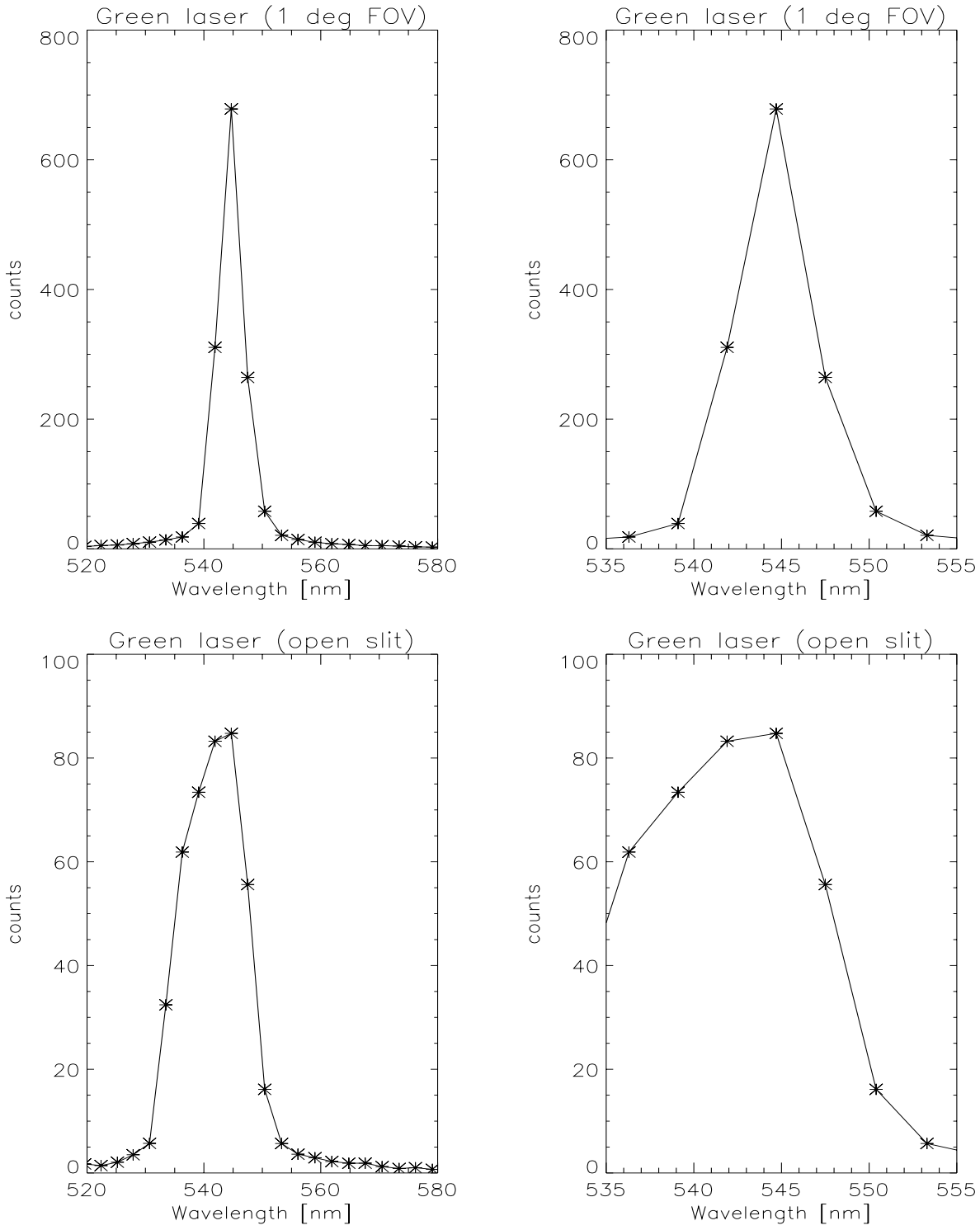

Figure 4.2: Spectrum of the green laser for the 1° FOV (top) and open slit aperture (bottom). The right column shows the same data but for a smaller wavelength range. The peak center for the 1° FOV data is shifted by about 1 detector element (2.8 nm) to shorter wavelengths when compared to the open slit aperture.

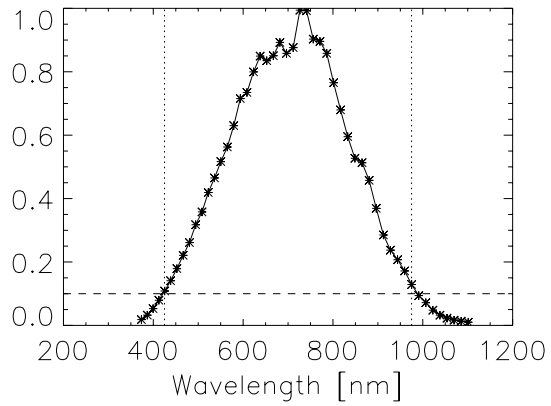

Figure 4.3: SE590 counts normalized to the maximum value of each respective spectrum, averaged over all samples. Stars indicate the values averaged over 5 detector elements (see section 4.3.1). The values below 0.1 (dashed line, corresponding to 10 % of the maximum value) have average detector noise levels higher than 2 %. For this study, only those wavelengths with a better average detector noise will be considered (425 nm to 975 nm, vertical dotted lines).

levels bigger than 2 % (0.2 % / 0.1 = 2 %). Thus we restrict the wavelength range used for this study from 425 nm to 975 nm (dotted line), this yields 38 channels after averaging.

4.4 Lamp Constancy and SE590 Detector Noise

The SE590 has an automatic dark current subtraction. But measurements with a cap blocking all incoming light still yield a signal of about 0.5 counts, averaged over all dark current measurements and wavelengths. We believe that this value is associated with a wrong offset in the data processing software, see (Rothkirch et al. 1999), and therefore subtract it from all our measurements. We estimate the error from dark current to be about 1 count, the digitization error is 0.5 counts. We will combine these two errors in $\sigma_{\text{dc}} = 1.5$ counts. In most cases, σ_{dc} is negligible because the measured signals are usually well above 100 counts.

In order to investigate the measurement errors, we measured the spectrum before (named M_j^b) and after (named M_j^a) each SE590 measurement series (named scenario) 'j' at $\theta_i = 30^\circ$ and $\theta_r = 0^\circ$. The time passed between these two measurements varies from 30 minutes to 2.5 hours. The differences between these measurements do not increase significantly with time, thus we found no evidence of a thermal drift of the system. A look at the differences suggests that they consist of a relative deviation (relative to the mean signal $M_j^m(\lambda) = (M_j^b(\lambda) + M_j^a(\lambda))/2$) plus a part that is caused by detector noise. Although in principle the relative deviation can also be caused by the detector, e.g. induced by temperature variations, it is far more likely that the relative deviation is caused by fluctuations of the lamp, because a change in the lamp intensity will result in a relative change of the measured signal. The lamp has a stabilized voltage source. Based on the results of previous measurements, we expected that the variation in signal due to these fluctuations is less than 1 %.

We regard the difference $\Delta_{\text{tot,j}} = M_j^b - M_j^a$ as being composed of a part proportional to the shape of the mean signal $\Delta_{\text{prop,j}}$ and a part independent of the shape of the mean signal $\Delta_{\text{ind,j}}$:

$$\Delta_{\text{prop,j}} + \Delta_{\text{ind,j}} = \Delta_{\text{tot,j}} = M_j^b - M_j^a \tag{4.1}$$

Our goal is to determine $\Delta_{\text{prop,j}}$ and $\Delta_{\text{ind,j}}$. We assumed that a change in lamp intensity $\Delta I_{\text{lamp,j}}(\lambda)$ is proportional to the spectrum of the lamp: $\Delta I_{\text{lamp,j}}(\lambda) = p_j \cdot I_{\text{lamp,j}}(\lambda)$, where p_j is a number (not a

function of wavelength) specific to each scenario j. Then $\Delta_{\text{prop,j}}$ can be written as

$$\Delta_{\text{prop,j}}(\lambda) = p_j \cdot M_j^m(\lambda) \tag{4.2}$$

Varying the parameter p_j we minimized $|\Delta_{\text{ind,j}}|$ (cf. equations 4.1 and 4.2):

$$|\Delta_{\text{ind,j}}(\lambda)| = |\Delta_{\text{tot,j}}(\lambda) - p_j \cdot M_j^m(\lambda)| = \text{ minimum} \tag{4.3}$$

because in this way the component of $\Delta_{\text{tot,j}}$ that is proportional to M_j^m is removed. The remaining spectrum is not proportional to the shape of M_j^m and can thus be associated with $\Delta_{\text{ind,j}}(\lambda)$.

We want to determine what change in lamp intensity is expected from one measurement to another ignoring whether this change corresponds to an increase or to a decrease. This is given by the average of the absolute of p_j:

$$\sigma_{\text{lamp}} = \frac{1}{n_j} \sum_j |p_j| = 0.003 \tag{4.4}$$

where n_j is the number of scenarios. We regard this value (0.3 %) as an estimate for the lamp constancy. The procedure of minimizing $\Delta_{\text{ind,j}}(\lambda)$ (eq.4.3) leads to an underestimation of $\Delta_{\text{ind,j}}(\lambda)$ and an overestimation of $\Delta_{\text{prop,j}}(\lambda)$. This can be understood imagining a $\Delta_{\text{tot,j}}(\lambda)$ created by random noise, where we would expect the component proportional to the mean spectrum to be zero. However, in this case eq.4.3 will still result in a nonzero p_j. From numerical simulations, we expect that for our case the overestimation of σ_{lamp} is between 5 % and 30 %.

The lamp constancy at the EGO was also determined by (Solheim et al. 1996), using a 100 W halogen lamp with similar results. The lamp constancy of the 1000 W lamp was also determined by (Sandmeier et al. 1998) at the EGO, but without a stabilized power source, resulting in a much larger time drift (about 2.7 % for a time interval of 1 hour).

The $\Delta_{\text{ind,j}}$ values obtained from the above minimization procedure (eq. 4.3) do not have any common characteristics and can be associated with random detector noise. Their standard deviations taken over wavelength

$$\sigma_{\Delta_{\text{ind,j}}} \equiv \sqrt{\frac{\sum_{\lambda=425}^{\lambda=975} \left(\Delta_{\text{ind,j}}(\lambda) - \frac{1}{n_\lambda} \sum_{\lambda=425}^{\lambda=975} \Delta_{\text{ind,j}}(\lambda)\right)^2}{n_\lambda - 1}} \tag{4.5}$$

where n_λ is the number of wavelength channels, range from 0.36 to 17.4 counts, varying by a factor of about 40. The values are shown in the left plot of fig. 4.4. They are correlated to the maximum value of M_j^m, because the SE590 chooses the integration time automatically in such a way that the maximum value of the spectrum is below the saturation level and above 50 % of the saturation level. The maximum value varies from 218.3 counts to 9140.0 counts. We divided $\Delta_{\text{ind,j}}$ by the maximum value of M_j^m and called the result $\Delta_{\text{norm,j}}$ because it is now normalized to the maximum detector signal. Then we computed the standard deviation $\sigma_{\Delta_{\text{norm,j}}}$ (fig. 4.4, right plot) analogous to equation 4.5. It can be seen that $\sigma_{\Delta_{\text{norm,j}}}$ only varies from 0.0012 to 0.0028, a factor of about 2, a much narrower range than the variation of $\sigma_{\Delta_{\text{ind,j}}}$. Thus it is reasonable to regard the average of $\sigma_{\Delta_{\text{norm,j}}}$

$$\frac{1}{n_j} \sum_j \sigma_{\Delta_{\text{norm,j}}} = 0.0019 \pm 0.0004 = \sigma_{\text{noise}} \tag{4.6}$$

as the detector noise level σ_{noise} with a statistical standard deviation of 0.0004. **We conclude that 0.2 % of the maximum detector signal is a good estimate of the error from detector noise and that the error from illumination constancy over time can be estimated to be 0.3 % of the detector signal.**

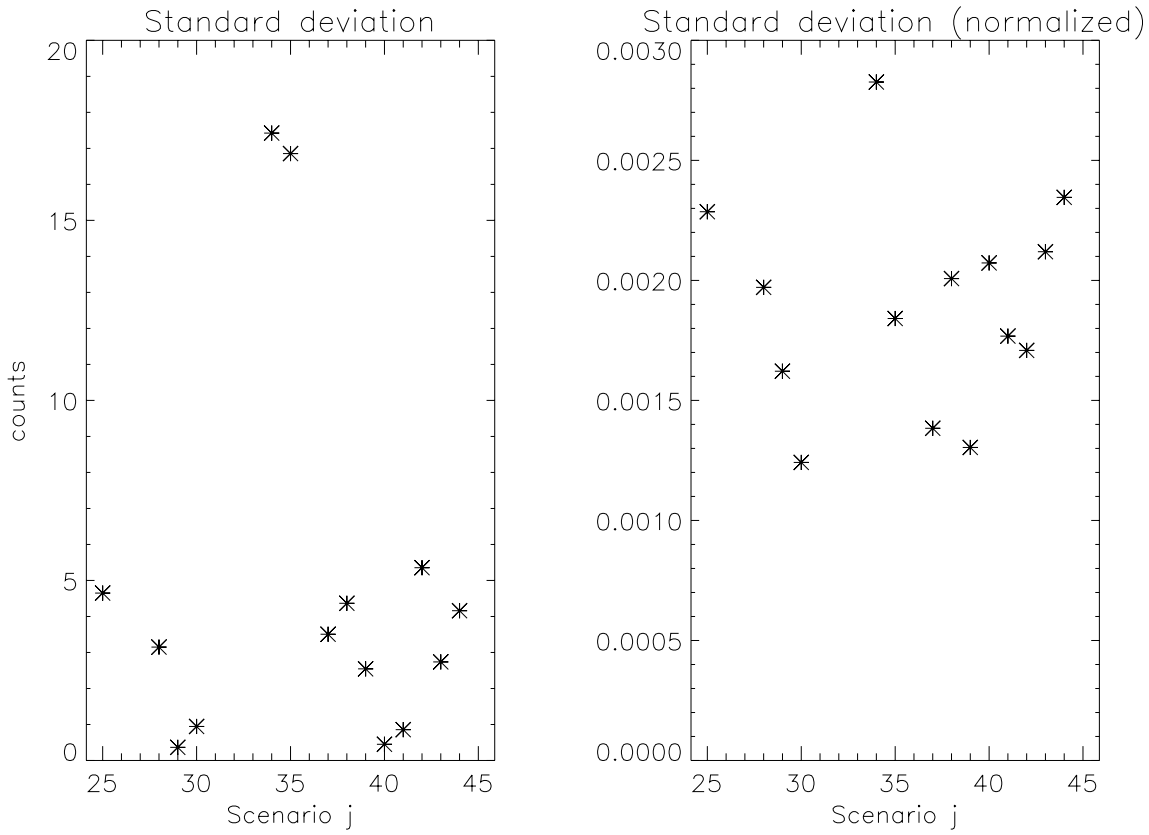

Figure 4.4: The left plot shows $\sigma_{\Delta_{\text{ind,j}}}$, the standard deviations of the before-after differences of each scenario after correcting for the relative differences, see eq. 4.5 for each scenario. The right plot shows these standard deviations after normalizing to the maximum detector signal ($\sigma_{\Delta_{\text{norm,j}}}$, see text). It can be seen that 0.002 is a good estimate for $\sigma_{\Delta_{\text{norm,j}}}$, whereas the variation of $\sigma_{\Delta_{\text{ind,j}}}$ is too large to allow a meaningful estimate of the average value.

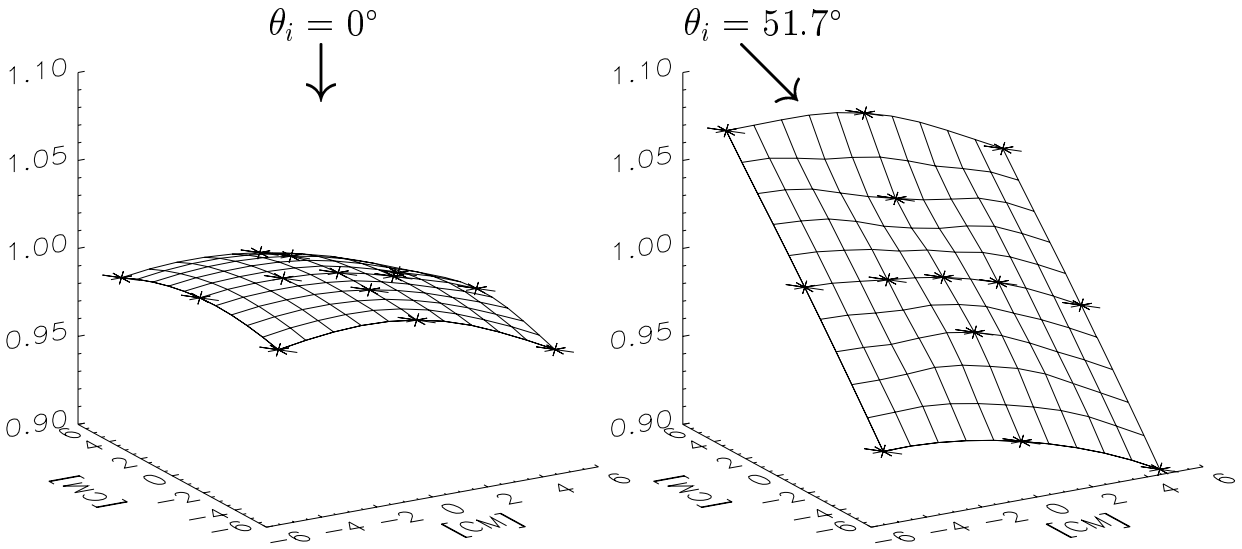

Figure 4.5: The lamp footprint, measured by moving a luxmeter over a 10 cm $\times$ 10 cm grid on the illuminated area, crosses indicate measurement points. The arrows indicate the lamp position: nadir illumination for the left plot, $\theta_i = 51.7°$ for the right plot. The lamp footprint for $\theta_i = 0°$ is quite homogeneous, $\theta_i = 51.7°$ shows a linear rise (about 15 %) towards the lamp.

4.5 Illumination Inhomogeneities

4.5.1 Luxmeter Measurements

In order to assess the spatial constancy of the light spot produced by the halogen lamp, we measured the spatial distribution of the incoming light intensity with the luxmeter 'MAVOLUX digital' for two different incident zenith angles, nadir and $\theta_i = 51.7°$. The instrument is available at EGO, see table 4.1 for technical specifications. Its sensor has a sensitive area with a diameter of 2 cm. We placed the sensor facing upward on several positions in a square in the illuminated spot. The length of the edges of the square was 10 cm. The resulting values normalized to the center of the square can be seen in fig. 4.5, 2D plots are shown in fig. 4.6. For light incident from nadir, the spatial distribution of the light intensity is very homogeneous. For $\theta_i = 51.7°$ the intensity close to the lamp is about 15 % higher than away from the lamp. The horizontal distribution is constant to about 3 %, the measurement error of the detector. Thus the left/right asymmetry observed by (Solheim et al. 1996) and (Sandmeier et al. 1998) is confirmed, but its impact is negligible [1] for the small FOV of $1°$ used in this study. The strong inhomogeneity of the vertical distribution (increase towards the lamp) can be explained by the large solid angle the lamp illuminates (we even set the lamp from 'spot' to 'flood' in order to achieve a homogenous illumination from nadir). Unless the light source emits parallel light rays (like e.g. a laser) the area closer to the light source will always be brighter than the area further away.

The luxmeter measurements show that the spatial distribution of the light intensity is quite linear within the measured square. If the center of the FOV of the detector would always coincide with the center of the light spot, there would be a negligible measurement error stemming from illumination inhomogeneities. However, the center of the FOV of the detector revolves approximately on a circle with a diameter of about 2 cm around the center if the detector is moved by $360°$ for detector zenith angles smaller or equal to $50°$, ac-

[1] Assuming a circular FOV of $1°$, a sensor views a circular target area of 3.4 cm diameter for zenith angle $\theta_r = 0°$.

Effective Range	0 ... 1999 W/m^2
Error for incandescent lamp and nadir illumination	$\pm 2.5\%$
Error for incandescent lamp and skew illumination	$\pm 3.0\%$
Diameter of detector area	20 mm
Spectral response (spectral filter used)	similar to human perception
Detector material	silicon

Table 4.1: Technical specifications for the MAVOLUX digital, see section 4.5, page 22). Manufacturer: GOSSEN BMBH - MESS- UND REGELUNGSTECHNIK, PB 1780, Naegelsbachstr. 25, D-8520 Erlangen, Germany

cording to measurements done previously (Hosgood 1997). We calculated the signal that would be measured from a lambertian target for both incident zenith angles ($\theta_i = 0^\circ, 51.7^\circ$), 3 viewing angles ($\theta_r = 0^\circ, 30^\circ, 50^\circ$) [2] and 4 azimuth angles ($\varphi = 0^\circ, 90^\circ, 180^\circ, 270^\circ$). For this reason we integrated the luxmeter measurements over the area covered by the FOV. The size of the area is determined by the viewing zenith angle θ_r (cosine dependence: area $A = A_0/\cos\theta_r$, where A_0 is the area of the FOV for $\theta_r = 0^\circ$), and the center of the area is determined by the azimuth angle, assuming the center revolves on a circle with a diameter of 2 cm. The results can be seen in fig. 4.7. Because of the approximate spatial linearity of the luxmeter measurements, the size of the FOV hardly influences the results. However, a change in azimuth causes the result to vary between 0.97 and 1.02 for $\theta_i = 51.7^\circ$, between 0.99 and 1.00 for $\theta_i = 0^\circ$ resp. **We thus estimate (first estimate, see below) the error stemming from illumination inhomogeneities to be 0.5 % for $\theta_i = 0^\circ$ and 2.5 % for $\theta_i = 51.7^\circ$** (half the maximum deviation). Although θ_r seems to have little influence according to our calculations, we do expect larger errors for large θ_r, because for large θ_r we expect an increase of the radius of the circle on which the FOV revolves (Hosgood 1997). (Solheim et al. 1996) reports that the displacement of the center of the FOV can reach up to 7 cm, increasing with θ_r.

4.5.2 Equivalent-Angle Measurements

The calculations of the previous section could be checked easily if we had a truly lambertian surface. The surfaces available to us are close to lambertian, but only to within a few percent, i.e. they are not suitable to check for deviations of 1 or 2 %. Another way of verifying the above calculations is to assume that the surface is rotationally symmetric. This assumption is confirmed for our samples by measurements of the surface topography at μm resolution. In this case, measurements with the detector at an azimuth angle of $\varphi = 90^\circ$ should yield the same as measurements with the detector at $\varphi = 270^\circ$ (in our measurement campaign, the azimuth angle of the light source was fixed to 0°). It is also possible to compare measurements of different detector azimuths where either the lamp or the detector are in nadir [3]. For detector in nadir ($\theta_r = 0^\circ$), we measured at detector azimuth positions $\varphi = 90^\circ$ and $\varphi = 180^\circ$ for lamp zenith angles $\theta_i = 30^\circ, 50^\circ$ and 65°. These measurements will be investigated in the following to estimate the error for $\theta_r = 0^\circ$, the comparison between $\varphi = 90^\circ$ and $\varphi = 270^\circ$ (only available for $\theta_i = 50^\circ$) will be used to estimate the error for arbitrary θ_r.

The measurements for different azimuth angles at $\theta_r = 0^\circ$ are available for 7 scenarios: Spectralon 50% reflectance, red roof tile, sanded roof paper, asphalt, red painted aluminum, blue concrete tile and red concrete tile. The relative differences (measurement at $\varphi = 90^\circ$ minus measurement at $\varphi = 180^\circ$ divided by measurement at $\varphi = 180^\circ$) were computed for $\theta_i = 30^\circ, 50^\circ$ and 65°, resp. It can be seen that because of their low signal for small wavelengths, the red surfaces have a very unstable signal in that wavelength

[2] For larger viewing angles the FOV becomes larger than the area where we took the luxmeter measurements

[3] If the detector is in nadir, a variation in azimuth means a rotation of the detector about its vertical axis.

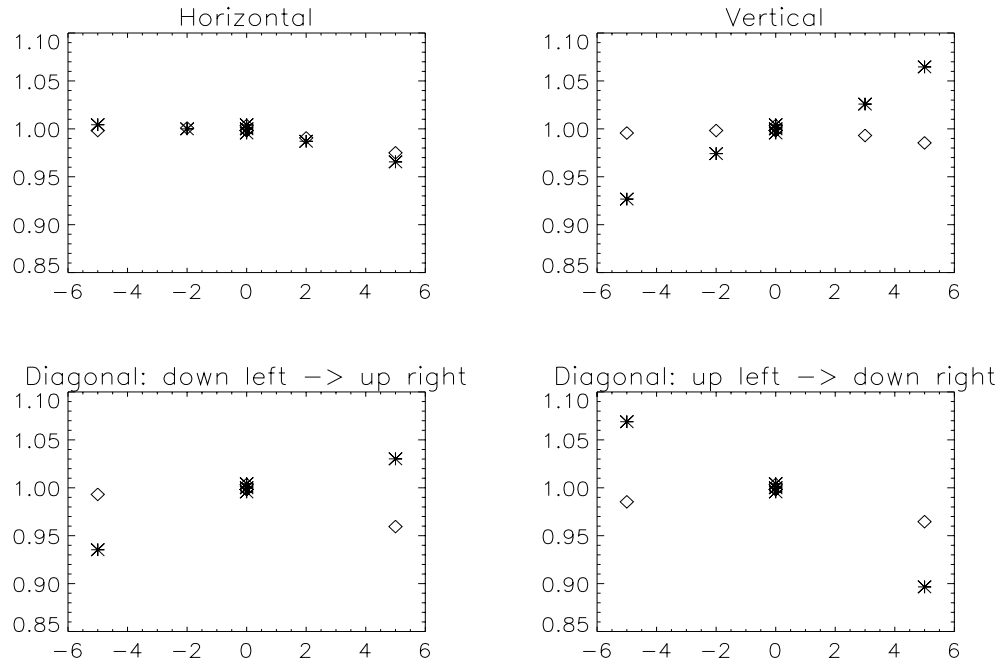

Figure 4.6: Lamp footprint from luxmeter measurements, shown as 2D plots (cf. fig. 4.5 on page 22 for a 3D plot). Stars indicate measurements at $\theta_i = 51.7°$, rhombs are measurements at $\theta_i = 0°$. In the plot titled 'Vertical' a 15 % rise can be seen when moving closer to the lamp for $\theta_i = 51.7°$. As expected, the plots titled 'Diagonal' show the largest variation because they cover the points the furthest away from the center. For $\theta_i = 0°$ the plot 'Horizontal' shows a slightly larger variation (0.98 to 1.00) then the plot 'Vertical' (0.99 to 1.00)

range. We excluded the wavelengths lower than 600 nm of these samples from the error estimation. We also excluded the sample 'asphalt' because of its color-heterogeneity (irregular colored patches distributed on its surface). The average absolute value of the relative deviations of these measurements is shown in fig. 4.8. For the nadir viewing measurements, it is computed by

$$\epsilon_{\theta_r=0°}(\theta_i) = \frac{1}{n_j} \cdot \sum_j \left| \frac{M(\theta_i, \theta_r = 0°, \varphi = 90°) - M(\theta_i, \theta_r = 0°, \varphi = 180°)}{M(\theta_i, \theta_r = 0°, \varphi = 180°)} \right| \tag{4.7}$$

$$j = \text{scenario},\ n_j = \text{number of scenarios}$$

Fig. 4.8 shows a strong rise of $\epsilon_{\theta_r=0°}$ with wavelength. According to (Sandmeier et al. 1998) the lamp footprint of a similar halogen lamp at the EGO does not change with wavelength. A sample inhomogeneity is highly unlikely, because the rise with wavelength can be seen for each single sample. There seems to be no reason why the spectral sensitivity should depend on the detector azimuth. Therefore a dispersion in the lamp optics is the most likely explanation. These data provide a good source for estimating the measurement error. It can be seen that for $\theta_i = 50°$ in the visible wavelength range (named VIS, $425\,\text{nm} < \lambda < 700\,\text{nm}$), $\epsilon_{\theta_r=0°}$ is about 1.5 % (second plot from the left in fig. 4.8), a value comparable to the 2.5 % estimated from the luxmeter measurements (the luxmeter is sensitive only in the VIS). There are no luxmeter measurements for $\theta_i = 30°$, but the error estimated from the $\theta_i = 0°$ luxmeter measurements of 0.5 % suggests that the error will drop the closer θ_i gets to nadir. This can be confirmed by fig. 4.8, for $\theta_i = 30°$ the value of $\epsilon_{\theta_r=0°}$ is about 1 % for VIS. For $\theta_i = 65°$ $\epsilon_{\theta_r=0°}$ rises to about 2 % in the VIS. We conclude that the luxmeter measurements and the $\theta_r = 0°$ measurements confirm each other. For NIR, $\epsilon_{\theta_r=0°}$ rises, the bigger θ_i the stronger, up to 6.5 % for $\theta_i = 65°$. We will rather use the $\theta_r = 0°$ measurements than the luxmeter measurements to determine the measurement error of the SE590, because

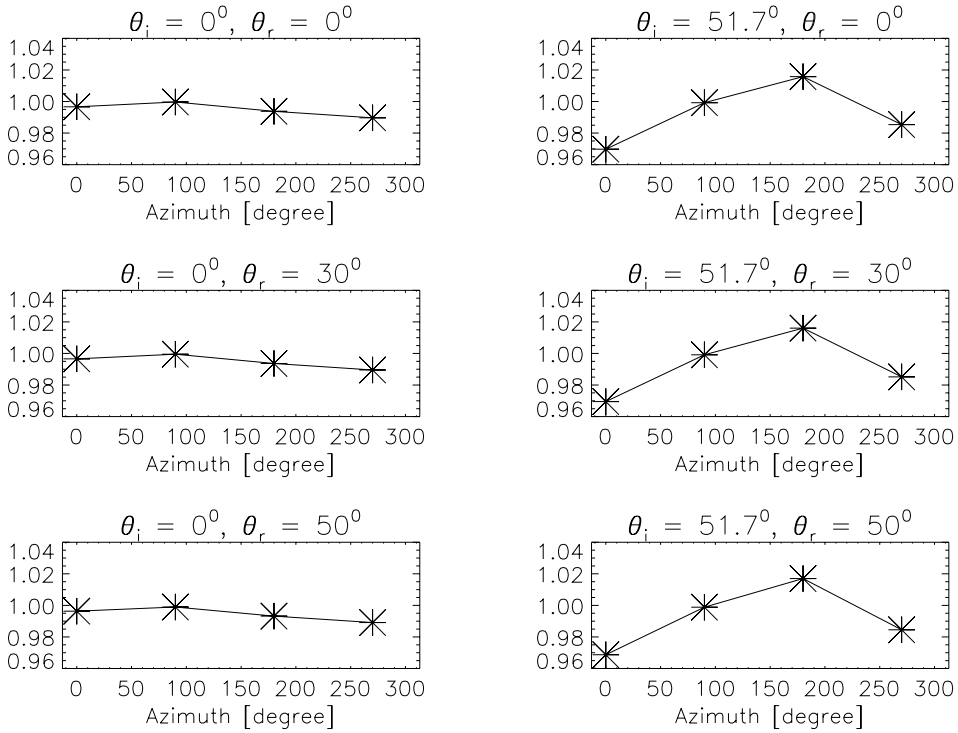

Figure 4.7: Radiances (normalized) calculated from the luxmeter measurements, assuming a lambertian surface and a FOV which revolves around a circle with a diameter of 2 cm. The left column shows $\theta_i = 0°$, the right column $\theta_i = 51.7°$, the first line shows $\theta_r = 0°$, the second line $\theta_r = 30°$, the third line $\theta_r = 50°$. All curves are normalized to the value that would be obtained if the luxmeter measurements were constant. The curves hardly vary with θ_r. The variation with azimuth angle is small for $\theta_i = 0°$ (0.99 to 1.00), larger for $\theta_i = 51.7°$ (0.97 to 1.02).

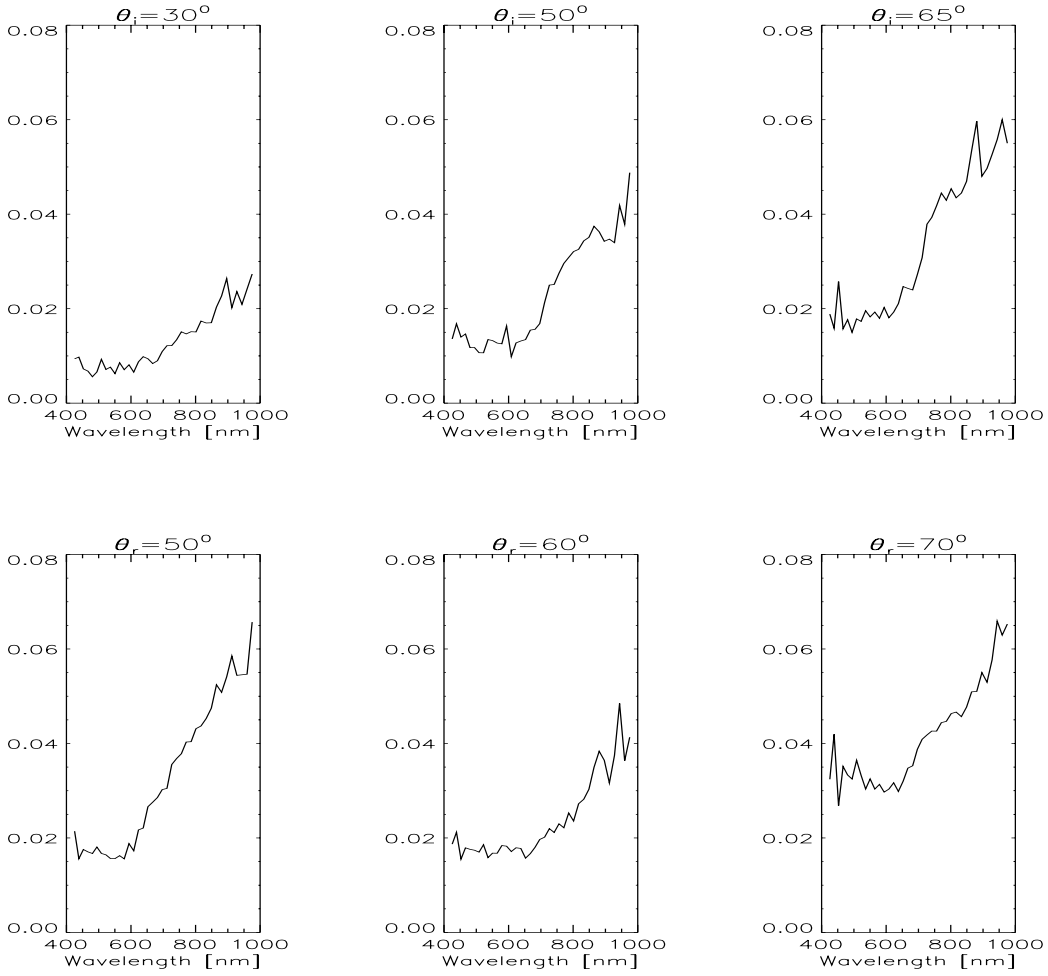

Figure 4.8: The top three plots show the average relative deviation $\epsilon_{\theta_r=0^\circ}(\theta_i)$ (see eq. 4.7) of the $\theta_r = 0^\circ$ measurements for different incidence angles θ_i. The bottom three plots show the average relative deviation $\epsilon_{\varphi=270^\circ}(\theta_r)$ (see eq. 4.8) for different viewing angles, derived from measurements with $\theta_i = 50^\circ$ and $\varphi = 90^\circ, 270^\circ$ resp. All the plots show a similar wavelength dependence.

1. the luxmeter measurements don't provide information on the NIR and even for VIS they are integrated over all wavelengths
2. not introducing a new detector eliminates the possibility of regarding unknown luxmeter peculiarities as measurement errors of the SE590 (luxmeter measurements are not standard procedures in the EGO facility)
3. the $\theta_r = 0^\circ$ measurements not only contain errors due to illumination inhomogeneities but also potential detector inherent errors (see section 4.4).

In order to estimate the measurement error for viewing angles away from nadir we examined the measurements at a detector azimuth of $\varphi = 270^\circ$ and an incidence angle of $\theta_i = 50^\circ$. For a surface with rotational symmetry, measurements at $\varphi = 270^\circ$ are equivalent to measurements at $\varphi = 90^\circ$. As we did above for the $\theta_r = 0^\circ$ measurements at $\varphi = 90^\circ$ and $\varphi = 180^\circ$, we compute the relative difference(signal at $\varphi = 90^\circ$ minus signal at $\varphi = 270^\circ$ divided by signal at $\varphi = 270^\circ$). Again we excluded the wavelengths lower than 600 nm of certain samples from the error estimation as well as the sample 'ashalt'. The average absolute value of the relative deviations of these measurements is computed as

$$\epsilon_{\varphi=270^\circ}(\theta_r) = \frac{1}{n_j} \cdot \sum_j \left| \frac{M(\theta_i = 50^\circ, \theta_r, \varphi = 90^\circ) - M(\theta_i = 50^\circ, \theta_r, \varphi = 270^\circ)}{M(\theta_i = 50^\circ, \theta_r, \varphi = 270^\circ)} \right| \tag{4.8}$$

(j = scenarios, n_j = number of scenarios) and shown in fig. 4.8. In the NIR, there is a rise with wavelength comparable to $\epsilon_{\theta_r=0^\circ}$, see fig. 4.8. In the VIS, the value of $\epsilon_{\varphi=270^\circ}(\theta_r = 50^\circ)$ of about 2 % agrees well with the value predicted from the luxmeter measurements of 2.5 % for $\theta_i = 50^\circ$, see section 4.5.1. The small rise with θ_r from 1.5 % for $\theta_r = 0^\circ$ to 2 % for $\theta_r = 50^\circ$, can be explained by the increase of the radius of the FOV with θ_r. This is also a very likely reason for the increase of $\epsilon_{\varphi=270^\circ}(\theta_r = 70^\circ)$ to about 4 % in the VIS, see fig. 4.8. The measurements for $\theta_r = 60^\circ$ do not fit perfectly into this picture: for VIS, $\epsilon_{\varphi=270^\circ}(\theta_r = 60^\circ)$ is not higher than $\epsilon_{\varphi=270^\circ}(\theta_r = 50^\circ)$, in the NIR it is even lower.

4.5.3 General Function for Illumination Inhomogeneity Error

In section 4.5.2 we derived the measurement errors at 6 different combinations of angles, see Fig.4.8 or equations 4.7 and 4.8. In order to obtain an error from illumination inhomogeneities for every combination of angles in our scenarios, we assumed that the relative error is a linear function of the inverse of the cosines of θ_i and θ_r:

$$\sigma_{\text{illu}} = \frac{a_0}{\cos\theta_i} + \frac{a_1}{\cos\theta_r} \text{ [dimensionless]} \tag{4.9}$$

This way the error increases with the FOV of the sensor ($\propto \frac{1}{\cos\theta_r}$, see section 4.5.1) and with the illuminated area of the lamp ($\propto \frac{1}{\cos\theta_i}$ if light emitted was parallel). The reason behind this choice is that the larger these areas, the more difficult it is to achieve a homogenous illumination. The two coefficients a_i were obtained by linear regression of eq. 4.9 to the 6 ϵ values derived in section 4.5.2 from equations 4.7 and 4.8, and are shown in Fig. 4.9 as a function of wavelength. We expect the illumination error to be a smooth function of wavelength, so we smoothed the obtained coefficients with a bin size of 5. It can be seen that there is no wavelength dependence of the error for coefficient a_1 (viewing angle dependence), but there is a strong rise for coefficient a_0 (illumination angle dependence) with wavelength. This confirms our assumption that there is a dispersion in the lamp optics (see fig. 4.8 on the wavelength dependence of $\sigma_{\theta_r=0^\circ}$).

The dashed line in fig. 4.9 gives approximated values. This approximation can be used if the illumination error needs to be evaluated for other measurement campaigns at the EGO and equivalent angle measurements are not available.

Examples of errors calculated with these coefficients are plotted in fig. 4.9 to show the increase with wavelength and zenith angle (minimum: 1%, maximum: 8 %).

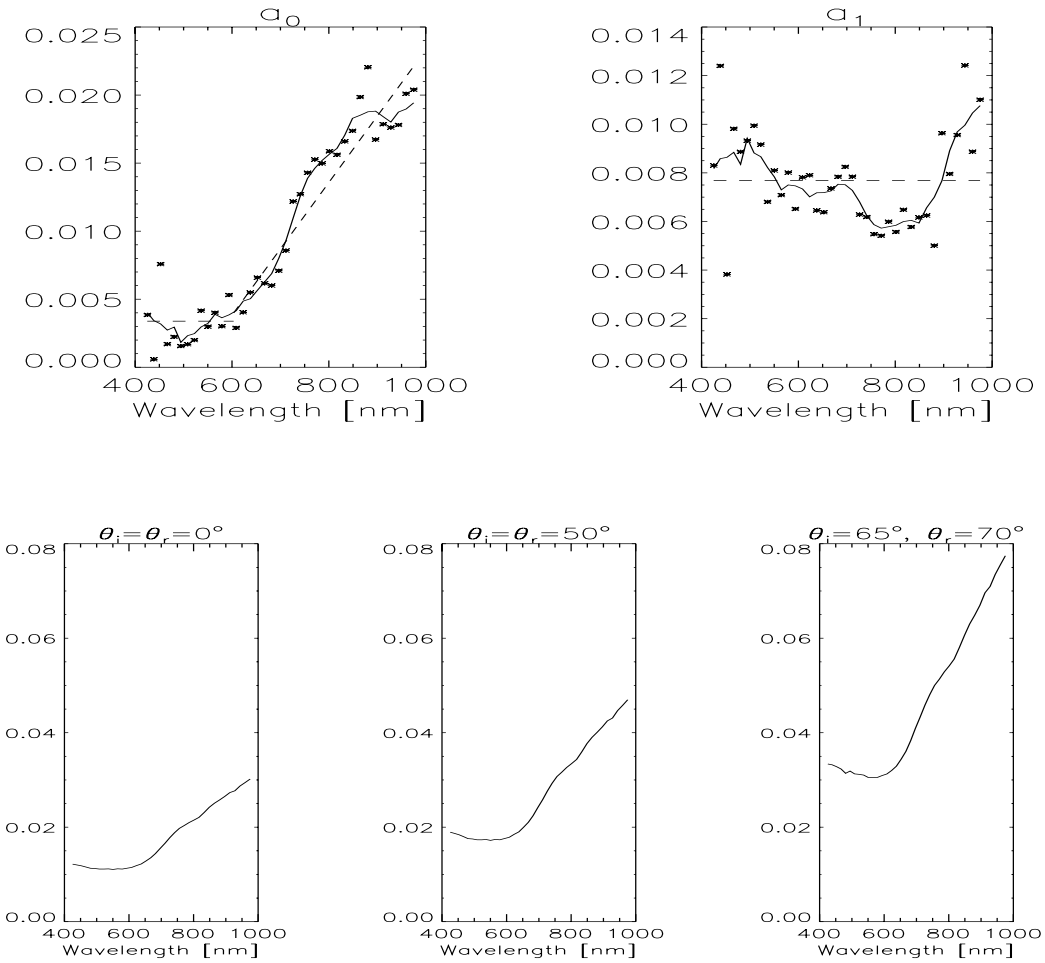

Figure 4.9: The two plots on the top show the coefficients to interpolate the illumination error. The stars show values obtained from eq. 4.9, the solid line shows the smoothed values (bin size of 5). The dashed line shows approximated values ($a_0 = 0.003$ for $\lambda < 600$ nm, $a_0 = -0.0254 + 0.0000488[\text{nm}]^{-1} \cdot \lambda$ for $\lambda > 600\,\text{nm}$, $a_1 = 0.008$).
The 3 plots on the bottom show examples of interpolated illumination error (see eq.4.9) for $\theta_i = \theta_r = 0°, 50°$ and $\theta_i = 65°, \theta_r = 70°$. $\theta_i = \theta_r = 0°$ has the smallest illumination error of any combination of angles, $\theta_i = 65°, \theta_r = 70°$ has the biggest illumination error (about 8 %). Due to our approach in eq.4.9, the calculated illumination error σ_{illu} does not depend on the azimuth angle.

4.6 Determination of the Irradiance

4.6.1 Constant Irradiance Versus View Angle Dependant Irradiance

In order to obtain BRDF values, it is necessary to divide the measurements by the incoming irradiance:

$$f_r = \frac{L_r(\theta_i, \theta_r, \varphi)}{E_i(\theta_i)} \tag{4.10}$$

There are no possibilities for an absolute calibration at EGO. The measured counts $M(\theta_i, \theta_r, \varphi)$ are proportional to the reflected radiance by an unknown factor c_{LM}: $L_r = M \cdot c_{LM}$. However, also the irradiance E_i determined below is proportional to this factor c_{LM}, which thus cancels in equation 4.10. Thus BRDF values can still be obtained without an absolute calibration of the reflected radiance L_r in SI units.

In principle there are two ways of determining the BRDF of a sample. Each way requires measurements with a reference panel. The first method assumes that all disagreements between measured values and the (assumed to be known) BRDF of the reference panel must be attributed to deficiencies of the instruments, either the measuring device (e.g. if the FOV of the detector is not correctly centered to the middle of the lamp spot) or the irradiance (e.g. the lamp doesn't provide spatially homogeneous irradiance). In this case each measurement of the sample must be divided by the measurement of the reference panel and be multiplied by the BRDF of the reference panel. This is equivalent to assuming that the irradiance is varying with viewing angle.

The second method assumes that the irradiance does not change with viewing angle. Only the albedo of the reference panel needs to be known, not the BRDF, and for each θ_i the reflected radiances must be integrated over the upper hemisphere. A good angular sampling is needed to pursue this second way. If it is assumed that the irradiance changes exactly with $\cos\theta_i$, this procedure needs to be done for only one θ_i.

We pursued the second way (assumption of constant irradiance) because for the first way it is crucial to know the BRDF of the reference panel exactly, a wrong reference BRDF will directly propagate to the sample BRDF. Also the assumption of a varying irradiance is more susceptible to single measurement errors. E.g., if the measurement of the reference panel at a certain combination of angles happens to be 5 % too high, the BRDF values of all the samples at this combination of angles will be calculated 5 % too low.

The strongest argument in favor of assuming that the irradiance changes with viewing angle is the correction for deficiencies of the instruments. However, these problems were investigated above and we can predict the error caused by them, whereas the BRDF of the reference panel is quite speculative.

In our case, about 40 measurements are available for each incident zenith angle. We did not require the irradiance to change with θ_i according to the cosine law, but computed the irradiance for each θ_i separately. This way deviations from the cosine law of the irradiance do not propagate into the calculation of the BRDF values.

At the end of this section it will be seen (fig. 4.11) that the computed BRDF values of all samples are in better accord with the theorem of reciprocity if a constant irradiance is assumed. Computing the BRDF while assuming the irradiance changes with viewing angle, the deviations are on average much larger. In the following a detailed description of the determination of the irradiance will be given.

4.6.2 Calculation of the Irradiance

As reference panels we used two Spectralon panels, both from Labsphere Inc., Boulder, Colorado: a 100 % reflecting Spectralon panel available at EGO and a 50 % Spectralon panel owned by our working group CENSIS. The BRDF of the 50 % Spectralon panel is described in (Meister 1995), (Meister et al. 1996b). We found that the BRDF of the 100 % Spectralon is very similar to the 50 % Spectralon after adjusting for albedo and a reduction of the intensity of the specular peak of the 50 % Spectralon by two thirds. The relatively

strong specular peak of the 50 % Spectralon shows that this panel should not be used as a reference panel without correcting for its BRDF.

The scenarios of the two Spectralon panels basically consist of measurements at 4 different incident zenith angles: $\theta_i = 0^\circ, 30^\circ, 50^\circ$ and 65°. The number of different combinations of viewing zenith angle θ_r and azimuth angle φ for each θ_i is 14, 61, 78, 45 resp. Thus the angular sampling exceeds the requirements for an integration over the upper hemisphere because of the slowly varying BRDF of the reference panels, except maybe for $\theta_i = 0^\circ$, where measurements at several azimuth angles could confirm our assumption of rotational symmetry. However, the luxmeter measurements (section 4.5.1) strongly support the assumption of rotational symmetry for $\theta_i = 0^\circ$.

The albedos of the reference panels are provided as a table for wavelengths from 250 to 2500 nm by the manufacturer. Because of the good angular sampling, in the calculation of the integral we abstained from a linear interpolation between viewing angles of the measured values. Instead $L_r(\theta_i, \theta_r, \varphi)$ was set to the measured value of the nearest viewing angle of the scenario.

The irradiances computed from the EGO-100%-Spectralon (solving eq. 3.11, page 14 for $E_i(\theta_i)$) are always lower than the irradiances computed from the Hamburg-50%-Spectralon, 4 % for $\theta_i = 0^\circ$, 10 % for $\theta_i = 65^\circ$. Possible error sources are wrong albedo calibrations (error given by manufacturer: 1 % for each panel), lamp constancy (estimated to be better than 1 %, see section 4.4), measurement and integration errors (we estimate them to be between 2 % and 4 %, depending on θ_i). Combining these errors leads to an overall error for each irradiance of about 3 to 5 %, depending on θ_i. Thus the two computed irradiance values lie within a reasonable range.

Using these two irradiances separately to compute the BRDF values, they show some significant differences:

- Using the irradiance from the Hamburg-50%-Spectralon, the computed BRDF values agree better with the BRDF derived in (Meister 1995). This is expected, because if the irradiance obtained from the Hamburg-50%-Spectralon is used to compute the BRDF values of the Hamburg-50%-Spectralon, this is equivalent to normalizing the measured values to the Hamburg-50%-Spectralon albedo. Using the irradiance from the EGO-100%-Spectralon, the albedo of the Hamburg-50%-Spectralon increases from 51.5 % (value given by manufacturer) to 53 % for $\theta_i = 0^\circ$ and 55 % for $\theta_i = 50^\circ$.

- The (Helmholtz) theorem of reciprocity (or reciprocity principle) states that exchanging incidence and viewing angle doesn't change the BRDF value: $f_r(\theta_i = \theta_1, \theta_r = \theta_2, \varphi) = f_r(\theta_i = \theta_2, \theta_r = \theta_1, \varphi)$. This theorem is fulfilled better when using the irradiance from the EGO-100%-Spectralon to compute the BRDF values. The average deviation is about 2 % smaller than if the Hamburg-50%-Spectralon irradiance is used to compute the BRDF values.

- Ideally, the irradiance is expected to be proportional to the cosine of the incidence angle. For a non-parallel light source like the halogen lamp some deviations are expected. The deviations from the cosine law are much larger for the irradiance from the Hamburg-50%-Spectralon than for the irradiance from the EGO-100%-Spectralon for $\theta_i = 65^\circ$: the irradiance from the EGO-100%-Spectralon is only 5 % higher than the value expected from the cosine law, the irradiance from the Hamburg-50%-Spectralon is about 10 % higher. For $\theta_i = 30^\circ$ the deviations between the two irradiances are negligible.

However, none of these differences is a strong enough argument to dismiss either the irradiance from the Hamburg-50%-Spectralon or the irradiance from the EGO-100%-Spectralon. So we decided to determine the irradiance by averaging these two measurements. The error associated with the irradiance σ_{irrad} will be computed as the statistical error of averages. As there are only two measurements, this yields an error equal to half the absolute of the difference of the two irradiances. We obtain $\sigma_{\text{irrad}} = 2.5$ %, 2.6 %, 4.5% and 5.1 % for $\theta_i = 0^\circ, 30^\circ, 50^\circ$ and 65° respectively. There is only a very small increase with wavelength.

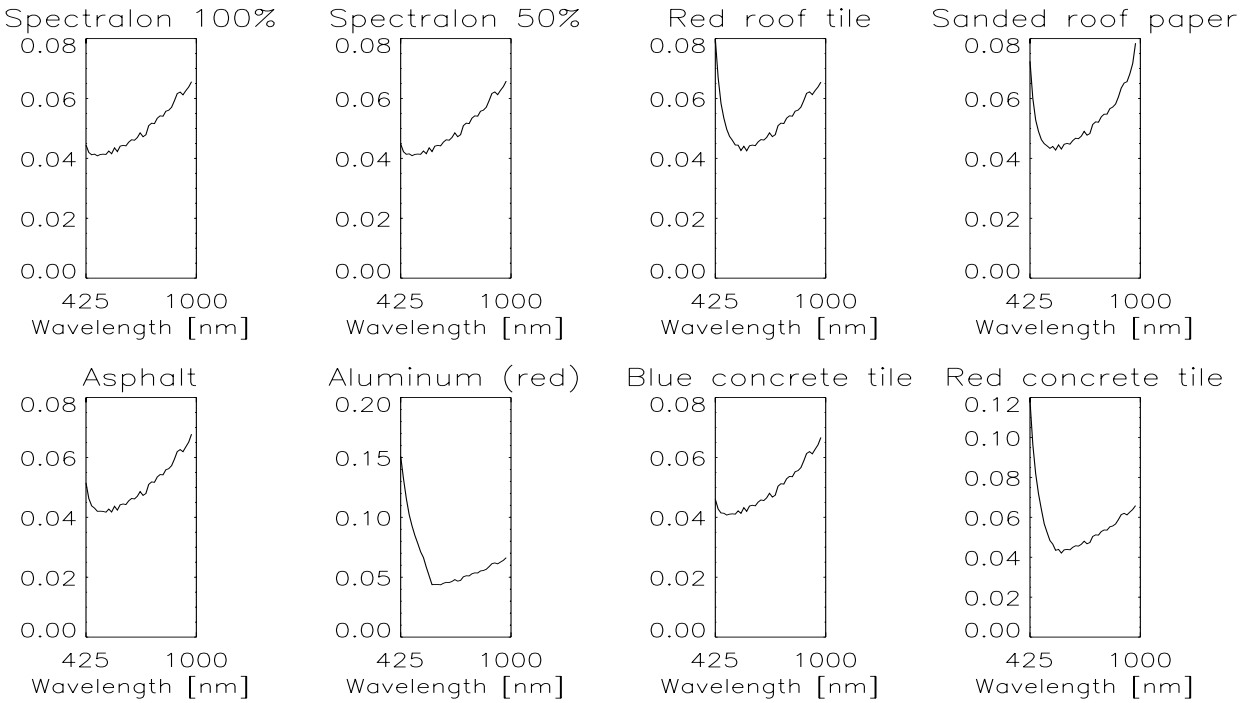

Figure 4.10: Average relative BRDF error σ_{f_r} (eq. 4.12) for 8 samples. The average is taken over all measurements (150 to 200). It usually varies between 4 % for short wavelengths and 6 % for long wavelengths. For those samples showing low reflectances in the blue and simultaneously high reflectances in the red/NIR (red roof tile, red painted aluminum, red concrete tile) the average error rises strongly for short wavelengths (14 % for red painted aluminum).

4.7 Total SE590 Measurement Error and Reciprocity Principle

Using the results from sections 4.4, 4.5 and 4.6, we can calculate the overall error with the law of error propagation:

$$\sigma^2_{L_r(\theta_i,\theta_r,\varphi))} = (\mathrm{MAX}_\lambda[L_r(\theta_i,\theta_r,\varphi,\lambda)]\cdot\sigma_{\mathrm{noise}})^2 + (L_r(\theta_i,\theta_r,\varphi)\cdot\sigma_{\mathrm{lamp}})^2 + (L_r(\theta_i,\theta_r,\varphi)\cdot\sigma_{\mathrm{illu}}(\theta_i,\theta_r,\varphi))^2 \tag{4.11}$$

$\sigma_{\mathrm{noise}}, \sigma_{\mathrm{lamp}}$ and σ_{illu} are given in equations 4.6, 4.4 and 4.9, respectively. The reflected radiance L_r is measured as a function of wavelength λ for each combination of angles $(\theta_i, \theta_r, \varphi)$. $\mathrm{MAX}_\lambda[L_r(\theta_i,\theta_r,\varphi,\lambda)]$ denotes the maximum value of the spectrum measured for L_r [count] for the combination $(\theta_i, \theta_r, \varphi)$. Using the irradiance error σ_{irrad} given in the paragraph above we obtain the error of a single BRDF measurement $f_r(\theta_i, \theta_r, \varphi, \lambda)$:

$$\sigma^2_{f_r} = (\frac{1}{E_i}\cdot\sigma_{L_r})^2 + (\frac{L_r}{E_i^2}\cdot\sigma_{\mathrm{irrad}})^2 \tag{4.12}$$

The error averaged over all measurements is shown for 8 samples in fig. 4.10. Usually it rises from 4 % at 425 nm to 6 % at 975 nm. Some samples have a low reflectance in the blue wavelength range and a high reflectance in the red/NIR wavelength range. For these samples, the detector noise term σ_{noise} produces a strong increase of the relative error for short wavelengths, up to 14 % for 'red painted aluminum'. This characteristic can also be expected for vegetation samples because of the low reflectance in the visible and the high reflectance in NIR.

We tested the reciprocity principle (explained in section 4.6.2) for 8 samples. We found 11 combinations of angles in each scenario where the theorem could be tested. The average deviation (averaged over the 11

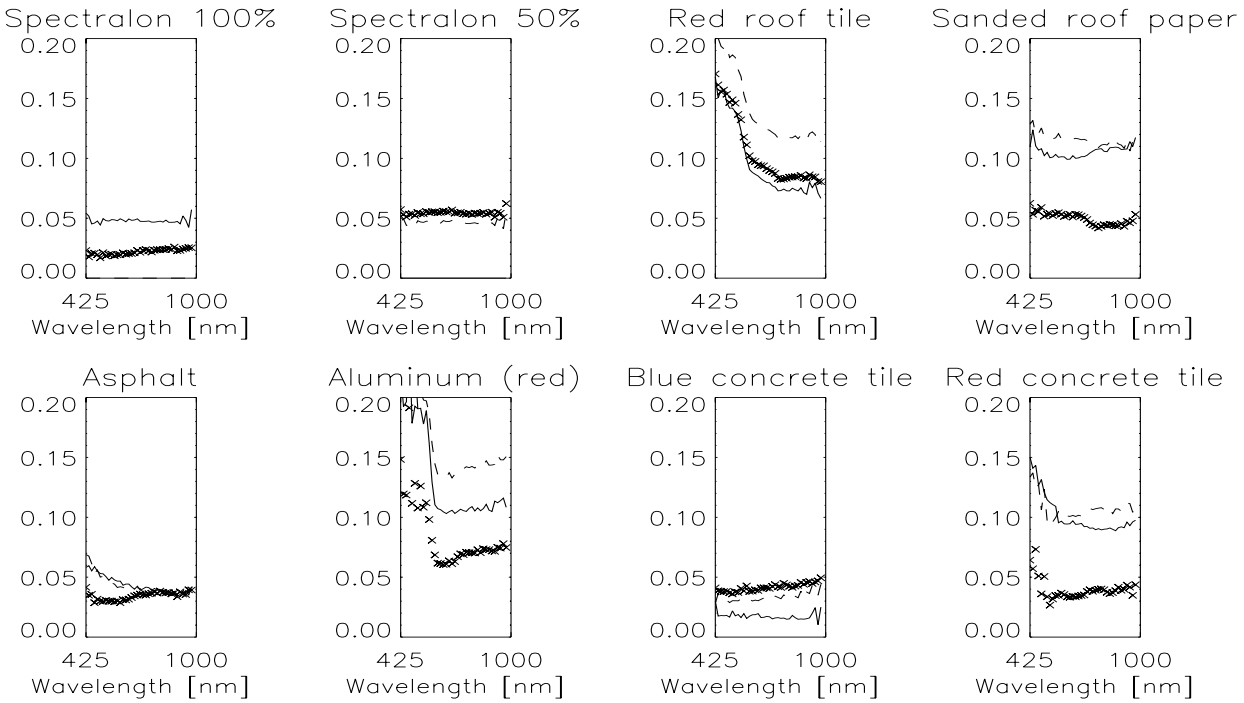

Figure 4.11: Averaged relative difference of the eleven reciprocity-pairs as a function of wavelength for 8 samples. The crosses show the results based on the assumption of constant irradiance for each θ_i, the solid line shows the results based on the assumption of varying irradiance using Hamburg-50%-Spectralon as reference, the dashed line using EGO-100%-Spectralon as reference. Assuming a constant irradiance improves the results considerably, the average relative difference is reduced to about 5 % for all samples except for 'Red roof tile' and 'Red aluminum'. The solid line is 0 for the sample 'Spectralon 50 %' and the dashed line is 0 for 'Spectralon 100 %' because these measurements have been normalized by themselves, thus a check for reciprocity will give zero deviation.

combinations of angles) is shown in fig. 4.11 as crosses. It is about 5 %, except for the samples red roof tile and red painted aluminum.

It is interesting to compare the results for the 2 different ways of computing the BRDF values (see section 4.6.1). If the first way is chosen (divide each measurement by the measurement of the reference panel at the same combination of angles,assumption that the irradiance varies with viewing angle), the deviations are on average about 2 % larger (solid line in fig. 4.11 for Hamburg-50%-Spectralon as reference panel, dashed line for EGO-100%-Spectralon as reference panel) than if the irradiance is assumed to be constant for each incidence zenith angle (crosses in fig. 4.11). This supports our decision to choose the second way. Although the validity of the reciprocity principle for BRDF measurements is still under discussion, our samples are strongly expected to obey the reciprocity principle, because for most of them the BRDF can be described in a first order approximation to be composed of a lambertian plus a specular part. The deviations observed from the reciprocity principle are most probably caused by the spatially inhomogeneous irradiance. The method assuming an irradiance independent of viewing angle performs an average that reduces the deviations. This is another reason why this method is better.

4.8 Description of the Detector ASDFieldspec

The ASDFieldspec is manufactured by Analytical Spectral Devices, Inc., Boulder, USA. We used the model 'FR', that covers a spectral range from 350 to 2500 nm.

The wavelengths below 1050 nm are detected by a plasma coupled photodiode array, the spectral resolution is 3 nm (FWHM), the sampling interval is 1.4 or 0.7 nm. Wavelengths above 1050 nm are detected by dual, 1/2 second-scanning, grating spectrometers with InGAs photodiodes. The spectral resolution is 10 nm (FWHM), the sampling interval is 2 nm. Wavelength accuracy is given as $\pm$ 1 nm, repeatability is given as $\pm$ 0.1 nm.

The digitization is 16 bits. There is an automatic dark current subtraction, the integration time is chosen automatically as well (between 16 ms and 10 minutes).

Unfortunately it is impossible to obtain raw data from the ASDFieldspec (called ASD from now on). The only output are two arrays of 2151 elements each: one contains the wavelengths (in integer steps: 350 nm, 351 nm, 352 nm, ..., 2500 nm), the other contains the measured value for the respective wavelength. No information on the data processing is available to us, but it is obvious from the integer wavelength array that some re-mapping has been done (in the NIR the sampling interval is 2 nm, so the output must be based on an interpolation algorithm). From experience with different spectroradiometers (e.g. IRIS (Kollewe 1995), OVID (Bartsch 1996)), we know that the transition from one grating to another is usually not smooth, but often discontinuous. This can also be seen for the ASD, see fig. 4.12.

In a first step, we averaged the ASD results to the same bin size as we used for the SE590, about 15 nm. Further averaging will be explained below. As is clear from above, the internal ASD software contains some smoothing algorithm, thus we don't expect to loose information by averaging.

Another disadvantage of the ASD is the fragile coupling to the goniometer: there is no direct linkage between a data take of the ASD and a movement of the goniometer. After each goniometer movement, a mechanical construction (made by the EGO engineers) presses the space bar on a laptop which is connected to the ASD. This is the sign for the ASD to take a single measurement. This system is not error proof, sometimes the ASD misses a data take, sometimes it makes additional measurements. It is not clear whether this problem is due to the construction described above or to an internal ASD error. If unnoticed, this kind of error can make a whole scenario worthless because the allocation of goniometer angles to measured radiance will be wrong.

Also the ASD can stop taking data completely, it then needs to be reinitialized. These two reasons make the ASD a poor candidate for long (more than 1 hour) scenarios. We only used the ASD for measurements in the principal plane that usually lasted about half an hour. The data were examined for missing or additional measurements, altogether 3 missing data takes and 1 additional measurement were discovered and corrected.

4.8.1 Wavelength Range and Resolution

The wavelength range of the ASD extends to 2500 nm. At this large wavelengths, the product of sensor sensitivity and intensity of the light emitted from the lamp is quite weak. Thus the influence of the dark current plays an important role. The effect can be seen in fig. 4.13, where two plots of the same angular combination where subtracted from each other: in the wavelength range of the first grating (450 to 1000 nm), the curve is very smooth, becoming rougher for the second grating (1000 to 1800 nm) and very rough for the third grating (1800 to 2500 nm). Thus we decided to increase the channel averaging for the second grating to three times the interval of the SE590 and for the third grating to seven times the interval of the SE590. Thus the wavelength resolution is 15 nm for the first grating, 45 nm for the second grating and 105 nm for the third grating. This will reduce the error due to the detector noise. The values after averaging are plotted in fig. 4.13, too.

Another point specific to the ASD is the transition between the gratings. We found stronger variations

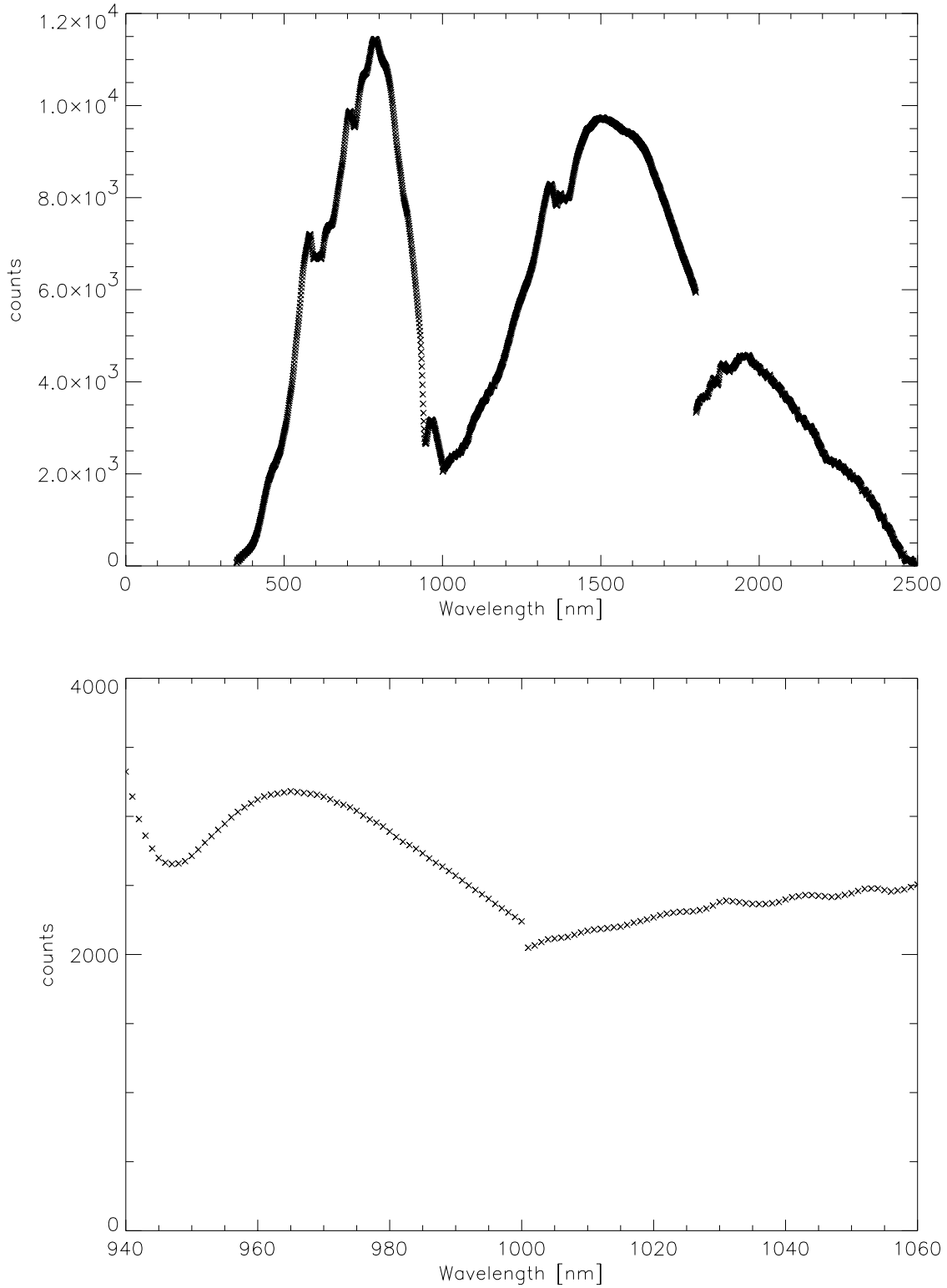

Figure 4.12: ASD 'original' data plotted as counts over wavelength for a measurement of the Spectralon panel (50 % reflectance) with $\theta_i = 30°, \theta_r = 0°$. The upper plot shows the transition between the gratings to be at 1800 nm. The lower plot shows the same data with a different plotting range for the wavelength, now it can be seen that the first transition is at 1000 nm.

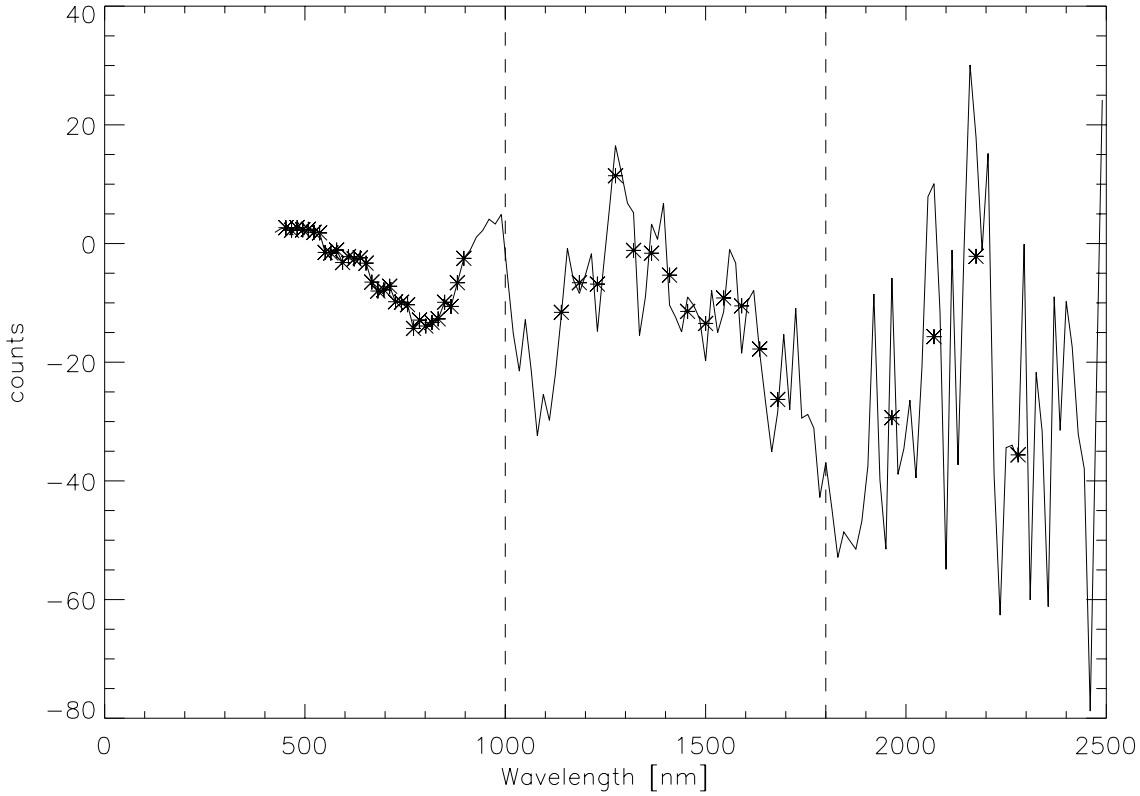

Figure 4.13: Noise of ASD as a function of wavelength. The plot shows the difference between two unprocessed ASD measurements of 100 % Spectralon with the same angles separated by 15 minutes. The solid line shows data averaged to 15 nm intervals. The solid line is smoothest for the first grating ($\lambda < 1000$nm) and roughest for the third grating ($\lambda > 1800$nm). The stars show the data after the averaging procedure described in section 4.8.1. The noise is significantly reduced, especially for the third grating.

for the wavelengths around the transition areas than elsewhere. Unfortunately, the documentation does not mention if any algorithm was used to smooth the transitions. For other sensors (OVID (Rothkirch 1997), IRIS (Kollewe 1995)) the transition between gratings often leads to discontinuities. This is why we excluded the wavelengths 900 to 1100 nm and 1700 to 1900 nm from our analysis.

4.9 BRDF Calculation for ASDFieldspec

4.9.1 Calculating Irradiance and its Error

For the SE590, the irradiance was calculated by an integration over the whole upper hemisphere, see section 4.6. The ASD measurements do not cover the whole hemisphere but are restricted to the principal plane, thus this procedure is not applicable to the ASD measurements.

The value for the irradiance calculated for the SE590 is only valid for the SE590 because it contains an unknown calibration factor, see section 4.6.1. Multiplying by the ratio of the measurements of a sample at an arbitrary combination of angles would solve this problem, but only for the common wavelength range of the SE590 and the ASD.

We thus chose another way to calculate the irradiance: we simply used a transform of equation 3.11

$$E_i(\theta_i) = \frac{L_r(\theta_i, \theta_r, \varphi)}{f_r(\theta_i, \theta_r, \varphi)} \tag{4.13}$$

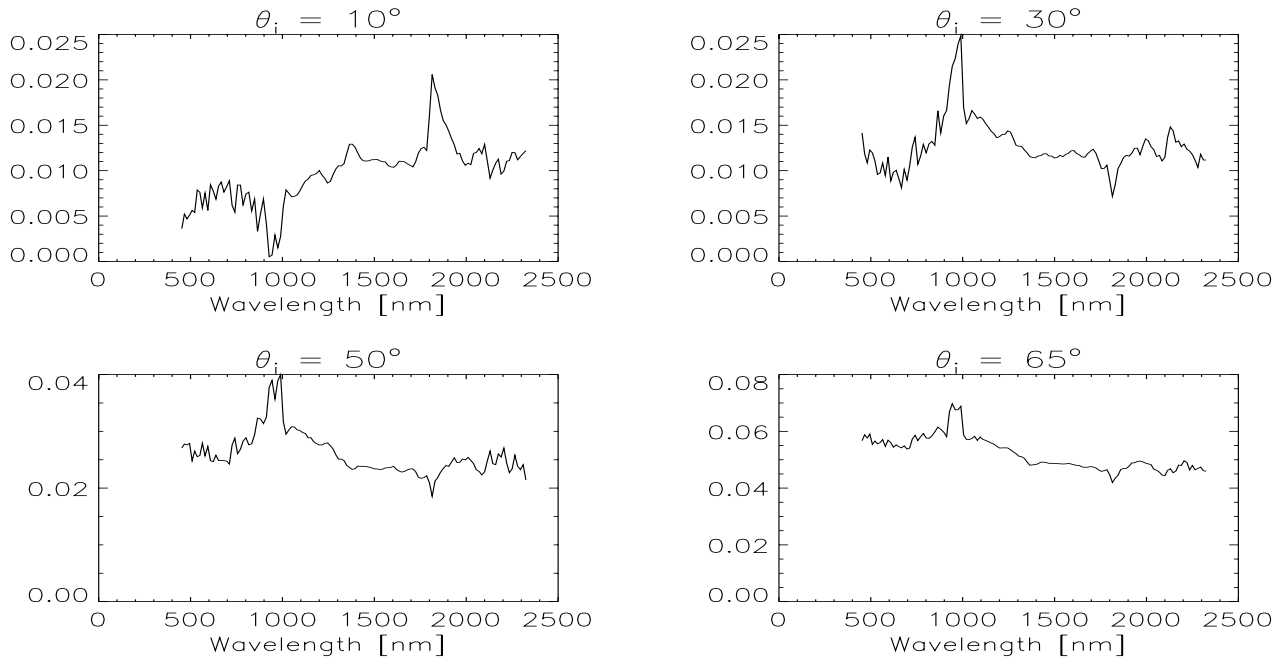

Figure 4.14: Relative ASD irradiance difference of the two reflectance panels for each angle of incidence. The values computed from the 50 % Spectralon were subtracted from the 100 % Spectralon and divided by the latter. The dependence of wavelength is weak, only at the grating transitions (1000 nm and 1800 nm) peaks or valleys can be seen.

and computed $E_i(\theta_i)$ for all available combinations of angles $(\theta_i, \theta_r, \varphi)$. For the wavelength range shared between ASD and SE590 we used the BRDF values obtained with the SE590. For those wavelengths where no SE590 measurements are available, we extrapolated the BRDF value from the closest wavelength shared between ASD and SE590 and adjusted for the different albedo (the albedo is known from the manufacturer for the whole wavelength range). E.g., if we want to calculate the irradiance at $\lambda = 2000$nm, we would divide the closest available BRDF value from the SE590 measurements ($f_r(\lambda = 975\text{nm})$) by the albedo at 975 nm and multiply by the albedo at 2000 nm. This is equivalent to assuming that the shape of the BRDF of the reference panels does not change with wavelength, a reasonable approximation.

Following the above approach, we calculated the irradiance for both reference panels (50 % and 100 % Spectralon) for every combination of angles (35 per scenario). For each panel separately we averaged over all combinations with the same incidence angle ($\theta_i = [10°, 30°, 50°, 65°]$). The relative difference between the irradiances from both panels can be seen in fig. 4.14. There is no clear wavelength dependence, except for the grating transitions, where peaks or valleys can be seen. Although these are only two measurements, we will regard this difference as the statistical error. This leads to relative irradiance errors of about 1 %, 1 %, 3 % and 5 % for $\theta_i = 10°, 30°, 50°$ and $65°$ resp. We estimate the methodical error of our method to about 2 % (mainly due to the averaging and the unknown behavior of the BRDF for wavelengths greater than 1000 nm), which will be added quadratically to yield overall relative irradiance errors of about 2 %, 2 %, 4 % and 5 % for the respective incidence angle.

4.9.2 Error Determination for ASD

We performed the same analysis of the instrument noise error σ_{noise} (eq. 4.6) as described in section 4.4. 17 scenarios contained measurements at the same angles. We assumed that the measurement processes (especially the choice of integration time) for the three gratings in the ASD are independent from each other.

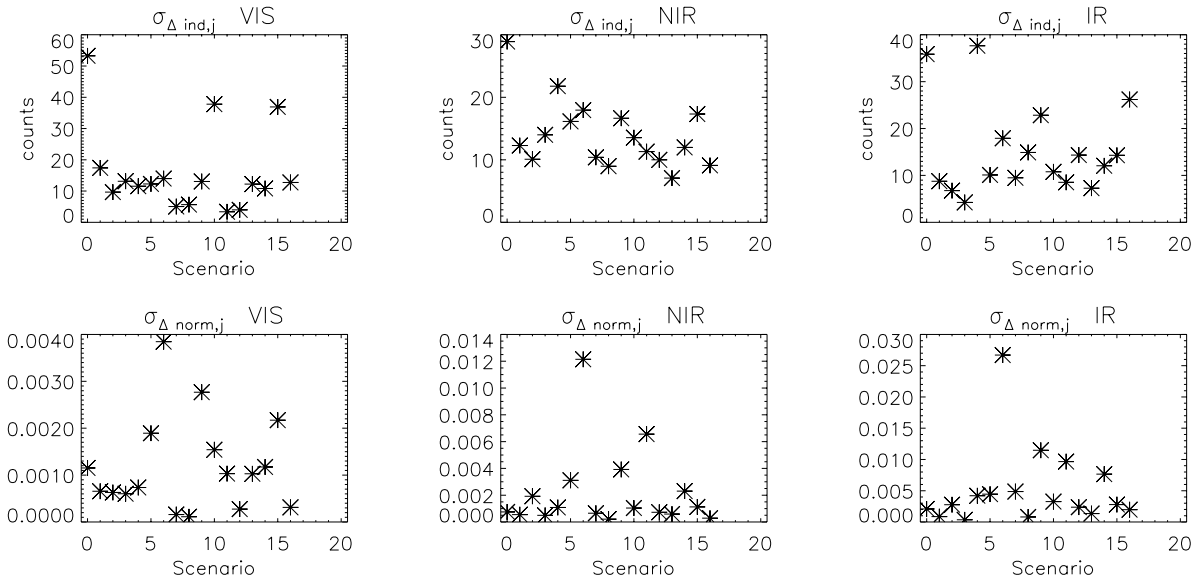

Figure 4.15: The top row shows $\sigma_{\Delta_{\mathrm{ind,j}}}$ for the ASD for each of the 17 scenarios. Left column shows the first grating, middle column the second grating and right column the third grating. The average values are $16 \pm 14, 14 \pm 5$ and 15 ± 10 counts for VIS, NIR and IR, respectively. Calculating $\sigma_{\Delta_{\mathrm{norm,j}}}$ (i.e. dividing by the maximum value of each spectrum) does not improve the results, which are shown in the bottom row, average values are $0.0011 \pm 0.0010, 0.0022 \pm 0.0030, 0.0052 \pm 0.0064$ for VIS, NIR and IR, resp.), in effect the relative variation even increases for NIR and IR.

Thus we calculated $\sigma_{\Delta_{\mathrm{ind,j}}}$ (see eq. 4.5) and $\sigma_{\Delta_{\mathrm{norm,j}}}$ for each grating separately (VIS, NIR and IR). Dividing by the maximum signal did not reduce the variation between scenarios, on the contrary, it rather increased (see fig. 4.15). This shows that the instrument noise of the ASD is not determined by the maximum intensity of the signal. In effect, it can be seen that the $\sigma_{\Delta_{\mathrm{ind,j}}}$ are quite constant already, with averages of $16 \pm 14, 14 \pm 5$ and 15 ± 10 counts for the three gratings respectively. Note that due to our extensive averaging for the longer wavelengths the error does not increase with wavelength.

We also calculated the deviation $\sigma_\Delta(\lambda)$ for each wavelength (i.e. averaging over the measurements of all $n_j = 17$ scenarios instead of averaging over the wavelength, see eq. 4.5):

$$\sigma_\Delta(\lambda) = \sqrt{\frac{\sum_{j=1}^{n_j} \left(\Delta_{\mathrm{ind,j}}(\lambda) - \frac{1}{n_j}\sum_{j=1}^{17} \Delta_{\mathrm{ind,j}}(\lambda)\right)^2}{n_j - 1}} \tag{4.14}$$

The resulting values are similar, ranging between 10 and 28 counts, with a mean value of 19 ± 5 counts. This indicates that the instrument noise is independent of illumination as well as sample reflectance and thus can be identified as dark current noise.

Dark current measurements of the ASD are shown in fig. 12.1 in the appendix. It can be seen that the average dark current is about 10 counts. However, the dark current is not distributed randomly for the first grating, as can be seen e.g. in the spectra 10, 21 and 26. Spectra 5 and 18 are very high for the last two gratings, but low for the first one. We suspect stray light to be the reason for these offsets. The root mean squared values of the measurements (after averaging over the wavelengths as described above) are shown as a function of wavelength in fig. 4.16. We attribute the small rise for short wavelengths (< 500 nm) to the stray light effects mentioned above, the strong rise for high wavelengths (starting at 1300 nm) to noise from thermal electrons.

For several wavelengths, the constancy of 30 measurements of the ASD without moving the goniometer is shown in the appendix, fig. 12.2 (time difference between consecutive measurements = 10 seconds). The

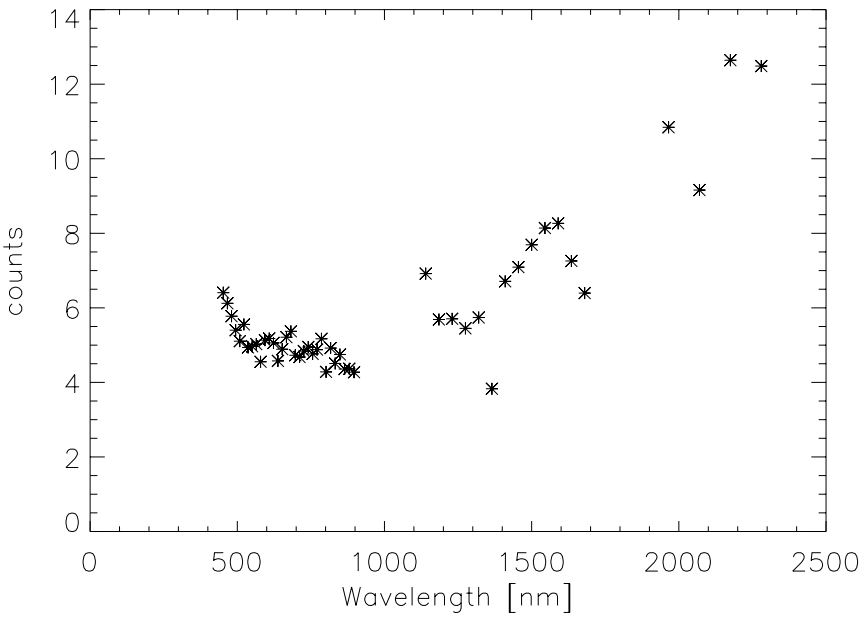

Figure 4.16: Root mean square values for 30 ASD dark current measurements (see fig. 12.1, appendix, for the individual measurements). The values rise from about 4 counts at 900 nm to about 13 counts at 2300 nm.

standard deviation of the signals is shown as a function of wavelength in fig. 4.17. It is lowest for the second grating, about 7 counts. The third grating has values from 10 to 15 counts. The first grating shows a small but steady rise from 14 to 15 counts. The rise is probably due to the decreasing sensitivity of the silicon detectors. Note that the results can also be influenced by short term lamp intensity fluctuations. The standard deviation is quite constant within each grating, thus it does not depend on the product of lamp intensity times detector sensitivity.

All these findings indicate that the instrument error of the ASD is absolute (not relative as for the SE590). **We decided to use an error of σ_{dc} = 20 counts** as a conservative and simple choice for the error propagation of the instrument error of the ASD. Our choice is based on the figures 4.15 (top row), 4.16 and 4.17.

The ASDFieldspec was designed for field measurements where the light intensity is usually much higher than in our laboratory setup. This may explain why the dominant instrument noise source in our case is the dark current.

Another indication that the ASD was set to its most sensitive mode is that there are several overflows for the specular measurements (e.g. all measurements with $\theta_i = \theta_r, \varphi = 180°$ for the sample 'Plastic' are overflows). Overflows can be identified because the (unprocessed) signals of neighboring channels are exactly equal. They were eliminated from the analysis. Problems at high intensities probably due to a nonlinearity of the response of the ASD when reaching the saturation level are discussed in section 5.7.2.

The error of the BRDF values f_r measured with the ASD is obtained with the same equation as for the SE590 (eq. 4.12), but with σ_{E_i} calculated as described in section 4.9.1. The formula to calculate σ_{L_r} is

$$\sigma^2_{L_r(\theta_i,\theta_r,\varphi)} = \left(L_r(\theta_i,\theta_r,\varphi)\cdot\sigma_{\mathrm{lamp}}\right)^2 + \left(L_r(\theta_i,\theta_r,\varphi)\cdot\sigma_{\mathrm{illu}}(\theta_i,\theta_r,\varphi)\right)^2 + \sigma^2_{\mathrm{dc}} \qquad (4.15)$$

where $\sigma_{\mathrm{dc}} = 20$ counts. σ_{illu} and σ_{lamp} are the same as in the corresponding equation for the SE590 (eq. 4.11). Averaged over all samples and wavelengths, the mean error is 4.9 %. The relative error is shown as a function of wavelength averaged over all samples in fig. 4.18 (fig. 12.3 in the appendix shows the plots for each sample separately).

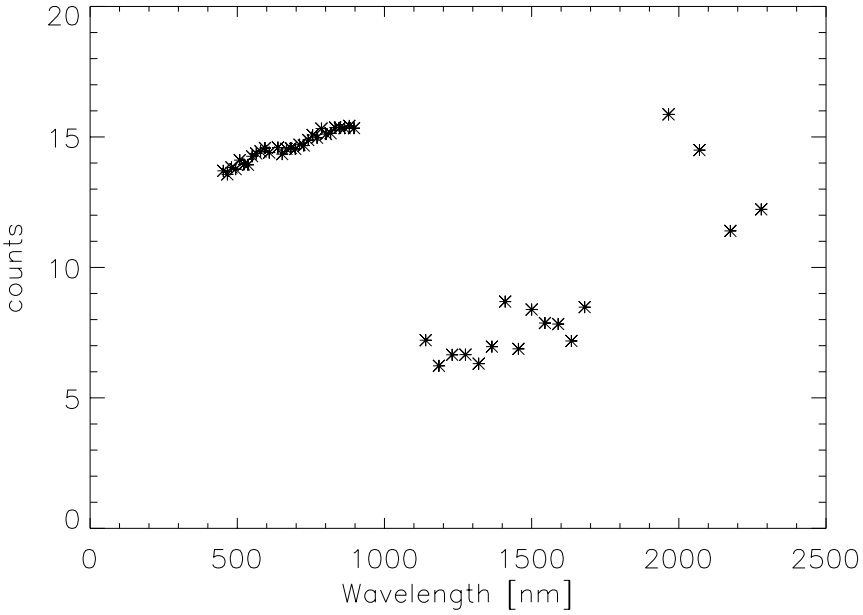

Figure 4.17: Standard deviation of 30 ASD constancy measurements, obtained by repeated measurements of Spectralon 100 % without moving the goniometer (see fig. 12.2, appendix, for the individual wavelengths).

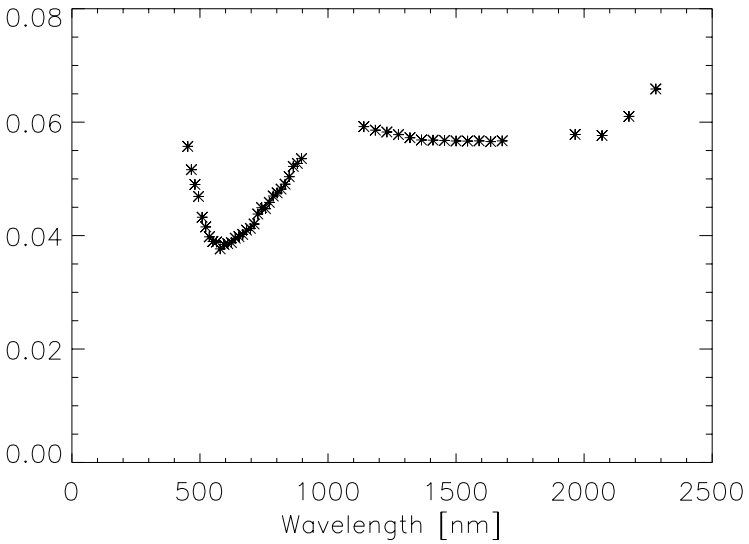

Figure 4.18: Relative error of the ASD measurements averaged over all samples and measurements.

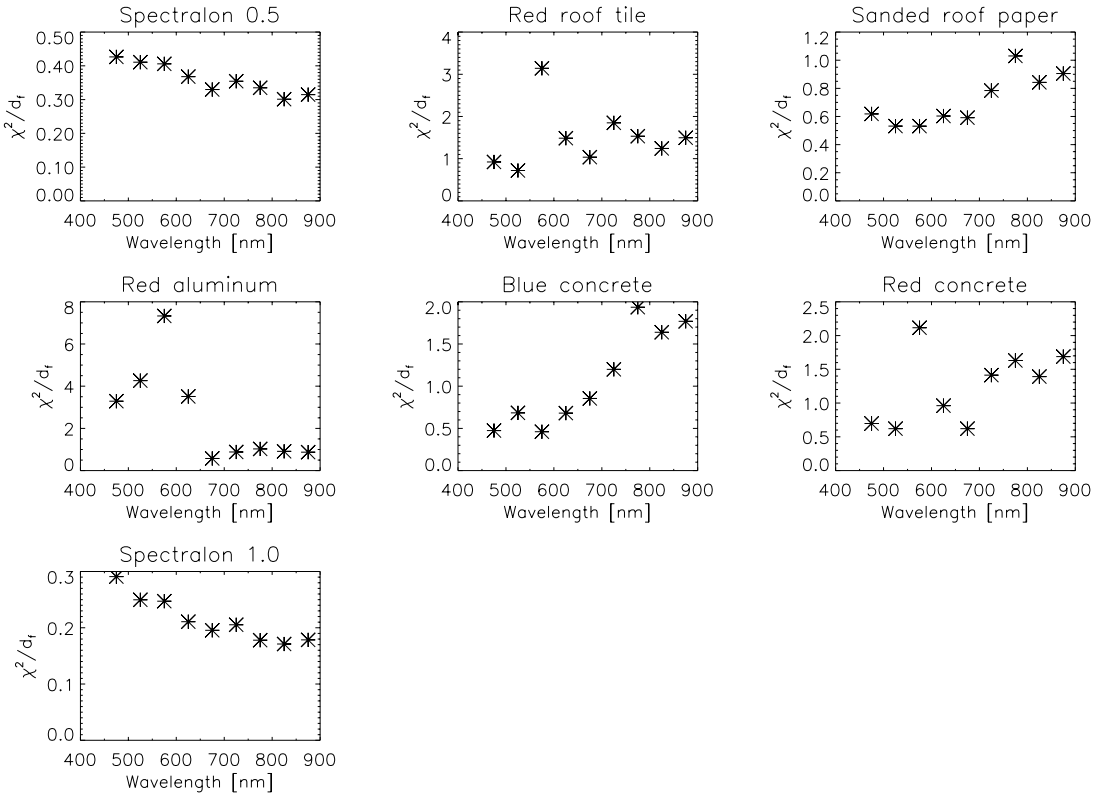

Figure 4.19: Agreement of SE590 and ASD measurements: the ratio of χ^2 (testing the hypothesis of eq. 4.16, that the ASD measurements are equal to the SE590 measurements) over the degrees of freedom d_f, in this case the number of measurements, varying between 10 and 20. For most samples, the hypothesis can be accepted, but for aluminum it is rejected.

4.10 Comparison of ASD and SE590 Measurements

Generally, the measurements of the ASDFieldspec and the SE590 agree quite well, as can be seen from figures 5.18 to 5.21, pp. 66 ff., in section 5.7.1.

A statistical comparison of the measured values is complicated by the fact that the wavelength channels of the ASD and the SE590 do not exactly correspond to each other, thus it is difficult to decide whether a deviation is due to sensor problems or due to a change of reflectance with wavelength. Thus we averaged the measured reflectances to intervals of 50 nm and tested, if the hypothesis

$$f_r^{\mathrm{SE590}} - f_r^{\mathrm{ASD}} = 0 \tag{4.16}$$

passes the χ^2 test. The resulting χ^2-values divided by the degrees of freedom d_f (the number of measurements in this case) are plotted in fig. 4.19. The number of measurements, where the same combinations of angles is available for both SE590 and ASD varies between 10 (aluminum) and 20 (Spectralon). It can be seen that χ^2/d_f is usually below one, thus the measured values of the ASD and the SE590 agree well. A peak can be seen in all 3 red samples (red roof tile, red aluminum, red concrete) at 575 nm. It is probably due to the rapid increase of the reflectance at this wavelength, which causes the deviations because of the different wavelength sampling of the two sensors. The aluminum measurements do not agree well, especially for shorter wavelengths. The other samples with a strong specular peak show a small increase above 700 nm, which is due to problems of the SE590, as will be shown in the following paragraph.

Fig. 4.20 shows that there is a significant difference between the ASD and the SE590 measurements above 700 nm for high intensities. The ratio of the measured radiance of the samples and the reference panel

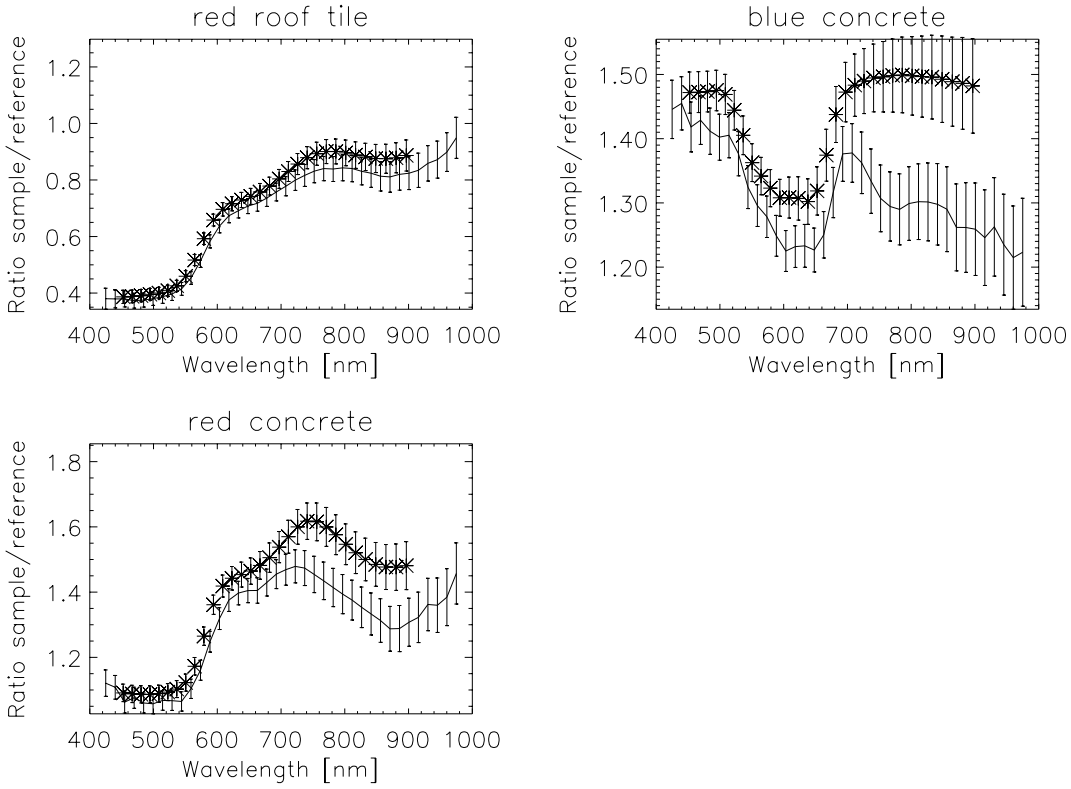

Figure 4.20: Deviations of the SE590 measurements from the ASD measurements at high intensities for $\lambda > 700$nm. The solid line shows SE590 reflected radiance divided by the reflected radiance of the reference panel 'Spectralon 0.5', both at $\theta_i = \theta_r = 50^\circ, \varphi = 180^\circ$. The stars show the respective ratio for the ASD measurements. The measurement errors are shown as vertical bars. Above 700 nm, the disagreement between the two curves extends beyond the error bars for the two samples with a strong specular peak.

Spectralon 0.5 at $\theta_i = \theta_r = 50^\circ, \varphi = 180^\circ$ is shown. For the sample 'red roof tile', which doesn't have a strong specular peak, both curves agree well. For the two concrete samples, which both have a strong specular peak, the ASD measurements are about 15 % higher. A similar pattern can be observed when dividing by the respective measurements of the Spectralon 1.0 panel. We will see later that the decrease of the SE590 from 700 nm to 770 nm can be seen in the specular albedo of all samples. Thus this decrease is probably a sign of a nonlinearity of the SE590 for high intensities above 700 nm, because at average intensities (i.e. for the diffuse component) no such decrease is detectable.

Chapter 5

BRDF of the Samples: Data and Models

5.1 Overview

This chapter shows how the measured data can be described by BRDF models. Two models were investigated: the specular reflectance model for rough surfaces by (Torrance & Sparrow 1967), and the BRDF model for rough surfaces by (Oren & Nayar 1995). We demonstrate that for the very rough surfaces 'asphalt' and 'sanded roof paper' the second model is in better agreement with the measurements, whereas for the other surfaces the first model is preferable. Previous *in situ* measurements with a goniometer table are shown to agree well with the laboratory data.

5.2 Angular Grid

The basic structure of the *European Goniometric Facility* EGO is depicted in fig. 4.1, page 16. The sample is to be placed in the center of the structure. Two quarter arcs can be moved on circular rails into any azimuth angle. On each arc, a sled is mounted, whose position determines the zenith angle. On the sleds, the lamp and the detector are mounted (see chapter 4 for a description of the available sensors and lamps). A measurement series consisting of the measurements and the positioning of the arcs and sleds is called 'scenario'. The positions of the arcs and the sleds are controlled by a PC program.

The input files needed to create the scenarios consist of commands for moving the two sleds and the detector arc, and commands to take radiometric measurements. The resulting angular combinations are shown in figures 5.1 and 5.2 for the ASD scenarios and the SE590 scenarios, respectively. The measurements with the ASD where only taken in forward scattering direction ($\varphi = 180^\circ$), varying the viewing angle θ_r from 0° to 70° with a 10° sampling rate for 4 different illumination angles ($\theta_i = 10^\circ, 30^\circ, 50^\circ, 65^\circ$).

The angular combinations for the measurements with the SE590 cover the whole range of relative azimuth angles $\varphi \in [0^\circ, 180^\circ]$. The densest coverage was chosen for the specular peaks at $\theta_i = 30^\circ$ and $\theta_i = 50^\circ$. We also measured the specular peak at $\theta_i = 65^\circ$, but with a less dense coverage.

Our second focus were measurements in backscattering direction to investigate the hotspot (in association with BRDF, 'hotspot' is referred to as an increase in reflectance when the viewing direction approaches the illumination direction). Here we took measurements in the principal plane as well as out of the principal plane again. The closest we could get to the hotspot direction was a relative angle of 10°, e.g. at ($\theta_i = 0^\circ, \theta_r = 10^\circ$) or ($\theta_i = 65^\circ, \theta_r = 55^\circ, \varphi = 0^\circ$). A closer positioning of sensor and light source was not possible because the devices might have touched each other.

To study the diffuse component, we measured across the principal plane ($\varphi = 90^\circ$) for 4 different illumination angles $\theta_i = 0^\circ, 30^\circ, 50^\circ, 65^\circ$. Note that at $\theta_i = 0^\circ$ the relative azimuth is not defined, thus these measurements also cover the specular peak or the hotspot, in case they are broad enough.

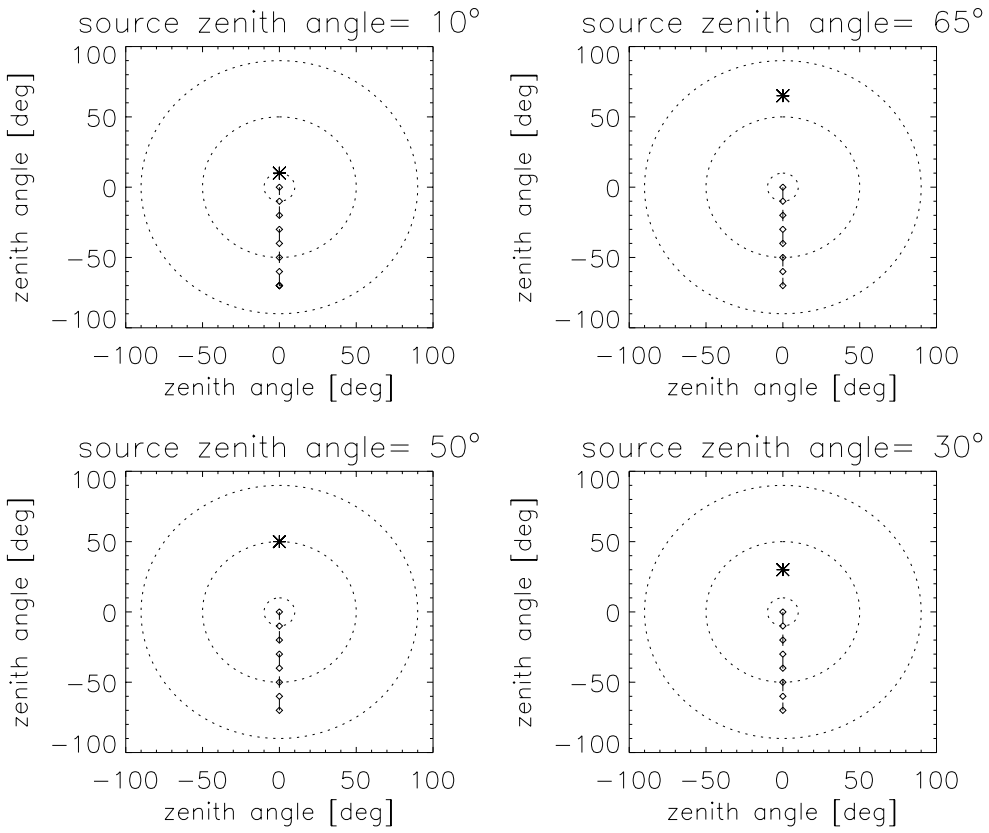

Figure 5.1: This figure shows the angular combinations for the ASD in polar plots. The inner circle (dotted line) corresponds to $\theta = 10°$, the middle circle to $\theta = 50°$, and the outer circle to $\theta = 90°$. The star indicates the position of the light source. The small rhombs show the angles at which the sensor took measurements. For the ASD, the azimuthal positions of the arcs was kept constant to save time. Thus all measurements were taken with a relative azimuth of $\varphi = 180°$.

The choice of angular combinations is a compromise between the available time and the required angular coverage. Especially moving the arcs on the circular rails is very time consuming, about 5 minutes to vary φ by $180°$. An ASD scenario lasted about 20 minutes, whereas the SE590 scenario took about 90 minutes. The ASD scenario consists of 35 angular combinations, the SE590 scenario of 166.

5.3 Torrance-Sparrow Model

The specular reflection model of rough surfaces by (Torrance & Sparrow 1967) has received widespread attention ((Ginneken et al. 1998), (Nayar et al. 1991), (Dana et al. 1999), (Meister et al. 1998c), (Rothkirch et al. 2000)). The specular peak of rough surfaces does not reach its maximum when the illumination zenith angle equals the reflection zenith angle (forward scattering direction), but the maximum is shifted towards higher reflection zenith angles. This behavior can be well described by the BRDF model of (Torrance & Sparrow 1967). We will call this model *TS model*. The BRDF f_r^{TS} is given by

$$\begin{aligned} f_r^{\mathrm{TS}} &= t_0 + t_1 \cdot f_r^{\mathrm{spec}} \quad , \\ f_r^{\mathrm{spec}} &= \frac{F(\theta_i, \theta_r, \varphi, n, k)}{\cos\theta_i \cos\theta_r} \cdot G(\theta_i, \theta_r, \varphi) \cdot \mathrm{e}^{-w^2\alpha^2} \quad , \end{aligned} \tag{5.1}$$

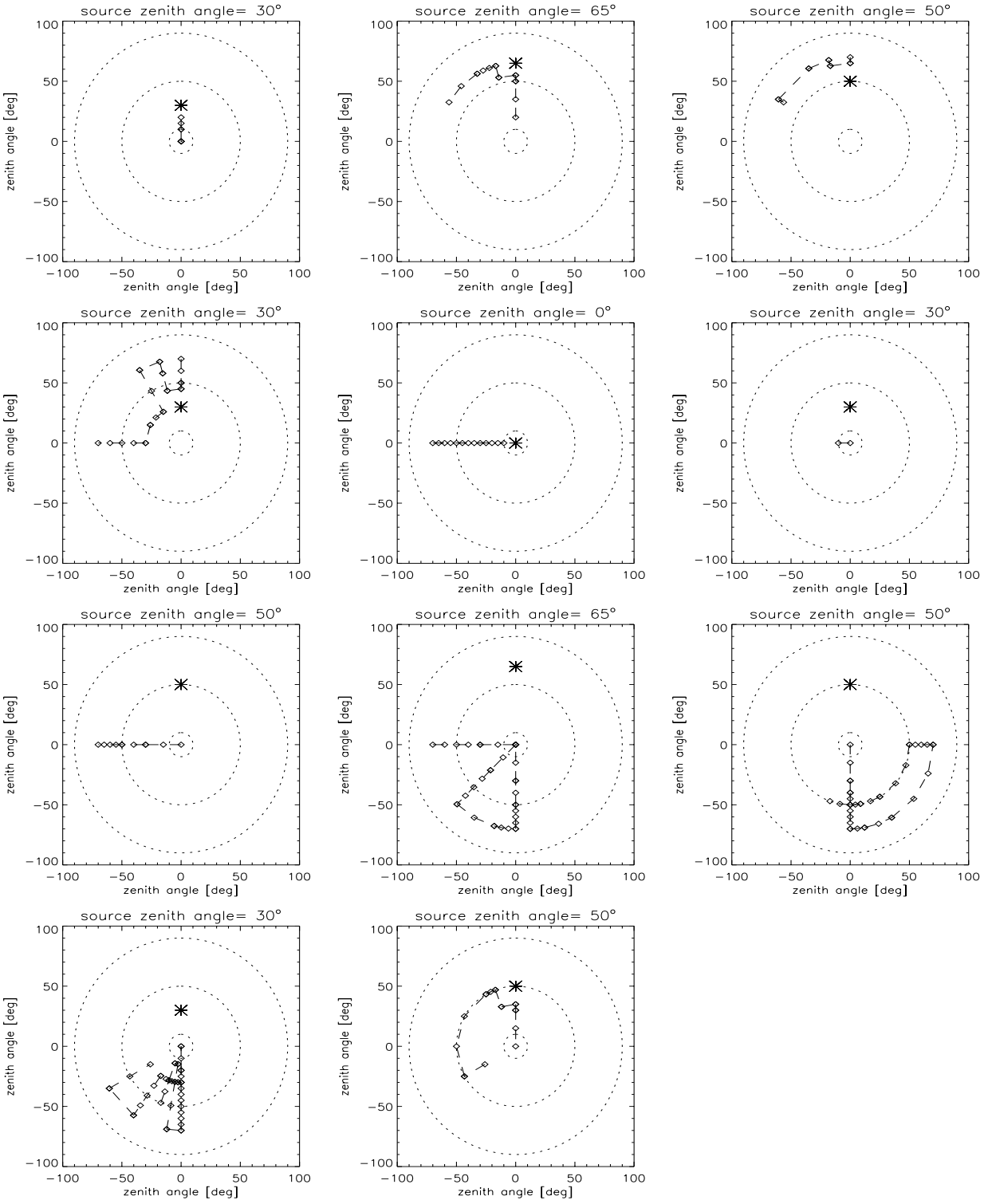

Figure 5.2: This figure shows the angular combinations for the SE590 in polar plots. The inner circle (dotted line) corresponds to $\theta = 10°$, the middle circle to $\theta = 50°$, and the outer circle to $\theta = 90°$. The star indicates the position of the light source. The small rhombs show the angles at which the sensor took measurements. The dashed line shows the movement of the detector. Each time the source angle is changed, a new plot is created.

where F is the Fresnel reflectance, given e.g. in (Hapke 1993). It is a function of the index of refraction n, the coefficient of absorption k and the local illumination angle θ_i' on the surface facet. This angle is determined by the zenith angles of incidence and reflection (θ_i, θ_r), and the relative azimuth angle φ:

$$\cos 2\theta_i' = \cos\theta_i \cos\theta_r - \sin\theta_i \sin\theta_r \cos\varphi \tag{5.2}$$

t_0 is the Lambertian component, t_1 describes the intensity of the specular component. G is the 'Geometric Attenuation Factor', which models effects of masking and shadowing, and takes on values between 0 and 1. In many cases, setting $G = 1$ is a very good approximation, (Meister et al. 2000), (Nayar et al. 1991). In this study, G is always exactly calculated. It is given by (Nayar et al. 1991)

$$G(\theta_i, \theta_r, \varphi) = \min\Big(1, \frac{2\cos\alpha\cos\theta_r}{\cos\theta_i'}, \frac{2\cos\alpha\cos\theta_i}{\cos\theta_i'}\Big) \tag{5.3}$$

Basically, the TS model assumes that the surface is made up of surface facets, whose normals have a Gaussian probability distribution $P(\alpha)$:

$$P(\alpha) \propto \mathrm{e}^{-w^2\alpha^2} \quad , \tag{5.4}$$

where α denotes the zenith angle of the surface facet normal and w determines the width of the distribution. (Torrance & Sparrow 1967) use α with the unit 'degree', thus w has the unit degree^{-1}. According to (Ginneken et al. 1998), α can be calculated from

$$\cos\alpha = (\cos\theta_i + \cos\theta_r) \cdot ((\cos\varphi\sin\theta_r + \sin\theta_i)^2 + \sin^2\varphi\sin^2\theta_r + (\cos\theta_i + \cos\theta_r)^2)^{-\frac{1}{2}} \quad . \tag{5.5}$$

In the TS model it is assumed that each surface facet is next to a surface facet whose surface normal has the same inclination α, but is oriented into the opposite direction (the azimuth angle of the second surface normal differs by 180 degrees from the azimuth angle of the first surface normal), forming a V-cavity (see fig.5.3, page 46). In fact, this a very *unrealistic* assumption, because the inclinations of neighboring facets are usually *uncorrelated*. This assumption was introduced because for this kind of V-cavity, it is possible to exactly derive the shadowing and masking effects analytically. These effects are expressed by the Geometric Attenuation Factor G.

The TS model does not make any assumptions on how the V-cavities connect to each other. It is possible to imagine neighboring V-cavities that are all parallel (heading into the same direction) (see fig. 1.2, page 3), but the TS model requires V-cavities that are running into all possible directions of infinite length. A realization of this leads to 'crossings' between V-cavities, but these crossings are not treated by the TS model. Thus it is not possible to create a consistent realization of the TS model. Another argument against understanding the TS model as a series of neighboring V-cavities is the necessity for these V-cavities to have the same maximum height (see fig. 5.3), a restriction that does not apply to the TS model.

We conclude that because of the unrealistic assumption of V-cavities, masking and shadowing effects are probably not well described by the TS model. These effects are the more important the rougher the surface, see e.g. (Meister et al. 2000).

5.4 Oren-Nayar Model

The BRDF model proposed by (Oren & Nayar 1995) (see also (Oren & Nayar 1994)) is based on the same assumptions on V-cavities as the TS model. We will call their model *ON model*. The description of the specular peak was adopted from the TS model. They also assume a Gaussian distribution of the inclinations of the surface facets, cf. eq. 5.4:

$$P(\alpha) \propto \mathrm{e}^{-\frac{\alpha^2}{2k_w^2}} \quad , \tag{5.6}$$

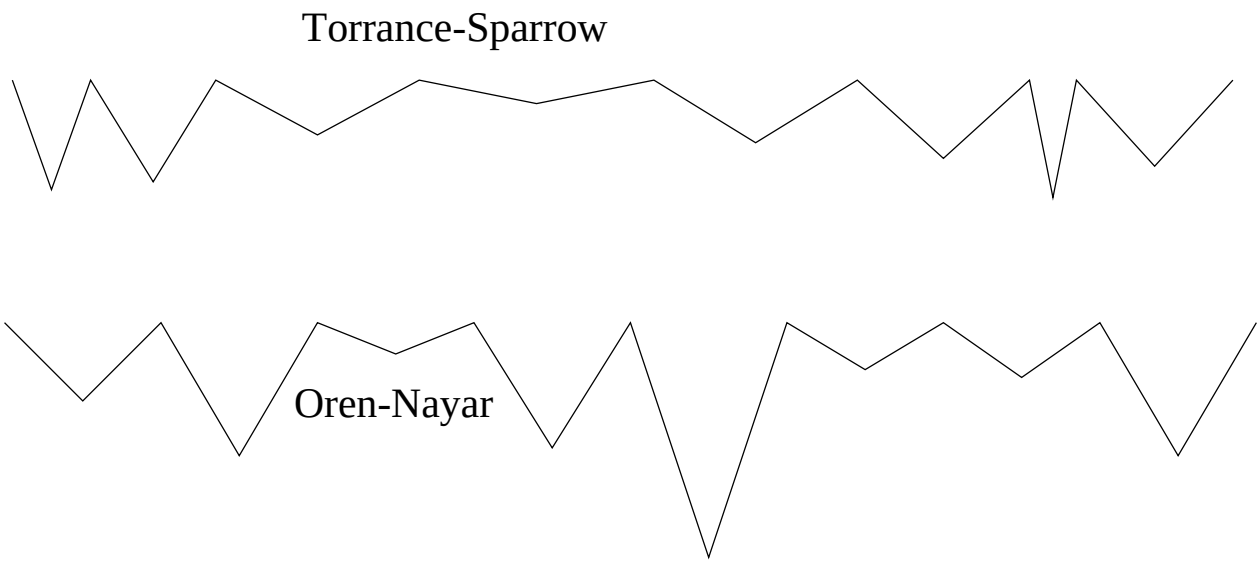

Figure 5.3: Neighboring V-cavities heading into the same direction. These surfaces are not appropriate realizations of the TS resp. ON model surfaces because they all head into the same direction and the peak of each cavity has the same height for the whole surface (see text). The difference between the two profiles is that the profile of the TS model has facets of constant length, whereas the profile of the ON model has cavities of constant length.

where the width parameter k_w is in radians. However, whereas (Torrance & Sparrow 1967) assume that the width of each surface facet is constant, (Oren & Nayar 1995) assume that the width of the total cavity is constant (see fig.5.3, the width of a surface facet of the Oren-Nayar surface varies considerably, but stays constant for the Torrance-Sparrow surface). Thus, for a surface facet with an inclination α, the length of the surface facet is $1/\cos\alpha$ times larger in the ON cavity than in the TS cavity. Both models assume a Gaussian distribution of inclinations α. This results in different widths of the specular peaks, because in the ON model the total area of inclined surface facets is larger than in the TS model. Analytically, the ON model has the same specular peak as the TS model, divided by $\cos\alpha$. (Oren & Nayar 1995) set the Fresnel reflectance equal to one, reasoning that it was difficult to obtain meaningful estimates of the refractive index n. Although we agree that the determination of the refractive index is difficult, we believe that setting the Fresnel reflectance to 1 requires further justification, because it seems more reasonable to estimate n (which usually varies between 1.3 and 2.0, (Wolff 1994), $n = 1.5$ is an average value often found in the literature (e.g.(Hapke 1993), (Stover 1995)). We did not follow their approach, but treated the refractive index like any other parameter in the model.

The important advantage of the ON model over the TS model is that the diffuse component is no longer assumed to be lambertian, but is modeled based on geometrical optics, taking effects of masking, shadowing and multiple reflections into account. The basic assumption is that each surface facet reflects lambertian. The resulting model is only numerical, but (Oren & Nayar 1995) give the following analytical approximation, which we use in this study. A Gaussian inclination distribution of the surface facets is assumed

$$P'(\alpha) \propto \mathrm{e}^{\frac{\alpha^2}{2k_w^2}} \quad . \tag{5.7}$$

We use the prime in P' to distinguish this distribution of equal cavity width from the distribution P introduced by (Torrance & Sparrow 1967) in eq. 5.4 for equal facet width. The direct illumination component of

reflectance of a surface characterized by eq. 5.7 is:

$$f_r^{\mathrm{dir}} = \frac{k_d}{\pi[sr]}(C_1 + C_2 \cdot \cos\varphi \tan\beta_2 + C_3 \cdot (1 - |\cos\varphi|) \cdot \tan\frac{\beta_1 + \beta_2}{2}) \tag{5.8}$$

$$\text{with } \beta_1 = \mathrm{Max}[\theta_i, \theta_r], \beta_2 = \mathrm{Min}[\theta_i, \theta_r]$$

$$C_1 = \frac{-k_w^2}{2k_w^2 + 0.66}, \quad C_3 = \frac{2k_w^2}{k_w^2 + 0.09}(\frac{\beta_1\beta_2}{\pi^2})^2$$

$$C_2 = \text{if} \cos\varphi \geq 0 : \frac{0.45k_w^2}{k_w^2 + 0.09}\sin\beta_1, \quad C_2 = \text{if} \cos\varphi < 0 : \frac{0.45k_w^2}{k_w^2 + 0.09}(\sin\beta_1 - (\frac{2\beta_2}{\pi})^3)$$

The multiple scattered component is approximated by

$$f_r^{\mathrm{ms}} = 0.17\frac{\rho^2}{\pi[\mathrm{sr}]}\frac{k_w^2}{k_w^2 + 0.13} \cdot (1 - \cos\varphi(\frac{2\beta_2}{\pi})^2) \quad . \tag{5.9}$$

The specular component is similar to f_r^{spec} as defined by (Torrance & Sparrow 1967) (eq. 5.1), but divided by $\cos\alpha$:

$$f_r^{\mathrm{ON-spec}} = \frac{F(\theta_i, \theta_r, \varphi, n, k)}{\cos\theta_i \cos\theta_r \cos\alpha} \cdot G(\theta_i, \theta_r, \varphi) \cdot \mathrm{e}^{\frac{\alpha^2}{-2k_w^2}} \quad . \tag{5.10}$$

We obtain the total BRDF as a linear combination of the diffuse and the specular component:

$$f_r^{\mathrm{ON}} = f_r^{\mathrm{dir}}(k_d, k_w) + f_r^{\mathrm{ms}}(k_d, k_w) + k_s \cdot f_r^{\mathrm{ON-spec}}(k_w) \quad . \tag{5.11}$$

The parameters determining this model are the diffuse albedo k_d, the width of the distribution of the surface inclinations k_w, and the intensity of the specular peak k_s, together with the index of refraction n and the index of absorption k.

5.5 Further BRDF Models

A BRDF model for man-made surfaces proposed by (Wolff 1996) predicts a strong decrease of the diffuse component for large zenith angles. As we did not find evidence for such a decrease in our data, we did not investigate this model any further.

Several BRDF models exist to predict the directional reflectance of soil (Hapke 1993), (Liang & Townshend 1996a), (Staylor & Suttles 1986). Their predictions qualitatively did not match with the BRDF values measured here.

Due to the completely different approach, we did not examine empirical or semi-empirical BRDF models that were primarily designed to either cover a large variety of BRDFs (Walthall et al. 1985), (Goel & Reynolds 1989), (Rahman et al. 1993), (Wanner et al. 1995), (Meister et al. 1996a) or are focused on vegetation (Jupp & Strahler 1991), (Kuusk 1995), (Ni et al. 1999), (Gastellu-Etchegorry et al. 1999).

5.6 Results of the SE590 Measurements

5.6.1 Angular Dependence

The plots in figures 5.7 to 5.14 show the BRDF values of different surface materials measured with the SE590 at two wavelengths: 450 nm and 660 nm (plots for 900 nm can be found in the appendix, pages 149 to 156). The error bars indicate the measurements at 660 nm, the crosses show the measurements at 450 nm (no errors are shown for the 450 nm measurements). The solid line shows the fit of the best fitting BRDF model

(either TS or ON) to the 660 nm data, the dashed line shows the fit to the 450 nm data. The parameters were fitted to the measurements of all angles simultaneously, but for each wavelength separately. In some cases (Spectralon samples and blue concrete) 450 nm and 660 nm data are so close together that they can hardly be discriminated, and we chose to plot only 660 nm. The models were fitted to the data using the programming package IDL by Research Systems, Inc., Boulder, Colorado, USA. A least squares algorithm was used to minimize χ^2. The parameter k was set to 0.25, see chapter 6. The respective plots for a wavelength of 900 nm are shown in the appendix, figures 12.4 to 12.11. An overview can be obtained from figures 5.5 and 5.6, where only the data in the principal plane for 660 nm is shown for $\theta_i = 30^\circ$ and $\theta_i = 50^\circ$.

For the Spectralon panels, the concrete tiles, 'red roof tile' and 'red aluminum', the TS model gives the best fit. For 'asphalt' and 'sanded roof paper', the two roughest samples, there is a strong increase in backscattering direction ($\varphi = 0^\circ$), which is modeled very well by the ON model. We expected the ON model to perform equally well as the TS model for the smoother surfaces, because in the limit of a perfectly flat surface, the diffuse component of the ON model becomes lambertian, like in the TS model. However, especially for the roughness of samples like 'red roof tile', the ON model predicts an increase in backscatter direction for large incidence zenith angles, that is not supported by the data. Another drawback of the ON model is that the values retrieved for the refractive index n are even higher than the values retrieved for the TS model. Although the values retrieved for the refractive index can only be regarded as estimates (see discussion on the parameters n and k in chapter 6), this is another disadvantage, because the values we retrieved for n from the TS model are probably already rather too high than too low. The reason for the worse performance of the ON model is probably the assumption of cavities of constant length (see section 5.4), because this is the only difference between the two models regarding the specular peak.

Overall, the model predictions agree remarkably well with the measured data. However, we want to note the following interesting deviations:

- For the sample 'red roof tile', at $\theta_i = 0^\circ$ the increase of the data when the detector is approaching the light source is not well modeled.
- The measured values at $\theta_i = 65^\circ$ and θ_r close to nadir are usually lower than the values predicted by the TS model (see 'Spectralon 0.5', 'red roof tile', 'aluminum' and 'blue concrete').
- For 'aluminum', the specular peak at $\theta_i = 65^\circ$ is underestimated by almost 40 %.
- The specular peak predicted by the ON model is shifted strongly towards higher zenith angles, but the measured data rather suggest a less strong shift, especially at $\theta_i = 50^\circ$.
- For the sample 'sanded roof paper', there is an edge at $\theta_i = 0^\circ$, $\varphi = 90^\circ$, $\theta_r = 60^\circ$ in the modeled data, because the value of G starts to become smaller than one. The data do not show this peak. The reason is that the increase with θ_r is not caused by the specular peak, as assumed by the model. The increase is due to the colored structure of the 'sanded roof paper' (bright quartz grains on black background). For increasing θ_r, the background is concealed, and only the bright quartz is seen by the detector.
- In the backscattering direction ($\varphi = 0^\circ$), almost all samples show an increase when θ_r approaches θ_i within 10° of a few percent. The increase is so small that it does not exceed the error bars, except for a small amount for 'asphalt' and 'red concrete' at $\theta_i = 30^\circ$. The common explanation for an increase in backscatter direction (*hotspot*) is the disappearance of shadows when the viewing direction approaches the source direction (Jupp & Strahler 1991). But this effect is already modeled by the ON model, and it produces a very broad increase, not such a localized increase. Furthermore the localized increase seems to be strongest for $\theta_i = 30^\circ$, whereas the amount of shadow increases for higher θ_i, thus from the shadow-hiding approach we would expect the increase at $\theta_i = 30^\circ$ to be weaker than at $\theta_i = 50$. We believe that the localized increase we are seeing in the data is due to *coherent backscatter* (Kuga

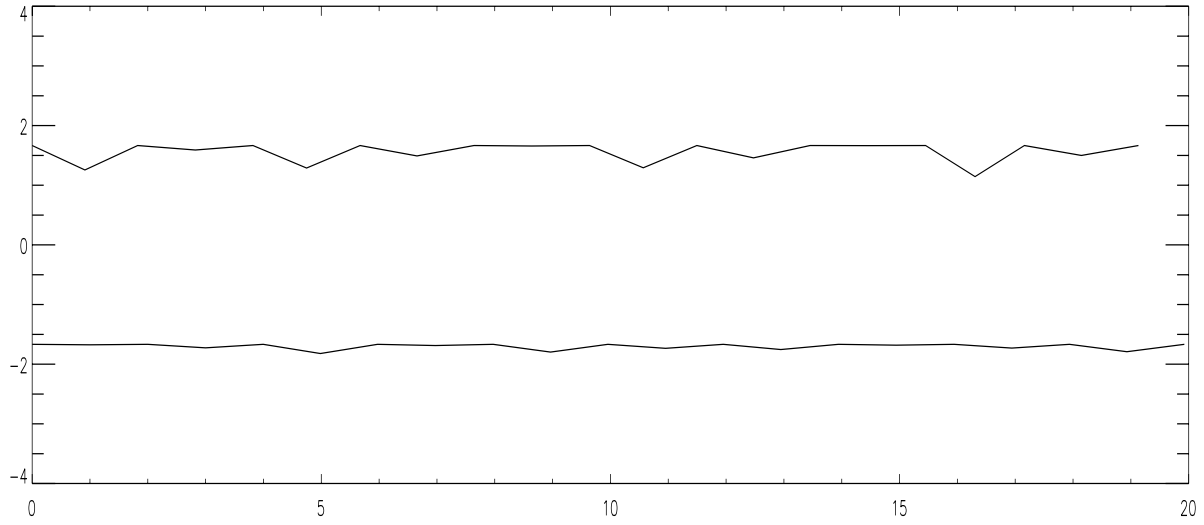

Figure 5.4: Computer generated one-dimensional surface profiles, corresponding to a surface with width parameter (see eq. 5.4) $w = 0.032$ (Spectralon 0.5, see table 5.1) for the profile above zero and to a surface with width parameter $w = 0.169$ (red aluminum) for the profile below zero.

& Ishimaru 1984), (Hapke et al. 1993), also called *weak photon localization*. It occurs if two partial waves associated with the same incident wave front travel the same multiply scattered path on the surface, but in opposite directions. Typical coherent-backscatter widths observed in the laboratory are of the order 0.5° (Hapke 1993), thus our data is clearly inappropriate to study these effects, because we can approach the direct backscatter direction $\theta_r = \theta_i, \varphi = 0^\circ$ only up to 10° because of the limitations of the EGO construction. Our data probably only show the beginning of the rise of the coherent backscatter peak.

The specular albedo ρ_s is calculated as the integral of the specular BRDF given by f_r^{spec} for the TS model ($f_r^{\mathrm{ON-spec}}$ for the ON model) over the projected solid angle $d\Omega_r = \sin\theta_r \cos\theta_r d\theta_r d\varphi$ (cf. (Nicodemus et al. 1977)) over the whole upper hemisphere. It usually depends on the illumination angle θ_i:

$$\rho_s(\theta_i) = \int_{\Omega_r} f_r^{\mathrm{spec}}(\theta_i, \theta_r, \varphi) d\Omega_r \tag{5.12}$$

The fitted parameters are given in table 5.1 and 5.2 at a wavelength of 660 nm, together with the specular albedo ρ_s at $\theta_i = 30^\circ$ and χ^2/d_f. If the latter value is greater than 1.3, the χ^2 test rejects the model. The samples 'red aluminum' and 'blue concrete' are rejected. The corresponding values for wavelengths λ of 425 nm and 900 nm are given in the appendix, tables 12.1 to 12.4.

In order to visualize the surface roughnesses associated with the fitted width parameters w, fig. 5.4 shows surface profiles generated with a roughness corresponding to $w = 0.032$ (Spectralon 0.5) above zero and $w = 0.169$ (red aluminum) below zero.

The specular albedo for Spectralon 0.5 is 0.024, i.e. about 5 % of the reflected radiance undergo a specular scattering process. For Spectralon 1.0, about 2 % of the reflected radiance is reflected specularly. These values are rather high, especially for Spectralon 1.0 we would have expected a specular albedo of about 1 % or less.

5.6.2 Wavelength Dependence

The wavelength dependence of the BRDF of rough surfaces can be understood best by investigating the wavelength dependence of the parameters retrieved from fitting BRDF models to the data. The reflectance [1]

[1] The diffuse reflectance can be obtained by multiplying coefficient t_0 with π, see figures 5.15 to 5.17.

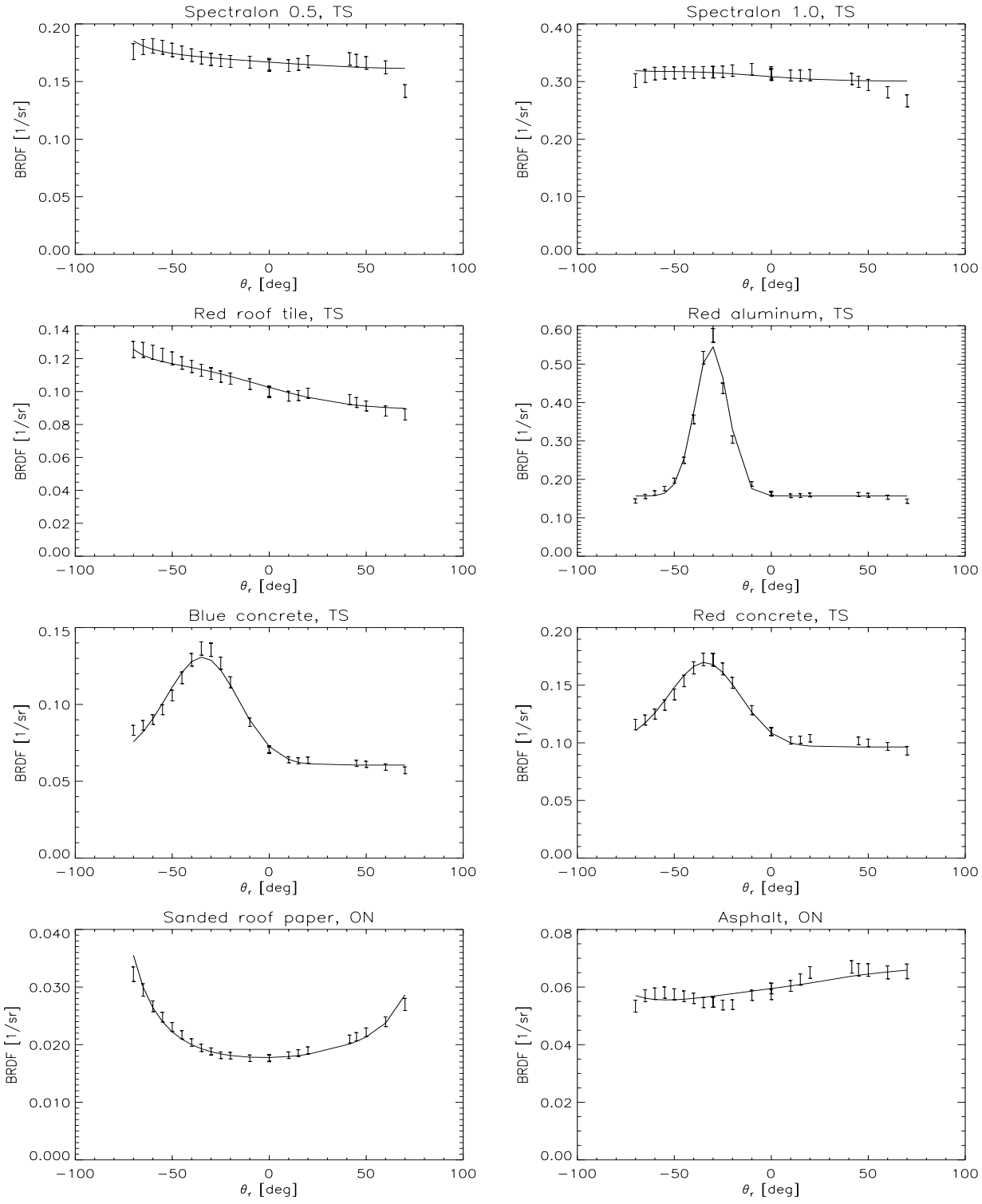

Figure 5.5: Models (TS, ON, resp.) fitted to BRDF measurements of the SE590 at 660 nm for $\theta_i = 30°$. Positive θ_r correspond to backward scattering ($\varphi = 0°$), negative θ_r to forward scattering ($\varphi = 180°$).

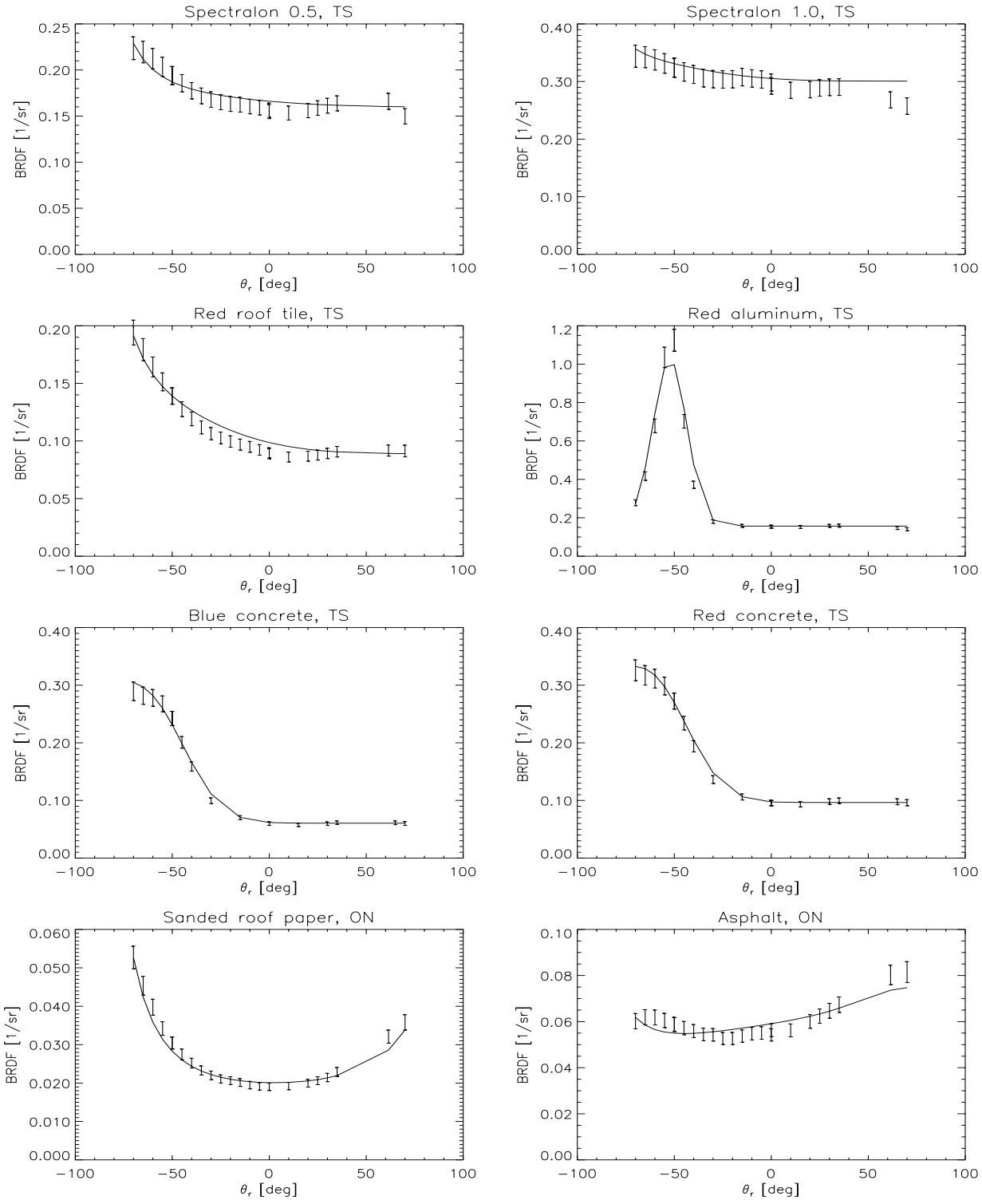

Figure 5.6: Models (TS, ON, resp.) fitted to BRDF measurements of the SE590 at 660 nm for $\theta_i = 50°$. Positive θ_r correspond to backward scattering ($\varphi = 0°$), negative θ_r to forward scattering ($\varphi = 180°$).

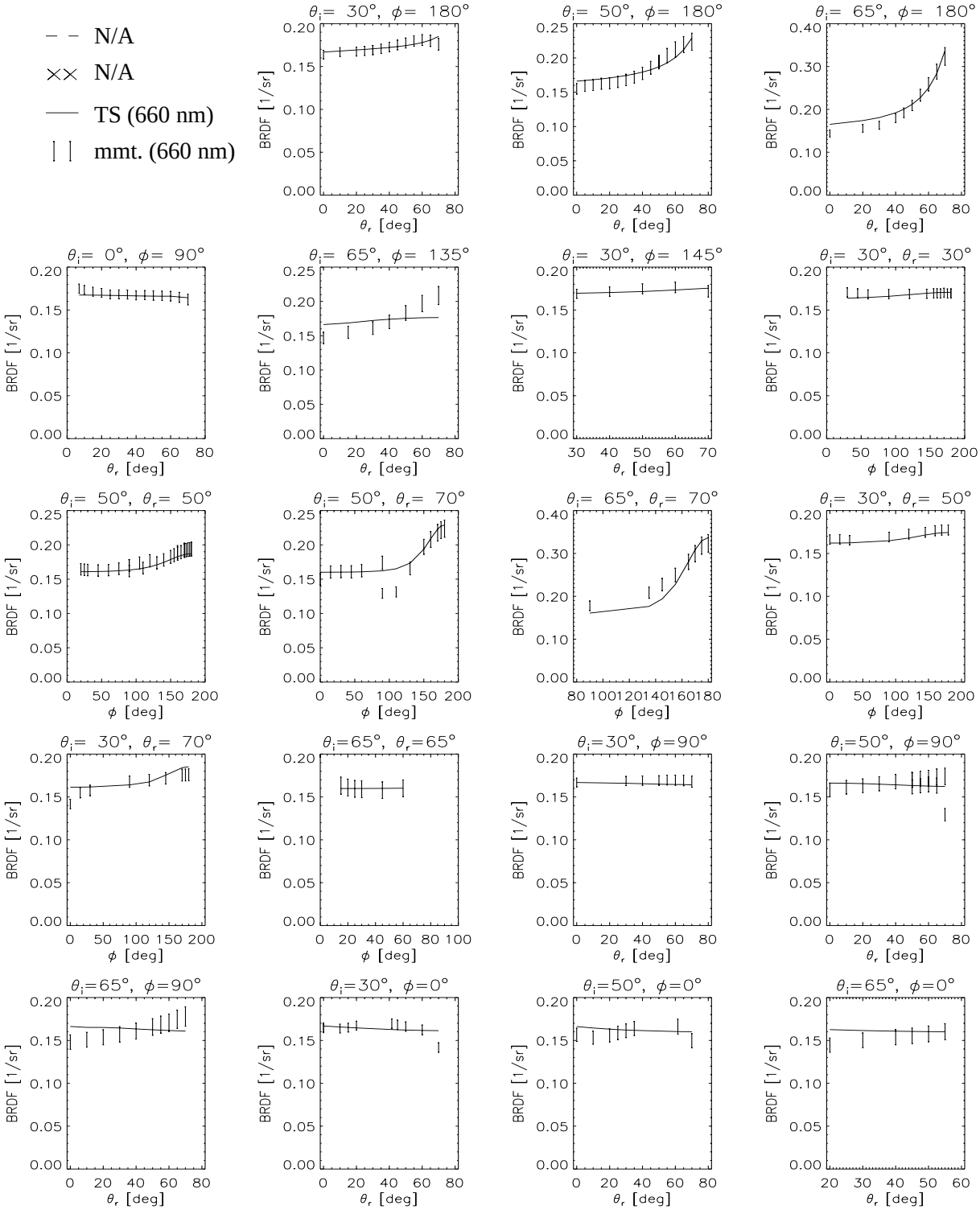

Figure 5.7: TS model fitted to BRDF measurements (mmt.) of the SE590 for Spectralon 0.5 at various angles. A lambertian surface with an albedo of 0.5 has a BRDF value of 0.159 (Spectralon 0.5 actually has an albedo of about 0.51).

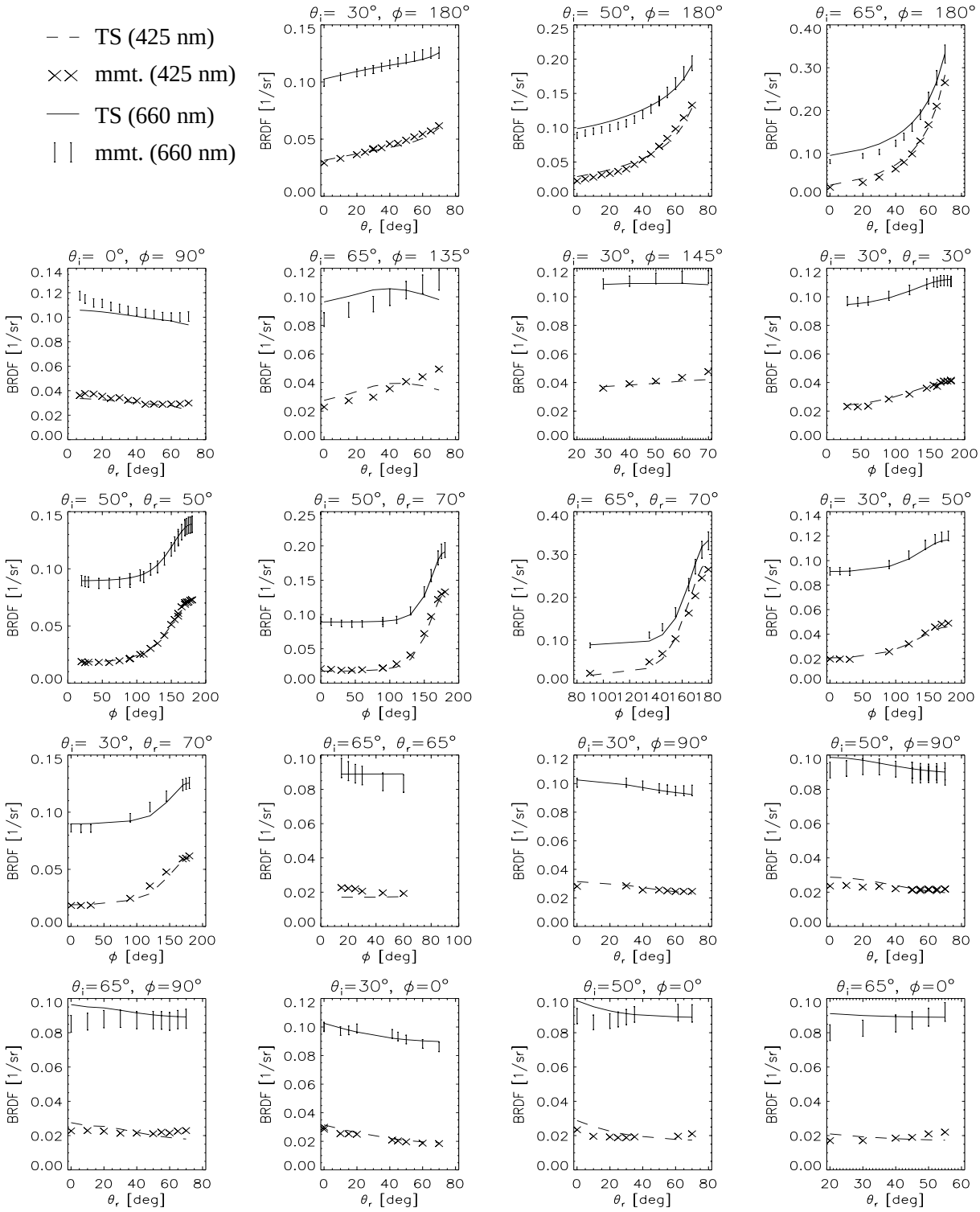

Figure 5.8: TS model fitted to BRDF measurements of the SE590 for 'red roof tile' at various angles.

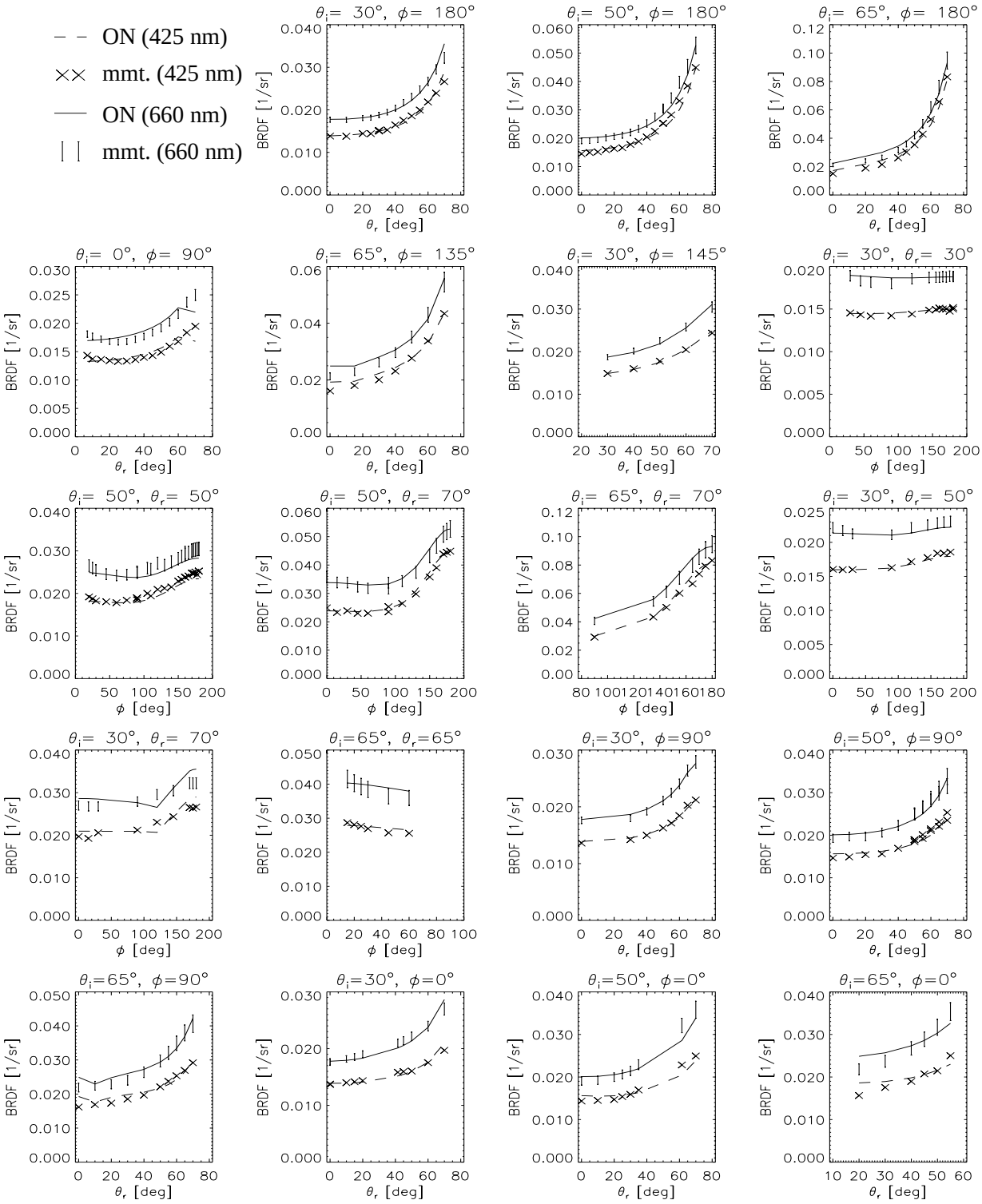

Figure 5.9: ON model fitted to BRDF measurements of the SE590 for 'sanded roof paper' at various angles.

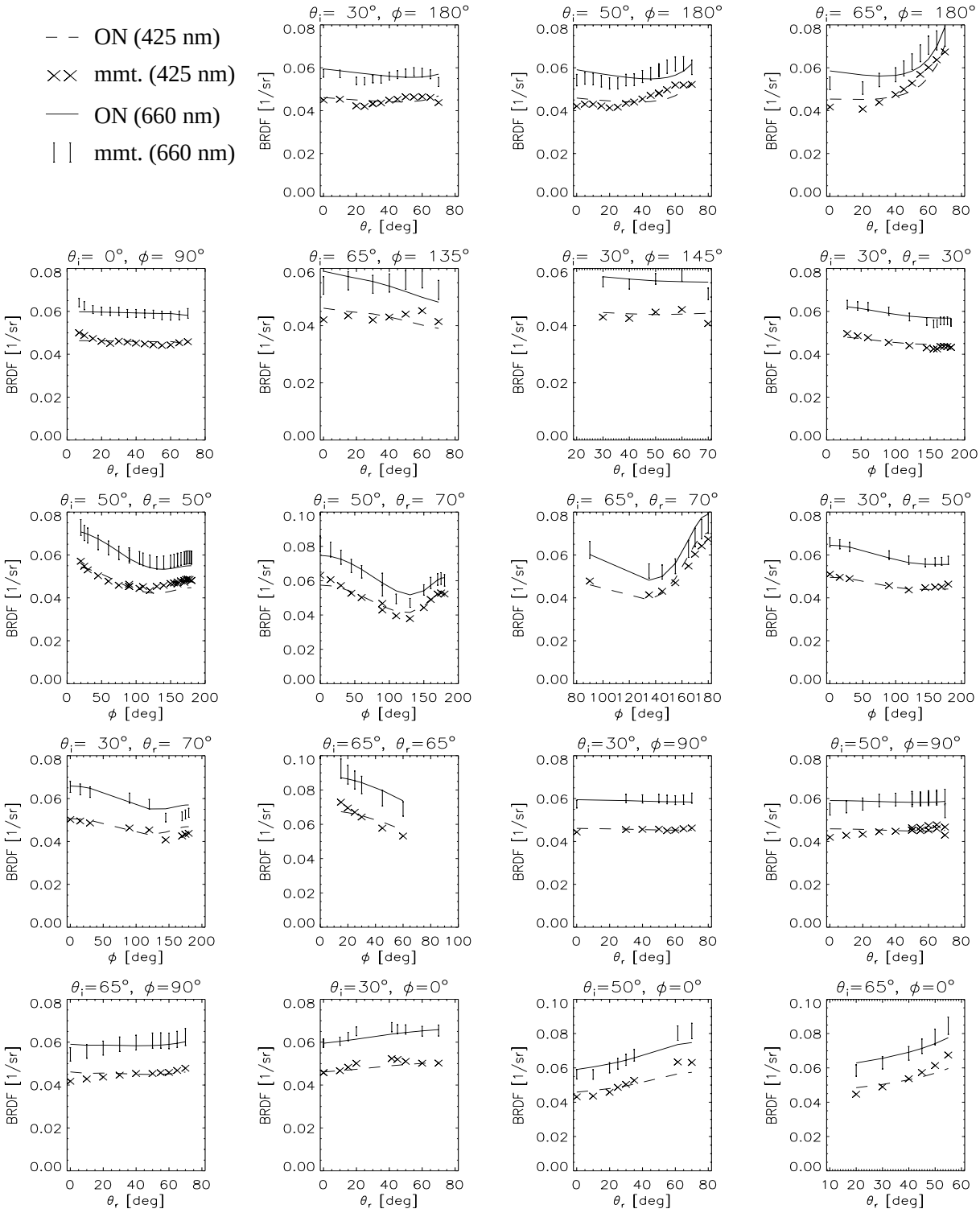

Figure 5.10: ON model fitted to BRDF measurements of the SE590 for 'asphalt' at various angles.

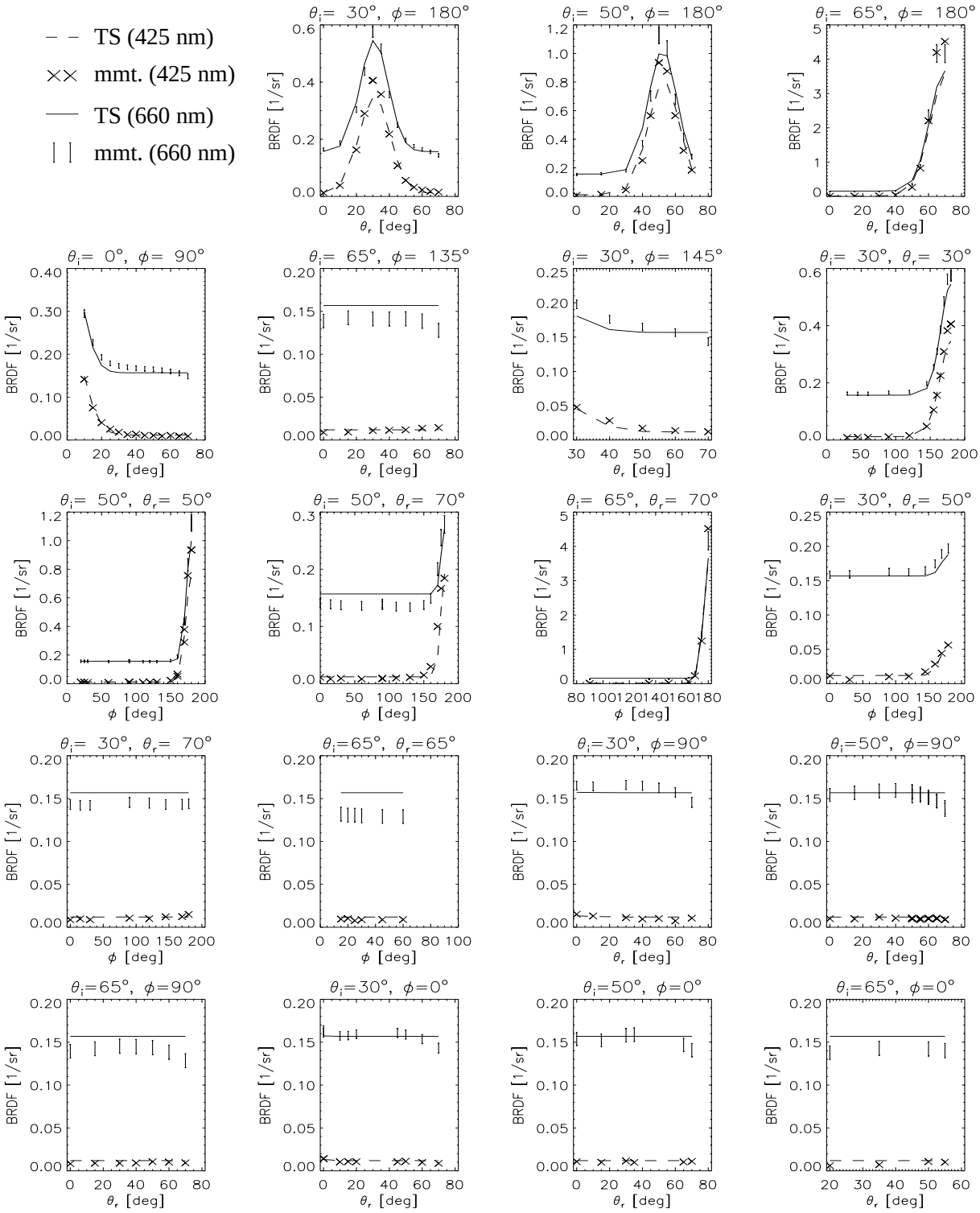

Figure 5.11: TS model fitted to BRDF measurements of the SE590 for ’aluminum’ at various angles.

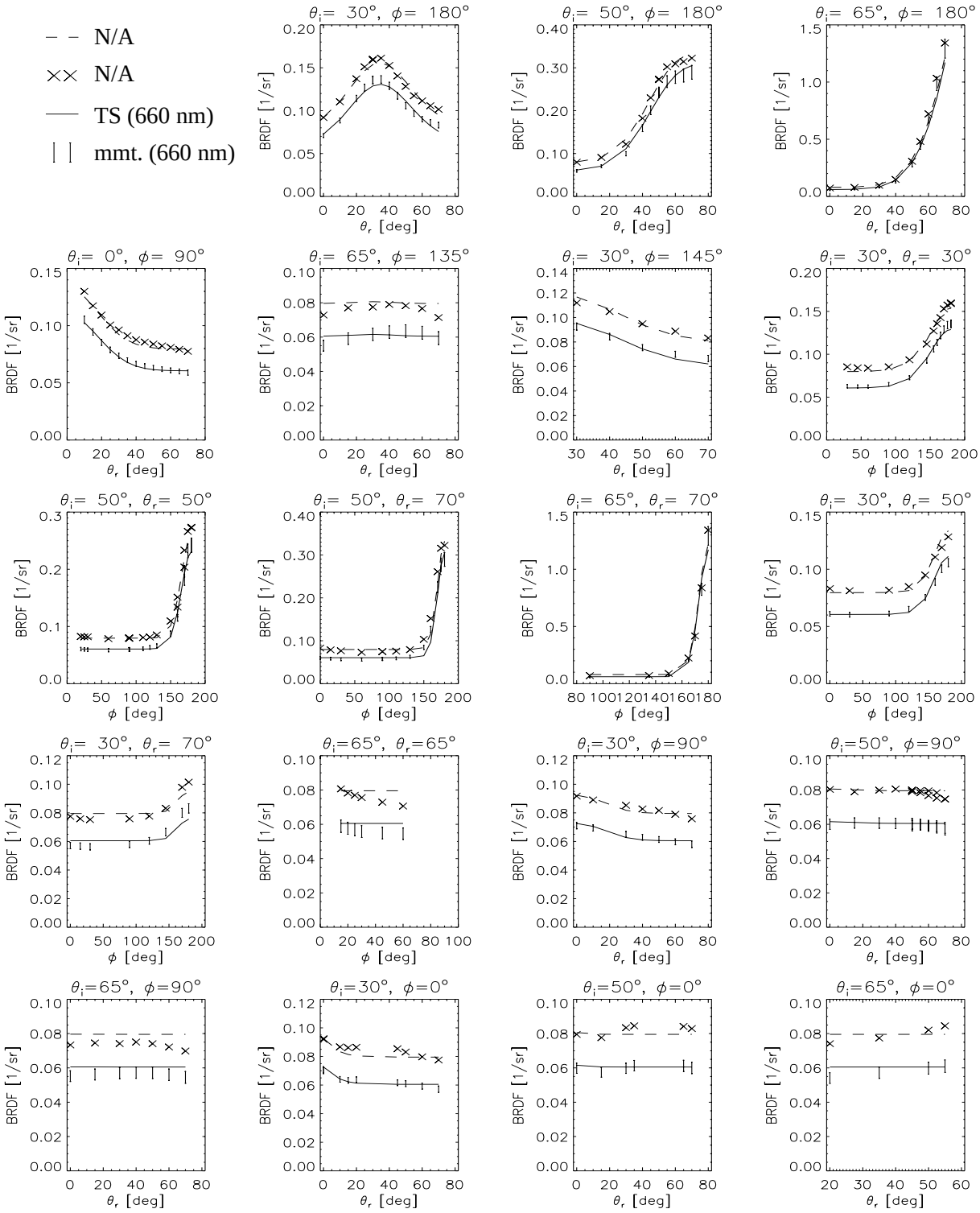

Figure 5.12: TS model fitted to BRDF measurements of the SE590 for 'blue concrete' at various angles.

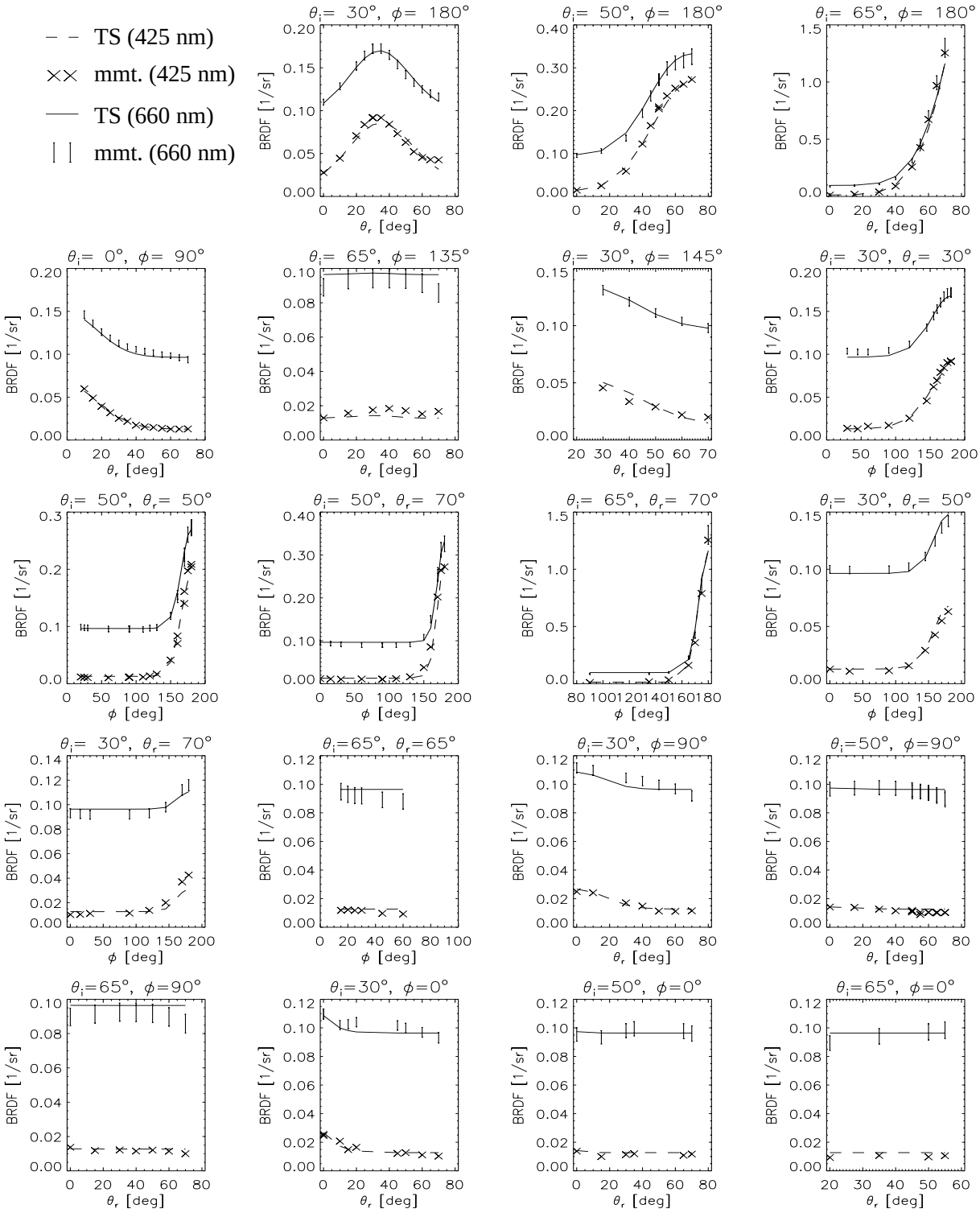

Figure 5.13: TS model fitted to BRDF measurements of the SE590 for ’red concrete’ at various angles.

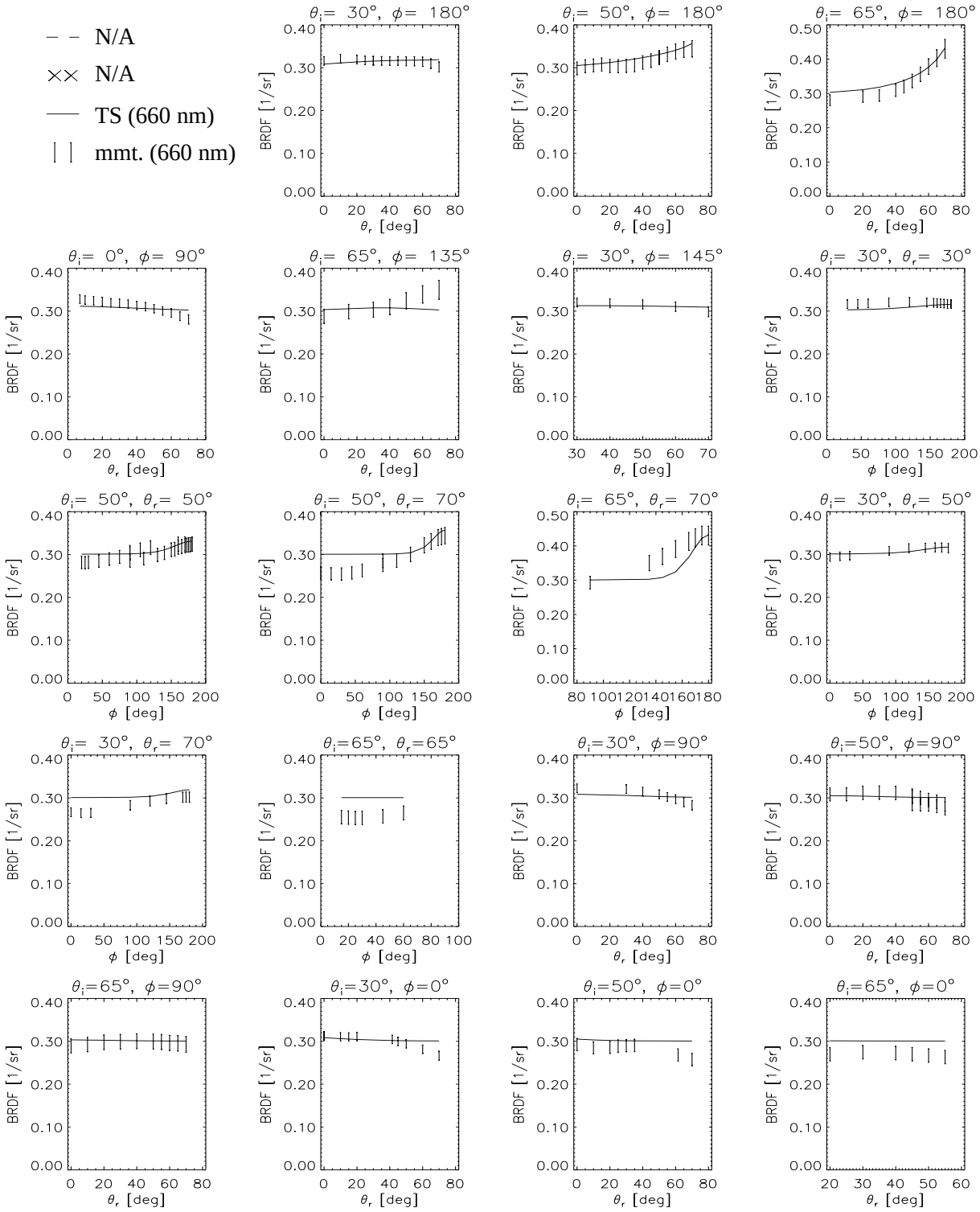

Figure 5.14: TS model fitted to BRDF measurements of the SE590 for Spectralon 1.0 at various angles.

Sample	$t_0\,[\mathrm{sr}^{-1}]$	$t_1\,[\mathrm{sr}^{-1}]$	$w\,[\mathrm{deg}^{-1}]$	n	ρ_s	χ^2/d_f
Spectralon 0.5	0.159 ± 0.002	0.16 ± 0.13	0.032 ± 0.002	1.53 ± 0.8	0.024	1.0
Red roof tile	0.0888 ± 0.0007	0.18 ± 0.10	0.040 ± 0.001	1.86 ± 0.9	0.035	1.3
Red aluminum	0.1568 ± 0.0006	3.01 ± 1.30	0.169 ± 0.002	1.84 ± 0.58	0.039	3.9
Blue concrete	0.0605 ± 0.0003	1.06 ± 0.26	0.083 ± 0.001	1.47 ± 0.16	0.028	1.5
Red concrete	0.0964 ± 0.0004	0.98 ± 0.29	0.0842 ± 0.001	1.53 ± 0.22	0.029	1.0
Spectralon 1.0	0.3006 ± 0.0017	0.09 ± 0.23	0.046 ± 0.005	2.06 ± 5.61	0.017	1.2

Table 5.1: Parameters obtained from fitting the TS model (eq. 5.1) to the SE590 data of the respective sample at a wavelength of 660 nm, and the specular albedo ρ_s (eq. 5.12) at $\theta_i = 30°$. The parameter k was set to 0.25. See text for a discussion of the errors of the parameters. The relative error of the specular albedo ρ_s is estimated to be about 5 %. The last column shows the χ^2 value over the degrees of freedom d_f.

Sample	k_d	$k_s\,[\mathrm{sr}^{-1}]$	$k_w\,[\mathrm{rad}]$	n	ρ_s	χ^2/d_f
Sanded roof paper	0.0357 ± 0.0005	0.053 ± 0.04	0.643 ± 0.004	2.3 ± 1.9	0.043	1.2
Asphalt (Cadr.)	0.1999 ± 0.0006	0.026 ± 0.06	0.36 ± 0.03	2.2 ± 6.4	0.011	1.0

Table 5.2: Parameters obtained from fitting the ON model (eq. 5.8) to the SE590 data of the respective sample at a wavelength of 660 nm. The parameter k was set to 0.25. See text for a discussion of the errors. The error of the specular albedo ρ_s is estimated to be about 5 % for the sample 'Asphalt'. The specular albedo of the sample 'Sanded roof paper' is considerably overestimated due to ignoring the black background, see page 7, probably by as much as 30 %. The last column shows the χ^2 value over the degrees of freedom d_f.

of a material can be calculated from the band structure in crystals (Kittel 1996). Figures 5.15, 5.16 and 5.17 show the coefficients of either the TS model or the ON model as a function of wavelength, as well as χ^2/d_f and the specular albedo.

For all samples, the drop of the specular albedo from 700 to 750 nm discussed in section 4.10 can be seen. Thus we will ignore wavelengths greater than 700 nm in the following discussion. Especially for the Spectralon panels, it can be seen that the diffuse component t_0 is not affected at all by this drop.

The diffuse component shows very strong variations (e.g. factor of 15 for the sample aluminum, see t_0 in fig. 5.16) except for Spectralon, whereas the specular parameters vary by only less than 15 % from their mean value. *The wavelength dependence of the specular component is not strongly related to the wavelength dependence of the diffuse component.*

All the samples with a red color show a maximum of the χ^2 value at 500 nm, the blue concrete shows a maximum at 600 nm. Thus a low reflectance (low compared to the maximum reflectance of the sample) combined with a small error (see section 4.7, fig. 4.10) leads to a rejection of the TS model. This might either be due to a more complicated BRDF at low reflectances, because high reflectances lead to higher multiple scattering [2] , which results in a more lambertian BRDF, or due to an underestimation of the error σ_{noise} (see eq. 4.6).

The values retrieved for n from the TS model are quite reasonable, they lie in the expected range of [1.3, 2.0] (Wolff 1994), with the exception of 'Spectralon 1.0', where the retrieved values of n are rather too

[2] A high reflectance leads to high multiple scattering because of small absorption. Consider this example: assume that snow consists of scattering particles with a single scattering albedo of 0.99 (i.e. 99 % of the incoming photons are reflected, 1 % absorbed) and that charcoal powder consists of scattering particles with a single scattering albedo of 0.05. A photon being scattered in snow has a 99 % chance of being reflected (high multiple scattering), whereas a photon being scattered in charcoal powder has only a 5 % chance of being reflected (low multiple scattering).

Sample	$t_0\,[\mathrm{sr}^{-1}]$	$t_1\,[\mathrm{sr}^{-1}]$	$w\,[\mathrm{deg}^{-1}]$	n	ρ_s	χ^2/d_f
Spectralon 1.0	0.2993 ± 0.0037	0.04 ± 0.31	0.078 ± 0.020	3.48 ± 45.4	0.008	1.3
Spectralon 0.5	0.1469 ± 0.0070	0.13 ± 0.43	0.040 ± 0.005	2.19 ± 8.3	0.038	0.4
Red concrete	0.0991 ± 0.0014	1.14 ± 0.52	0.090 ± 0.002	1.51 ± 0.32	0.028	1.2
Blue concrete	0.0688 ± 0.0009	1.31 ± 0.96	0.089 ± 0.002	1.43 ± 0.35	0.027	1.3
Green roof paper	0.0263 ± 0.0005	0.03 ± 0.02	0.056 ± 0.014	0.87 ± 0.17	0.001	5.2
Red roof tile	0.0891 ± 0.0039	0.21 ± 0.28	0.045 ± 0.003	1.90 ± 2.24	0.030	2.4
Roof tile (Opal)	0.0656 ± 0.0012	0.87 ± 0.40	0.069 ± 0.002	1.39 ± 0.24	0.027	1.3
Dirty roof tile	0.0693 ± 0.002	0.05 ± 0.14	0.018 ± 0.030	1.06 ± 1.07	0.004	3.3
Red roof paper	0.0372 ± 0.0005	0.03 ± 0.05	0.070 ± 0.021	0.95 ± 0.40	< 0.001	4.0
Brown slate	0.0210 ± 0.0004	1.13 ± 0.40	0.085 ± 0.001	1.42 ± 0.17	0.025	5.1
Sanded roof paper	0.0090 ± 0.0014	0.065 ± 0.070	0.013 ± 0.002	1.96 ± 2.1	0.032	2.4
Red Aluminum	0.1588 ± 0.0014	2.00 ± 1.55	0.168 ± 0.002	2.22 ± 1.86	0.041	3.5
Black concrete	0.0136 ± 0.0005	0.77 ± 0.26	0.062 ± 0.001	1.35 ± 0.14	0.027	2.9
Walkway	0.0769 ± 0.003	0.02 ± 0.33	0.037 ± 0.010	2.92 ± 78.6	0.010	1.7
Asphalt (Ispra)	0.0668 ± 0.0009	0.013 ± 0.13	0.080 ± 0.027	2.34 ± 28.0	0.001	1.32
Green slate	0.0315 ± 0.0004	1.71 ± 0.51	0.101 ± 0.001	1.49 ± 0.19	0.032	3.72
Red slate	0.0897 ± 0.0009	1.57 ± 0.62	0.119 ± 0.002	1.58 ± 0.34	0.026	7.0
Wall paper	0.255 ± 0.002	0.03 ± 0.51	0.263 ± 0.845	1.00 ± 4.52	< 0.001	2.5

Table 5.3: Parameters obtained from fitting the TS model (eq. 5.1) to the ASD data of the respective sample at a wavelength of 660 nm. The parameter k was set to 0.25. See text for a discussion of the errors. The error of the specular albedo ρ_s is estimated to be about 0.01, because ASD measurements were performed at a far worse angular grid than the SE590 measurements, and furthermore model and measurements do not agree as well as for the SE590 measurements (compare the χ^2/d_f of this table with the according column in table 5.1).

high. However, the values retrieved from the ON model are usually above 2.0, only for the sample 'Asphalt (Cadrezzate)' for the suspicious wavelengths greater than 700 nm n falls below 2. Thus it is probably better to set $n = 1.5$ when using the ON model.

5.7 Results of the ASD Measurements

5.7.1 Angular Dependence

The plots in figures 5.18 to 5.21 show the BRDF values measured with the ASD at 660 nm. The error bars are shown for each measured value. The solid line shows a fit of the TS model to the data. It can be seen that the TS model is capable of describing the measurements qualitatively very well. The resulting parameters of the TS model are given in table 5.3, along with the specular albedo ρ_s and χ^2/d_f. The latter shows that the TS model is rejected by the χ^2 test for several samples. For a discussion of the errors of the fitted parameters, see section 6.2.

The sample roof tile (Opal), the concrete tiles and the slate samples show a well defined specular peak for $\theta_i = 10^\circ$ and $\theta_i = 30^\circ$. At $\theta_i = 10^\circ$, the maximum measured value is always at $\theta_r = 10^\circ$. At $\theta_i = 30^\circ$, the shift of the maximum to higher viewing zenith angles can be seen for the samples with the broadest specular peak, 'roof tile (Opal)' and 'black concrete', who have their maximum at $\theta_r = 40^\circ$. At $\theta_i = 50^\circ$, only the samples 'red slate' and 'green slate' show a well defined specular maximum, the other samples rise up to the maximum measured viewing angle $\theta_r = 70^\circ$.

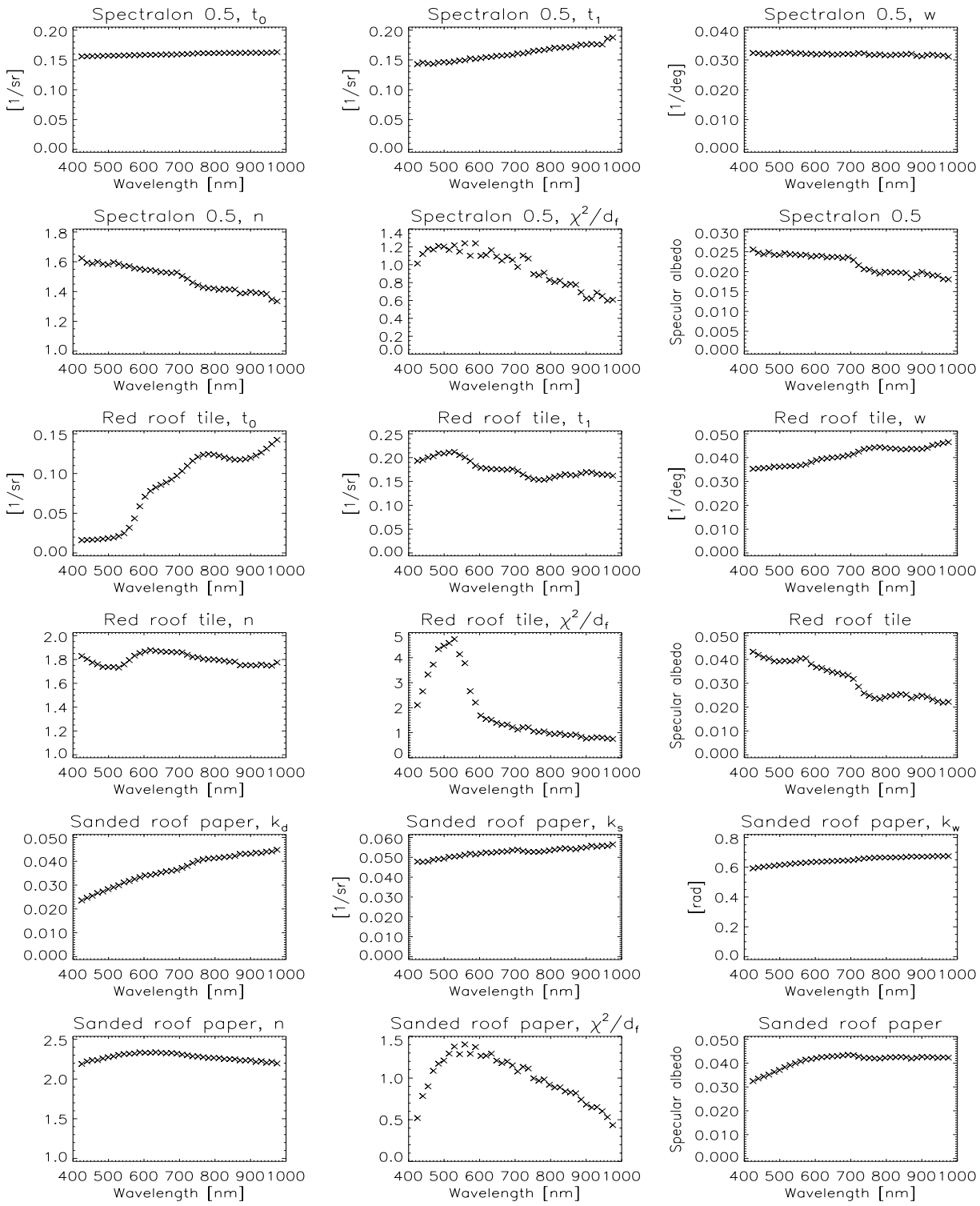

Figure 5.15: Wavelength dependence of the parameters of the BRDF models as a function of wavelength, fitted to the SE590 measurements (1/3). t_0, t_1 and w denote parameters from the TS model, k_d, k_s and k_w denote parameters from the ON model. Furthermore the ratio of χ^2 over the degrees of freedom d_f and the specular albedo at $\theta_i = 30°$ is shown.

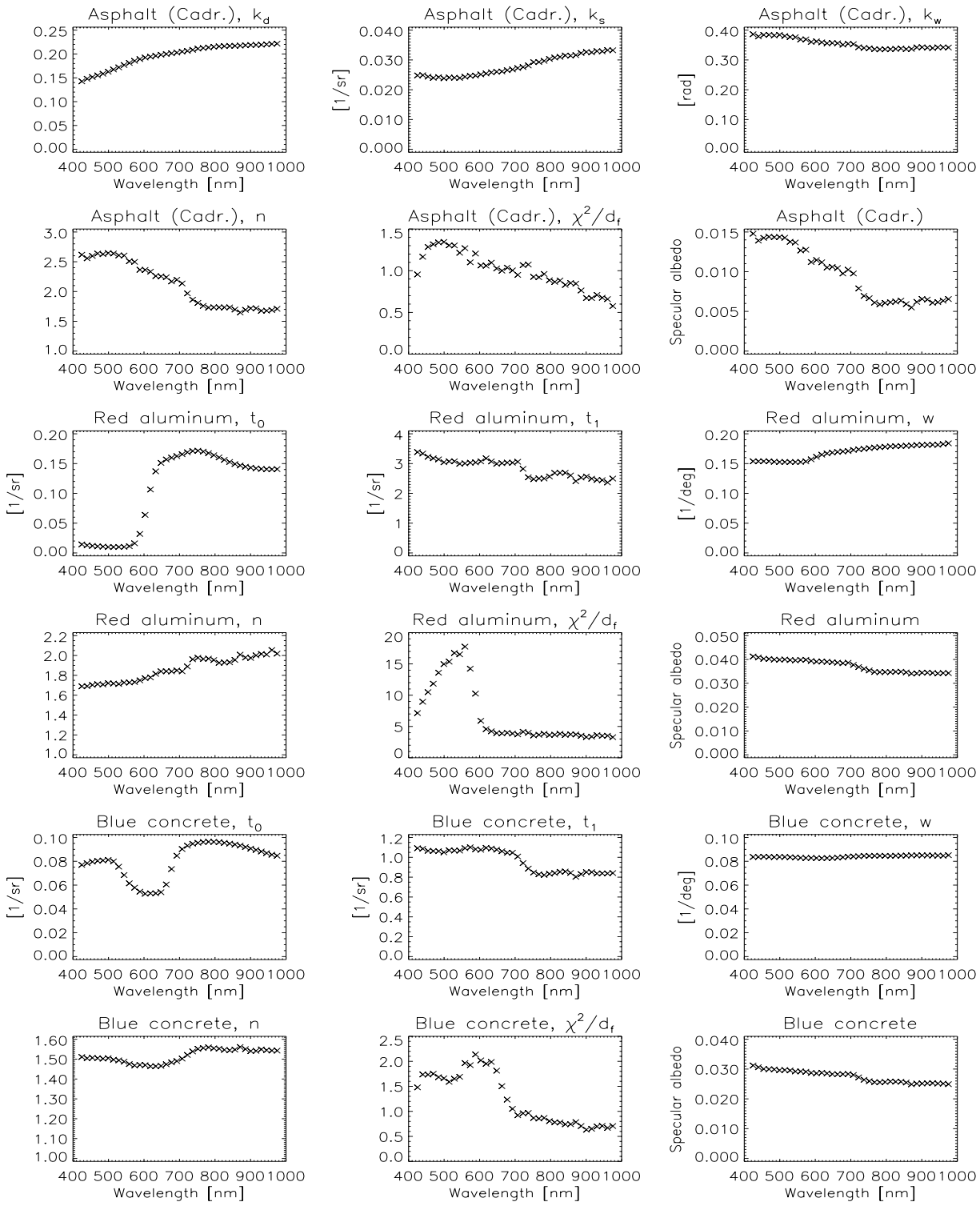

Figure 5.16: Wavelength dependence of the parameters of the BRDF models as a function of wavelength, fitted to the SE590 measurements (2/3). t_0, t_1 and w denote parameters from the TS model, k_d, k_s and k_w denote parameters from the ON model. Furthermore the ratio of χ^2 over the degrees of freedom d_f and the specular albedo at $\theta_i = 30°$ is shown.

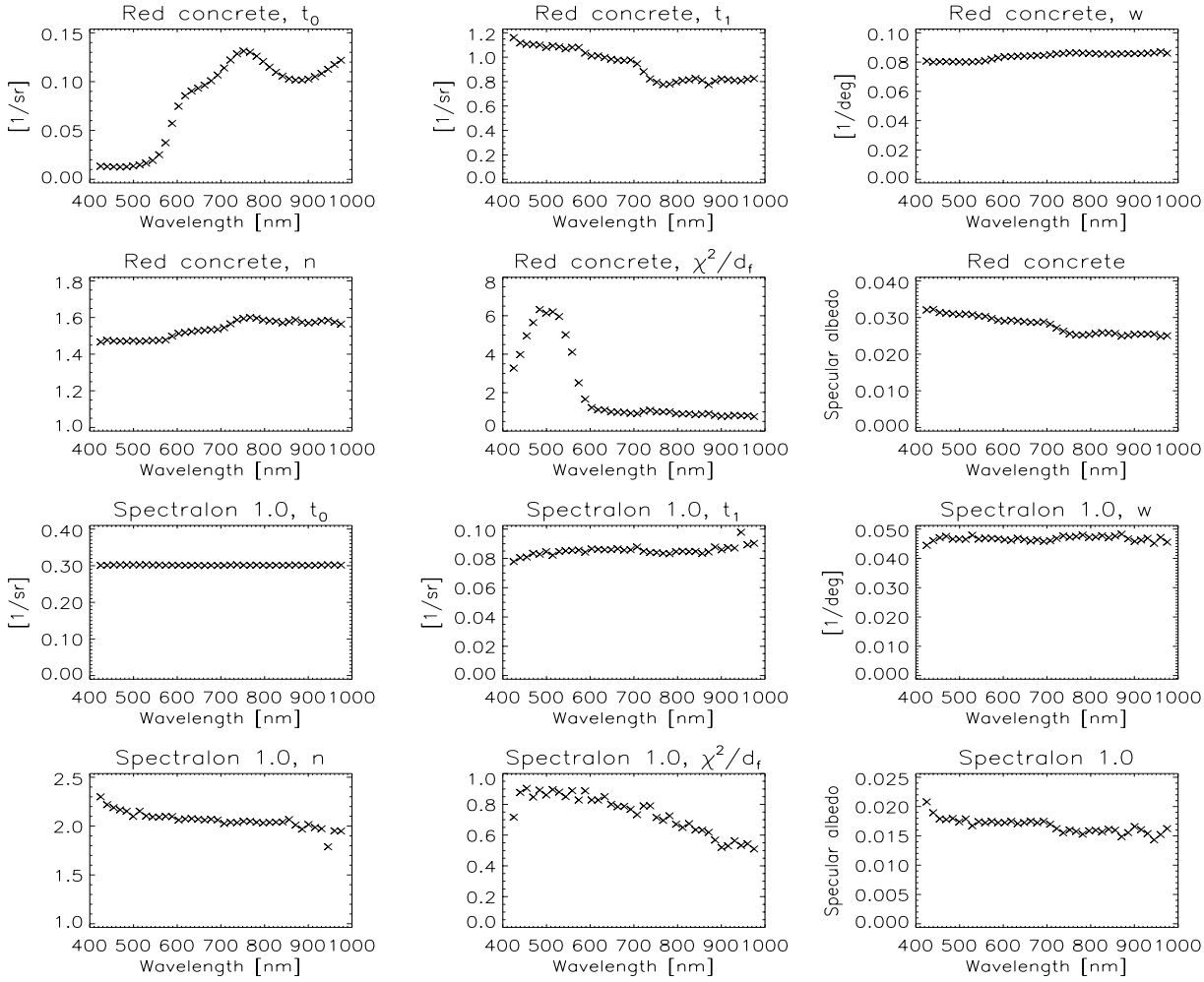

Figure 5.17: Wavelength dependence of the parameters of the BRDF models as a function of wavelength, fitted to the SE590 measurements (3/3). t_0, t_1 and w denote parameters from the TS model. The ratio of χ^2 over the degrees of freedom d_f and the specular albedo at $\theta_i = 30°$ is shown, too.

The Spectralon panels, the samples 'red roof tile' and 'dirty roof tile', the roof papers, walkway, Ispra-asphalt and wallpaper do not show a well defined specular maximum. Thus for these samples it is hard to decide whether the rise at large viewing angles is due to a specular peak or due to a non-lambertian diffuse component, caused by (internal) volume scattering. However, it is very likely that the rise is indeed due to *specular* reflectance, because the TS model can describe the shape quite well, and the surfaces are all very rough, which is in accord with the prediction of a large shift of the maximum of the specular peak. The rise can not be explained by a BRDF model applying geometrical optics to *diffuse* scattering on rough surface structures, because this would predict a decrease in forward scattering direction, not an increase as we see it in the data.

The specular component of the BRDF for the sample 'plastic' could not be modeled from the ASD measurements, because all measurements of this sample in the specular direction $\theta_i = \theta_r$ are overflows, thus only the lambertian component of the TS model is plotted. It is interesting to note that at $\theta_i = 65^\circ$, the measured BRDF value at $\theta_r = 70^\circ$ of about 0.8 is much higher than the measured BRDF value at $\theta_r = 60^\circ$ of about 0.35, although both angles are 5° away from the specular direction $\theta_i = \theta_r$. This is again in accord with the prediction of the TS model of a shift of the specular peak towards larger zenith angles.

For several samples, measurements with the SE590 are available as well. They are shown as stars, together with their error bars. As we showed in section 4.10, the results from both instruments agree very well at the wavelength $\lambda = 660$nm.

5.7.2 Wavelength Dependence

The ASDFieldspec consists of 3 units that cover different wavelength ranges, see section 4.8.1. We processed data from the second unit in the wavelength range 1100 nm to 1700 nm and data from the third unit from 1900 nm to 2300 nm. We will show that both these units show features that make them unreliable for the analysis of specular reflectance measurements.

Fig. 5.23 shows the specular albedo derived from fitting the TS model to the ASD data. Triangles show the specular albedo at $\theta_i = 30^\circ$, stars at $\theta_i = 50^\circ$. It can be seen that in the wavelength range of the second unit, the shape of the curve is always given by a decrease from 1100 nm to 1400 nm, from 1400 nm to 1700 the curve continues relatively flat. This shape is so consistent that it is most likely produced by saturation problems of the ASD at high intensities (below we will see that this shape does not occur for the diffuse component). From the black-body spectrum shown in fig. 5.22 for 2850 K (a typical temperature of a halogen tungsten bulb like the one used in this study) we see that the maximum intensity is emitted at about 1000 nm. But fig. 4.12 on page 34 shows very low measured counts at 1100 nm inspite of the high lamp intensity, i.e. the ASD is not very sensitive at this wavelength.

In the wavelength range 1900 nm to 2300 nm, there is a consistent pattern as well: the specular albedo rises with wavelength for $\theta_i = 50^\circ$ much stronger than for $\theta_i = 30^\circ$, with the exception of the sample 'red roof tile', which has a very broad specular peak and thus does not reflect as strong intensities in the specular direction as the other samples. The rise could be due to a saturation problem as well, because the reflected radiances are higher for $\theta_i = 50^\circ$ than for $\theta_i = 30^\circ$, by about 80 % for $n = 1.5$ and $k = 0.25$. Although it is also possible that the rise of the specular albedo at $\theta_i = 50^\circ$ is caused by a decrease of n in that wavelength range, it is rather unlikely to occur for all samples with a sharp specular peak.

A strict treatment would thus discard all wavelengths from measurements of the second as well as from the third unit for high intensities. However, it is very likely that the errors resulting from these saturation problems are in the range of less than 30 %, because all the obviously saturated measurements have already been discarded, see section 4.9.2, page 38. Thus we can derive from the wavelength dependence of the specular albedo (see Figures 12.12 to 12.15, page 157 to 160, appendix) that it usually varies less than 30 % over the wavelength range 450 nm to 2300 nm. This is significantly less than the variation in the diffuse component. E.g. the diffuse component of 'red concrete' shows a drop from 1900 nm to 2300 nm of about 50

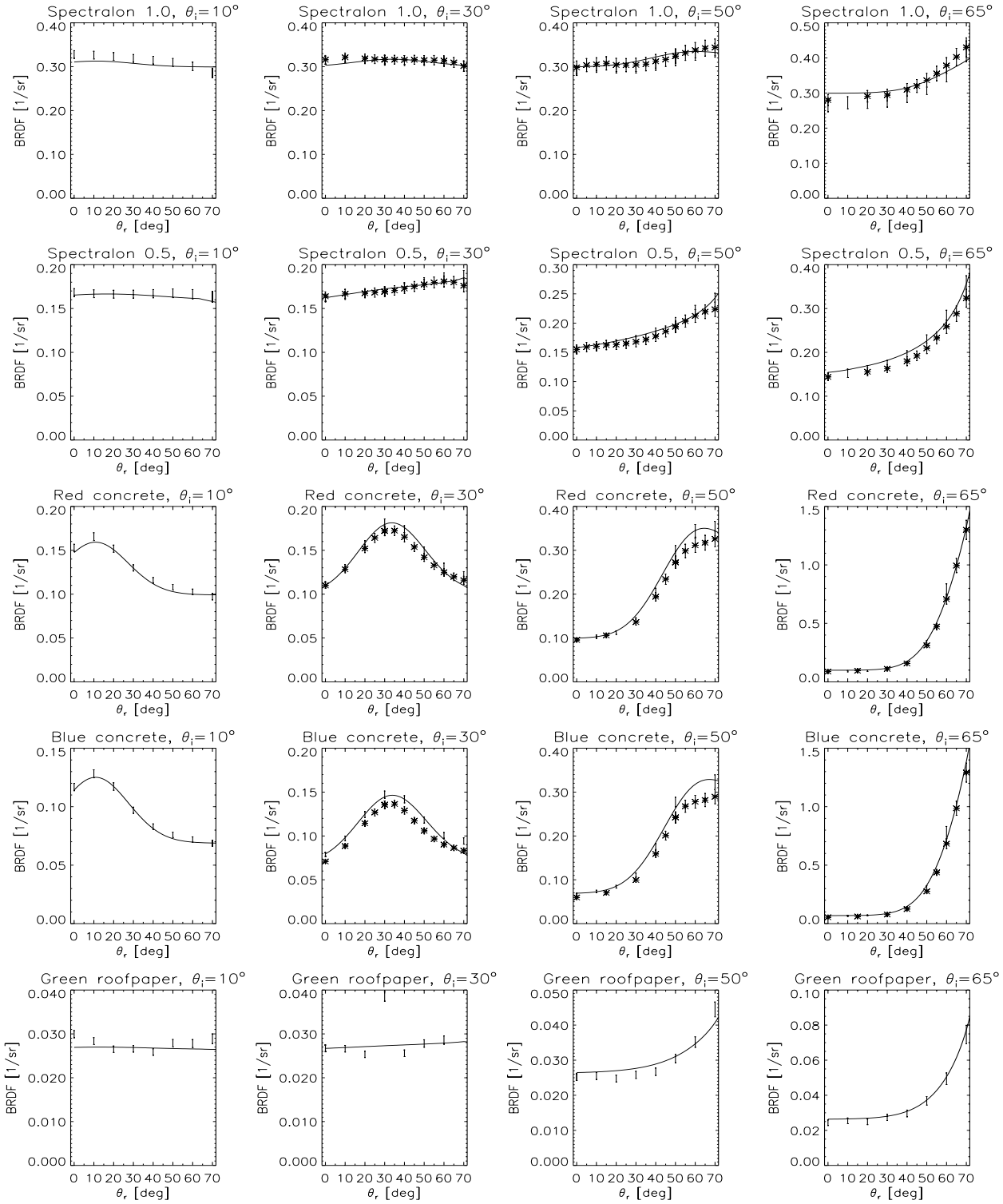

Figure 5.18: TS model (solid line) fitted to BRDF measurements of the ASDFieldspec at 660 nm (error bars) for several samples in forward scattering direction ($\varphi = 180°$) for 4 different illumination angles θ_i. Stars show the respective measurements with the SE590.

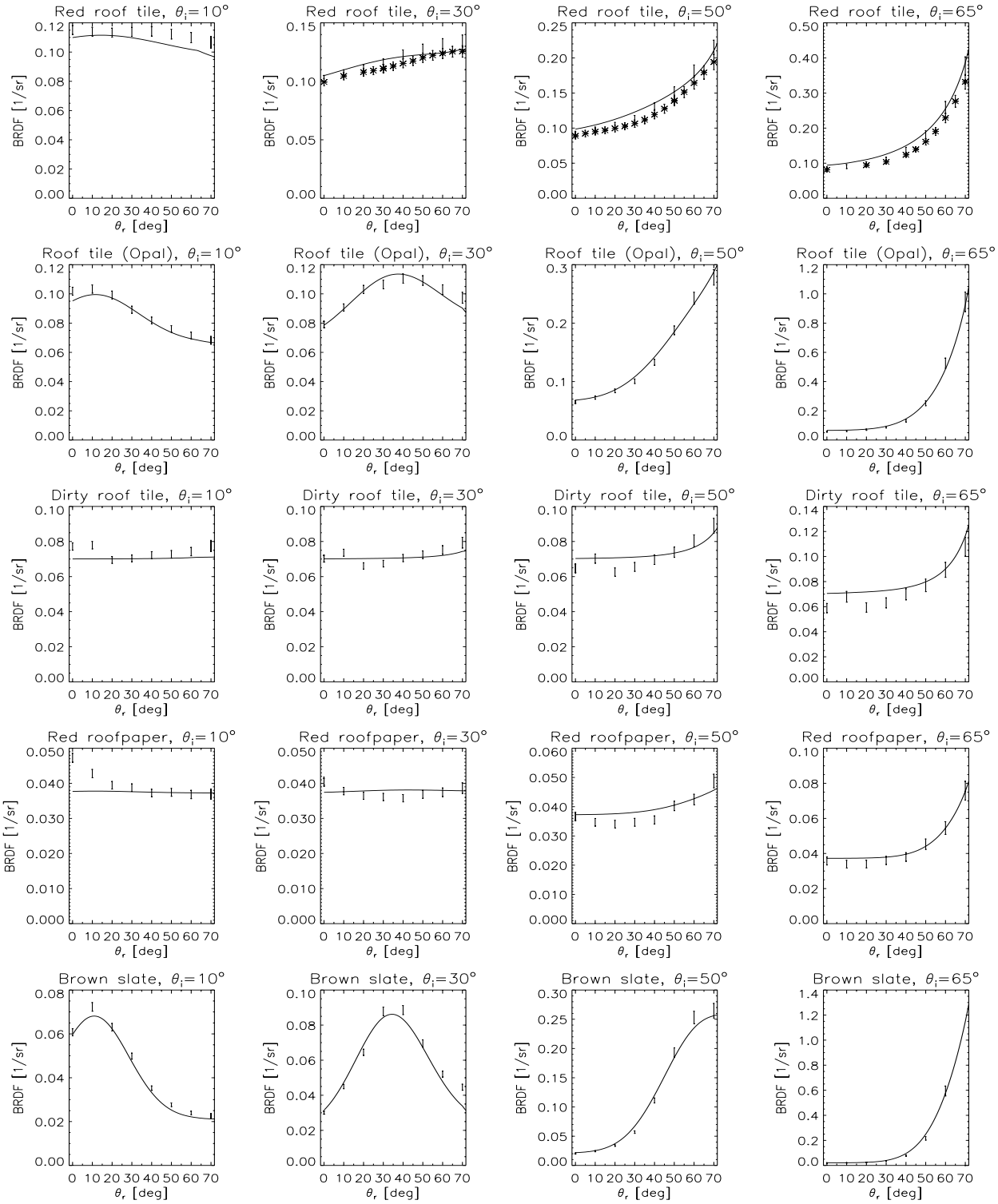

Figure 5.19: TS model (solid line) fitted to BRDF measurements of the ASDFieldspec at 660 nm (error bars) for several samples in forward scattering direction ($\varphi = 180°$) for 4 different illumination angles θ_i. Stars show the respective measurements with the SE590.

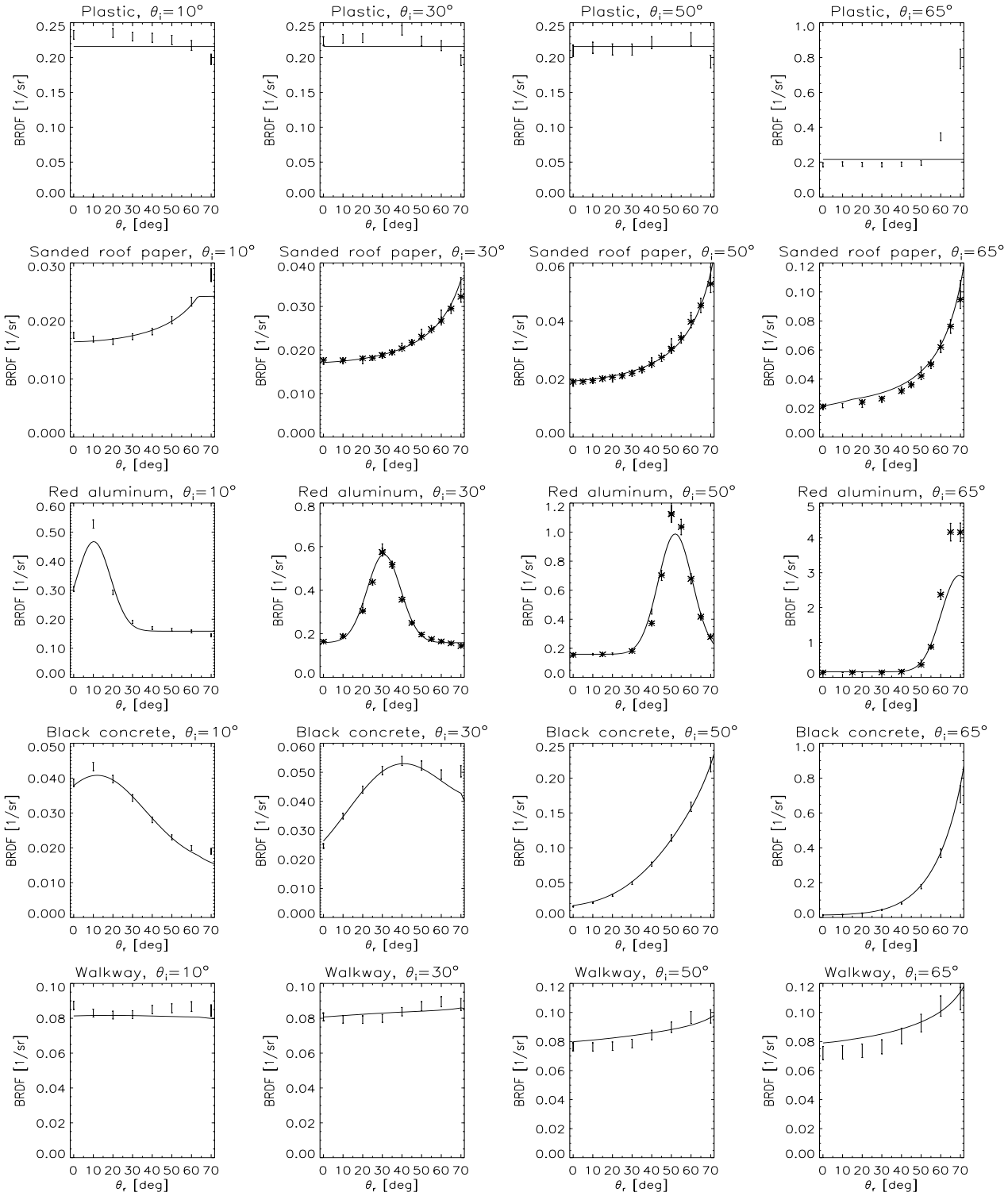

Figure 5.20: TS model (solid line) fitted to BRDF measurements of the ASDFieldspec at 660 nm (error bars) for several samples in forward scattering direction $(\varphi = 180°)$ for 4 different illumination angles θ_i. Stars show the respective measurements with the SE590.

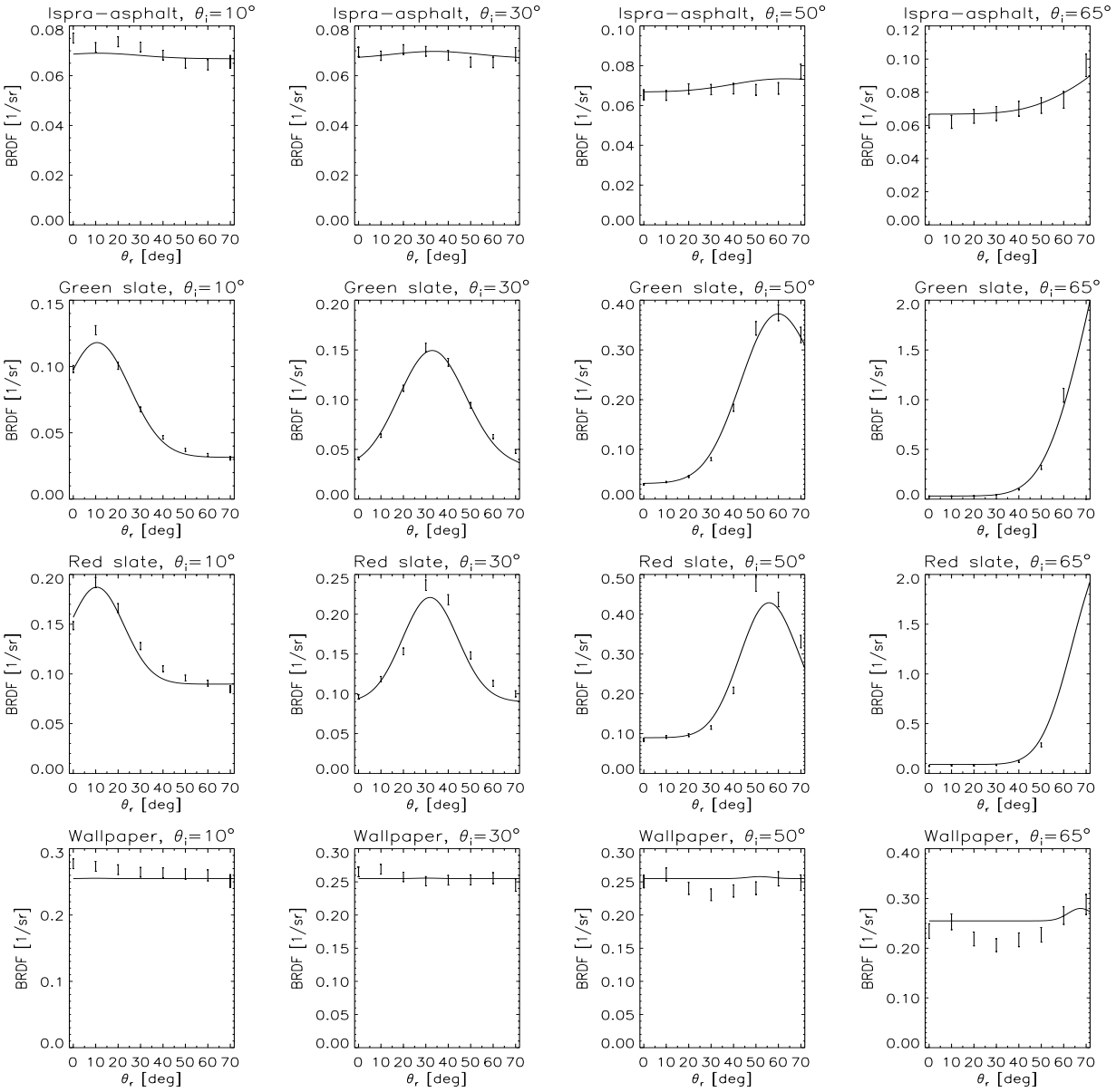

Figure 5.21: TS model (solid line) fitted to BRDF measurements of the ASDFieldspec at 660 nm (error bars) for several samples in forward scattering direction $(\varphi = 180°)$ for 4 different illumination angles θ_i. Stars show the respective measurements with the SE590.

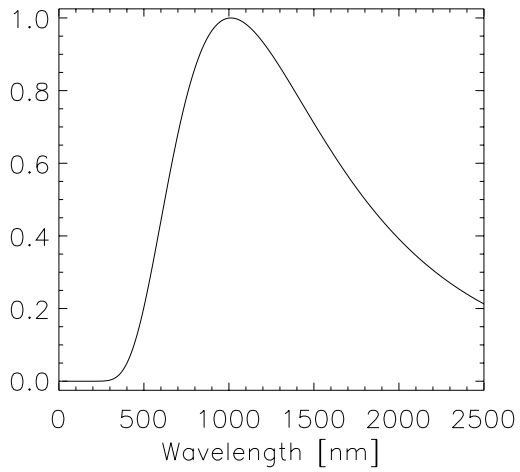

Figure 5.22: The normalized black-body spectrum for a temperature of 2850 K. The maximum is at about 1000 nm.

%, the diffuse component of 'green slate' drops by 50 % from 1100 nm to 1700 nm, red concrete rises from 0.015 sr^{-1} at 450 nm to 0.18 sr^{-1} at 1200 nm and drops to 0.06 sr^{-1} at 2300 nm. None of these variations is accompanied by a similar variation in the specular albedo. *Thus the ASD measurements suggest that the specular reflectance does not depend on the diffuse component for the full wavelength range from 450 nm to 2300 nm*.

Another problem of our ASD measurements is illustrated in fig. 5.24. The stars show the specular width (parameter w from the TS model) derived from ASD measurements of the first unit (wavelength range 450 nm to 900 nm), the solid line shows w derived from SE590 measurements, the dashed line shows w derived from SE590 measurements choosing only angular combinations with $\varphi = 180^\circ$. The dashed line differs from the solid line by about 10 %, being either too high or too low. This illustrates a problem discussed by (Lucht & Lewis 2000): the available angles have a critical influence on the parameters derived from BRDF measurements. As the solid line is derived from the best angular coverage, it is the most reliable one. It can be seen that the stars are about 10 % higher than the solid line. Thus the error to be associated with the parameter w derived from the ASD measurements is at least 10 %.

It is obvious that this deviation is indeed related to the angular coverage and not to sensor problems: The ASD measurements also have $\varphi = 180^\circ$ for all angles, although the choice of zenith angles is slightly different (e.g. the ASD measured at $\theta_i = 10^\circ$). Stars and dashed line agree well for the concrete samples, the deviations above 700 nm are due to the SE590, see above. For 'red roof tile', w derived from the ASD measurements is about 10 % higher than w derived from SE590 measurements with $\varphi = 180^\circ$, but this deviation is still much smaller than the deviation of the stars and and the solid line.

In the TS model, the diffuse component is given by the lambertian component t_0 multiplied by π. It is shown in fig. 5.25 as a function of wavelength. The statistical error for t_0 is usually about 1 %, see table 5.3. However, we expect the lambertian assumption to be true to only about 5 % on average for our samples. Thus the accuracy of the diffuse albedo is also estimated to be 5 %.

The reflectances cover a wide range of values. The strongest variations can be found for wavelengths below 900 nm, above 1100 nm the reflectances are quite smooth. It is interesting to note that for several samples, which we expect to be abundant in remotely sensed images of urban areas, like roof tiles and asphalt, the reflectance increases strongly with wavelength. Furthermore it can be seen that painted surfaces show distinct peaks (produced by the color pigments), whereas the diffuse reflectance of non-painted surfaces varies smoothly with wavelength.

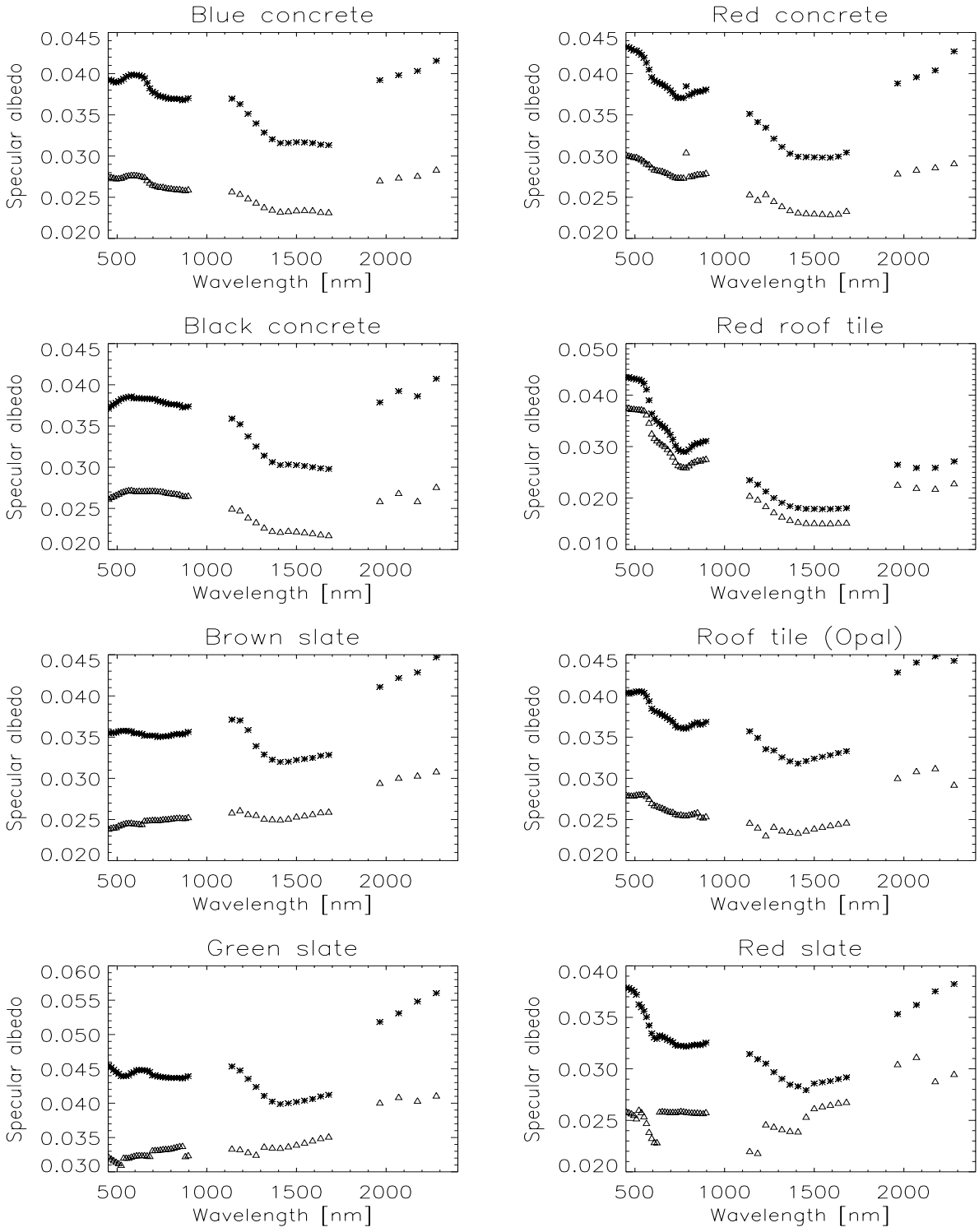

Figure 5.23: Comparison of the specular albedo at different incident zenith angles θ_i, derived from fitting the TS model to the ASD data. The triangles show the specular albedo at $\theta_i = 30°$, the stars show the specular albedo at $\theta_i = 50°$.

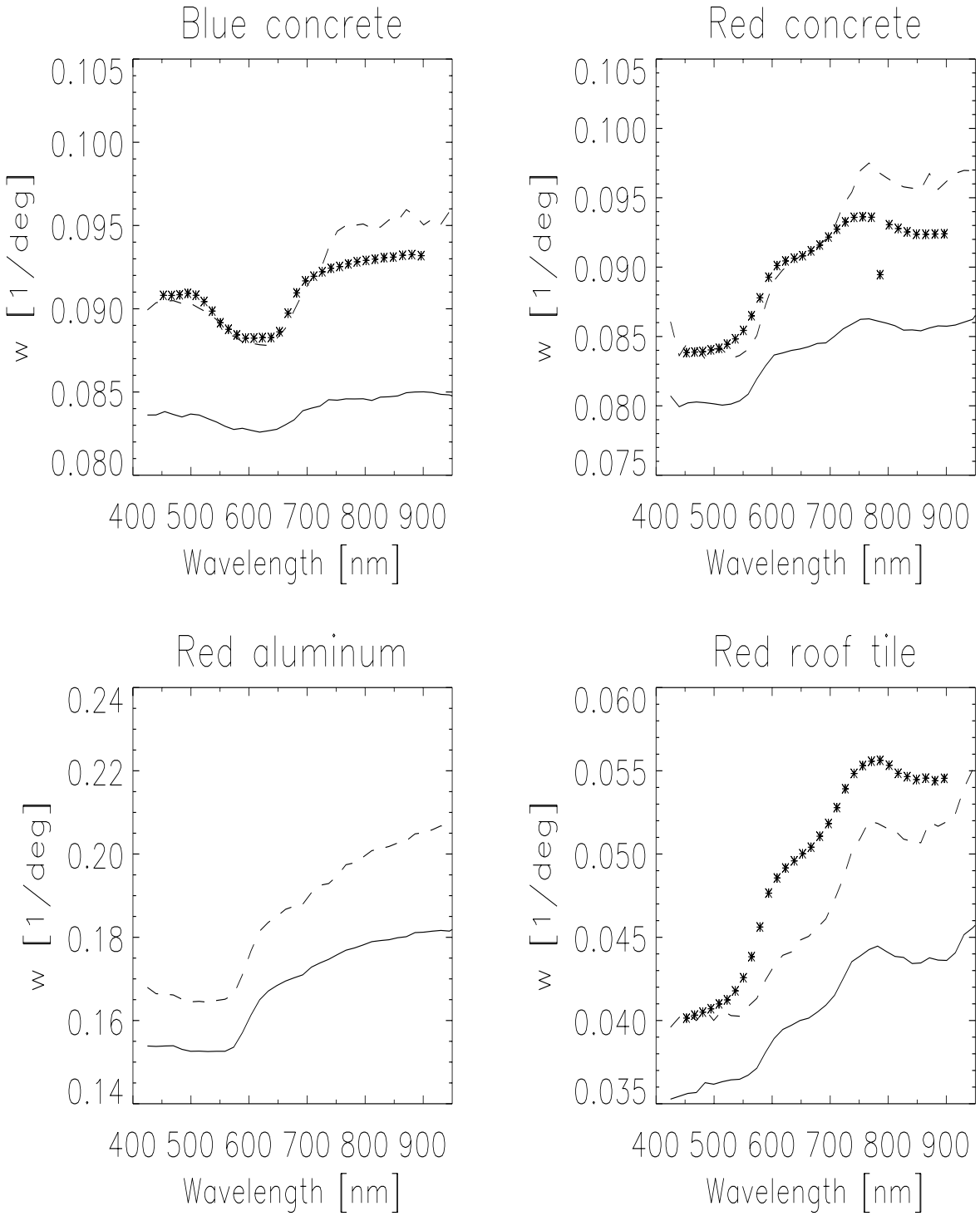

Figure 5.24: Comparison of the specular width parameters w derived from fitting the TS model to ASD and SE590 data. Solid line shows w when fitting to all SE590 measurements. Dashed line shows w when fitting only to SE590 measurements with $\varphi = 180°$. Stars show w when fitting to ASD measurements, who also have φ restricted to $180°$, but a slightly different zenith angle coverage.

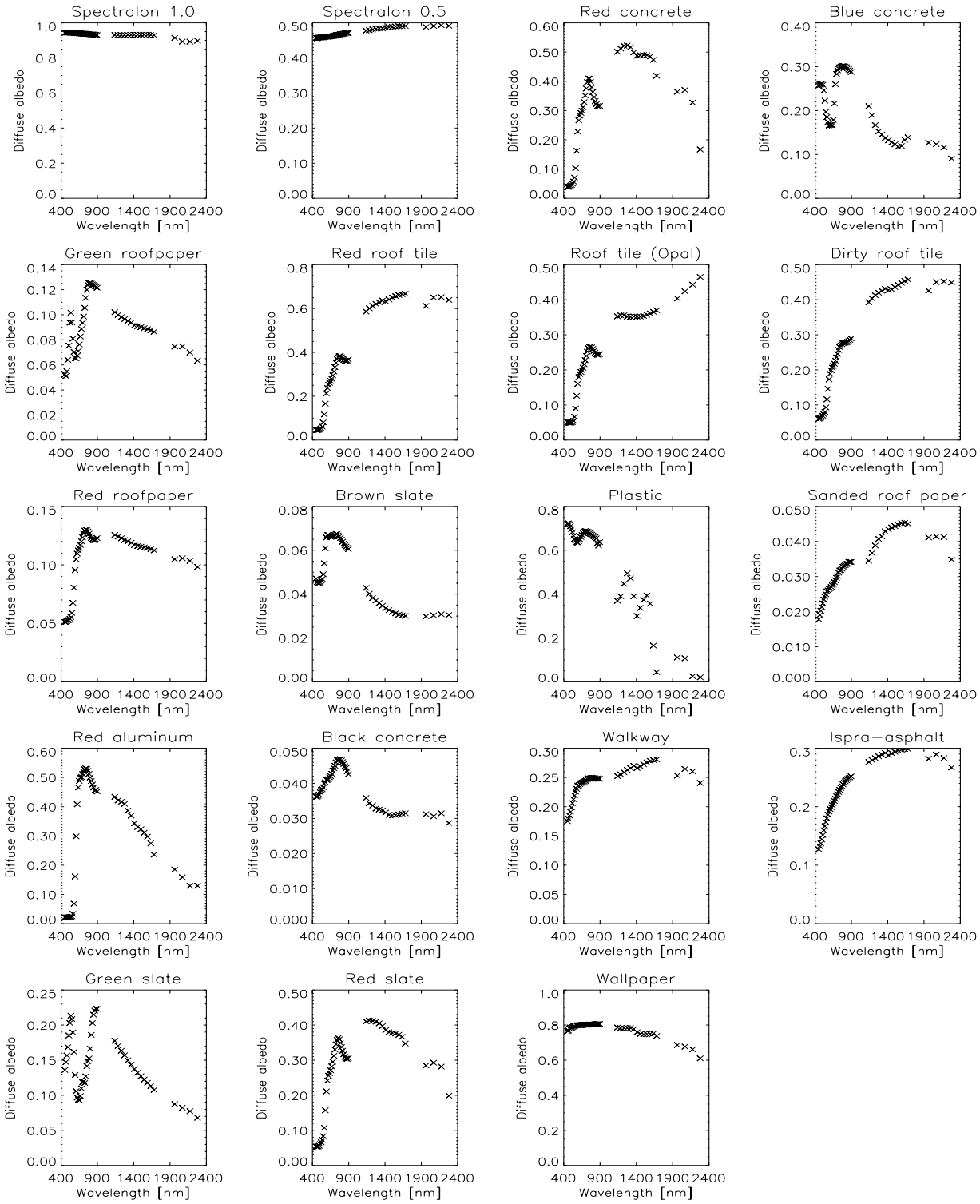

Figure 5.25: The diffuse component derived from fitting the ASD data to the TS model is shown as a function of wavelength. In the TS model, the diffuse component is given by the lambertian component t_0 multiplied by π.

5.8 Comparison with Previous Measurements

The BRDF of several of the samples used in this study had been measured before in a field measurement campaign (Meister 1995) using the spectrometer OVID (Bartsch et al. 1994). The samples were placed on a goniometer table, which made it possible to measure at different combinations of angles without moving the detector. BRDF values were obtained for 35 different combinations of angles. The illumination angle was given by the sun position. The varying sun position made it impossible to measure exactly a regular grid of angles, thus we cannot compare the measurements directly. However, the *in situ* measurements cover the whole upper hemisphere at different illumination angles, similar to the laboratory SE590 measurements, and an empirical function was fitted to these measurements. The χ^2 test shows that the *in situ* BRDF data can be well described by the empirical function. Thus we can compare this function with the SE590 measurements and the TS model.

The empirical function consists of a combination of polynomials of angles proposed by (Walthall et al. 1985), modified by (Liang & Strahler 1994) to account for the reciprocity principle, and extended by a specular peak by (Meister 1995):

$$f_r = a_0 + a_1 \cdot (\theta_i^2 + \theta_r^2) + a_2 \cdot (\theta_i \cdot \theta_r)^2 + a_3 \cdot \theta_i \cdot \theta_r \cdot \cos(\nu) + a_4 \cdot \mathrm{e}^{\mathrm{a_5} \cdot (\theta_\mathrm{i} \cdot \theta_\mathrm{r})^2} \cdot \mathrm{e}^{-\mathrm{a_6} \cdot \psi^2} \tag{5.13}$$

where ψ is the relative angle to the specular direction:

$$\cos\psi \equiv -\sin\theta_i \sin\theta_r \cos\varphi + \cos\theta_i \cos\theta_r \tag{5.14}$$

see (Meister et al. 1998c) for more details on the specular term. The fitted parameter values a_0 to a_6 are given in (Meister 1995). Three samples were measured with the SE590 *and* the goniometer table: red roof tile, red aluminum and Spectralon 0.5. The Spectralon 0.5 was measured in the laboratory, and a different empirical function was fitted to the data:

$$f_r = a_0 - a_1 \cdot (\theta_i^4 + \theta_r^4) + a_2 \cdot (\theta_i \cdot \theta_r)^3 \cdot \mathrm{e}^{-\mathrm{a_3} \cdot \psi^2} + \mathrm{a_4} \cdot (\nu - \frac{\pi}{2}) \cdot \sqrt{\theta_\mathrm{i} \cdot \theta_\mathrm{r}} \tag{5.15}$$

The comparison for the Spectralon 0.5 is shown in fig. 5.26. The center of the horizontal bars shows the BRDF value measured with the SE590, the horizontal bars themselves indicate the measurement error. It can be seen that the overall agreement between the empirical function (dashed line) and the data measured with the SE590 is very good. In some cases, the dashed line fits even better than the TS model (solid line), especially for $\theta_i = 65°, \phi = 135°$. The TS model agrees considerably better for $\theta_i = 50°, \phi = 180°$, $\theta_i = 65°, \phi = 180°$, $\theta_i = 65°, \theta_r = 70°$, the specular peak of the empirical function is too high for these plots.

Fig. 5.28 shows the comparison of the empirical function of eq. 5.13 with the SE590 data for the sample 'red aluminum'. The specular peaks agree remarkably well for $\theta_i = 30°, \phi = 180°$ and $\theta_i = 50°, \phi = 180°$. For $\theta_i = 65°, \phi = 180°$ the specular peak derived from the goniometer table data reaches only half the maximum value of the specular peak derived from the SE590 data. A likely reason for this deviation is the angular sampling of the goniometer table data. The closest angular combination to the specular direction $\theta_i = 65°, \theta_r = 65°, \phi = 180°$ available in the dataset by (Meister 1995) is $\theta_i = 72°, \theta_r = 66°, \phi = 180°$, i.e. the maximum of the specular peak was not measured. In this case, an empirical function cannot be expected to provide good results.

The diffuse component of the empirical function of 'red aluminum' shows a decrease with increasing zenith angles that is not well supported by the data, see e.g. $\theta_i = 30°, \phi = 90°$ or $\theta_i = 50°, \phi = 0°$. On the other hand, for $\theta_i = 65°, \phi = 90°$ the predictions by the empirical function are in much better agreement with the SE590 data than the TS model.

The comparison for the red roof tile is shown in fig. 5.27. The angles far off the specular direction agree very well. But there is a strong rise for $\theta_i = 65°, \phi = 135°$, and a very strong overestimation of the width

perpendicular to the plane of incidence for $\theta_i = 65°, \theta_r = 70°$. A possible reason for these deviations is a feature of the specular peak discussed in the following chapter: the width of the specular peak perpendicular to the plane of incidence decreases with the incidence angle. **This feature is not modeled by the empirical functions of equations 5.13 and 5.15**. Thus the TS model is clearly preferable to the empirical functions for surfaces with a strong specular peak and a diffuse Lambertian component. The coarse angular grid of the goniometer table measurements prevented the shortcomings of the empirical functions to be noticed in the study by (Meister 1995).

For $\theta_i = 30°, \phi = 180°$ a specular peak is modeled that is not supported by the data. This may also be due to shortcomings of the empirical function, which is not capable of modeling the shift of the specular peak towards large zenith angles as well as the TS model.

The diffuse component of the red roof tile agrees quite well for goniometer table data and SE590 data, in fact it is difficult to decide whether the empirical function or the TS model agree better with the SE590 data.

Comparisons of the empirical function and the TS model derived from ASD data for the samples 'plastic', 'walkway' and 'brown slate' are shown in fig. 12.16 in the appendix. They are far less informative, because the ASD data was only taken in the forward scattering direction. Furthermore the ASD measurements of the sample plastic in the specular direction were overflows. The empirical function fitted to the goniometer table data shows a specular peak that is much broader than what we estimated from the ASD data (a width of less than $3°$). The BRDF of samples with a sharp specular peak cannot be determined with an angular grid as coarse as the one used in (Meister 1995). The empirical function for the sample 'brown slate' agrees quite well with the ASD data. The 'walkway' samples used at the EGO measurement campaign and in (Meister 1995) were not identical, thus the differences could be due to different surface properties.

We conclude that there is a good overall agreement between the BRDFs derived from goniometer table data and laboratory data. Because of the controlled measurement conditions and the finer angular grid at which BRDF values were measured, the laboratory data must be seen as more reliable. However, figures 5.27 and 5.28 show that *in situ* BRDF measurements using a goniometer table can yield comparable results. We expect the agreement to improve if a physically based function like the TS model is used to describe the goniometer table data as well.

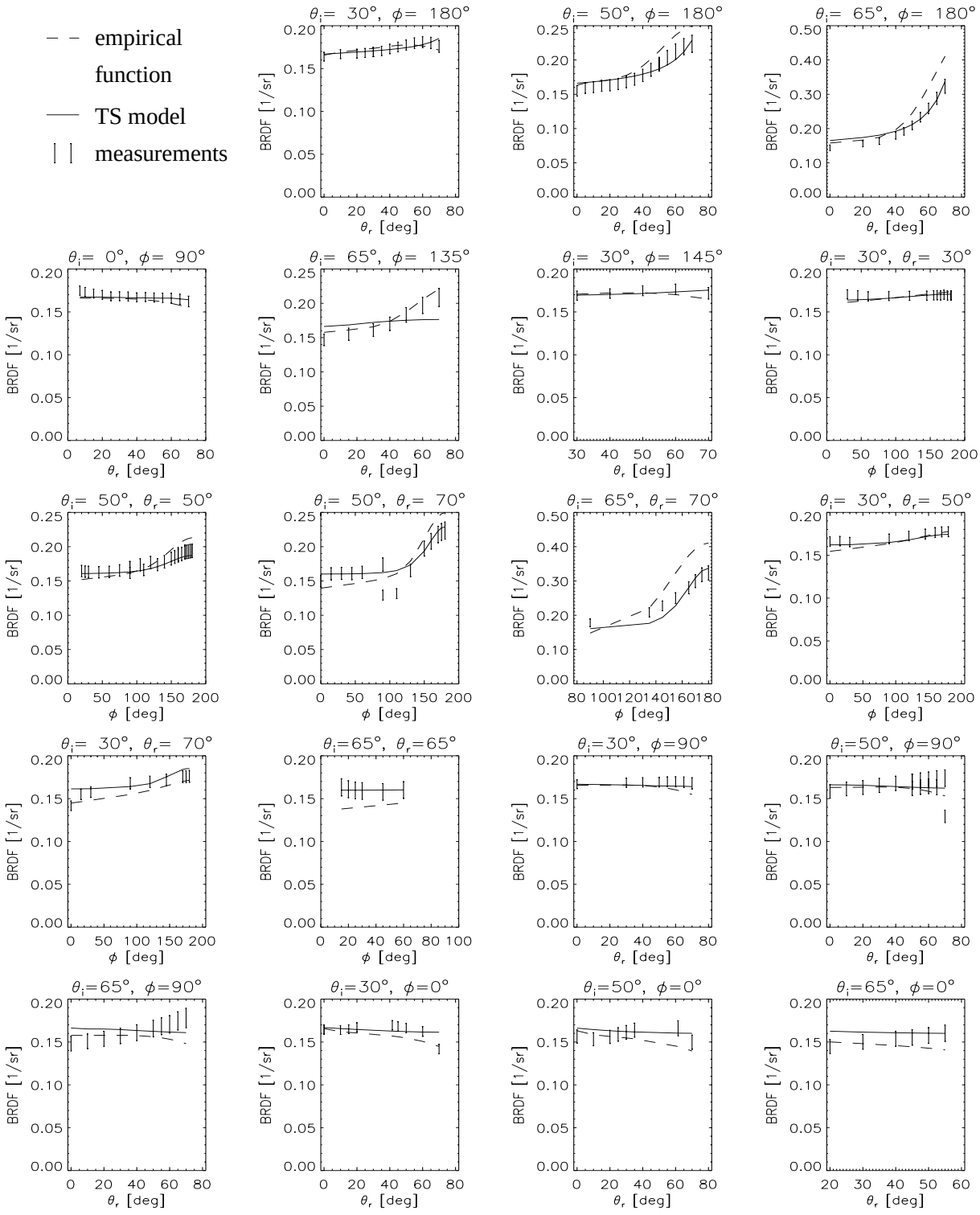

Figure 5.26: TS model (solid line) fitted to BRDF measurements of the SE590 at 660 nm (error bars) and the empirical function of (Meister 1995) (dashed line) for Spectralon 0.5.

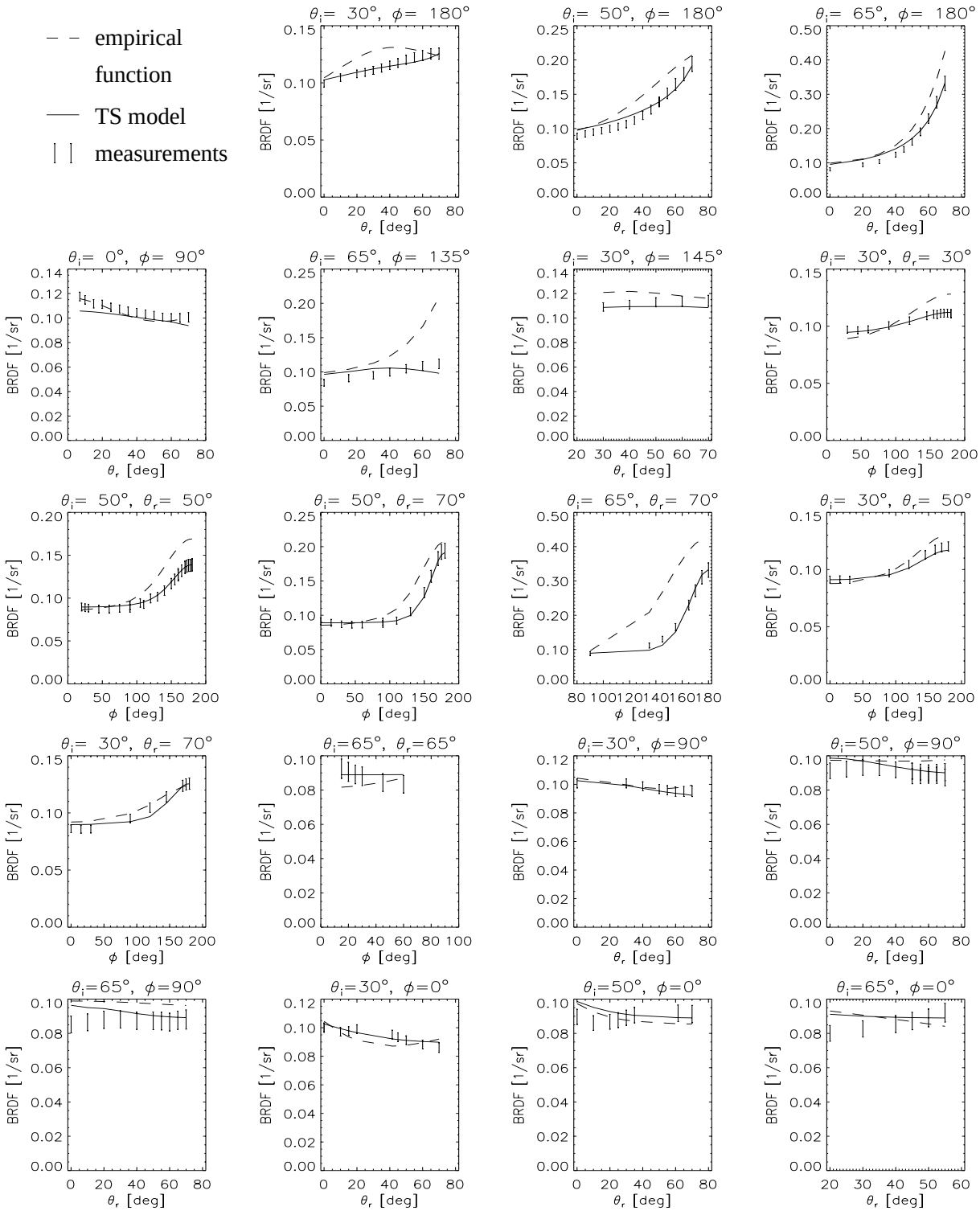

Figure 5.27: TS model (solid line) fitted to BRDF measurements of the SE590 at 660 nm (error bars) and the empirical function of (Meister 1995) (dashed line) for 'red roof tile'.

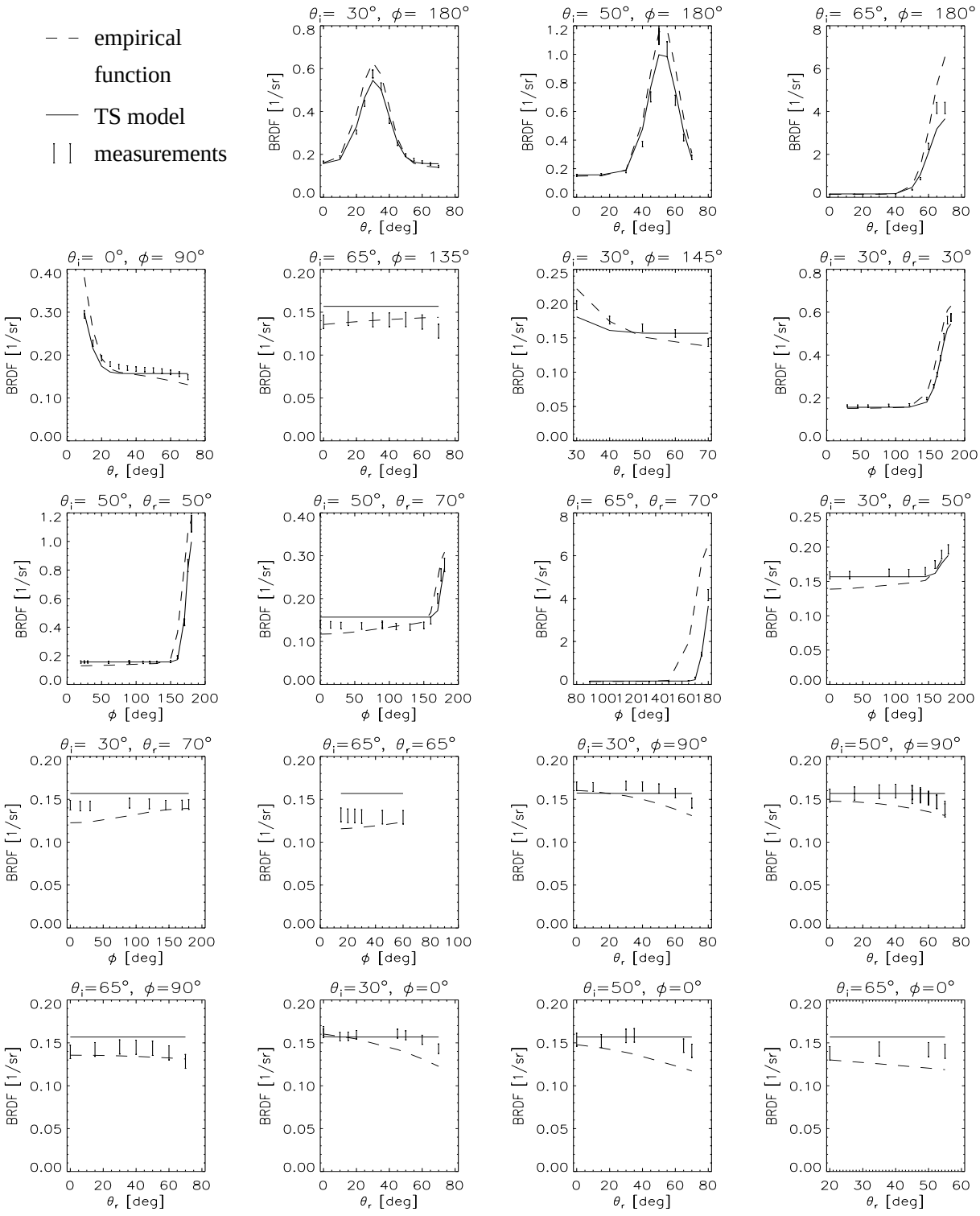

Figure 5.28: TS model (solid line) fitted to BRDF measurements of the SE590 at 660 nm (error bars) and the empirical function of (Meister 1995) (dashed line) for 'red aluminum'.

Chapter 6

The Width of the Specular Peak Perpendicular to the Principal Plane

6.1 Overview

The shape of the specular peak of rough surfaces is needed for applications in computer vision (like image rendering, object recognition) and remote sensing for all problems that involve the specular BRDF of rough surfaces, e.g. classification or change detection. In this chapter, the width of the principal plane perpendicular to the principal plane is investigated.

We compared the BRDF model of (Torrance & Sparrow 1967) to BRDF measurements of 4 man-made surfaces with very different roughnesses. We found that the width of the specular peak perpendicular to the principal plane decreases strongly with increasing illumination zenith angle, in the data as well as in the model. This feature of the specular peak has not been acknowledged before in the literature, e.g. the widely used specular BRDF model by (Phong 1975) assumes a constant width.

A model analysis shows that the width perpendicular to the principal plane is approximately proportional to the cosine of the illumination angle θ_i, the deviations are determined by the roughness of the surface. This relation is accompanied by an increase in reflectance in the specular direction in the principal plane that is stronger by a factor of $1/\cos\theta_i$ than the increase for a perfectly smooth surface.

A comparison with results from (Rothkirch et al. 2000) suggests that the TS model overestimates the increase of the specular albedo with increasing illumination angle.

Preliminary results of this chapter have been published in (Meister et al. 2000).

6.2 Measurements and Model Results

For this chapter, we will restrict the analysis to a wavelength of 660 nm, because at this wavelength we can obtain the coefficient of absorption k from (Rothkirch et al. 2000) for the sample 'roof tile'.

We fitted the parameters of the TS model to our data using a least-square fitting routine from the programming package IDL. We did not use measurements with a relative azimuth φ smaller than 90°, because we want to focus our investigation on the specular peak. For the roof tile we obtained 145 measurements, for the other 3 samples 122 measurements. The TS model is driven by 5 parameters: t_0, t_1, w, n and k. Thus the number of measurements is clearly sufficient. But the parameters k and n cannot be retrieved simultaneously, their effect on the Fresnel reflectance in conjunction with the specular intensity parameter t_1 is not unique for illumination angles $\leq 70^\circ$. This can be seen from fig. 6.1. The solid line shows the Fresnel reflectance for $k = 0$ and $n = 1.5$ as a function of illumination angle θ_i. The crosses show the Fresnel reflectance for $k = 0.4$ and $n = 1.35$, normalized to the value $\theta_i = 0^\circ$ of the solid line. It can be seen that different

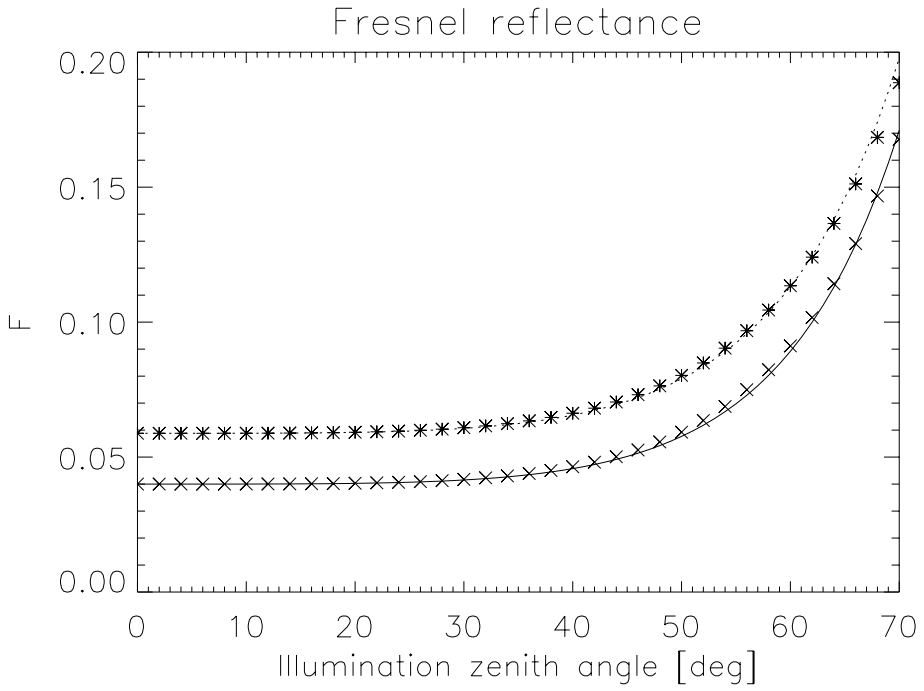

Figure 6.1: The Fresnel reflectance for unpolarized illumination as a function of illumination angle for different parameters n, k. The solid line shows the Fresnel reflectance for $k = 0$ and $n = 1.5$, the crosses show the Fresnel reflectance for $k = 0.4$ and $n = 1.35$, normalized to the value $\theta_i = 0^\circ$ of the solid line. The dotted line shows the Fresnel reflectance for $k = 0.2, n = 1.6$, the stars show the Fresnel reflectance for $k = 0.55, n = 1.4$, normalized to the value of the dotted line at $\theta_i = 0^\circ$. It can be seen that different parameters k produce a very similar shape of the Fresnel reflectance if the index of refraction n is adjusted.

parameters k produce a very similar shape of the Fresnel reflectance if the index of refraction n and the specular intensity parameter t_1 are adjusted. The dotted line (Fresnel reflectance with $k = 0.2, n = 1.6$) shows another example: it can hardly be separated from the stars (Fresnel reflectance with $k = 0.55, n = 1.4$, normalized to the value of the dotted line at $\theta_i = 0^\circ$). Thus it is impossible to retrieve the parameters k, n and the specular intensity parameter from BRDF measurements if neither of them is known. Additional information can be obtained from e.g. polarized BRDF measurements (as presented in (Rothkirch et al. 2000)), which allow a much better discrimination between the parameters n and k.

Previous authors have set $k = 0$, like e.g. (Ginneken et al. 1998). However, $k = 0$ is incompatible with the polarized BRDF measurements presented in (Rothkirch et al. 2000) on the same red roof tile as used in this study. We adopted the value of $k = 0.25$ from (Rothkirch et al. 2000) and set this parameter constant for all samples. The value $n = 1.87$ we obtain from fitting (see table 6.1) using $k = 0.25$ is higher than the value given in (Rothkirch et al. 2000) ($n = 1.35$). The fact that our fitting result for n is too high suggests that the TS model overestimates the increase of the specular albedo with increasing θ_i (assuming that $n = 1.35$ is the true value), because a low value of n is accompanied by a strong increase of the specular albedo with increasing θ_i.

parameter that is Thus we conclude that the Fresnel parameters n and k retrieved by fitting can describe the shape of the specular peak very well, but from unpolarized BRDF measurements it is impossible to determine reliable values for n and k. However, it is reassuring that the retrieved values are within the expected range for dielectrics ($n \in [1.3, 2.0]$ (Wolff 1994).

The fitted parameters t_0, t_1, w and n are given in table 6.1 for the 4 samples. d_f denotes the degrees of

Sample	$t_0\,[\mathrm{sr}^{-1}]$	$t_1\,[\mathrm{sr}^{-1}]$	$w\,[\mathrm{deg}^{-1}]$	n	k	χ^2/d_f
Roof tile	0.082 ± 0.001	0.18 ± 0.09	0.040 ± 0.001	1.87 ± 0.84	0.25 ± 2.97	1.5
Red concrete	0.0903 ± 0.0004	1.00 ± 0.27	0.084 ± 0.001	1.52 ± 0.20	0.25 ± 0.51	1.1
Blue concrete	0.0531 ± 0.0002	1.09 ± 0.24	0.083 ± 0.001	1.46 ± 0.14	0.25 ± 0.33	2.0
Red Aluminum	0.1370 ± 0.0005	3.1 ± 1.2	0.167 ± 0.001	1.81 ± 0.49	0.25 ± 1.81	4.2

Table 6.1: Parameters obtained from fitting the TS model (eq. 5.1) to the SE590 BRDF data at a wavelength of 633 nm. The parameter k was set to 0.25. See text for a discussion of the errors. The parameters at a wavelength of 660 nm were presented in table 5.1.

freedom (number of measurements (N) minus number of parameters (5 in this case)), χ^2 is defined as

$$\chi^2 = \sum_i^N \frac{(f_{r,i}^{\mathrm{measured}} - f_{r,i}^{\mathrm{modelled}})^2}{\sigma_i^2} \tag{6.1}$$

where σ_i is the measurement error of the i'th measured BRDF value $f_{r,i}^{\mathrm{measured}}$.

The fit only passes the χ^2 test for 'red concrete', the acceptance threshold for χ^2 is about 1.3 for a significance level of 1 % (Brandt 1992). The rejection of 'blue concrete' and 'red roof tile' is due to the diffuse component, e.g. at a wavelength channel of 680 nm, $\chi^2 = 1.3$), see also figures 5.15 and 5.16. The rejection of 'red aluminum' must be attributed to both the specular and the diffuse component, because the intensity of the specular peak is predicted too low for high illumination angles, see fig. 6.2.

The errors were calculated according to (Brandt 1992) using a Taylor expansion because of the nonlinearity of the TS model. Here we treated k as a free parameter (although we actually used the fixed value of 0.25) to be able to calculate the uncertainty for this parameter. The errors can only be seen as rough estimates, because the Taylor expansion of the Fresnel reflectance with respect to the parameter k

$$F(k + \sigma_k) = F(k) + \frac{\partial F}{\partial k} \cdot \sigma_k \tag{6.2}$$

is a poor approximation for the large σ_k of table 6.1.

The model BRDF values are plotted in figs. 6.2 and 6.3 (solid line), together with measured values (crosses). The measurement errors are plotted as vertical bars, often they are so small that they can hardly be seen in the plot. The plots show that the model fits the measurements quite well, the strongest deviations occur for the sample red aluminum, where the intensity of the specular peak is underestimated.

Fig. 6.2 shows the well known shift of the maximum of the specular peak towards higher zenith angles (especially for $\theta_i = 50°$). The roof tile has a very broad specular peak, the aluminum has a very sharp specular peak, and the width of the specular peak of the concrete tiles is in between.

6.3 Width of the Specular Peak Perpendicular to the Principal Plane

Fig. 6.3 shows the feature of the specular peak that this chapter focuses upon. The BRDF values are plotted as a function of the relative azimuth angle φ, with $\theta_r = \theta_i$ for $\theta_i = 30°, 50°$, and $\theta_r = 70°$ for $\theta_i = 65°$. It can be seen that the width of the peaks with respect to the azimuth angle decreases dramatically with increasing zenith angle. It can be seen that the azimuthal width reduces by about 50 % when increasing θ_i from $30°$ to $50°$, and by about 75 % when increasing θ_i from $30°$ to $65°$. The dramatic change of shape of the specular peak data, which is obviously in accord with the TS model, is not predicted by simpler models like e.g. the Phong model (Phong 1975). For a better comparison[1], the last plot in each row shows the modeled values

[1]Even the Phong model shows a decrease of the azimuthal width with increasing zenith angle (however less strong than the TS model) due to the definition of the azimuth angle.

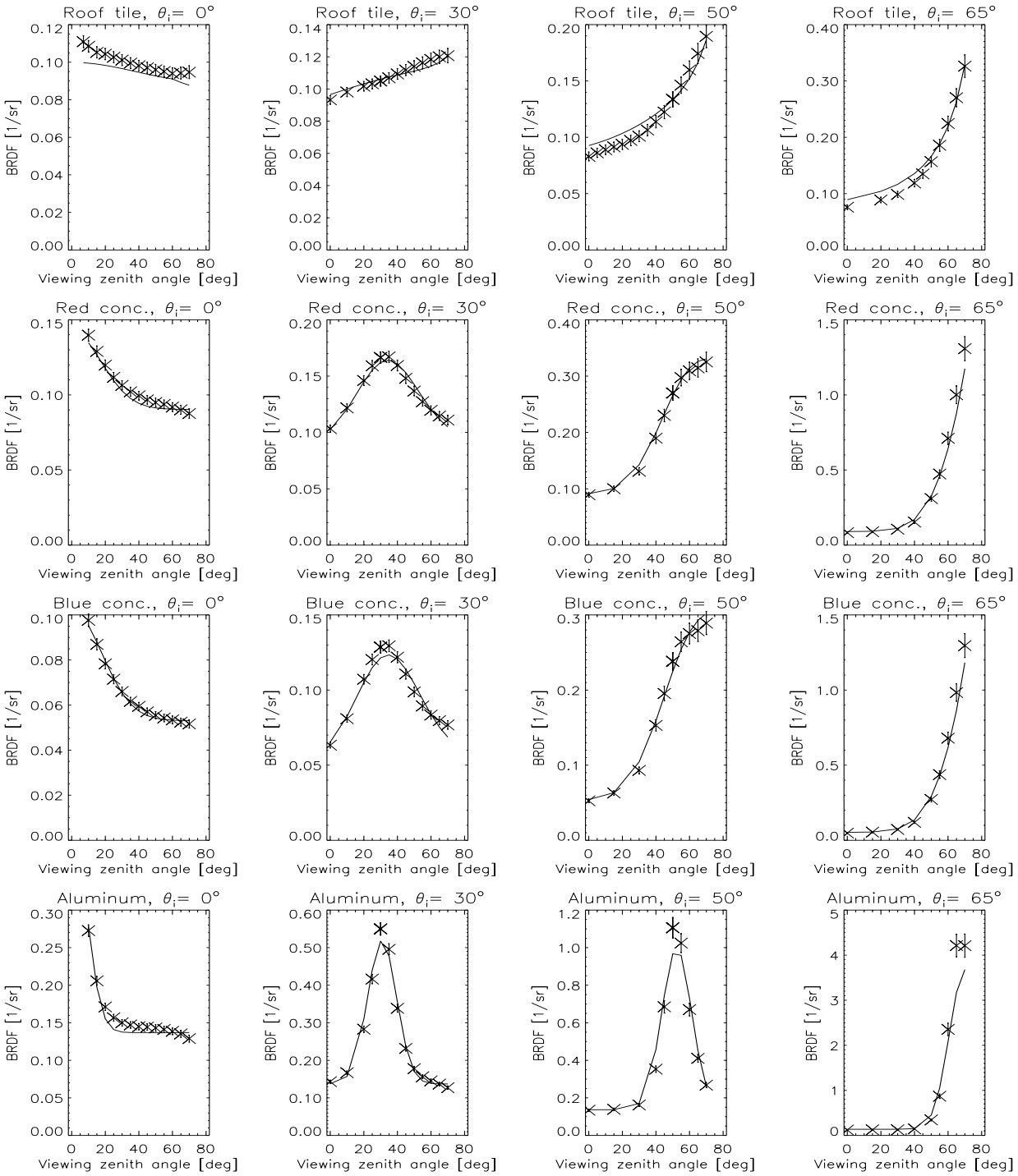

Figure 6.2: BRDF of the samples at different illumination angles θ_i as a function of viewing zenith angle θ_r in forward scattering direction ($\varphi = 180°$). Stars denote measured values, the solid line shows the TS model predictions using the parameters from table 6.1. The samples have specular peaks of different intensity and width (widest for roof tile, narrowest for aluminum). The vertical bars within the stars show the measurement error. The shift of the maximum of the specular peak towards higher zenith angles can be seen especially well at illumination angle $\theta_i = 50°$.

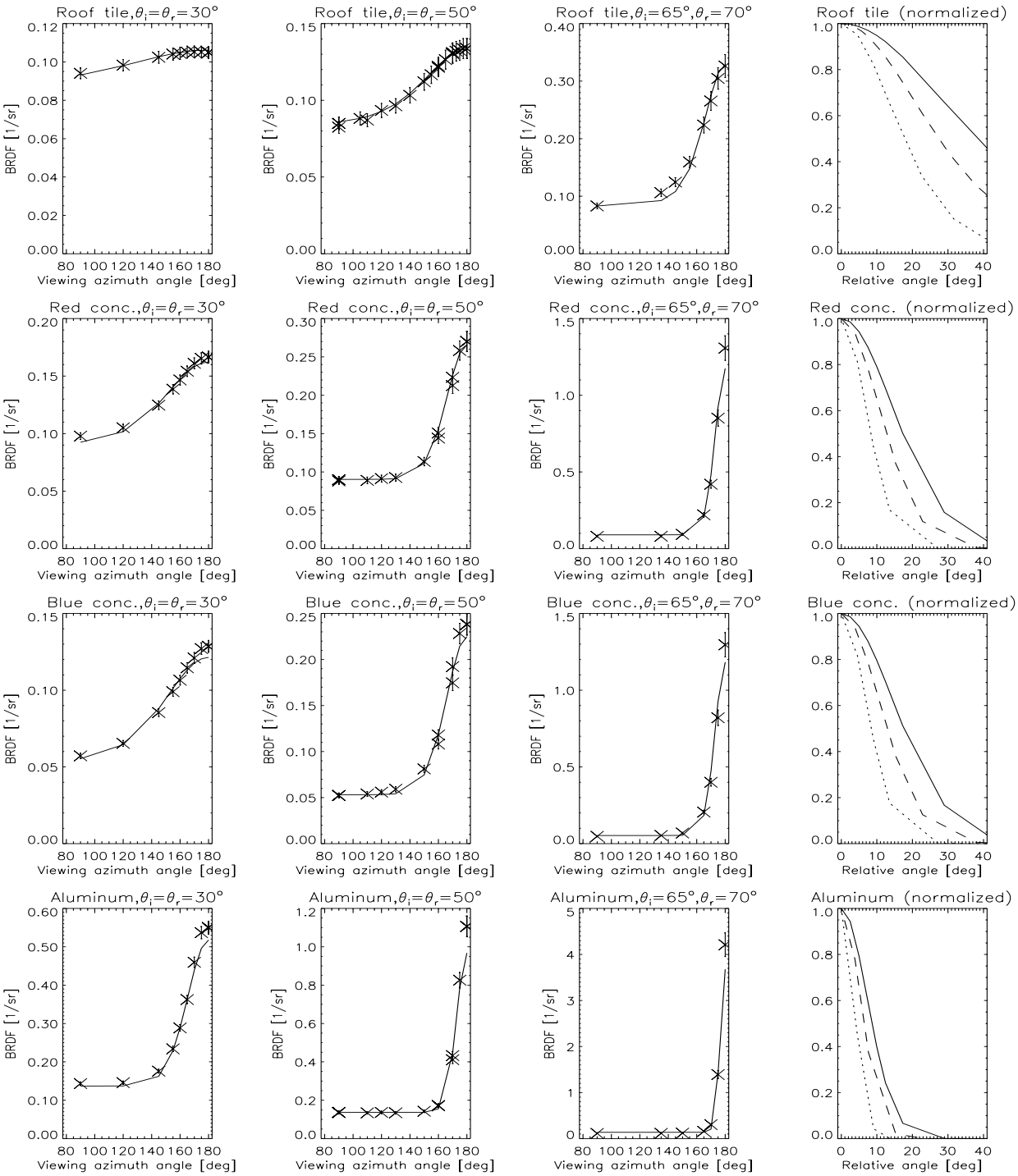

Figure 6.3: BRDF of the samples at constant zenith angles θ_i, θ_r as a function of azimuth angle φ. Stars denote measured values, the solid line shows the TS model predictions using the parameters from table 6.1. The vertical bars within the stars show the measurement error. The last column shows the modeled specular peak only (i.e. the modeled values minus the coefficient t_0) normalized to its maximum value, emas a function of the angle relative to the specular direction. Solid line shows $\theta_i = \theta_r = 30°$, dashed line shows $\theta_i = \theta_r = 50°$ and dotted line shows $\theta_i = \theta_r = 65°$. It can be seen that the width of the specular peak decreases with increasing illumination angle.

minus t_0 (i.e. the specular peak, without the diffuse component) of the three previous plots[2]normalized to the maximum value. The data are plotted *as a function of the angle relative to the specular direction* (defined as ψ in eq.5.14 on page 74), to emphasize the decrease of the width of the specular peak perpendicular to the principal plane. For a BRDF model with a constant width perpendicular to the principal plane like the Phong model, the 3 lines would lie exactly on top of each other.

The mathematical explanation for this effect can be found in eq. 5.5. Let us assume an illumination zenith angle of $\theta_i = 45°$. To direct the incoming ray to either $[\theta_r = 35°, \varphi = 180°]$ or $[\theta_r = 55°, \varphi = 180°]$, i.e. a deviation of $10°$ off the specular direction $[\theta_r = 45°, \varphi = 180°]$ *within the principal plane*, a surface facet with normal $\alpha = 5°$ is needed according to eq. 5.5 (oriented towards the light source for $\theta_r = 35°$, oriented away from the light source for $\theta_r = 55°$, see also eq. 6.3 below). *This result is independent of* θ_i. To direct the ray to $[\theta_r = 45°, \varphi = 170°]$, i.e. $10°$ *out of the principal plane*, we also need a surface facet with a normal of $5°$. *But this result depends strongly on* θ_i. For $\theta_i = 65°$, we need a surface facet with a normal of $\alpha = 10.6°$ to direct the ray to $[\theta_r = 65°, \varphi = 170°]$. For $\theta_i = 30°$, we need a surface normal of only $\alpha = 2.9°$. The amount of surface facets with normal α is given by eq. 5.4. $\alpha = 0°$ is the most abundant surface normal, the probability of a surface facet having the normal α decreases monotonously with α. This means that there are more surface facets with a normal of $\alpha = 2.9°$ (needed to direct the light towards $[\theta_r = 30°, \varphi = 170°]$ with $\theta_i = 30°$) than surface facets with a normal of $\alpha = 10.6°$ (needed to direct the light towards $[\theta_r = 65°, \varphi = 170°]$ with $\theta_i = 65°$). Thus the intensity of reflected light is stronger at $[\theta_i = \theta_r = 30°, \varphi = 170°]$ than at $[\theta_i = \theta_r = 65°, \varphi = 170°]$, i.e. the azimuthal width of the specular peak decreases for high illumination angles.

It is easy to see that the zenithal width of the specular peak does not depend on the zenith angle, because in the principal plane (forward scattering, i.e. $\varphi = 180°$) α is given by (Torrance & Sparrow 1967)

$$\alpha = \frac{\theta_r - \theta_i}{2} \tag{6.3}$$

and deriving α with respect to θ_r yields a constant value $1/2$. Thus to increase the angle of reflection θ_r by $1°$, the surface facet must be tilted an additional $0.5°$ to achieve specular scattering, *independent of* θ_i. Deriving α with respect to φ with $\theta_i = \theta_r$, eq. 5.5 must be used. The result is shown in fig. 6.4 as a function of θ_i. Obviously the derivative increases strongly with θ_i. E.g., increasing $\varphi = 180°$ by $1°$ requires an increase of α by $\approx 2.8°$ at $\theta_i = 80°$, but at $\theta_i = 30°$ an increase of α of only $\approx 0.3°$ is needed.

This effect was confirmed by a simple experiment: we directed a laser towards a tilted mirror at a high illumination angle, and turned the mirror around its axis. The light beam hit a vertical plane, and we marked the path of the light ray while turning the mirror. After projecting the vertical plane onto a sphere covering the upper hemisphere, we obtained an ellipse, the larger axis in the vertical, the smaller axis in the horizontal direction (note that the specular peak predicted by the TS model is not an ellipse due to the Fresnel reflectance F, the Geometric Attenuation Factor G, and most notably the division by the cosines of the zenith angles, see eq. 5.1).

It is important to recognize that only the *shape* of the specular peak changes with illumination angle. The overall *intensity* of the specular peak does depend on the illumination angle, but only because of the Fresnel Reflectance F (and masking and shadowing effects). The effect of the reduction in azimuthal width on the total intensity is compensated by the division by the cosine of the illumination zenith angle $\cos\theta_i$ in eq. 5.1. This is another interesting effect predicted by the TS model: for a rough surface, the increase of the BRDF in the specular direction ($\theta_r = \theta_i, \varphi = 180°$) as a function of the illumination angle θ_i is stronger than for a smooth surface, by a factor of $1/\cos(\theta_i)$. This is shown in fig. 6.5, where the solid line shows the BRF for a perfectly smooth surface, and the dashed and the dotted line show the BRFs for a rough surface, normalized to the BRF of the smooth surface at $\theta_i = 0°$.

[2]We rather used values at $\theta_r = \theta_i = 65$ instead of the values at $\theta_r = 70°, \theta_i = 65$ because this allows a consistent comparison.

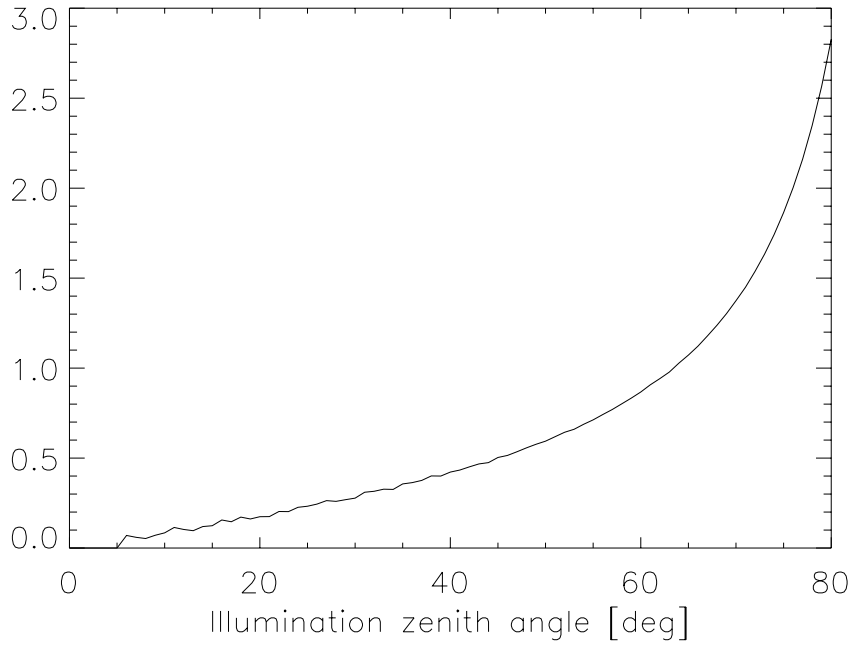

Figure 6.4: The derivative of α (eq. 5.5) with respect to φ as a function of the illumination zenith angle θ_i with $\theta_r = \theta_i$ and φ increasing from 180°. The small variations for illumination angles toward 0 are produced by computational limits.

We use BRF rather than BRDF, because the BRDF of a perfectly smooth surface is a delta function (only BRF is directly measurable). BRF is defined as (Nicodemus et al. 1977)

$$BRF(\omega_i, \omega_r) = \frac{\pi}{\Omega_i \Omega_r} \cdot \int_{\omega_i} \int_{\omega_r} f_r(\theta_i, \phi_i, \theta_r, \phi_r) d\Omega_r d\Omega_i \tag{6.4}$$

For our purpose, the integration has to be carried out over the aperture of sensor and light source.

Assuming that the irradiance covers the full field of view of the detector, the BRF for a perfectly smooth surface in the specular direction is given by

$$\begin{aligned} BRF(\theta_i = \theta_r, \varphi = 180^\circ, \Omega_i, \Omega_r) \approx \pi \cdot \frac{L_r}{E_i} = \pi \cdot \frac{L_r}{E_0 \cdot \cos\theta_i} = \\ \pi \cdot \frac{L_0 \cdot F(n,k,\theta_i)}{E_0 \cdot \cos\theta_i} = \pi \cdot \frac{L_0 \cdot F(n,k,\theta_i)}{\pi \cdot L_0 \cdot \cos\theta_i} = \frac{F(n,k,\theta_i)}{\cos\theta_i} \end{aligned} \tag{6.5}$$

where E_0 is the irradiance for nadir illumination and L_0 is the radiance of the light source.

In fact, we expect masking and shadowing effects to reduce the increase of the BRF's of rough surfaces, unfortunately the TS model predicts neither masking nor shadowing at all in the specular direction ($\theta_r = \theta_i, \varphi = 180^\circ$), which is probably not very realistic. Especially for large zenith angles masking and shadowing effects become important.

We define 'specular albedo' as the directional-hemispherical reflectance as defined by (Nicodemus et al. 1977) due to the specular peak. It can be calculated by integrating eq. 5.1 over the projected solid angle $d\Omega$ of the upper hemisphere, setting $t_0 = 0$. The stronger increase in intensity in the principal plane of the BRF of a rough surface compared to a smooth surface is shown in fig.6.5. It *does not* result in an increase in specular albedo. We will show that the *width of the specular peak perpendicular to the principal plane*

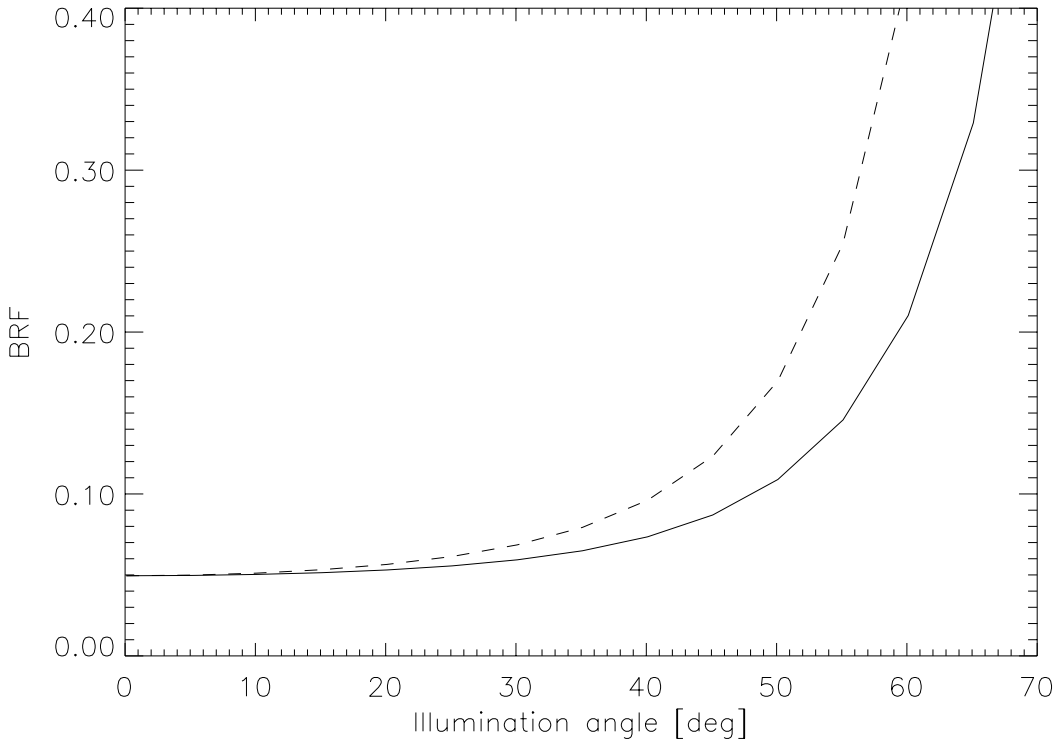

Figure 6.5: The solid line shows the BRF in the specular direction ($\theta_r = \theta_i, \varphi = 180°$) for a perfectly smooth surface, the dashed line shows the BRF in the specular direction for a rough surface, normalized to the BRF value of the smooth surface at $\theta_i = 0°$. The Fresnel reflectance is determined by $n = 1.5$ and $k = 0.25$ in both cases. The width of the specular peak is assumed to be much larger than the aperture of the sensor.

decreases approximately proportional to $\cos\theta_i$, and this effect cancels the *increase in intensity in the principal plane*.

The stronger increase of the BRDF in the TS model as compared to the BRF of a perfectly smooth surface led (Nayar et al. 1991) to reject the TS model for very smooth surfaces. Our findings shed new light on this topic and extend the possible range of applicability of the TS model even to very smooth surfaces. However, for very smooth surfaces it is necessary to verify that the aperture of the sensor is small enough to allow the approximation $BRF \approx \pi \cdot f_r$, otherwise the BRF predicted by the TS model has to be calculated from eq. 6.5.

It is difficult to judge the width of the specular peak from fig. 6.3, because the azimuthal width covered by a fixed solid angle decreases with increasing zenith angle (a solid angle covering $\Delta\theta = \Delta\varphi = 1°$ at $\theta = 90°$ still has a zenithal width of $\Delta\theta = 1°$ at nadir, but an azimuthal width of $\Delta\varphi = 180°$). Thus we determined the angle perpendicular to the principal plane, at which the BRDF value due to the specular peak drops to half its maximum value. The Full Width Half Maximum (FWHM) perpendicular to the principal plane is twice this angle, because the *full* width extends to either side of the specular peak. More specifically, for every illumination angle, we computed the BRDF values for all angles lying on the line on the unit sphere connecting the specular direction $\theta_r = \theta_i, \varphi = 180°$ and $\theta_r = 90°, \varphi = 90°$ (this line is always perpendicular to the principal plane, see fig. 6.6). The relative angle between that angle on the line, whose BRDF value is half the maximum value is the desired angle. The maximum value is at the specular direction $\theta_r = \theta_i, \varphi = 180°$.

Fig. 6.7 shows the FWHM of the specular peak perpendicular to the principal plane for the samples as

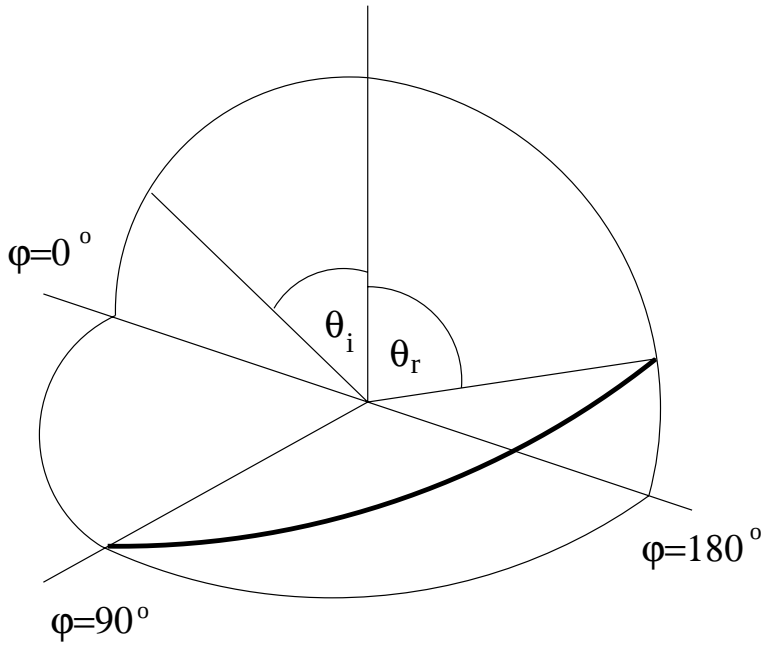

Figure 6.6: The sketch shows the unit sphere and the light path for perfect specular direction ($\theta_i = \theta_r, \varphi = 180^\circ$) as thin lines. The thick line shows the angles perpendicular to the principal plane referred to in section 6.3 to calculate the FWHM. The thick line runs on the unit sphere, connecting the specular direction and ($\theta_r = 90^\circ, \varphi = 90^\circ$).

a function of the illumination angle, derived from the TS model using the parameters from table 6.1. The FWHM at $\theta_i = 0^\circ$ in the principal plane is the same as the FWHM perpendicular to the principal plane at $\theta_i = 0^\circ$. For our samples, the FWHM is given by $114.9^\circ, 41.4^\circ, 42.1^\circ$ and 19.9°, for roof tile, red concrete, blue concrete and aluminum, resp. *It can be seen that the FWHM perpendicular to the principal plane decreases approximately proportional to the cosine of* θ_i. Thus we plotted in fig. 6.8 the ratio of the FWHM and $\cos\theta_i$ and normalized it to the nadir value. The deviations from the decrease with $\cos\theta_i$ are smallest for 'aluminum', which is the smoothest surface of our samples. The concrete tiles show deviations only up to 5 %. The sample 'roof tile', which is the roughest surface in our study, shows much stronger deviations. The most likely reason for the deviations are masking and shadowing effects, which are strongest for the roughest surface.

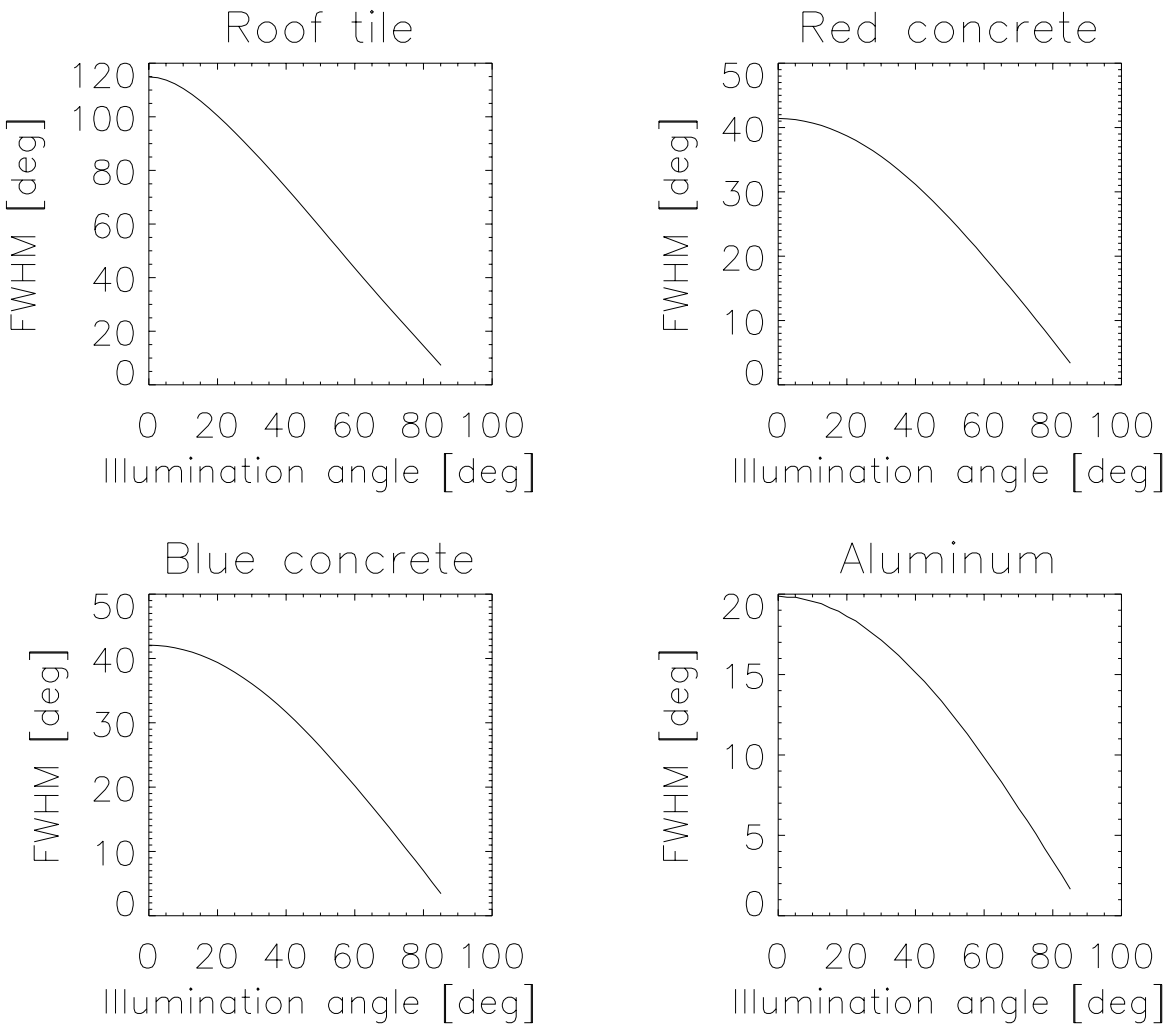

Figure 6.7: The FWHM of the specular peak perpendicular to the principal plane as a function of the illumination angle θ_i for the 4 samples. The FWHM decreases approximately proportional to $\cos\theta_i$, see fig. 6.8. At $\theta_i = 0°$, the FWHM in the principal plane and perpendicular to the principal plane are identical. Thus, e.g. for the sample 'aluminum', at $\theta_r \approx 20°/2 = 10°$ the measured radiance has dropped to half its maximum value (maximum value for $\theta_i = 0°$ at $\theta_r = 0°$).

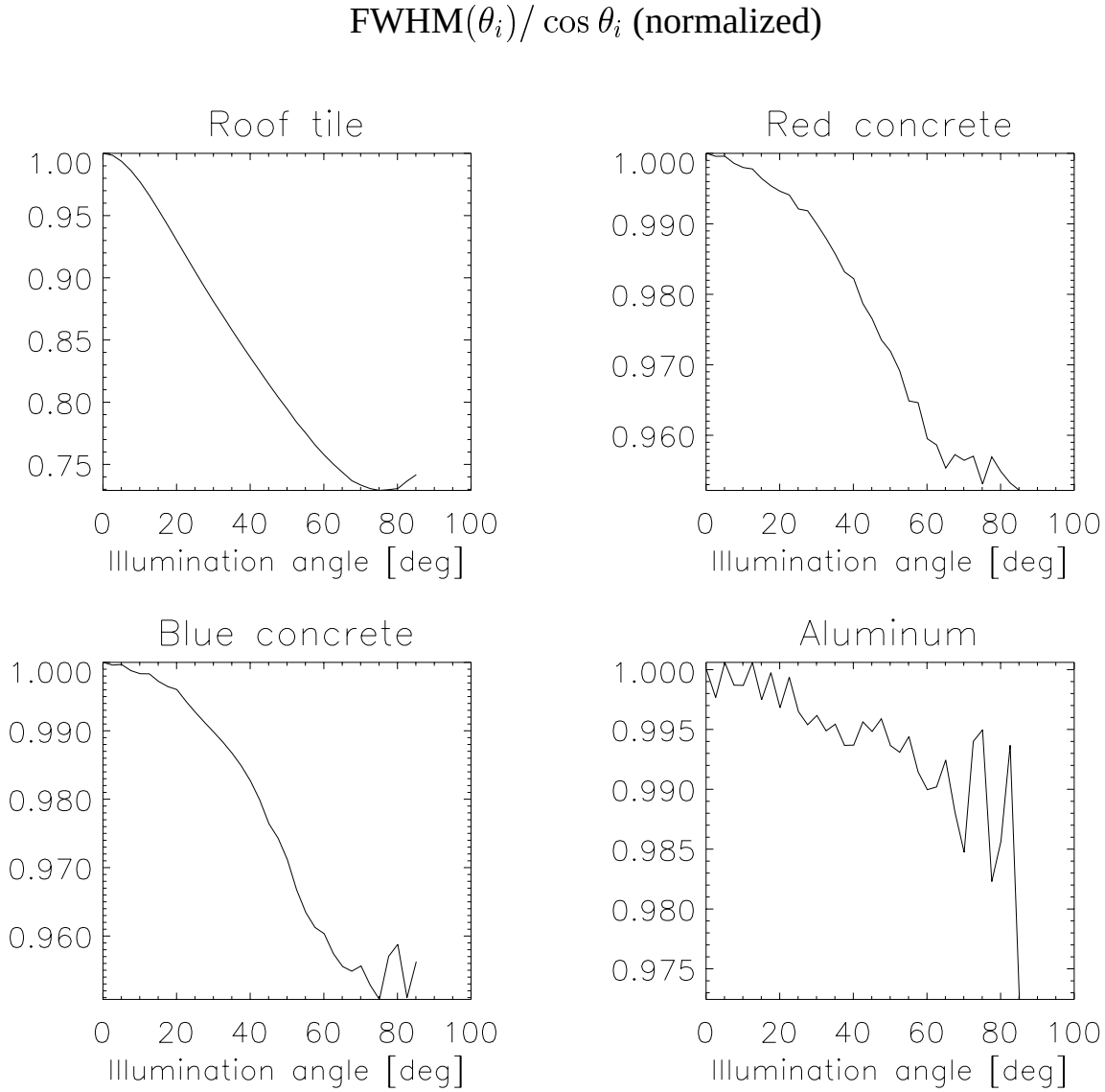

Figure 6.8: The FWHM perpendicular to the principal plane (cf. fig. 6.7) divided by the cosine of the illumination angle θ_i normalized to the value at $\theta_i = 0°$ as a function of θ_i for the 4 samples. The plots show that the FWHM decreases proportional to the cosine of θ_i for the concrete tiles and the aluminum sample, with deviations up to 5 % for the concrete tiles and only up to 2.5 % for the aluminum sample. The very rough sample 'roof tile' shows much stronger deviations.

Chapter 7

Surface Topography

7.1 Abstract

Although the surface structure of the TS model and the ON model is impossible to realize physically, the two models use the inclination distribution of surface facets, which is in fact a parameter that can be measured. We acquired surface topography data for eight samples. The data have a vertical resolution of 0.16 μm, and a horizontal resolution of 1 μm for profiles of 1 mm length and a horizontal resolution of 1.24 μm for profiles of 10 mm length. We derived the average surface inclination from the topography data and compared it to the average surface inclination derived from BRDF measurements. Without averaging, the average inclination of the surface normals strongly exceeds the values expected from BRDF measurements. After spatially averaging the data the agreement is poor, about $\pm$ 50 % after averaging with a spatial bin size of 20 μm. We do not know whether the failure to link the topography measurements with one common binsize to the reflectance data is due to an inappropriate resolution of the topography data or to an insufficient theoretical approach. One possible explanation is that indeed each surface has its own characteristic facet size. This hypothesis is supported by the similar 'best-fitting' bin sizes within each material type

7.2 Data Acquisition

We made an arrangement with Prof. Weckenmann at the 'Chair of Quality Management and Manufacturing Metrology' in Erlangen, Germany to measure the topography of 12 of our samples with the optical profiler RM 600, produced by Feinprüf Perthen GmbH, Göttingen, Germany. The profiler uses the focus-detection principle. A laser with a wavelength of 780 nm is focused on the surface by moving an objective, see fig. 7.1. A focus detector decides whether the light spot on the surface is in focus. If yes, the position of the objective is converted to a surface profile point by the path sensor. The exact procedure is not made public by the manufacturer for competitive reasons. The vertical resolution is 0.16 μm, the smallest horizontal resolution is 1 μm. The profiles are limited to a maximum of 8192 data points. The maximum vertical range is restricted to 0.6 mm. The reflectance of the sample must be higher than 2 % and less than 95 %. The spot of the laser on the sample has a diameter of 1 μm. The maximum profile inclination is 13° for specular surfaces without a strong diffuse component and 80° for diffuse surfaces (like e.g. paper). The complete system consists of the laser-optical distance sensor, a positioning table based on piezo components, and a controlling and data processing computer. The repositioning accuracy of the positioning table is better than 2 μm.

For each sample, we ordered two kinds of measurements: 1000 neighboring profiles with 1000 data points in each profile, with a horizontal resolution of 1 μm, resulting in a measured square of 1 mm $\times$ 1 mm, and a single profile with a horizontal resolution of 1.24 μm of 8191 data points, resulting in a line of 10 mm length. Both kinds of measurements were executed twice, each at a different location of the sample.

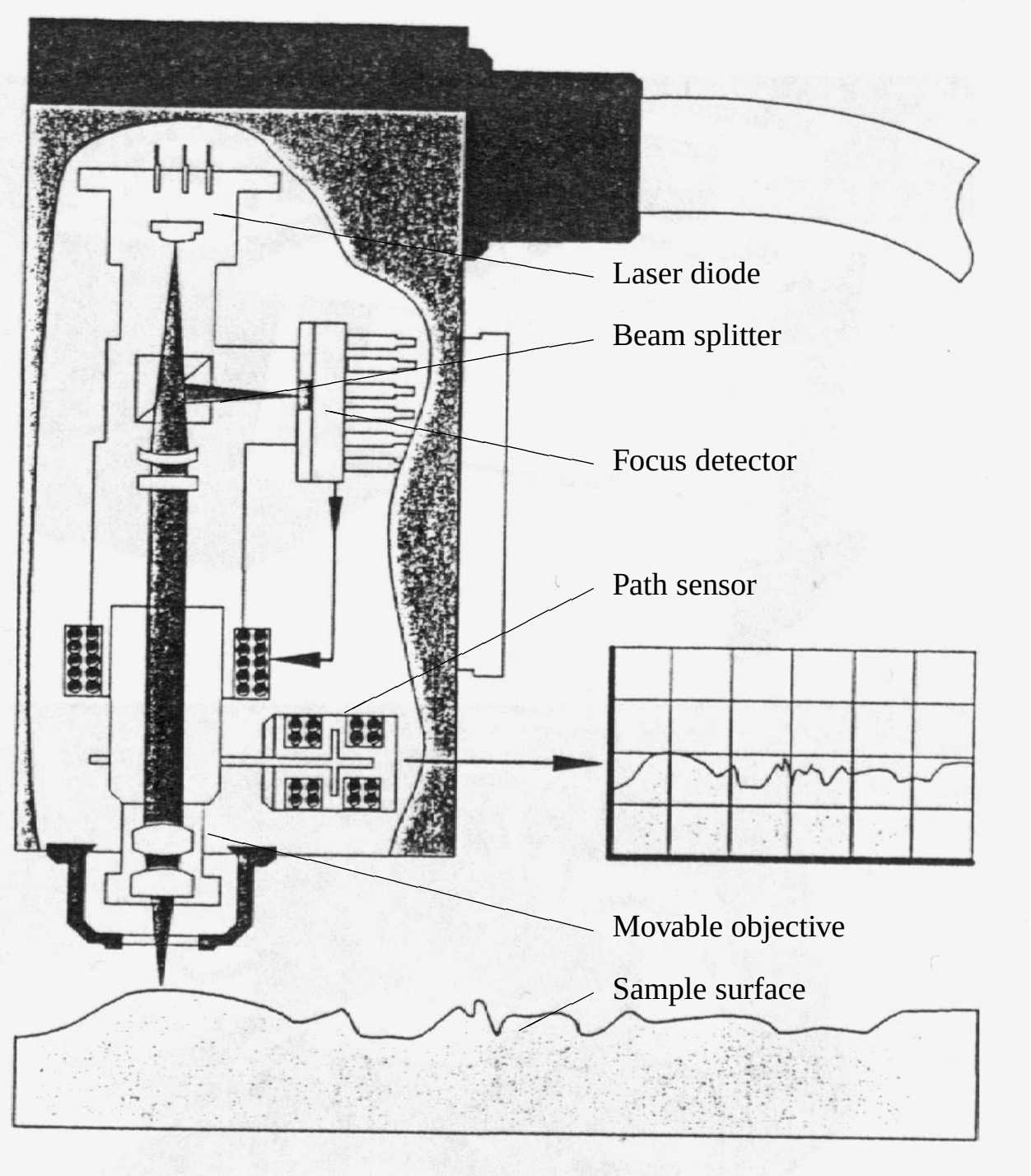

Figure 7.1: This sketch (provided by Feinprüf Perthen GmbH, Göttingen, Germany) shows the optical profiler RM600 used in this study to obtain the topography measurements.

Out of the 12 samples we provided, 4 could not be measured with the RM600. For 'asphalt' and 'wall paper', the maximum allowed vertical range of 0.6 mm was exceeded, for the samples 'green roof paper' and 'sanded roof paper' the RM600 was not able to deal with the frequent color changes of these samples. No profiles with a horizontal resolution of 10 μm are available for the sample 'Roof tile Opal', due to an inattentiveness of the operator of the instrument in Erlangen that was noticed too late.

7.3 Qualitative Analysis

Figures 7.2 and 7.3 show selected data from the topography measurements at different scales. The first column shows the measurement of 10 mm length (8091 data doints), the second shows the 500th profile of the 1 μm horizontal resolution measurement series (1000 data points), the third column shows an enlargement of the center of this profile (data points 450 to 550). The last column shows only 11 data points (495 to 505), with the y-axis scaled in such a way that it also extends to about 10 μm, the same as the x-axis. In this way, the slopes of the curves in the last column are similar to the measured slopes, whereas for the 3 previous columns they are greatly exaggerated due to the different scaling of the axes. It can be seen that the average slope in the last column is quite high, especially for the sample 'Red roof tile'. It is also interesting to note that the assumption of the TS model and the ON model of V-cavities is not realistic, in our data the surface normals of neighboring surface facets usually do not form a V.

3-dimensional profiles are shown in figures 7.4, 7.5 and 7.6. for the very rough surface 'red roof tile', the relatively smooth surface 'blue concrete' and the very smooth surface 'red aluminum'. The respective plots for the remaining samples are shown in the appendix, figures 12.17 to 12.21, pages 12.17 to 12.21.

7.4 Quantitative Analysis

7.4.1 Evaluated Quantities

We extracted several statistical quantities from the topography data:

- $\sigma_z[\mu\mathrm{m}]$, the root mean square deviation of the heights (Thomas 1999). It is given by

$$\sigma_z = \sqrt{\frac{1}{L}\int_0^L z^2(x)dx} \tag{7.1}$$

  where L is the profile length and $z(x)$ is the measured profile.

- $\beta[\mu\mathrm{m}]$, the correlation length, defined as the distance, at which the autocorrelation function drops to e^{-1} (Thomas 1999). Points separated by distances greater than the correlation length are considered statistically independent. The autocorrelation function is given by (Ogilvy 1992):

$$C(X) = \frac{1}{\sigma_z}\int_{-\infty}^{\infty} z(x)z(x+X)p(z)dz \tag{7.2}$$

  where $p(z)dz$ is the probability that a profile point has a height from z to $z+dz$.

- $\sigma_\alpha[\mathrm{deg}]$, the root mean squared inclination of the surface normal. The surface normal σ_α^x between 2 height points of a line profile in the $x-$direction is given by the arcus tangent of the slope (height difference of the two points divided by their distance). The average surface inclination in 3 dimensions can be calculated by multiplying with $\pi/2$ according to (Nayak 1971), assuming the surface to be

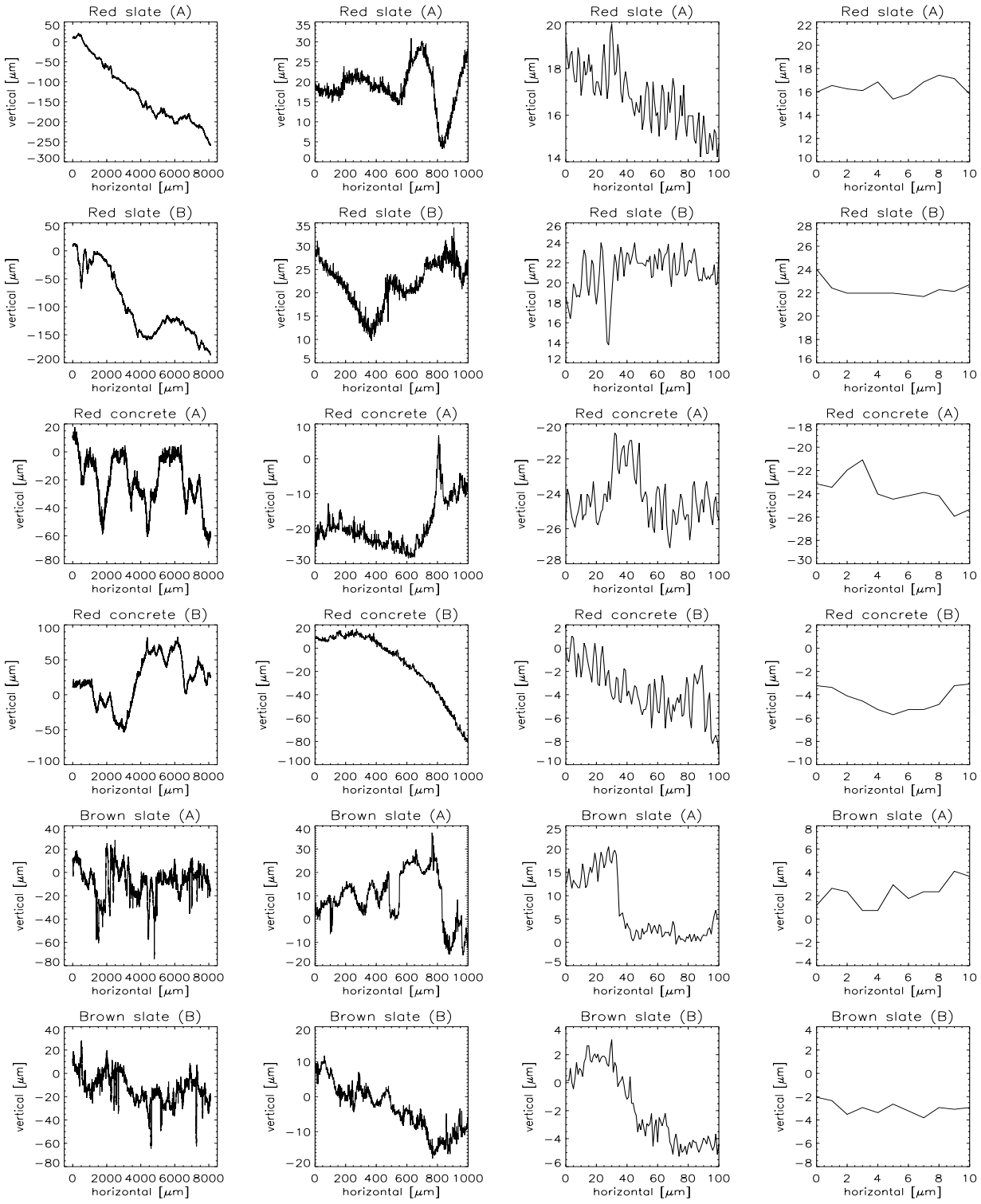

Figure 7.2: Topography data. The left column shows the two profiles of 10 mm length, the second column shows one profile of each measurement series of 1 mm length, the third column shows the central 100 data points of the profile of the previous column, and the right column shows the central 10 data points of the previous column.

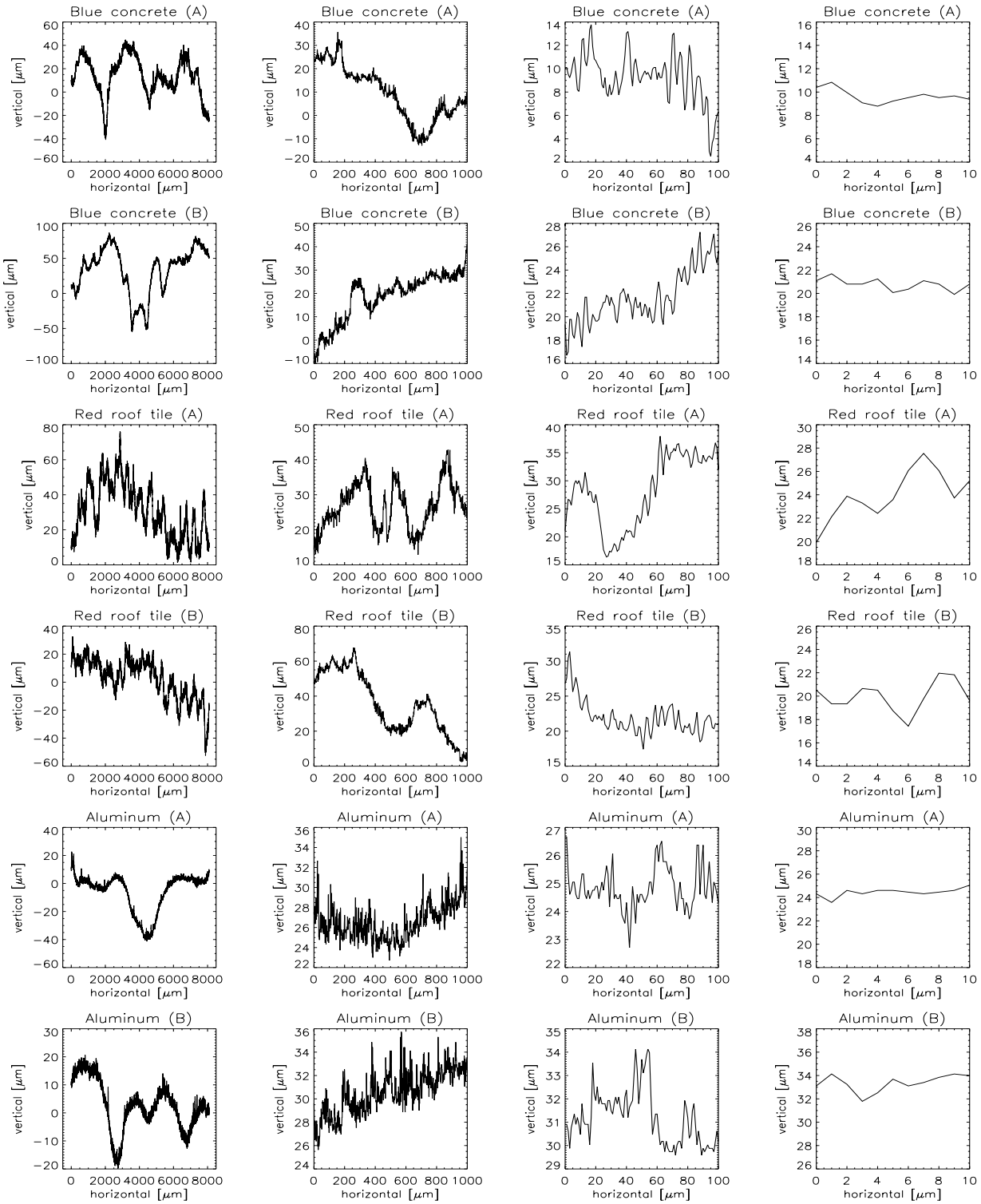

Figure 7.3: Topography data. The left column shows the two profiles of 10 mm length, the second column shows one profile of each measurement series of 1 mm length, the third column shows the central 100 data points of the profile of the previous column, and the right column shows the central 10 data points of the previous column.

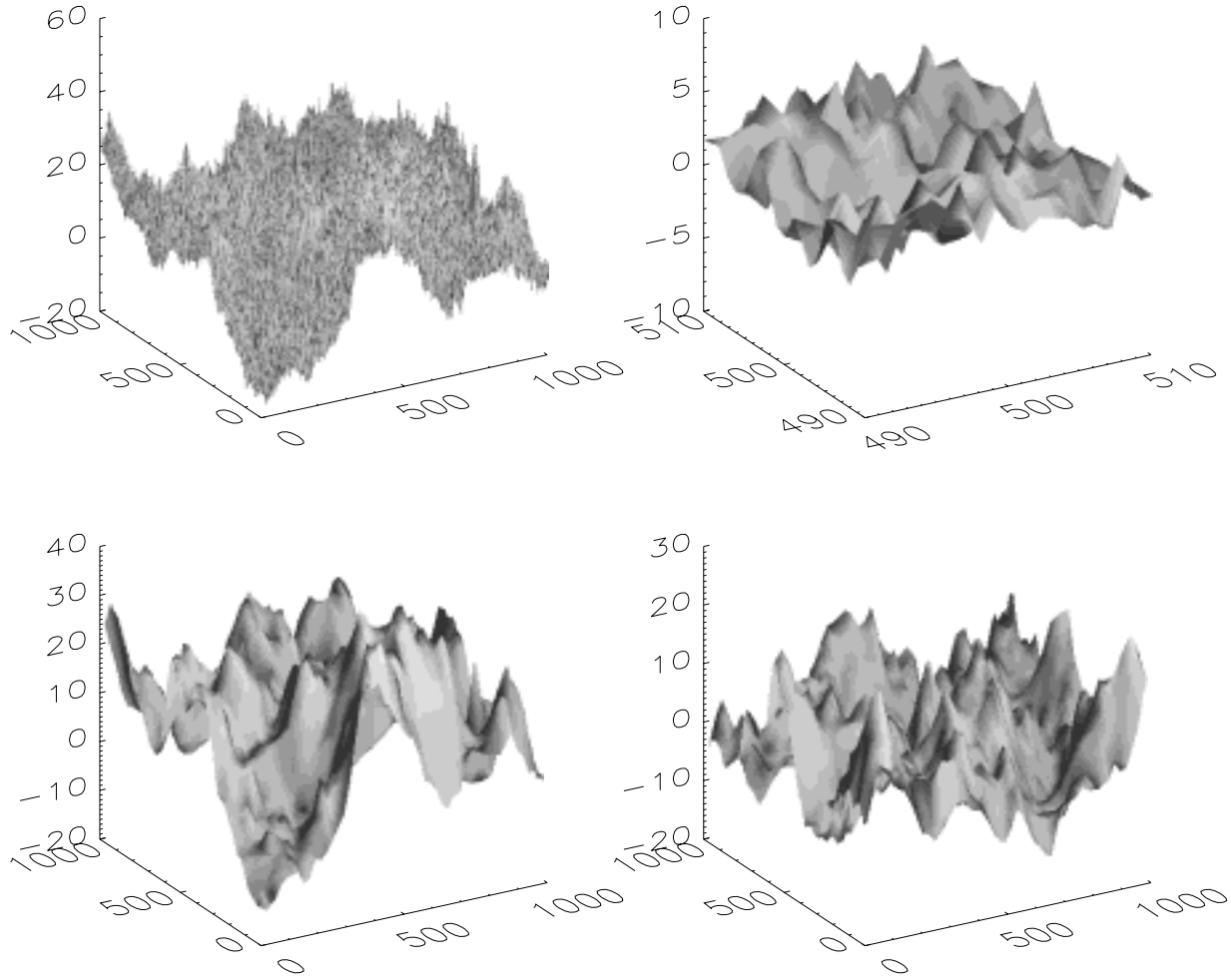

Figure 7.4: Topography data of the sample 'red roof tile'. The first of the original data sets (corrected by a mean plane) of 1000 points x 1000 points is shown at top left. A subset of 20 points x 20 points taken from the center of the sampling area is shown top right. The result of averaging the original data with a bin size of 20 points times 20 points is shown on bottom left. The result after averaging for the second data set is shown bottom right. Note that only for the plot top right the vertical scale is scaled similarly to the horizontal axes.

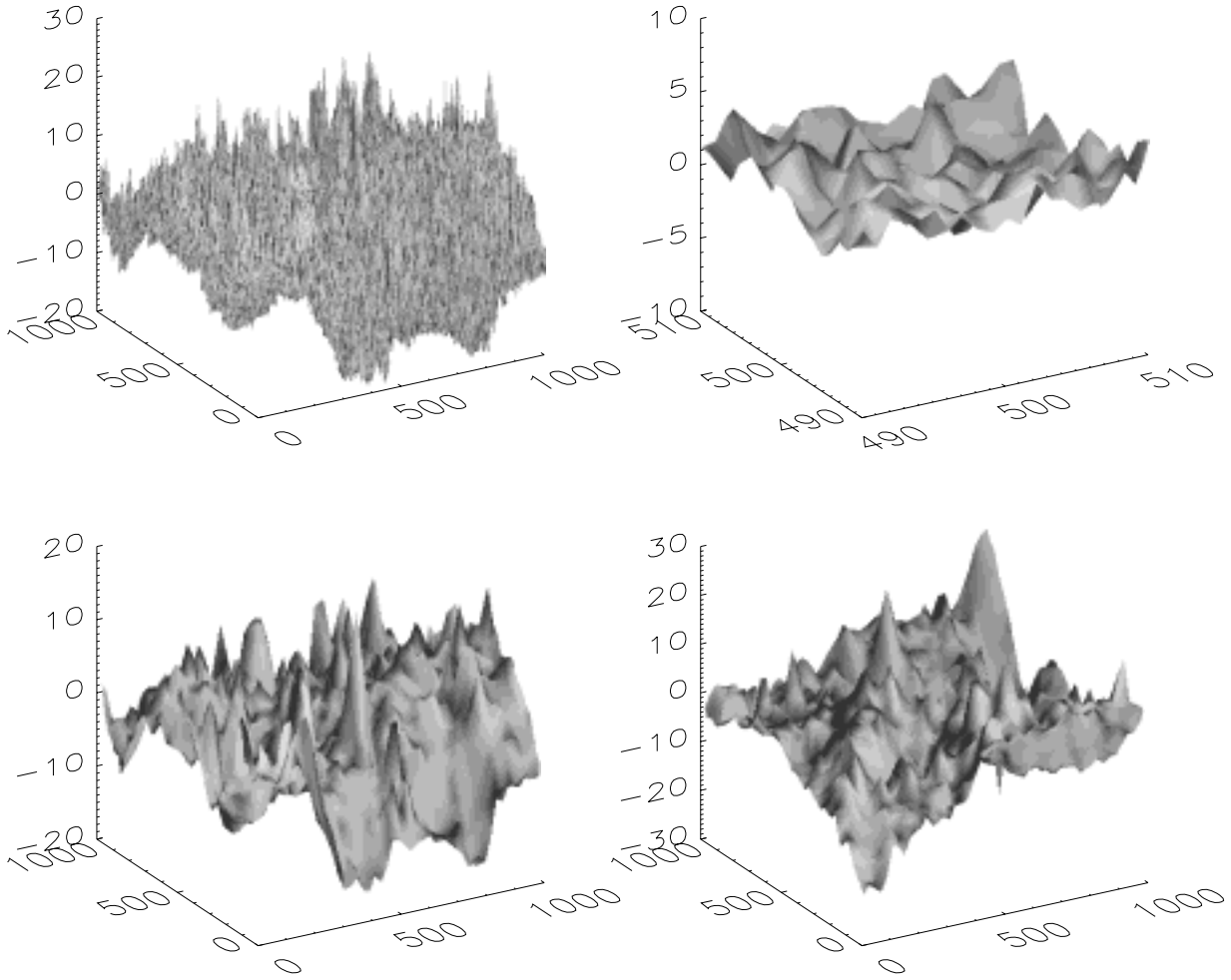

Figure 7.5: Topography data of the sample 'blue concrete'. The first of the original data sets (corrected by a mean plane) of 1000 points x 1000 points is shown at top left. A subset of 20 points x 20 points taken from the center of the sampling area is shown top right. The result of averaging the original data with a bin size of 20 points times 20 points is shown on bottom left. The result after averaging for the second data set is shown bottom right. Note that only for the plot top right the vertical scale is scaled similarly to the horizontal axes.

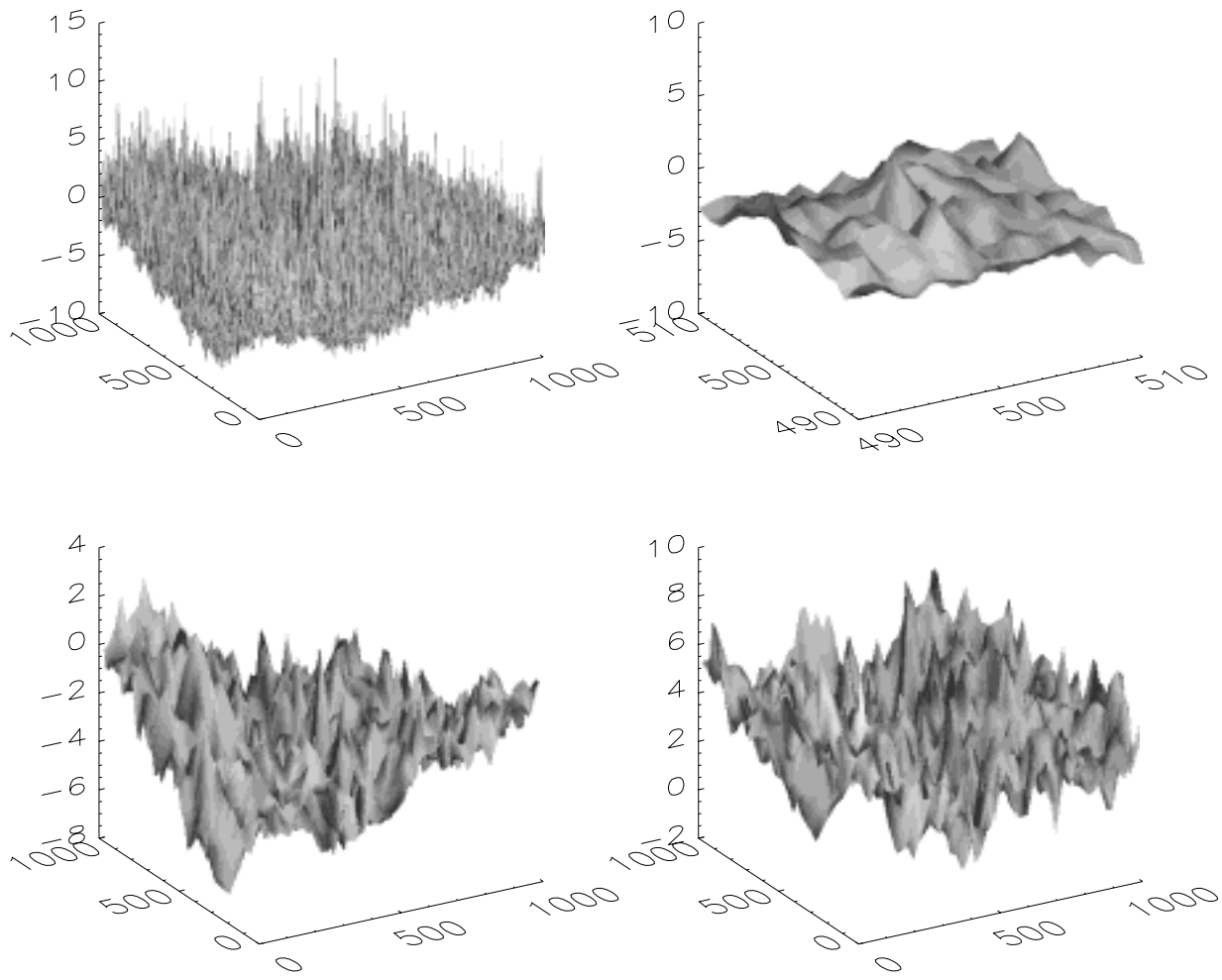

Figure 7.6: Topography data of the sample 'red aluminum'. The first of the original data sets (corrected by a mean plane) of 1000 points x 1000 points is shown at top left. A subset of 20 points x 20 points taken from the center of the sampling area is shown top right. The result of averaging the original data with a bin size of 20 points times 20 points is shown on bottom left. The result after averaging for the second data set is shown bottom right. See chapter 7 for a discussion of the topography measurements. Note that only for the plot top right the vertical scale is scaled similarly to the horizontal axes.

created by a random process, stationary[1] and isotropic in the $x-$ and $y-$direction. (Thomas 1999) suggests to calculate the surface inclination for a 3-D profile as

$$\sigma_\alpha = \sqrt{\frac{1}{(m-1)(n-1)} \sum_{i=2}^{m} \sum_{j=2}^{n} ((\frac{z(i,j) - z(i-1,j)}{\Delta x})^2 + (\frac{(z(i,j) - z(i,j-1)}{\Delta y})^2)} \qquad (7.3)$$

following a recommendation by (Stout et al. 1993). We used eq. 7.3 to compute σ_α for the areal data sets with 1000 neighboring profiles and the method proposed by (Nayak 1971) for the single line data sets of 8091 data points.

- $\sigma_\alpha^{20}[\mathrm{deg}]$, the root mean squared inclination of the surface normal after averaging the surface with a bin size of 20 μm, i.e the 1000×1000 data points were reduced to 50×50 data points.

These values are given in table 7.1, together with the root mean squared inclination of the surface normal derived from the widths of the specular peak of the BRDF measurements presented in chapter 5. We used the widths derived from the ON model (section 5.4), because the ON model assumes cavities of constant diameter, which is equivalent to the constant horizontal resolution of our topography measurements, whereas the TS model assumes a constant length of the facets. σ_α^{SE590} is calculated by (cf. eq. 5.6)

$$(\sigma_\alpha^{SE590})^2 = (\int_0^{\pi/2} \mathrm{e}^{\frac{-\alpha^2}{2k_w^2}} \mathrm{d}\alpha)^{-1} \cdot \int_0^{\pi/2} \alpha^2 \cdot \mathrm{e}^{\frac{-\alpha^2}{2k_w^2}} \mathrm{d}\alpha \qquad (7.4)$$

and σ_α^{ASD} accordingly. We also calculated $\sigma_\alpha^{\gamma'}$, the equivalent of $\sigma_\alpha^{20}[\mathrm{deg}]$ for the following $\gamma'([\mu\mathrm{m}]$: 3, 4, 8, 10, 15, ,30 ,40, 50, 75, 100, 200. We define γ as that γ', where $\sigma_\alpha^{\gamma'}$ agrees best with σ_α^{ASD}. γ can be understood as the spatial dimension over which the light averages the surface topography according to the ON model.

The popular *Rayleigh criterion* (Kraus & Schneider 1988) states that a surface is smooth if the inequality

$$\sigma_z < \frac{\lambda}{8 \cos\theta_i} \qquad (7.5)$$

is fulfilled. The wavelength range of the radiometric sensors of this study extends to 2.4 μm, thus none of the surfaces measured (except plastic) can be considered smooth, i.e. they must be described as rough surfaces.

7.4.2 Comparison of BRDF Parameters and Topography Parameters

The values for the average surface inclination $\sigma_\alpha^{\mathrm{SE590}}$ and $\sigma_\alpha^{\mathrm{ASD}}$ derived from the BRDF model are significantly lower than σ_α derived from the topography data. The reason is that the assumption of specularly reflecting facets requires facets that are much larger than the wavelength of the incoming light. In a model study for water waves, (Brown 1978) suggested to apply geometrical optics only for facet lengths greater than 3 times the wavelength of the incoming light. Averaging with a bin size of 3 μm improved the agreement between $\sigma_\alpha^{\mathrm{ASD}}$ and σ_α considerably, but still average surface inclinations of the topography data is far too low. Thus we averaged the topography data with a bin size of 20 μm, which is considerably larger than the smallest wavelength measured in the BRDF measurements of 0.45 μm. The disagreement between the average inclinations derived from BRDF models and topography data decreases to deviations of 50 % on average. [2] A bin size of 20 μm results in 4 samples agreeing within 25 % ('roof tile Opal', concrete tiles and 'red

[1] 'Stationary' means that the averaged parameters characterizing the surface do not depend on the location where the parameters where measured.

[2] We tried averaging over bin sizes different from 20 μm ($\sigma_\alpha^{\gamma'}$, see above), as well as filtering high topography frequencies through Fourier analysis, but the results did not improve on average.

aluminum'). It is especially disappointing to see that there is not even a strong correlation between $\sigma_\alpha^{\mathrm{ASD}}$, σ_α or σ_α^{20}: although generally, an increase in $\sigma_\alpha^{\mathrm{ASD}}$ is accompanied by an increase in σ_α or σ_α^{20}, there are some exceptions, compare e.g. 'red roof tile' and 'brown slate'. This dashes the hope of finding a common averaging bin sizes fitting better than the 20 μm chosen here.

But because the TS model predicts the shape of the specular peak very well, it is of interest to determine the size of the surface patches that make up the V-cavities (see section 5.3) of the TS model. The actual size of the surface patches is not a parameter in the TS model (eq. 5.1, it is only required that it is much larger than the wavelength of the incident light.) Thus the size of the V-cavity cannot be determined from fitting the TS model to BRDF measurements. **The topography measurements show that the size of the surface patches must be in the 20 μm range.** This is also confirmed by the fact that the width of the specular peak derived from BRDF measurements is relatively independent of wavelength, which is only possible if the size of the scattering structure (the surface patch of the V-cavity in the TS model) is significantly larger than the wavelength of the incident light (varying from 0.425 μm to 2.35 μm for our measurements). Unfortunately, it is not possible to determine a precise number from our data, because the best agreement between σ_α^{ASD} and $\sigma_\alpha^{\gamma'}$ varies from averaging over squares with edges from about 10 nm to 75 nm.

It is possible that the resolution of the RM600 is not appropriate for measuring the surfaces on the scale needed to model the reflection of light. It is open what the actual surface structure on the 1 μm scale could be in the right column of figures 7.2 and 7.3, especially for samples with a very rough structure like e.g. 'red roof tile'. The assumption of a linear profile between each point is possibly strongly simplifying for the data with 1 μm resolution. However, it is very likely that a linear profile is adequate after averaging with a 20 μm bin size.

Another problem might be the diameter of the laser focus of the RM600 of 1 μm. It is very difficult for a system with such a large footprint to determine slopes as large as seen for the sample 'red roof tile'. But again, this should be a minor problem after averaging with a 20 μm bin size, because the average slope decreases significantly.

Thus the most likely reason for the bad agreement between the topography data and the BRDF data is an insufficient theoretical approach. One possible way for further research might be to eliminate areas of the surface that surpass a certain roughness threshold and evaluate the facet inclination only from those parts of the surface that have a roughness that is lower than this threshold.

Maybe there is no one common bin size that is suitable for every surface. Maybe the value of γ indicates the typical size of a facet for the respective sample. Unfortunately, it is not easy to verify this hypothesis. But it is supported by the similar values of γ for the different kinds of materials: for concrete $\gamma \approx 30$, for slate $\gamma \approx 75$, and for baked clay ('red roof tile' and 'Opal tile') $\gamma \approx 10$.

7.4.3 Further Remarks

The quantities root mean square roughness σ_z and the correlation length β usually are not directly used in BRDF models of rough surfaces. We show them here to demonstrate that they are indeed not strongly correlated to the specular peak widths, although an increase in σ_z is often accompanied by an increase in peak width (with e.g. 'roof tile Opal' being a clear exception). The increase of both quantities with horizontal resolution is in qualitative accordance with results from (Sayles & Thomas 1978) and (Thomas & Sayles 1975) for natural as well as man-made surfaces. (Sayles & Thomas 1978) predict an increase of σ_z with the square root of the length of the profile, thus we would expect for the ratio of σ_z of the 10 mm profile to σ_z of the 1 mm profile of $\sqrt{10} \approx 3.2$. The ratios from table 6.1 are given by 1.8, 1.6, 2.4, 3.1, 3.6, 7.1 and 2.6 for the samples 'red roof tile', 'brown slate', 'blue concrete, 'red concrete', 'red slate', 'red aluminum' and 'plastic', resp.

Sample	$\sigma_z[\mu\mathrm{m}]$	$\beta[\mu\mathrm{m}]$	$\sigma_\alpha[\mathrm{deg}]$	$\sigma_\alpha^{20}[\mathrm{deg}]$	$\gamma[\mu\mathrm{m}]$	$\sigma_\alpha^{\gamma}[\mathrm{deg}]$	$\sigma_\alpha^{\mathrm{ASD}}[\mathrm{deg}]$
Red roof tile 1	5.6 ± 0.7	71 ± 18	68.2	10.4	8	15.4	16.1 ± 0.9
Red roof tile 2	7.3 ± 1.3	88 ± 17	68.4	12.4	10	15.7	
Red roof tile 3	11.4 ± 2.6	185 ± 47	66.3	8.0			
Tile Opal 1	3.1 ± 0.6	51 ± 28	63.5	7.4	10	10.4	10.6 ± 0.4
Tile Opal 2	4.0 ± 0.8	75 ± 20	63.3	8.0	10	10.6	
Brown slate 1	9.4 ± 3.3	60 ± 20	68.7	21.9	100	7.5	8.3 ± 0.1
Brown slate 2	6.1 ± 1.8	39 ± 15	66.7	19.4	50	9.5	
Brown slate 3	12.6 ± 2.0	200 ± 98	65.7	7.5			
Red conc. 1	5.9 ± 1.4	> 100	65.7	10.0	30	8.2	8.1 ± 0.2
Red conc. 2	8.9 ± 2.9	> 100	66.0	10.1	75	7.9	
Red conc. 3	23.2 ± 8.8	558 ± 281	63.2	6.1			
Blue conc. 1	5.8 ± 1.7	86 ± 17	64.0	10.3	30	8.3	8.0 ± 0.1
Blue conc. 2	4.8 ± 0.7	83 ± 23	64.1	9.3	30	7.2	
Blue conc.3	12.9 ± 4.7	595 ± 286	62.4	6.2			
Red slate 1	6.8 ± 1.7	91 ± 19	60.3	9.3	75	6.2	6.0 ± 0.3
Red slate 2	5.3 ± 1.6	89 ± 19	59.0	8.0	75	5.6	
Red slate 3	21.6 ± 7.4	> 800	58.0	5.4			
Red alu. 1	1.5 ± 0.2	18 ± 13	54.0	3.7	15	4.8	5.0 ± 0.6
Red alu. 2	1.5 ± 0.3	27 ± 27	53.9	3.7	15	4.8	
Red alu. 3	10.7 ± 4.0	> 800	48.4	5.4			
Plastic 1	0.25 ± 0.05	3 ± 4	19.7	0.5	(≥ 4)	(≤ 2.3)	$(< 2.8 \pm 0.1)$
Plastic 2	0.25 ± 0.10	3 ± 4	18.8	0.6	(≥ 4)	(≤ 2.9)	
Plastic 3	0.65 ± 0.07	622 ± 124	20.2	1.1			

Table 7.1: Topography statistics of the samples. Two measurement series consisting of 1000 parallel profiles were taken for each sample at two different locations on the surface of the sample with a 1 μm spacing interval with 1000 measured points each. They are referred to as '1' and '2'. Another measurement series consisting of only two profiles with a 1.24 μm spacing interval with 8091 measured points each is referred to as '3'. σ_z is the average root mean squared roughness of the surface profile, β is the correlation length, σ_α is the average root mean squared inclination, σ_α^{20} is the same quantity after averaging the profiles over 20 μm. For each quantity the standard deviation is given, computed from the 1000 profiles available for each measurement series. The following two columns show the bin size γ, for which the averaging process resulted in the best agreement with the BRDF data, and the respective value σ_α^{γ}. The last column shows the average root mean squared inclination of the surface patches derived from BRDF measurements of ASDFieldspec, averaged over the wavelength range 450 nm to 700 nm (18 channels) and the standard deviation resulting from the averaging over wavelength. For the SE590 only 4 of the respective values are available: 'red roof tile': 20.0 ± 0.3 ; 'red concrete': 8.8 ± 0.2 ; 'blue concrete': 8.7 ± 0.1 ; 'red aluminum': 4.5 ± 0.2. The samples are arranged in the order of decreasing width of the specular peak as measured by the ASDFieldspec.

Chapter 8

Angular Dependence of the DAEDALUS Sensitivity Function

8.1 Overview

The DAEDALUS AADS 1268 is a multispectral line scanner with 11 spectral channels and 716 pixels per line. This chapter presents a post-flight calibration method to correct the data for dependence of the detector sensitivity on the scanning angle. An area has to be found where only negligible BRDF effects are expected across the principle plane for zenith angles smaller than the maximum scanning angle. The area does not need to be homogenous, but it must extend over a whole scan line. In our case the runway of the Nuremberg airport was chosen. The pixels of the scan line acquired when crossing the runway at right angles were divided by the respective pixels of the overflight parallel to the runway after georegistration. The resulting angular sensitivity functions show variations up to 15 % (depending on channel), similar to findings from a laboratory experiment done 3 years earlier. A comparison with laboratory data from a DAEDALUS scanner operated in Australia shows similar results, except for channels 2 and 8. In order to correct the acquired image data for this effect, simple linear correction functions can be used for each scanning direction (left/right) separately. Some of the results of this chapter have been published in (Meister et al. 1999a).

8.2 Description of the Detector

This thesis is part of a research program to study urban areas by multispectral remote sensing. Several data campaigns were flown in cooperation with DLR (Oberpfaffenhofen) with the DAEDALUS AADS 1268 line scanner.

A scan line from the DAEDALUS scanner contains 716 pixels for each of the 11 spectral channels. The wavelength distribution of the channels is given in table 9.2, channel 11 records the surface brightness temperature and will not be included in this investigation. Channels 1 to 5 cover the visible wavelength band, channels 6 to 10 are in the infrared. Channel 1 is the least reliable channel because of its strong noise.

The maximum scan angle is $\theta_r = 43^\circ$ to both sides. The scan starts at the right when looking from the plane down to the ground, so pixel number 0 corresponds to a scanning direction to the right as seen from the sensor. Each pixel covers an angular range of $2 \times 43^\circ/716 = 0.12^\circ$, ground resolution at a flight height of 300 m is about 0.7 m for nadir. The pixel ground resolution rises with $\cos\theta_r^{-2}$, i.e. at the maximum scan angle the diameter of a pixel has risen to twice its value at nadir. The imagery can be corrected for this panoramic distortion (Wiemker 1996), expanding the number of pixels per line from 716 to 1000 in our case.

	Visibility	Type of Atmosphere	Type of aerosol
Values / Sets	10 KM , 30 KM	US Standard 1976, Mid-latitude summer, Amberg 1997	Rural, Urban

Table 8.1: Parameter sets used to determine angular variation of atmospheric correction

8.2.1 DAEDALUS Error Sources

A detailed description of the reflectance errors resulting from DAEDALUS measurements can be found in Rothkirch et al. (1998). The error σ_R/R associated with a single pixel is estimated to about 11 %, depending on wavelength. This error can be reduced by averaging over homogeneous pixels. However, errors due to miscalibration will persist. Fortunately, these errors can be neglected for BRDF investigations, because for BRDF effects the absolute reflectance is less important than the relative change of reflectance. Excluding effects from inhomogeneous targets and registration problems, we estimate the 'BRDF error' of DAEDALUS data to be about 5 % after correction for the angular sensitivity function, presented below.

8.3 Error from the Atmospheric Correction

To obtain reflectance images from airborne scanner data, the impact of the atmosphere has to be taken into account. Because of the complexity of radiative transfer in the atmosphere, numerical atmospheric transmission codes, such as MODTRAN (Anderson et al. (1995), Smith et al. (1993)) or 6S (Vermote et al. (1997b)) have to be used to correct the measured radiances. Our data are atmospherically corrected using the package SENSAT-5 (Richter (1990), Richter (1992)) which is based on MODTRAN. SENSAT computes the radiances that will be measured for several different reflectance values (R = 0.0, 0.1, 0.3 and 0.6), based on atmospheric input parameters such as visibility, aerosol type, temperature profile etc. Thus a lookup table is created (for each reflectance and all viewing angles), and the radiances measured by the sensor can be converted to reflectances by linear interpolation. A major problem for atmospheric correction is the determination of the atmospheric input parameters. In order to estimate the error of the atmospheric correction for our case, we calculated the atmospheric correction for several different parameter sets (keeping the parameter sets within reasonable limits). The standard deviation of the results will give an estimation of the error of the atmospheric correction.

For our case, we are only interested in the angular deviations, so the radiances calculated by SENSAT were normalized to nadir. The parameter sets are given in table 8.1, the results (averaged over the 12 combinations ($2 \times 3 \times 2 = 12$)from table 8.1) are shown as a function of viewing angle in fig. 8.1 for a reflectance of $R = 0.1$ and in fig. 8.2 for $R = 0.3$. The relative azimuth angle is 68.5° for negative viewing angles and 111.5° for positive viewing angles. These angles were chosen to match the data we will process below. The standard deviations are plotted as error bars. As all results are normalized to nadir, the standard deviations are always zero at nadir. The angular deviations for R = 0.3 are always less than 1 %, so are the standard deviations. The strongest angular deviations occur for R = 0.1 and channel 1: at $\pm 40^\circ$ the radiance predicted by SENSAT is more than 3 % higher than at nadir, the standard deviation is about 2.5 %. The standard deviation decreases strongly for higher channels. Also the angular deviations become smaller, for channels 9 and 10 there is even a small decrease at $\pm 40^\circ$ compared to nadir.

The reflectance of the runway of the Nuremberg airport is about 10 %, see fig. 8.4. This means that for our study, the reflectance error due to uncertainties of the atmospheric correction stemming from the unknown input parameters can be estimated to be about 2.5 % for channel 1 (equal to the standard deviation in fig. 8.1), decreasing for higher channels (1 % for channel 7, 0.2 % for channel 10).

The last two plots of fig. 8.1 are not relevant to the angular correction, however they demonstrate the overall uncertainty of atmospheric correction in case the input parameters are not well known. The first of these

last plots shows the average of the radiances predicted by MODTRAN using all 12 possible combinations of the input parameters from table 8.1 as a function of wavelength. The very last plot shows the relative standard deviations of these radiances. Although the reflected radiance L_r for visible wavelengths is far stronger than in NIR, the standard deviation of L_r decreases from 15 % to 5 %. Fortunately, this high error only needs to be considered when comparing images from different overflights with different atmospheres.

8.4 Angular Sensitivity Function ASF

The angular sensitivity function ASF(θ_r) of the sensor is the ratio of the measured radiance at the viewing angle θ_r (also called *look angle* to the measured radiance at nadir $(\theta_r = 0^\circ)$ assuming a true constant radiance reaching the detector. The biggest obstacle in determining the ASF is providing a homogenous illumination source. If the ASF is constant and if the radiance reaching the detector is independent of scanning direction θ_r, all pixels will give the same value. Volker Amman at the German Aerospace Establishment DLR (Oberpfaffenhofen) has performed such a test in the laboratory in 1994 (private communication), pointing the DAEDALUS into an integrating sphere with a diameter of 2 m. For channels 2 to 9 the difference between maximum and minimum measurement was about 5 %, but almost 20 % for channel 1, see fig.8.5, dashed line. However, it remains open to what extent these measurements are influenced by inhomogeneities of the integrating sphere.

There has been no determination of the ASF immediately prior to the 1997 flight campaign over Nuremberg. Because BRDF effects deduced from the data crucially depend on the ASF, we present a method to derive the ASF from our image data. As the instrument was reconditioned since 1994, the ASF as determined by the DLR is significantly different from the 1997 ASF for some channels.

8.5 ASF Determination Method

8.5.1 General Outline

In principle, the ASF can simply be determined from a scan line over a spatially homogeneous target. In practice, it is almost impossible to find targets with the required homogeneity in urban areas. Urban areas are characterized by a high spatial variance of reflectance. In order to accommodate for this effect, we divided a scanning line that was obtained crossing the runway of the Nuremberg airport by the georegistered data of an overflight along the runway, see fig. 8.3. For a lambertian surface and a constant ASF, the expected result is 1 for all pixels. This procedure is only possible when there is at least one pair of flight tracks perpendicular to each other and the calibration area is seen from both tracks. This means that unfortunately this method is not applicable to the image data of our group from previous years, as all the flight tracks from previous years are parallel. In case the BRDF of the calibration area chosen is not known, it is furthermore necessary to use scans perpendicular to the sun azimuth, in order to avoid specular or hot spot effects (see chapter 5). Although the strongest BRDF effects are expected in the principal plane, across the principal plane BRDF effects are possible too. However, these effects are symmetric with respect to nadir ($\theta_r = 0^\circ$) if the calibration area is rotationally symmetric. Symmetric ASF effects cannot be detected by our procedure if the BRDF of the surface is unknown.

8.5.2 Choice of Calibration Area

The best suited surface in our data is the runway of the airport Nuremberg for the following reasons:

- BRDF effects of the surface (asphalt) across the principle plane in the angular range covered by DAEDALUS (maximum scan angle: 43°) are small. The sun angle of $\theta_i = 40^\circ$ ensures that there

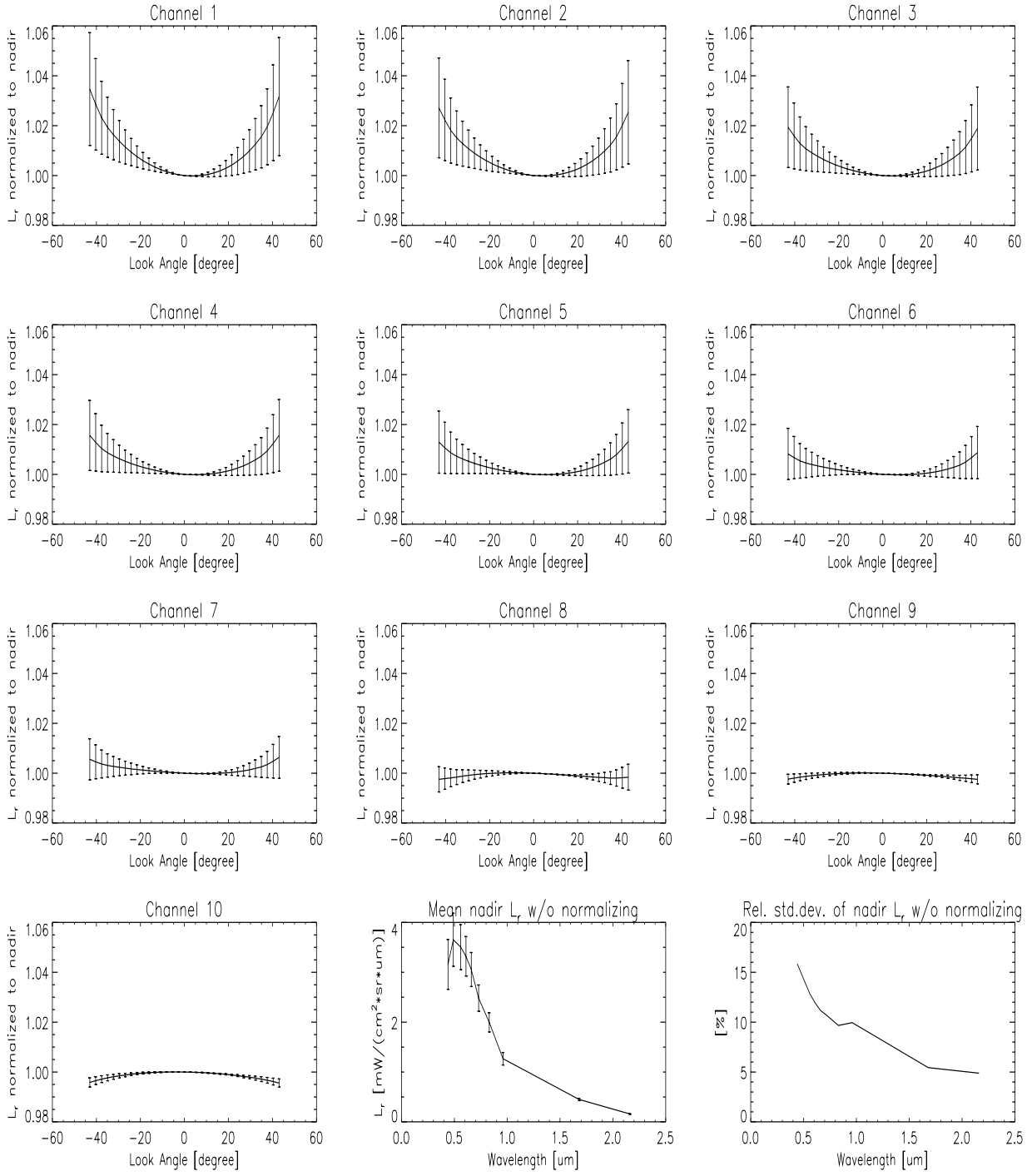

Figure 8.1: Standard deviation of the MODTRAN atmospheric correction normalized to nadir for R =0.1 using all 12 combinations of the parameter sets from table 8.1. The standard deviations vary from 2.5 % for channel 1 to 0.2 % for channel 10. The last two plots show the average of the 12 radiances predicted by MODTRAN without normalizing and the relative standard deviations without normalizing) as a function of wavelength.

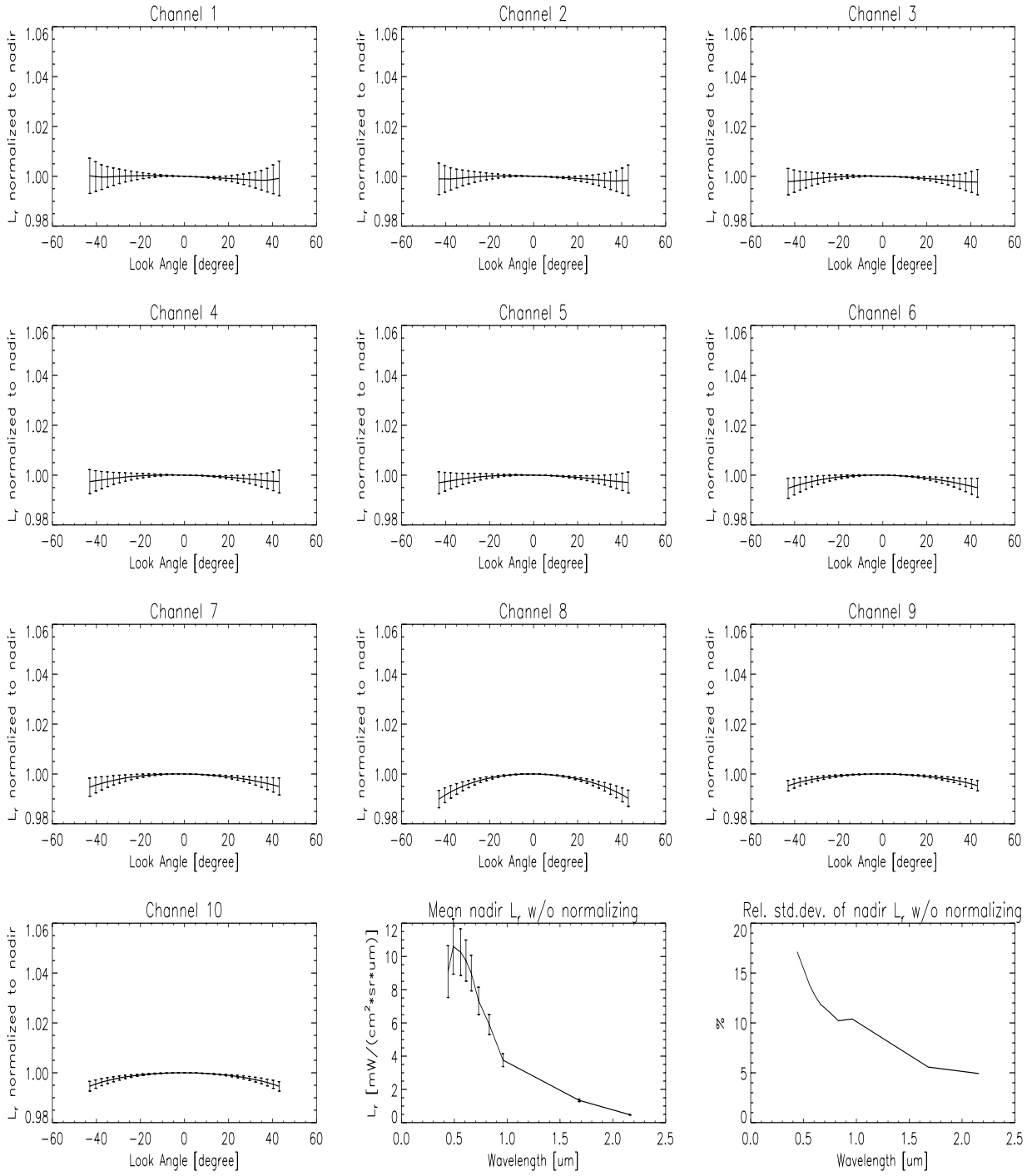

Figure 8.2: Standard deviation of the MODTRAN atmospheric correction for $R = 0.3$. The standard deviations are always less than 1 %, much smaller than in the case of R =0.1, see fig. 8.1. The last two plots show the average of the 12 radiances predicted by MODTRAN without normalizing and the relative standard deviations without normalizing as a function of wavelength.

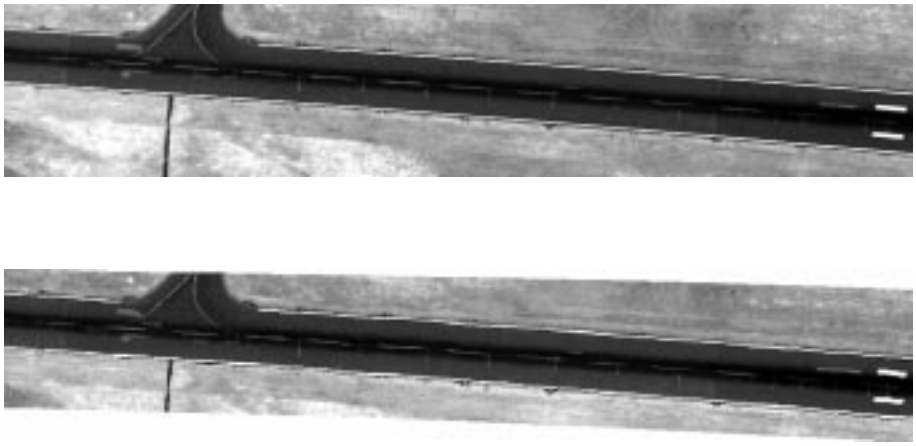

Figure 8.3: These pictures show the area chosen for ASF determination, a runway of the Nuremberg airport. The reflectance image of DAEDALUS channel 7 is plotted. The upper picture shows the cross-runway scan, the lower picture shows the along-runway scan after registration to the above picture.

are neither effects from a broad hot spot or a broad specular peak that might be expected for a sun positioned in nadir, nor will there be any strong BRDF effects that typically occur for zenith angles larger than 60° (note that the BRDF variations for the sample 'asphalt' in chapter 5 (fig. 5.10, page 55) increase with θ_i). The relative angle of the scan direction to the sun azimuth is 68.5° for the scan to the left and 111.5° for the scan to the right. So the relative angle is only 21.5° smaller resp. bigger than 90° corresponding to the direction across the principal plane.

- The area stretches from the very left of the DAEDALUS scan to the very right, so that almost all pixels can be included in the investigation. Only those pixels containing the white strip on the right of the picture have to be excluded.
- The reflectance profile of the area is quite homogeneous, although deviations of up to 20 % occur, see the profile shown in fig. 8.4.
- The width of the runway is about 50 pixels. Thus averaging over the width will dismiss random sensor noise to a large amount. Small scale inhomogeneities will also be smoothed after averaging. The 2 bright white stripes on the right in fig. 8.3 were excluded for our analysis.
- Small landmarks on the side of the runway allow a very exact registration of the along-runway scan onto the cross-runway scan. The registration accuracy is estimated to be about one pixel.
- A change in reflectance that occurred between the cross-runway scan and the along-runway scan is highly unlikely, in contrast to e.g. streets highly frequented by cars.

In the laboratory measurements of chapter 5, the sample 'asphalt' showed a very lambertian BRDF across the principal plane (see fig. 5.10, $\theta_i = 30^\circ, \varphi = 90^\circ$ and $\theta_i = 50^\circ, \varphi = 90^\circ$, the angular combination of the DAEDALUS flight track is about $\theta_i = 40^\circ, \varphi = 70^\circ/110^\circ$). Although the asphalt of the laboratory measurement might be different from the asphalt on the Nuremberg runway, the laboratory measurements support the choice of an asphalt surface as calibration area.

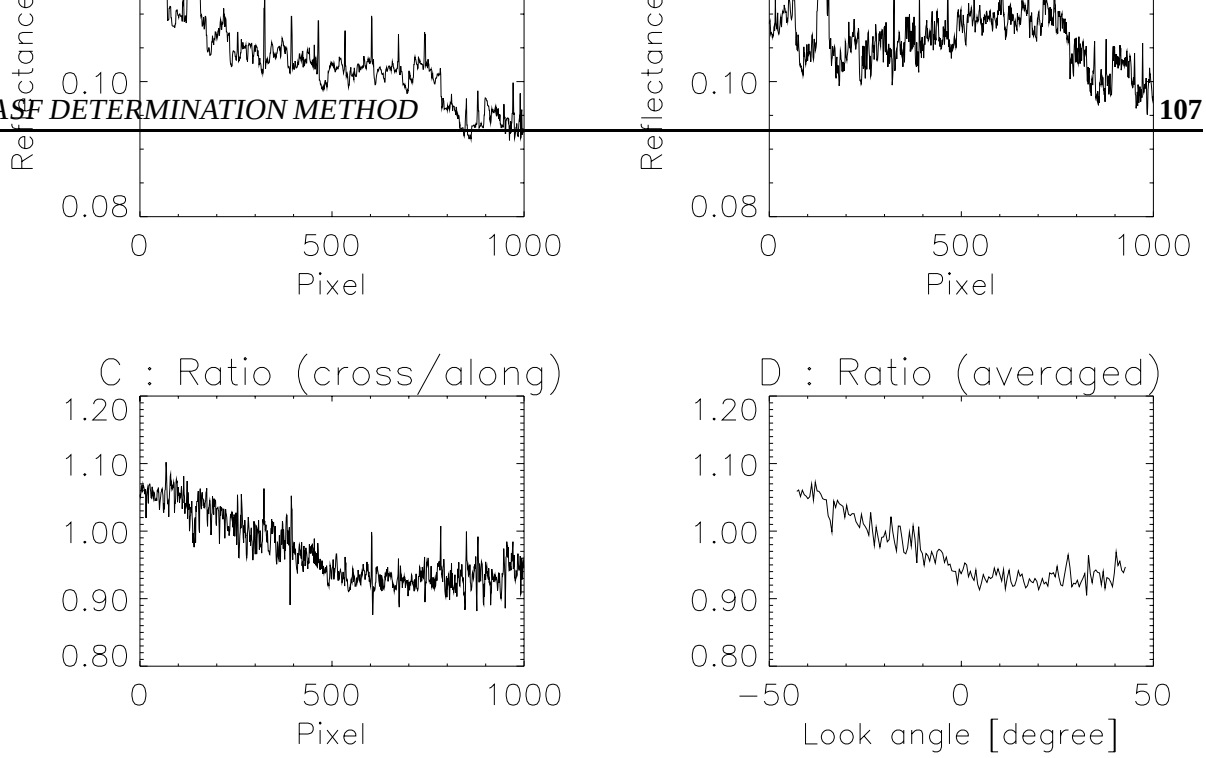

Figure 8.4: The upper plots show the reflectance of the runway in channel 7 as a function of pixel number. The original amount of 716 pixels increased to 1000 after the panoramic distortion was removed. The upper left plot (A) shows the profile from the cross-runway scan, the upper right picture (B) shows the profile of the along-runway scan after registration (cf. fig. 8.3). Plot C is the ratio of A and B. Most of the characteristic changes from plots A and B disappeared. The remaining high frequency changes can largely be attributed to the registration accuracy (estimated to be about 1 pixel). Registration errors can be identified as deviations that are immediately followed by a deviation with reversed sign. After mapping the 1000 panoramic pixels back to the 716 DAEDALUS pixels and averaging over 4 pixels, these effects are removed too, see plot D. D shows the ASF as a function of DAEDALUS look angle.

8.5.3 ASF Calculation

To obtain the ASF, the steps described below were performed. As image data, we did not use raw data but reflectance images, because the reflectance images have been processed by Rothkirch et al. (1998) with MODTRAN to eliminate atmospheric effects.

1. Correct the images for panoramic distortion. Register the along-runway scan image to the cross-runway scan image (see fig. 8.3).

2. Average the values over the width of the runway for both images. The results are shown in fig. 8.4, plots A and B.

3. Divide the cross-runway scan by the along-runway scan. The ratio gives the ASF and is shown in fig. 8.4, plots C and D for channel 7, and in fig. 8.5 for all channels (solid line).

4. Normalize the results to the nadir value.

For a lambertian surface, the ratio averaged over all angles should equal 1. But in the principal plane, the surface is not lambertian, as can be seen from a cross-runway scan acquired in the morning (not shown). This means, that the average of the ratio will depend on the scan angle of the runway in the along-runway scan. However, this is not a problem here because we are not determining an absolute ASF but a relative ASF, therefore we can normalize our results without loosing information.

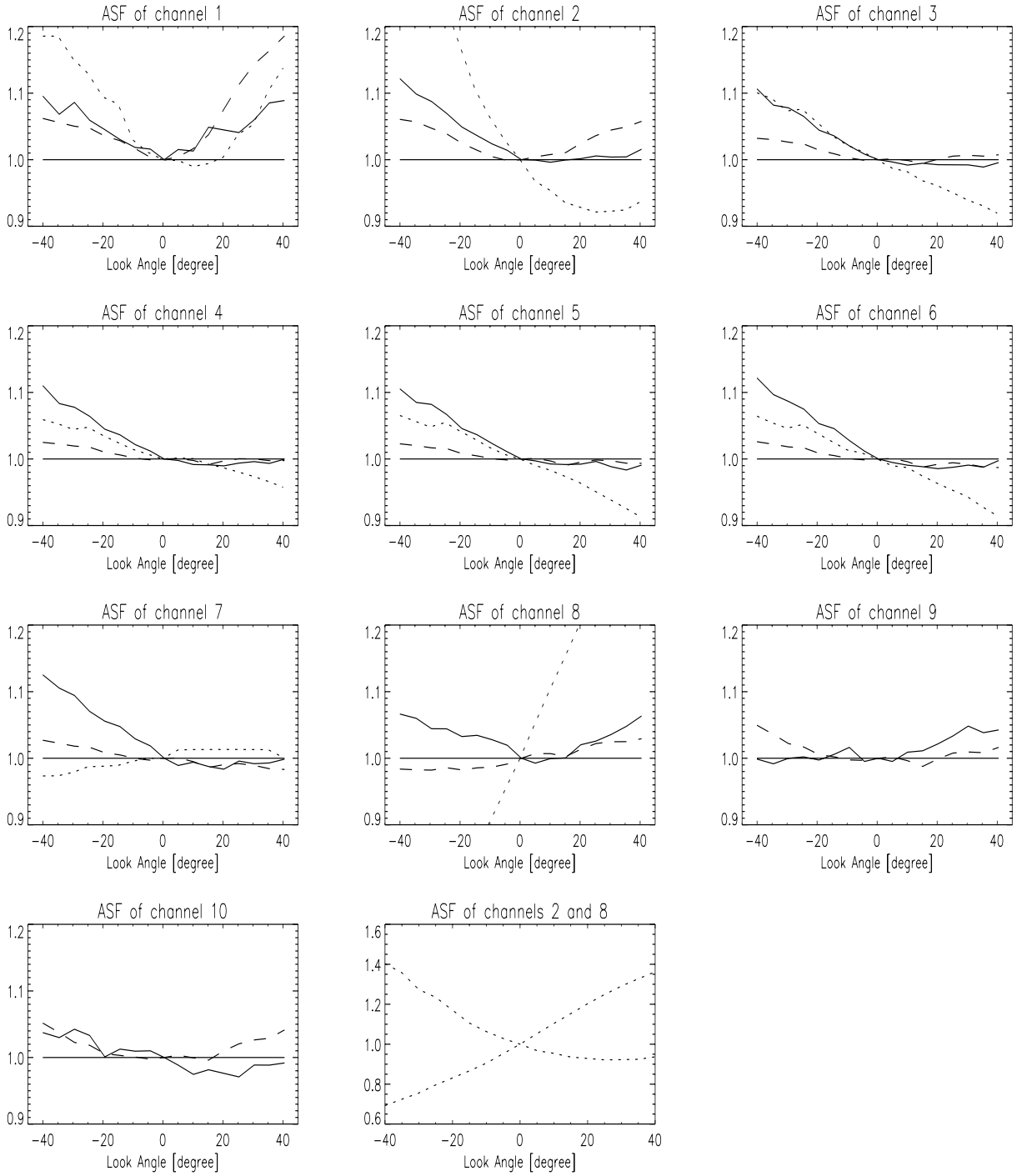

Figure 8.5: The ASF for the first 10 DAEDALUS channels as a function of DAEDALUS look angle, normalized to nadir and averaged to intervals of 5 degrees. Negative look angles correspond to the right direction as seen from the DAEDALUS. Solid line is the ASF determined from the Nuremberg image data, dashed line is the ASF determined by DLR laboratory measurements. Dotted line is the ASF determined by laboratory measurements for the DAEDALUS operated in Australia (available only for channels 1 to 8). The last plot shows the ASF for channels 2 and 8 for the Australian DAEDALUS with an enlarged vertical plotting range.

8.6 Results and Discussion

A possible reason for a non-uniformity of the ASF is a slight misadjustment of the scanner optics. If the ray alignment between rotating mirror and primary paraboloid is not perfect, a non-uniform ASF is possible.

The ASF averaged over 7 pixels are shown as a function of viewing angle in fig. 8.6. There is a uniform characteristic of channels 2 to 7: at angles about $-40°$ the ASF is about 12 % higher than at nadir, for positive scan angles it is quite constant. The rise with negative zenith angles looks very linear. Channel 1 shows a rise (about 10 %) with both positive and negative angles. The same behavior can be seen in channel 8, but at $\pm 40°$ the rise is only 7 % above the nadir value. The sensitivity of channel 9 rises a little towards increasing zenith angles, the sensitivity of channel 10 rises for negative zenith angles (each about 5 %).

An ASF laboratory measurement (directing the DAEDALUS FOV into an integrating sphere) performed by the DLR in 1994 shows similar results, but the angular deviations are only about 5 % (exception: channel 1 with 20 %), see dashed line in fig.8.5. The spectral behavior looks very similar for channels 3 to 7. But channel 2 rises for positive angles, channel 8 does not rise for negative angles, channel 9 rises with negative zenith angles and channel 10 rises symmetrically about nadir, in contrary to our findings. We do expect changes between the 1994 DLR data and our results from August 1997, because the scanner was overhauled and readjusted in early 1997.

ASF measurements for another DAEDALUS AADS 1268 were made in Australia for channels 1 to 8. The DAEDALUS was placed in front of a light source and turned to obtain different look angles. The results are shown in fig. 8.5 as a dotted line. Channels 3 to 6 are quite similar in shape to our measurements, there is a rise for negative angles of about 10 to 20 %. Channel 2 shows a rise of 40 % for negative zenith angles, for channel 8 the value at $40°$ is almost twice as high as the value at $-40°$. The shape of the ASF for channel 1 is similar to the ASF from the DAEDALUS operated by DLR, but the rise for negative zenith angles is twice as strong. Except for channel 2, these results are confirmed by flight data over a desert area from the previous year (not shown).

This shows that the results derived from the Nuremberg image data are of the same order of magnitude as results from other groups, obtained by different methods. Our method has the advantage of determining the ASF after takeoff right after (or before) the actual image data are acquired. Thus vibrations during takeoff or landing which may lead to a change of the ray alignment in the DAEDALUS are not a problem. Furthermore we do not have to provide a constant light source in the laboratory.

There are several possible error sources for our method: imprecise atmospheric correction, sensor noise, registration errors, rapid illumination variations during data take and surface BRDF effects. Varying the atmosphere parameters within reasonable limits, we estimate the first error source to be about 2 %, see chapter 8.3. Registration errors can be neglected due to the easy registration of the runway and the averaging over an area of 2000 pixels, the same is true for sensor noise. Presumably BRDF effects of the asphalt of the Nuremberg runway are small, from a comparison with the BRDF measurements of the sample 'asphalt' of chapter 5 (see fig. 5.10, page 55) we estimate the error from the Lambertian assumption to 3 %. Assuming the illumination variations to be 2 %, error propagation leads to an overall error of about 4 % in the ASF.

The results of our method can be confirmed (or improved) if immediately after the cross-runway scan of the test area another cross-runway scan heading into the reverse direction is performed (in our case heading north instead of heading south). Unfortunately, during our campaign no such flights were performed.

8.7 Angular Correction of the DAEDALUS Data

The DAEDALUS data are calibrated by the DLR with an integrating sphere of known radiance. The calibration is performed using the average of the pixels in the center (numbered 355 to 361, leftmost pixel equals 1). Therefore, to correct the DAEDALUS reflectance data with the ASF, we must divide the data by the ASF

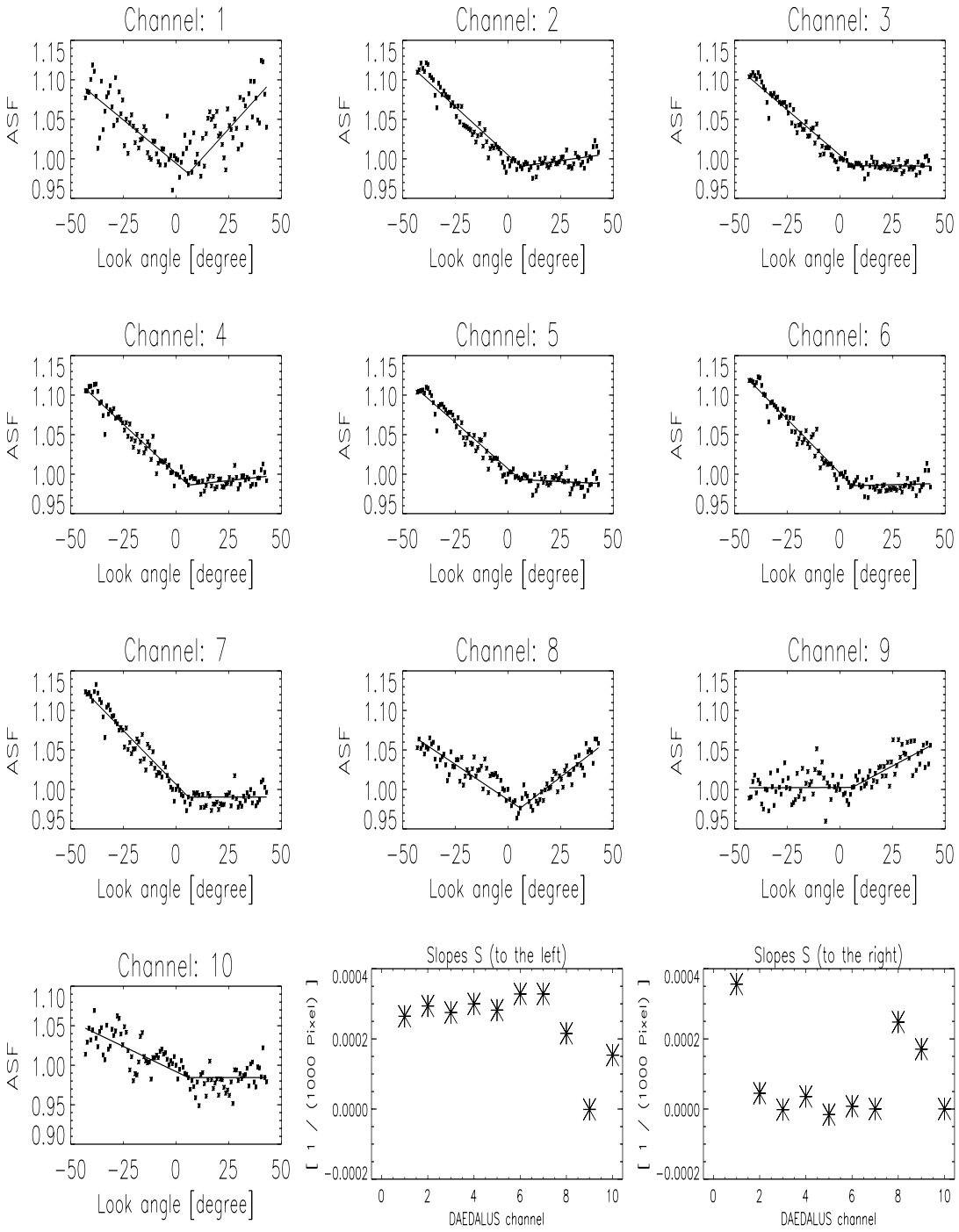

Figure 8.6: The ASF for the first 10 DAEDALUS channels as a function of DAEDALUS look angle, normalized to nadir and averaged over only 7 pixels. Negative look angles correspond to the right direction as seen from the DAEDALUS. The points are measured values, the straight lines are the best fits (see chapter 8.7). The last two plots show the values of the slopes S to the left resp. right from table 8.2.

and multiply the result with the average of the ASF of the pixels 355 to 361:

$$R^{\mathrm{corrected}}(x,y) = R^{\mathrm{DLR-calib.}}(x,y) \cdot \frac{ASF^{\mathrm{center}}}{ASF(x)} \tag{8.1}$$
$$x = \mathrm{row}, y = \mathrm{line}, ASF^{\mathrm{center}} \equiv \frac{1}{7}\sum_{x=355}^{361} ASF(x)$$

As can be seen from fig. 8.5, there is still some noise (about 2 %) in the ASF. In order to avoid superimposing this noise on all the data, we fitted straight lines to the ASFs (least squares method), two for each channel: one going to the left, the other one going to the right. The starting pixel for the lines was determined by computing the χ^2 values using every pixel (one after another) as a starting pixel. The smallest χ^2 (summed over all channels) was obtained for pixel # 410 (we assigned # 1 to the first pixel, not #0 as many computer languages do). The slope of the fitted lines is given in table 8.2 on page 111. The offset is equal to the ASF value at pixel # 410. The equation for evaluating the ASF for each channel is

$$ASF(x) = h + (410 - x) \cdot S_{\mathrm{left}} \text{ if } x \leq 410 \tag{8.2}$$
$$ASF(x) = h + (x - 410) \cdot S_{\mathrm{right}} \text{ if } x > 410$$

where x is the 'image row' or '# of pixel'. The offset h and the slopes $S_{\mathrm{left}}, S_{,\mathrm{right}}$ are given in table 8.2 on page 111 and are plotted in fig. 8.6 in the last two plots. It can be seen that the ASF does not vary much for channels 2 to 7.

Channel	S_{left} [(1000 Pixel)$^{-1}$]	S_{right} [(1000 Pixel)$^{-1}$]	Offset h	χ^2/d_f
1	0.265	0.356	0.981	0.7
2	0.294	0.045	0.991	1.0
3	0.275	-0.002	0.991	0.7
4	0.300	0.036	0.986	0.8
5	0.282	-0.016	0.993	0.7
6	-0.016	0.008	0.985	0.8
7	0.328	0.000	0.990	1.2
8	0.216	0.248	0.976	0.4
9	-0.001	0.171	1.00	0.6
10	0.154	0.000	0.984	0.7

Table 8.2: Slopes and offsets for the straight lines describing the ASF, see eq. 8.2.

The table also shows χ^2/d_f for each channel. It is always lower than the acceptance threshold, which is 1.4 in this case. This means it is possible to describe the ASF in each channel with two straight lines. As we do not exactly know the physical reasons for the non-uniformity of the ASF, we cannot claim that describing the ASF by two straight lines is the best solution. However, the low χ^2 values indicate that we found a reasonable way to recalibrate our data. This function was used in the studies of chapter 9 and Meister et al. (1999b).

The angular recalibration should take place *before* the calibration by ground truth measurements. In case the ground reference targets are measured by DAEDALUS close to nadir, the recalibration can also be performed *after* the calibration by ground truth measurements. In principle, an angular correction should be done *before* the atmospheric correction. In our case, the atmospheric correction (MODTRAN) is quite linear with respect to small (about 10 %) changes in radiance, so the angular recalibration can also be done *after* the atmospheric correction.

Chapter 9

Large Scale Bidirectional Reflectance Model for Urban Areas

9.1 Abstract

A BRDF model for urban areas for pixel-sizes of more than 500 m x 500 m is developed. Possible applications include albedo calculation, improvement of classification and change detection algorithms, simulated global BRDF maps and refinement of atmospheric correction algorithms. The model combines the BRDF effects at several scales (street grid, intermediate sized objects, microscale). We present modeling results as well as a comparison with measured data. The basic features of the urban BRDF are the hotspot and the independence of its shape from wavelength in the range 450 nm $\leq \lambda \leq$ 2300 nm. An index proposed recently by (Sandmeier & Itten 1999) called NDAX promises great benefits in the identification of urban areas in global multiangular data sets. An analytical function that approximates the model is proposed for easy implementation and fast computation. The main idea of the model is to combine results of the previous chapters on the small scale BRDF of man made surfaces with the large scale geometric structure of streets. The measured data presented in this chapter have been published in (Meister et al. 1999b).

9.2 Basic Model Idea

In chapter 5 we have demonstrated that geometric reflection provides a robust description of BRDF of rough surfaces. In particular, (Torrance & Sparrow 1967) and (Oren & Nayar 1995) have approximated rough surfaces successfully by cavity type structures. We have extended this approach and developed a geometrical 'street structure', which simulates reflection and shadowing in urban areas. Our motivation is to provide a model for inclusion of urban BRDF effects in algorithms for global monitoring through satellite sensors like MODIS (Wanner et al. 1997), MISR (Diner et al. 1991), POLDER (Leroy et al. 1997) and MERIS (Bezy & Gourmelon 1999) with pixel-diameters in the km range. So far such algorithms only include BRDF effects of vegetated and bare soil areas (Hu et al. 1997), (Strugnell et al. 1998).

9.3 Street Structure

The core of our BRDF model is built upon the street structure shown in fig. 9.1. The urban area is modeled as a superposition of street structures heading into different directions. This superposition will be called city structure. It is impossible to physically realize such a city structure, for the same reasons as in the cavity model by (Torrance & Sparrow 1967), see the discussion in section 5.3, page 45.

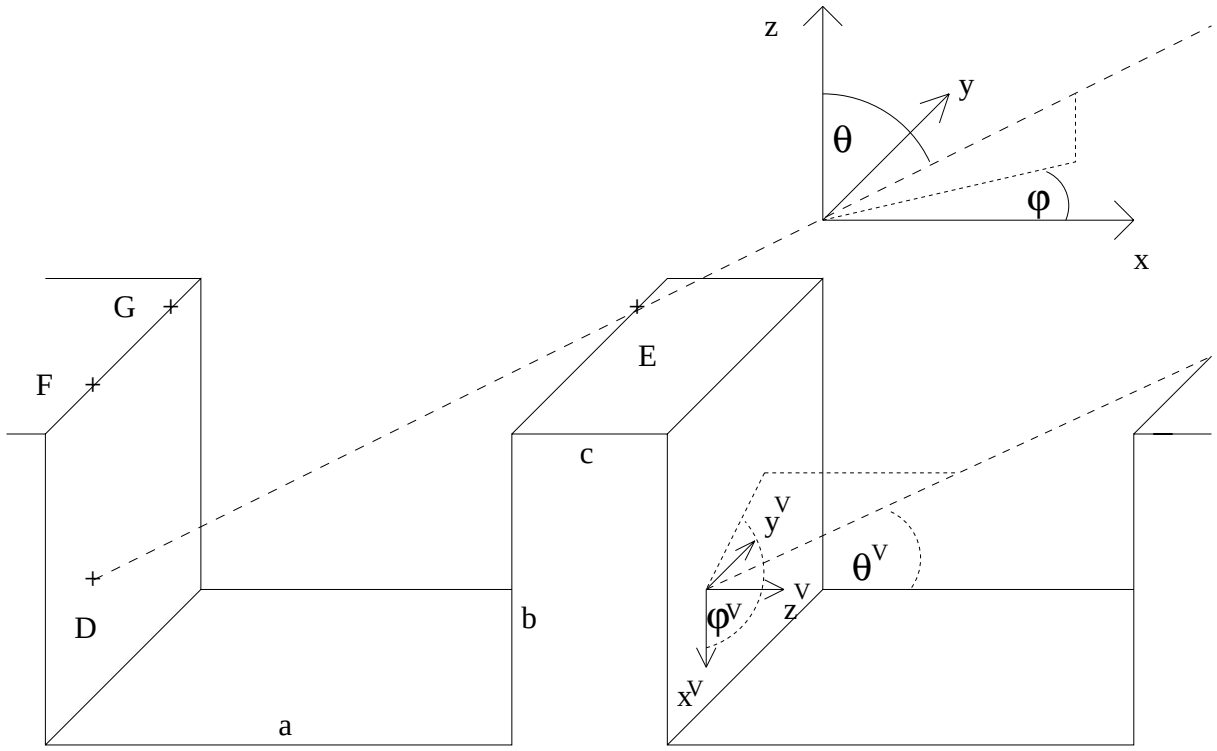

Figure 9.1: Sketch of the street structure. 'a' defines the width of the street, 'b' the height of the buildings and 'c' the width of the roofs. Capital letters denote points referred to in the text. The dotted line denotes either a ray of light (in this case point 'D' is the lowest illuminated point on the vertical area) or a line of viewing (in this case point 'D' is the lowest point visible to the sensor). The coordinate system up right defines the zenith (θ) and azimuth (φ) angles of incidence and reflection with respect to the surface of the earth. The turned coordinate system (x^V, y^V,z^V, bottom right) defines these angles with respect to the left vertical area (see section 9.4.2).

The *street structure* as defined here consists of a street with width a and buildings of height b bordering the street, the roofs (width c) of the buildings are assumed to be flat. The influence of inclined roofs will be considered later, see section 9.6.2. The street structure is straight and indefinitely long. This approach is similar to the approach used by (Torrance & Sparrow 1967) and (Oren & Nayar 1995) who modeled the BRDF of rough surfaces assuming the surface to consist of specular resp. Lambertian indefinitely long V-cavities. In this chapter, a pixel of an urban area is modeled by the reflection from an array of street structures. Although this is a physically impossible city (because of the neglect of crossings between streets that are not parallel) the basic structure of a city relevant for BRDF effects is captured by this model.

In addition to this large scale structure, modeling on a *smaller scale* is also needed. We assume that objects are placed on every surface (roof surface, wall surface or street surface). These objects are significantly smaller than the surface itself. Later on we will assign an average BRDF to each facet of the resulting profile. This average BRDF is the result of a combination of BRDF measurements of several surfaces typical for urban areas. All these effects are combined to yield the overall urban BRDF, see below.

The street structure can be described by 3 parameters in our model, see fig. 9.1:

- the width of the street itself ('a')
- the height of the bordering buildings ('b')
- and the width of the buildings (roofs) ('c')

Openings between buildings *alongside* the street are ignored. Extended courtyards between buildings are being treated as street areas in the model, and thus are included to first order. The street is supposed to have a length greater than the diameter of the field of view of the sensor (or 'infinite length'), which is equivalent to neglecting the implications of the ending of a street.

For deriving geometric optical BRDF effects, it is sufficient to model the relative size of the structure (Jupp & Strahler 1991). Thus we can require the width parameters to sum to one:

$$a + c = 1 \tag{9.1}$$

which reduces the number of parameters to two ('a' and 'b', $a \in [0, 1], b \in [0, \infty]$). a, b and c are dimensionless because they only model the relative size.

The main advantages of this simple structure are the low number of parameters and the straightforward application of geometrical optics (see below). As mentioned above, the structure not only describes two buildings separated by a street, but also two buildings separated by e.g. a backyard. I.e., a building doesn't need to be bordered by a street on each side, our structure also describes the common feature of blocks of houses surrounding a backyard (neglecting the 'edge' effects produced by the corners of the backyard, see above). The parameters a, b and c should be chosen in such a way that they describe the *average* structure of the urban area under investigation.

Our coordinate system is oriented in such a way that the street is running parallel to the y-axis and perpendicular to the x-axis, see fig. 9.1. This means that at a viewing azimuth angle of $\varphi_r = 0^\circ$ a sensor is viewing the structure perpendicular to the direction of the street and from the right in fig. 9.1, at $\varphi_r = 180^\circ$ from the left. The reader views fig. 9.1 from about $\varphi_r = 300^\circ$.

9.4 Application of Geometrical Optics to the Street Structure

The BRDF arising from the street structure strongly depends on the amount of shadow present in the viewed area. Because of the simplicity of the street structure (shown in fig. 9.1) it is straightforward to calculate the viewed and shadowed proportions using geometrical optics. To further simplify our approach, we will assume that all components (roofs, streets and walls) have the *same color*. Although this is a very unrealistic assumption, in practice it will hardly be possible to determine universal values for the different component colors. This can only be done if specific knowledge about the city under investigation is available (e.g. all roofs in this city are red). In case the component colors are known, they can easily be integrated into our model by replacing the correct values for the albedo ρ in eqs. 9.3, 9.9, 9.10 and 9.17 below.

9.4.1 Top Horizontal Areas

For all illumination and viewing angles, the whole 'roof' area (width 'c') will always be fully illuminated and viewed. In our simplified model all buildings have the same height. Therefore shadowing of low buildings by tall buildings does not occur. For now, we will assume that the roof area reflects like a Lambertian surface (small scale BRDF effects will be introduced later). Lambertian surfaces reflect a constant radiance in all directions proportional to the albedo ρ (dimensionless) and the incoming irradiance $E_i(\theta_i) = E_i(\theta_i = 0^\circ) \cdot \cos\theta_i$ if the area covered by the sensor is smaller than the total area of the illuminated surface. In this

case, the radiance reflected by all roofs from within one pixel (denoted L_r^c, the letter 'c' refers to the width of the roof) is

$$L_r^c = c \cdot \frac{\rho}{\pi} \cdot E_i(\theta_i) \qquad [\mathrm{W} \cdot \mathrm{m}^{-2} \cdot \mathrm{sr}^{-1} \cdot \mu\mathrm{m}^{-1}] \tag{9.2}$$

(the unit $\mu\mathrm{m}^{-1}$ is caused by the spectral definition of the radiance (radiance per wavelength), π has the unit [sr] as in (Nicodemus et al. 1977)). But for now, we only model a single street structure that is considerably smaller than the sensor's field of view. Thus we have to multiply eq. 9.2 by the ratio of the area of the street structure and the area of the field of view (FOV) of the sensor. If the area covered by the FOV of the sensor looking from nadir equals A_0, its area increases with viewing zenith angle as $A_0 / \cos\theta_r$. Assuming the street structure covers an area A_S, the radiance reflected by the top horizontal areas is therefore

$$L_r^c = \frac{A_S}{A_0} \cdot c \cdot \frac{\rho}{\pi} \cdot E_i(\theta_i = 0^\circ) \cdot \cos\theta_i \cdot \cos\theta_r. \tag{9.3}$$

In the following more complicated derivations, we will talk e.g. about the 'area b', meaning in fact area $b \cdot A_S$, to improve readability. It will be shown that A_S (as well as A_0) will cancel in the final equations anyway.

9.4.2 Vertical Areas

For the vertical areas of the street structure, the situation is more complicated, because parts of the vertical area may be shadowed or masked (hidden from view) and the angles of incidence and reflection need to be calculated in the coordinate system of the respective area.

Consider the light ray (dashed line) in fig. 9.1. It reaches the street structure at point 'D', almost being obstructed by point 'E'. Thus all the area below point 'D' will be in shadow. To determine the illuminated proportion of the vertical area 'b', we have to calculate the distance between 'D' and 'F' ($\overline{DF}$). It is given by

$$\overline{DF} = \frac{\overline{FE}}{\tan\theta_i} \tag{9.4}$$

and $\overline{FE}$ is given by

$$\overline{FE} = \frac{\overline{GE}}{|\cos\varphi_i|} = \frac{a}{|\cos\varphi_i|} \tag{9.5}$$

(index i means 'incident'). In case the light ray enters the structure from the left instead of from the right, the azimuth angle φ_i will be greater than 90°, its cosine will be negative and the light ray will hit the right wall instead of the left wall. The equations are the same, but with $\cos\varphi_i$ replaced by $-\cos\varphi_i$. Thus we divided by the absolute of $\cos\varphi_i$ in eq. 9.5 to cover both cases.

Obviously, the illuminated area can never exceed the total area b, thus we have to introduce the constraint $\overline{DF} \leq b$. Unfortunately, these kind of constraints will prevent our model from being analytical, and only numerical solutions will be possible. This is one of the reasons why we will also give an analytical approximation to the model.

In order to calculate the viewed area of the vertical part of the structure, the same argument as above applies with the incoming light ray replaced by the viewing ray. Thus it is sufficient to simply replace θ_i and φ_i by θ_r and φ_r in equations 9.4 and 9.5 (index r means 'reflected').

We will calculate the contributions of the vertical areas similar to eq. 9.3. We replace the angles $\theta_{i/r}, \varphi_{i/r}$ by their equivalents $\theta_{i/r}^V, \varphi_{i/r}^V$ in the turned coordinate system for each vertical area, see fig. 9.1. In the turned coordinate system, the z-axis points in the same direction as the surface normal, the x-axis points downward for the left vertical area and upwards for the right vertical area, the y-axis remains unchanged. We obtain for the left vertical area:

$$\begin{aligned} \theta_i^{VL} &= \arccos(\cos\varphi_\mathrm{i} \cdot \sin\theta_\mathrm{i}) \\ \varphi_i^{VL} &= \arccos(\frac{-\cos\theta_\mathrm{i}}{\sin\theta_\mathrm{i}^\mathrm{VL}}) \end{aligned} \tag{9.6}$$

The above equation can easily be verified: $\cos\theta_i^{VL}$ is the z component in the turned coordinate system. The turned z-axis equals the original x-axis, and the original x component equals $\cos\varphi_i \sin\theta_i$.

Similarly, for the right vertical area:

$$\theta_i^{VR} = \arccos(-\cos\varphi_\mathrm{i} \cdot \sin\theta_\mathrm{i}) \tag{9.7}$$
$$\varphi_i^{VR} = \arccos(\frac{\cos\theta_\mathrm{i}}{\sin\theta_\mathrm{i}^{\mathrm{VR}}}).$$

The azimuth angles are calculated here (although they are not needed for Lambertian surfaces) because later we will assign a non-Lambertian BRDF to each surface that depends on the azimuth. In the case of $\varphi_i = 0°$, eq. 9.6 can be simplified to

$$\cos\theta_i^{VL} = \sin\theta_i \tag{9.8}$$

and we can deduce that $\theta_i^{VL} = 90° - \theta_i$, which is obviously correct for $\varphi_i = 0°$.

For the viewing angles $\theta_r^{VL}, \varphi_r^{VL}, \theta_r^{VR}$ and φ_r^{VR} the same formulae apply with θ_i and φ_i replaced by θ_r and φ_r. Values of zenith angles $\theta^V > 90°$ will be set to $90°$, corresponding to a vertical area either being completely in shadow or completely hidden. This allows us to express the contributions from the right vertical area as (cf. eq. 9.3):

$$L_r^{bR} = \frac{A_S}{A_0} \cdot \min(\overline{\mathrm{DF}}(\theta_\mathrm{i}^{\mathrm{VR}}, \varphi_\mathrm{i}^{\mathrm{VR}}); \overline{\mathrm{DF}}(\theta_\mathrm{r}^{\mathrm{VR}}, \varphi_\mathrm{r}^{\mathrm{VR}})) \cdot \frac{\rho}{\pi}$$
$$\cdot E_i(\theta_i = 0°) \cdot (\cos\theta_i^{VR} \cdot \cos\theta_r^{VR}) \tag{9.9}$$

We take the minimum of each value of $\overline{DF}$ because if e.g. a larger area is illuminated than viewed, only the viewed area contributes to the reflected radiation. Thus $\min(\overline{\mathrm{DF}}(\theta_\mathrm{i}^{\mathrm{V}}, \varphi_\mathrm{i}^{\mathrm{V}}); \overline{\mathrm{DF}}(\theta_\mathrm{r}^{\mathrm{V}}, \varphi_\mathrm{r}^{\mathrm{V}}))$ is the area illuminated *and* viewed. Remember that b is the maximum value possible for $\overline{DF}$.

The contribution from the left vertical area is obtained by just replacing the index L by R:

$$L_r^{bL} = \frac{A_S}{A_0} \cdot \min(\overline{\mathrm{DF}}(\theta_\mathrm{i}^{\mathrm{VL}}, \varphi_\mathrm{i}^{\mathrm{VL}}); \overline{\mathrm{DF}}(\theta_\mathrm{r}^{\mathrm{VL}}, \varphi_\mathrm{r}^{\mathrm{VL}})) \cdot \frac{\rho}{\pi}$$
$$\cdot E_i(\theta_i = 0°) \cdot (\cos\theta_i^{VL} \cdot \cos\theta_r^{VL}) \tag{9.10}$$

The total radiance is simply the sum of both areas:

$$L_r^b = L_r^{bL} + L_r^{bR} \tag{9.11}$$

Note that at least one of the cosine products at the end of equations 9.10 or 9.9 will be zero because they are facing opposite directions. This is why zenith angles larger than $90°$ are set to $90°$.

9.4.3 Bottom Horizontal Areas

The last contribution that needs to be added is that of the lower horizontal area (with width 'a'). The width of the shadowed area will be denoted by 'a_s', the width of the hidden area by 'a_h', see fig. 9.2. If either variable is positive, the shadowed respective hidden area borders the right vertical area, if either variable is negative it borders the left vertical area. We will explain the derivation of 'a_h', the derivation of 'a_s' is analogous.

The viewing ray (dashed line incident from the right in fig. 9.2) is almost obstructed by point 'J' and hits the bottom horizontal area at point 'H'. We define point 'I' as the point along the border of the vertical area and the lower horizontal area with the closest distance to point 'H'. The distance between points 'H' and 'I' equals 'a_h', the variable to be determined. It is equal to

$$\overline{HI} = \overline{HK} \cdot \cos\varphi_r \tag{9.12}$$

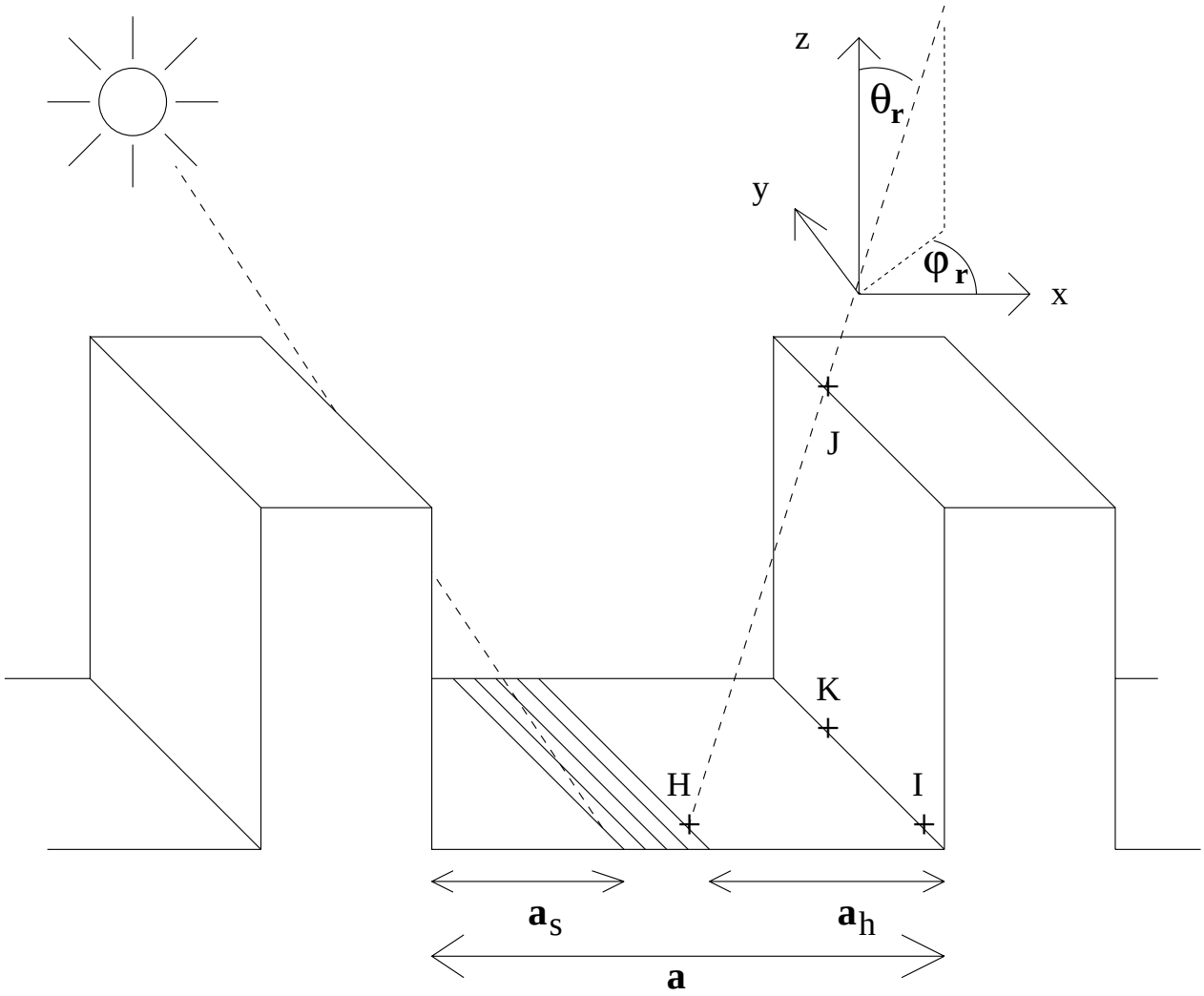

Figure 9.2: Sketch of the street structure to explain the derivation of shadowed (a_s) and hidden (a_h) areas on the bottom horizontal area in case the scene is illuminated from the left and viewed by the sensor at θ_r and φ_r from the right . Only the hatched area $a - |a_s| - |a_h|$ (see eq. 9.16, a_h is positive, a_s is negative) is illuminated and viewed.

where point 'K' is the projection of point 'J' from the upper edge of the vertical area to its lower edge. $\overline{HK}$ is given by

$$\overline{HK} = \overline{JK} \cdot \tan\theta_r \tag{9.13}$$

where $\overline{JK}$ equals 'b'. Thus we can simply write

$$a_h = b \cdot \tan\theta_r \cdot \cos\varphi_r \tag{9.14}$$

and substituting the illumination angles for the viewing angles

$$a_s = b \cdot \tan\theta_i \cdot \cos\varphi_i \tag{9.15}$$

Note that for azimuth angles greater than $90°$ s resp. h become negative. This allows us the following distinction of cases for the viewed and illuminated area a_{vi}:

$$\begin{aligned} s \cdot h >= 0 : a_{vi} &= a - \max(|\mathrm{a_s}|, |\mathrm{a_h}|) \\ s \cdot h < 0 : a_{vi} &= a - |a_s| - |a_h| \end{aligned} \tag{9.16}$$

If illumination and viewing direction are on the same side (either left or right), $a_s \cdot a_h$ is greater than zero, and we have to subtract the maximum of $(|a_s|, |a_h|)$ from a. If illumination and viewing direction are on opposite sides, we have to subtract both $|a_s|$ and $|a_h|$ from a. Again, we must constrain the value of a_{vi} to be greater or equal zero. The reflected radiance from the bottom horizontal area is thus (cf. eq. 9.3)

$$L_r^a = \frac{A_S}{A_0} \cdot a_{vs} \cdot \frac{\rho}{\pi} \cdot E_i(\theta_i = 0°) \cdot \cos\theta_i \cdot \cos\theta_r \tag{9.17}$$

9.4.4 BRDF of a Pixel

In a last step to determine the reflected radiance L_r of the urban pixel, we have to sum up the 3 contributions L_r^a, L_r^b, L_r^c and to multiply them with the number of occurrence of the street structure in the pixel, which is given by $(A_0/\cos\theta_r)/A_S$, see section 9.4.1. To obtain the BRDF, we have to divide by the incoming irradiance E_i:

$$f_r = \frac{(L_r^a + L_r^b + L_r^a) \cdot ((A_0/\cos\theta_r)/A_S)}{E_i(\theta_i = 0°) \cdot \cos\theta_i} \tag{9.18}$$

Note that the quantities A_0, A_S and $E_i(\theta_i = 0°)$ cancel because they all occur in L_r^a, L_r^b and L_r^c. But neither $\cos\theta_r$ nor $\cos\theta_i$ cancel because in L_r^b the zenith angles θ had to be replaced by their vertical equivalents θ^V. It is also worth mentioning that the albedo ρ can be factorized as it is assumed to be equal for all surfaces.

9.4.5 Sample Plots

To better understand the effect of each contribution of the areas a, b and c to the overall urban BRDF, we show their intensities in fig. 9.3. We assume all 3 parameters a, b and c to be of equal value. From eq. 9.1 it follows that their values will be set to 0.5. For simplicity, we set the surface albedo ρ to 1.

If φ_i is equal to $90°$ or $270°$, the contributions of the vertical structures become zero because they are not illuminated. Setting φ_r to $90°$ resp. $270°$ would yield a BRDF independent of viewing zenith angle θ_r, because there is neither masking nor shadowing (at this stage, we assume the areas a, b and c to be Lambertian). Thus we demonstrate the contributions of the areas a, b and c in the principal plane ($\varphi_i = 0°, \varphi_r = 0°$ resp. $\varphi_\mathrm{r} = 180°$, negative zenith angles correspond to $\varphi_r = 180°$). We chose illumination angles of $\theta_i = 0°, \theta_i = 30°$ and $\theta_i = 60°$.

The solid line shows the combined contributions, the stars show the BRDF created by the vertical areas, the crosses show the BRDF of the bottom horizontal area, and the diamonds show the BRDF of the top

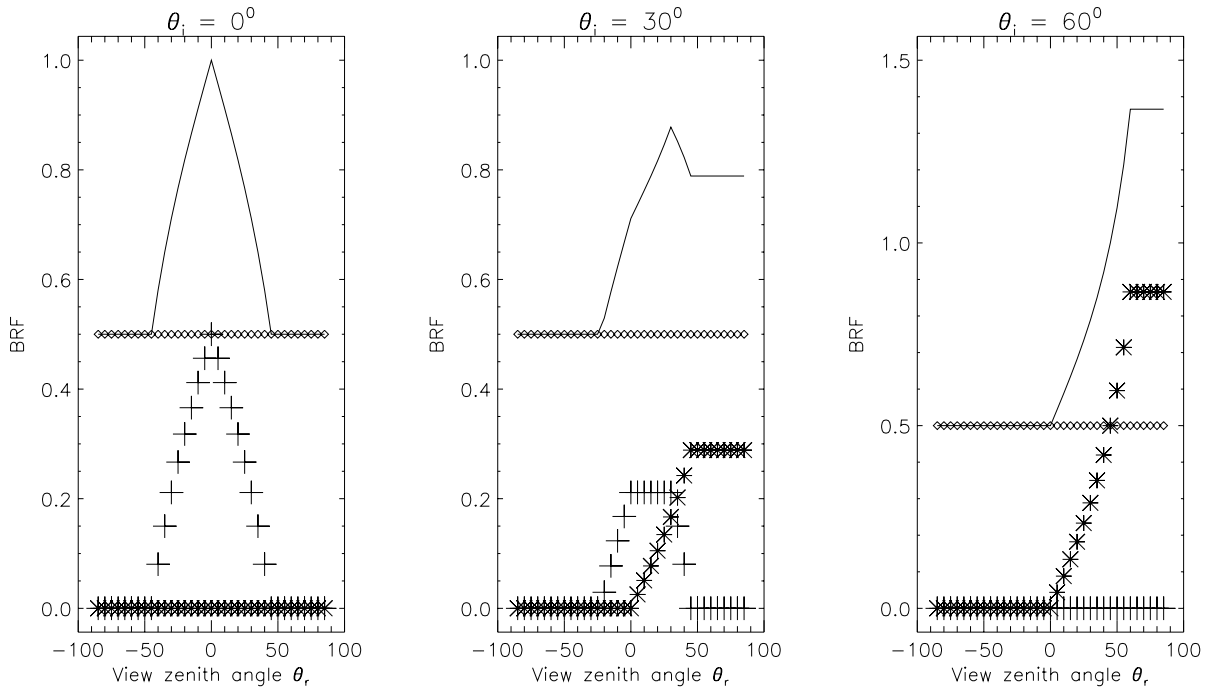

Figure 9.3: BRF produced by the areas $a(+), b(*)$ and c ($\diamond$) (cf. fig. 9.1) for a single street structure assuming each area to be flat and Lambertian with albedo $\rho = 1$. The contributions of each area are added to yield the total BRF (solid line) of a single street structure. The parameters of the street structure are $a = b = c = 0.5$. BRF values are shown for different incident zenith angles θ_i in the principal plane ($\varphi_i = 0°$, $\varphi_r = 0°$ for positive view zenith angles, $\varphi_r = 180°$ for negative zenith angles). The contribution of area c (roof) is constant, area a (street) determines the angular behavior at $\theta_i = 0°$, area b (walls) determines the angular behavior at $\theta_i = 60°$.

horizontal area. The top horizontal area gives a constant contribution (because it is a lambertian surface that is never shadowed or hidden) of 0.5 for all zenith angles.

The bottom horizontal area does not contribute for $\theta_i = 60°$, because it is completely shadowed. It does contribute fully at $\theta_i = 0°, \theta_r = 0°$. For increasing view zenith angles the contribution decreases because the bottom area hidden from view increases.

The vertical areas do not reflect for $\theta_i = 0°$, because in the coordinate system of the vertical areas the light hits the surface at an angle of $90°$, thus the irradiance is zero. The vertical areas contribute strongly for $\theta_i = 60°$, because in their coordinate system the irradiance is greater than for the horizontal areas. Note that the overall BRF (BRF $\cong \pi \cdot$ BRDF) even increases to a value greater than the albedo of the individual surfaces ($\rho = 1$).

For $\theta_i = 30°$ all 3 areas contribute to the total BRDF, creating a pronounced hot spot. The contribution of the vertical area reaches a plateau for large zenith angles in backward scattering directions, because two effects exactly cancel each other: the viewed vertical area is inversely proportional to $\tan\theta_r$ (eq. 9.4), but the cosine of the viewing zenith angle in the vertical system is proportional to $\sin\theta_r$ (eq. 9.6). Dividing by $\cos\theta_r$ (eq. 9.18) yields $\tan\theta_r$, which cancels with the $\tan\theta_r$ from eq. 9.4, thus resulting in a plateau.

Summarizing, we can say that our model in its simplest form produces a hot spot for all incidence angles if the scene is viewed and illuminated from φ_i and φ_r equal to $0°$ or $180°$, and that the reflectance in backward direction is significantly higher than in forward scattering direction. However, if the illumination or viewing angle is parallel to the street direction (φ_i resp. φ_r equal $90°$ or $270°$), the BRDF becomes independent of the respective zenith angle (θ_i or θ_r), thus there is no hot spot characteristic (cf fig. 9.4 in the following section).

9.4.6 Superposition

The overall reflected radiance measured by a pixel is the sum of all the street structures covered by the pixel. In reality, the streets do not all have the same heading. E.g. in many North American cities the street structure is very regular, with streets heading either north/south or east/west. In this case, the BRDFs of only two structures have to be superimposed to yield the overall BRDF. However, in most parts of the world, the street structure is far less regular, and there is no a priori preferred street heading. In this case, the contributions from all directions have to be superimposed. This has the advantage that the modeled surface shows *rotational symmetry* for all rotation angles and therefore the resulting BRDF depends only on the relative azimuth $\varphi = |\varphi_i - \varphi_r|$ and not on φ_i and φ_r explicitly. (The North American city structure is rotationally invariant only for rotation angles of $90°, 180°$ and $270°$.) In this study, we will assume rotational symmetry for all rotation angles (no preferred street headings) because it is a better approximation to most cities, and because the handling (e.g. visualization) of a BRDF that depends explicitly on φ_i and φ_r is even more tedious than in the case of a BRDF that depends only on $\varphi = |\varphi_i - \varphi_r|$. However, all further developments of our model described below could be applied to the case of a regularly structured city without rotational symmetry as well.

Fig. 9.4 shows the BRDF according to eq. 9.18 of the street structure used in section 9.4.5 ($a = b = c = 0.5$) in the principal plane ($\varphi_r = \varphi_i$ resp. $\varphi_r = \varphi_i + 180°$, negative azimuth angles correspond to $\varphi_r = \varphi_i + 180°$) for 3 different illumination azimuths: $\varphi_i = 0°, 45°$ and $90°$. For $\varphi_i = 90°$, the BRDF is constant, the other two cases show a distinct hotspot. $\varphi_i = 0°$ is the same configuration as in fig. 9.3, thus the solid line of fig. 9.3 corresponds to the crosses in fig. 9.4. It can be seen that the BRDF is not a linear function of φ_i, in this case the average of the BRDF of $\varphi_i = 0°$ and $\varphi_i = 90°$ would have yielded the same BRDF as for $\varphi_i = 45°$, which is clearly not the case. Unfortunately, this implies that the BRDF of a regularly structured city can be quite different from a city with rotational symmetry.

Fig. 9.4 also shows the superposition of street structures heading into all possible directions (rotationally symmetric city structure, solid line). The superposition is equivalent to averaging over all street structure directions, which in this case was done with a $1°$ binning. It is sufficient to superimpose all directions $\in [0°,$

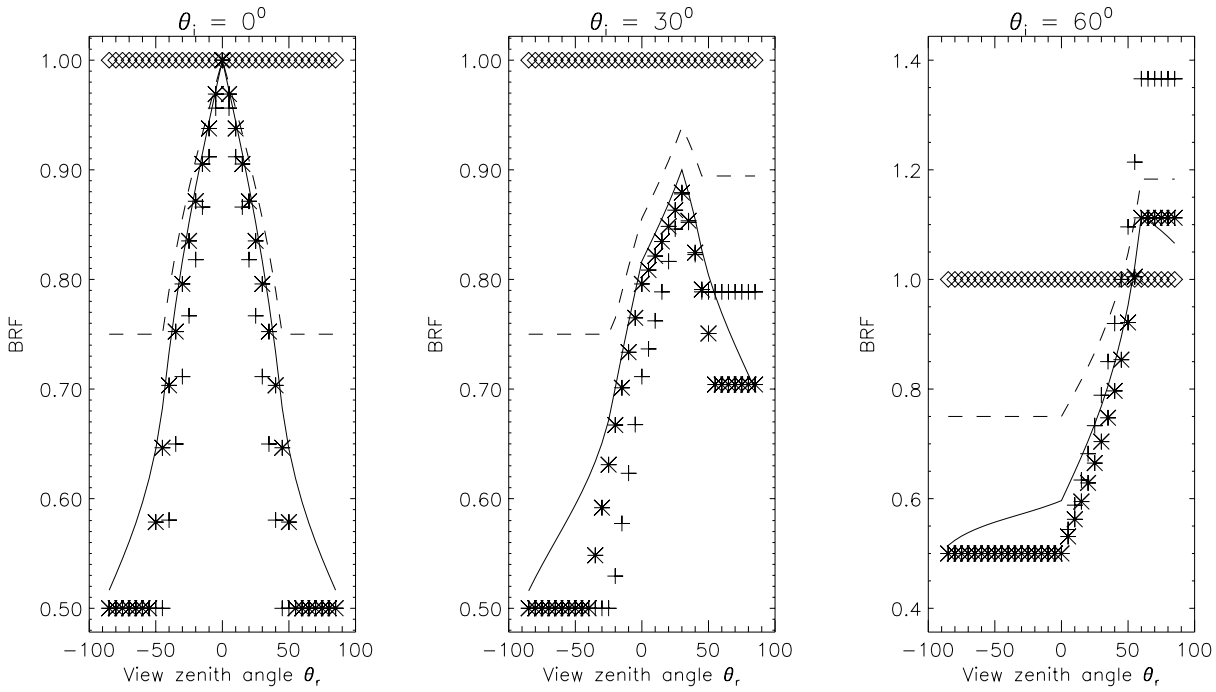

Figure 9.4: BRF in the principal plane of the street structure oriented into different directions. Turning the street structure by x° is equivalent to setting $\varphi_i = \varphi_r = x^\circ$. The BRFs are shown for the following cases: +: $\varphi_i = \varphi_r = 0^\circ$, *: $\varphi_i = \varphi_r = 45^\circ$, diamonds: $\varphi_i = \varphi_r = 90^\circ$. The solid line is the average over all directions $\varphi_i = \varphi_r \in [0^\circ, .., 180^\circ]$ and corresponds to the BRF of a city structure with rotational symmetry. The parameters of the street structure are $a = b = c = 0.5$. The dashed line is the average of only two perpendicular directions ($\varphi_i = \varphi_r = 0^\circ, 90^\circ$) and corresponds to the BRF of a typical North American city structure (streets running north/south and east/west) viewed from $\varphi_r = 0^\circ, 90^\circ, 180^\circ$ or 270°. The BRF of a North American city structure viewed from $\varphi_r = 45^\circ, 135^\circ, 225^\circ$ or 315° is equivalent to the line given by the '+' symbols. These are the limiting cases, for all remaining φ_r the BRF values of a North American city structure will be between the dashed line and the '+' symbols.

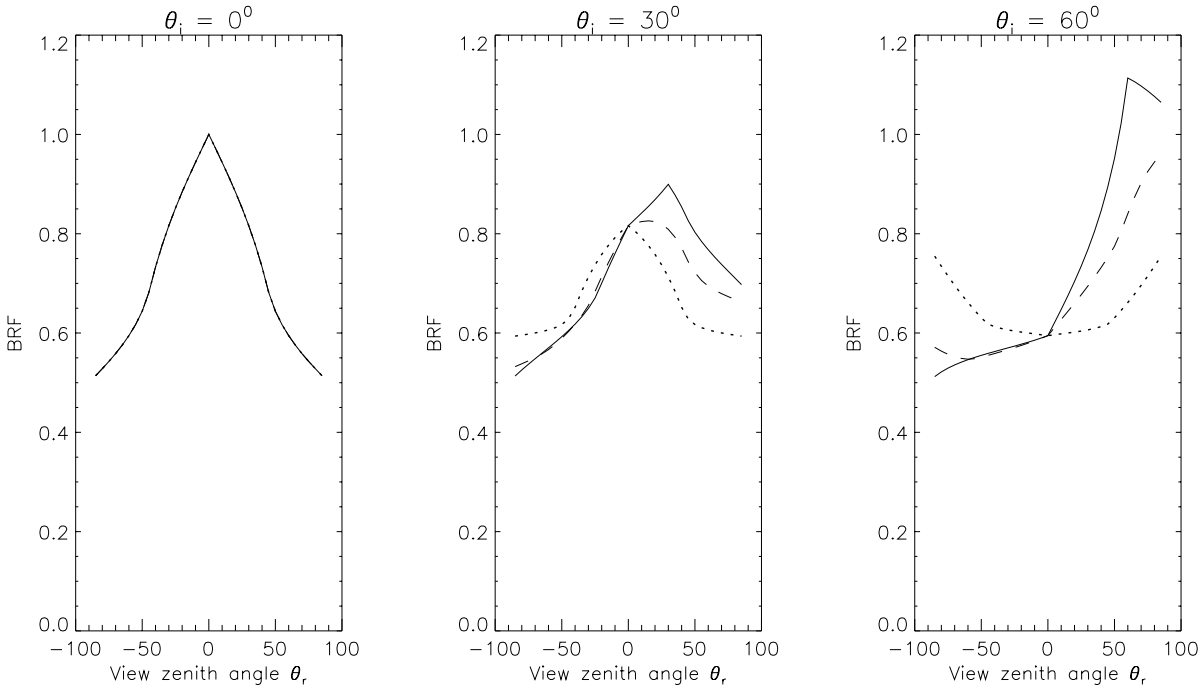

Figure 9.5: City structure BRF (rotationally symmetric) without intermediate or small scale BRDF effects for different relative azimuths. Solid line: $\varphi = 0°/180°$, dashed line: $\varphi = 45°/135°$, dotted line: $\varphi = 90°$. The solid line in this figure is the same as the solid line in fig. 9.4. The parameters of the street structure are $a = b = c = 0.5$.

$180°$], because in our model a street heading south is equivalent to a street heading north, so there is no need to evaluate the directions $\in [180°, 360°]$. The BRDF resulting from this superposition shows a clear maximum at backscatter direction (hot spot) for all illumination zenith angles θ_i.

For the case of a North American city structure (rotational symmetry only for rotation angles $90°, 180°, 270°$) the BRDF is more complex because it depends on an additional parameter. It is shown in fig. 9.4 for two cases: if viewing the city parallel to a street (dashed line) and for viewing the city at an azimuth of $45°$ away from the street heading ('+' symbols). These are the two limiting cases, all BRF values are contained between the dashed line and the '+' symbols.

Fig. 9.5 shows the overall BRDF for different relative azimuths: as above for $\varphi = 0°/180°$, but also for $\varphi = 45°/135°$ and $\varphi = 90°$. Of course, for $\theta_i = 0°$ (left plot) or $\theta_r = 0°$ (center of each plot) all curves coincide because the relative azimuth is meaningless if either zenith angle is in nadir. It is interesting to take a closer look at the curve for $\theta_i = 60°$ and $\varphi = 90°$: the shape resembles a valley, whereas for $\theta_i = 0°$ it resembles a mountain. This unusual characteristic could be used as a supporting feature in classification algorithms to discriminate urban from non-urban areas. The strong rise of the 'valley walls' occurs only for viewing zenith angles larger than $50°$, so for measurements with smaller viewing zenith angles the BRDF across the principal plane will appear near to Lambertian. Another interesting feature to point out is that the BRDF is quite linear with respect to φ: the average of $\varphi = 0°/180°$ and $\varphi = 90°$ is close to $\varphi = 45°/135°$.

9.5 Intermediate Structure

Our urban model consisting of streets so far captures the large scale structure of a city. But our simple approach of assuming the surfaces a, b and c to be flat systematically underestimates the amount of shadow present in a real city. In a real city, there will be balconies, cars, chimneys, human beings, etc., with the potential of casting shadows. We refer to these objects as 'intermediate structure', because their sizes are

between the large scale street structure treated above and the microscale structure treated in the following section. Because of the large variety of this intermediate structure, it is obviously impossible to develop a detailed model. We make the following assumptions:

- Height and width of each object are equal.
- The center of each object is separated from the center of another object by a distance of 5 times its height. This second object has the same size as the first one.
- The length of the object is considerably greater than its width (for reasons given below).

The first two assumptions can be seen as an attempt to describe the 'average intermediate structure' of a city in an extremely simple way. The third assumption is equivalent to the assumption of 'infinite length' which we also used for the street structure. We introduce this assumption because it enables us to use the same algorithm as developed in the above chapters, setting $b = c = 0.2$ and $a = 0.8$, cf. fig. 9.1. The BRDF model becomes iterative with a 1-step iteration. Note that although the first assumption fixes the relative size of the object (height equals width), it does not fix the absolute size, allowing cars as well as chimneys to be the object of the intermediate structure. We will apply this intermediate structure only to man-made surfaces, vegetated surfaces are assumed to be flat. All headings of the intermediate structure are superimposed, yielding a rotationally symmetric surface, see section 9.4.6. To save computing time, a bin size of 10° was chosen for the superposition on the intermediate as well as for the large scale. This choice leads to a sufficient rotational symmetry (better than 0.5 %). The intermediate structure reduces the width of the hotspot, see fig. 9.8.

9.6 Microstructure

In a final step, we have to consider the BRDF of the surfaces itself (e.g. the BRDF of asphalt, roof tile, grass lawn, etc.). We refer to the BRDF of a homogenous surface with a diameter of 1 to 10 cm as caused by 'microstructure', although e.g. the BRDF caused by grass leaves or the roughness of asphalt is produced by structures in the mm to cm range, and not in the μm range.

Our goal in this section is to derive an 'average urban microstructure BRDF'. Therefore, the components of the urban scenery must be determined (asphalt, all kinds of roof covers, grass, trees, wall paint, etc.), the amount of each component must be determined, and the BRDF of each component needs to be known as well.

9.6.1 Vegetation

Every urban area contains some areas of vegetation, but their fraction of the total urban area can vary from negligible to dominant. Trees are difficult to integrate into our model, because of their complex 3-dimensional shape and their unknown BRDF (so far, only BRDFs of forests have been modeled (see e.g. (Ni et al. 1999), (Gastellu-Etchegorry et al. 1999)), the BRDF of a single tree seems to transcend the basic concept of BRDF, because BRDF is defined for a homogeneous flat surface (Nicodemus et al. 1977)). We thus restrict the determination of the BRDF of vegetated urban surfaces to grass (lawns). Grass has been measured and modeled extensively ((Kimes 1983), (Deering et al. 1992), (Sandmeier & Itten 1998), (Qin et al. 1999), (Kriebel 1978)). For this study, we will use the grass BRDF data set by (Sandmeier & Itten 1999). It has a very good angular sampling for viewing angles, but it is restricted to one solar zenith angle ($\theta_i = 35^\circ$). The data set is hyperspectral in the range 450 to 2450 nm, a similar range is available for the man-made surfaces, see below. It was obtained using the field goniometer FIGOS and is publicly available. A very convenient

analytical empirical function describing the data is given in (Meister et al. 1998b):

$$BRF = \pi \cdot BRDF = k_0 + k_1 \cdot (\theta_i^0 + \theta_r) + k_2 \cdot \mathrm{e}^{b_1 \cdot (\theta_i^0 \cdot \theta_r)^2} \cdot \mathrm{e}^{-b_2 \cdot g} + k_3 \cdot \mathrm{e}^{b_3 \cdot (\theta_i^0 \cdot \theta_r)^2} \cdot \mathrm{e}^{-b_4 \cdot \psi^2} \tag{9.19}$$

where ψ is the relative angle to the specular direction, see eq.5.14 on page 74. θ_i^0 equals the solar zenith angle at which the measurements where performed ($\theta_i = 35°$). g is the relative angle between viewing and illumination direction:

$$\cos g = \cos\theta_i \cos\theta_r + \sin\theta_i \sin\theta_r \cos\varphi \tag{9.20}$$

The coefficients k_i depend on wavelength, the coefficients b_i are fixed for each sample. The underlying assumption is that the shape of the hotspot and the forward scattering term are primarily determined by the geometry of the canopy and therefore do not depend on wavelength, whereas the intensity of these two terms can vary with wavelength primarily due to the change of reflectance with wavelength. The coefficients have the following physical meaning:

- k_0 = Lambertian component (diffuse scattering)
- k_1 = intensity of the bowl-shape
- k_2 = intensity of the hotspot peak
- k_3 = intensity of the specular peak

b_2 and b_4 determine the width of the peaks, b_1 and b_3 allow the intensity of the peaks to vary with zenith angles. Values for the parameters k_i and b_i are given in the appendix, table 12.5, page 167.

We fixed the angle θ_i^0 (but not θ_i in the equations for ψ and g) to its equivalent in radians of $35°$, because only for $\theta_i = 35°$ the empirical function is verified to describe the data well. This makes the function violate the theorem of reciprocity, but it prevents producing unreasonable results for oblique zenith angles, which is more important for this study. The basic important feature of the function is the shape and the intensity of the hotspot and its dependence on wavelength. We will use this function to describe all urban areas covered with vegetation, not discriminating between grass, bushes or trees. [1]

9.6.2 Man-Made Surfaces

We will model the average urban man-made surface as a *weighted average* of the samples from the EGO measurement campaign. We will use the ASD data, because they offer a larger variety of samples and cover a larger wavelength range. The poor quality of the specular ASD measurements is of only minor importance here, because the most influential contribution to the total urban BRDF is the diffuse component.

For each combination of angles, the BRDF value of the average surface $f_r^{\mathrm{AVG}}(\theta_i, \theta_r, \varphi)$ is a linear combination of the BRDF values of the individual samples $f_r^{\mathrm{Sample(i)}}(\theta_i, \theta_r, \varphi)$:

$$f_r^{\mathrm{AVG}}(\theta_i, \theta_r, \varphi) = \frac{1}{N} \cdot \sum_{i=1}^{N} w_i \cdot f_r^{\mathrm{Sample(i)}}(\theta_i, \theta_r, \varphi) \tag{9.21}$$

The samples and the choice of weights w_i are given in table 9.1. It is an estimate of the overall relative occurrence of these materials in western cities. The biggest shortcoming is the lack of surfaces describing painted walls. Furthermore asphalt can vary strongly in color, but is only represented by one sample here. Due to the individual character of each city, strong variations of the albedo can be expected (e.g. a city with red roofs versus a city with grey roofs). However, f_r^{AVG} is a useful approximation to describe the *shape* of the BRDF of urban surfaces.

[1] The measured BRDFs of forests vary considerably, depending on the type of tree, tree density, the season, etc. However, the most common features are a hotspot and a bowl-shape.

Weight w_i	Sample
30 %	Asphalt
15 %	Concrete (walkway)
10 %	Dirty roof tile
10 %	Sanded roof paper
5 %	Green/black roof paper
5 %	Brown Slate
5 %	Red roof tile (sample A)
5 %	Red roof tile (sample B)
5 %	Black concrete tile
2.5 %	Red concrete tile
2.5 %	Blue concrete tile
2.5 %	Green Slate
2.5 %	Red Slate

Table 9.1: Weights used to compose the average small scale urban BRDF, see eq. 9.21.

We fitted the coefficients of the Torrance and Sparrow model (eq. 5.1) for the f_r^{AVG} resulting from eq. 9.21. We found that the coefficients of the specular peak are quite constant with respect to wavelength, the average values being $t_1 = 0.92\,\mathrm{sr}^{-1}, w = 0.095\,\mathrm{deg}^{-1}, n = 1.39$ and $k = 0.2$. The value of $w = 0.095\,\mathrm{deg}^{-1}$ implies that the average inclination of the specularly reflecting facets in the Torrance and Sparrow model (and thus the width of the specular peak) is 5.8°.

The Lambertian coefficient t_0 is shown in fig. 9.6 as a function of wavelength (dashed line), as well as the BRDF in forward scattering direction to give an idea of the width and magnitude of the specular peak. Table 12.5 in the appendix, page 167 gives the respective diffuse albedo at the DAEDALUS wavelengths.

The specular peak produces a non negligible part of the albedo (difference between solid and dashed line in fig. 9.6, left part). The average man-made surface determined above reflects about 2 % of the incoming light specularly (1.3 %, 1.6 %, 3.1 % for $\theta_i = 0^\circ, 40^\circ, 60^\circ$, resp.). Thus, depending on wavelength, 5 to 15 % of the albedo are produced by the specular peak:

$$\frac{A(f_r^{\mathrm{spec}})}{A(f_r^{\mathrm{TS}})} = \frac{\int_\Omega f_r^{\mathrm{spec}} \mathrm{d}\Omega}{\int_\Omega f_r^{\mathrm{TS}} \mathrm{d}\Omega} = 0.05 \text{ to } 0.15 \tag{9.22}$$

where Ω denotes the upper hemisphere ($\mathrm{d}\Omega = \sin\theta_r \cos\theta_r \mathrm{d}\theta_\mathrm{r} \mathrm{d}\varphi$, the integration is carried out over the angles of reflection, thus A can be a function of θ_i.)

Surfaces exposed to outdoor conditions for long periods of time may show a weaker specular pattern than the samples chosen for the EGO measurement campaign. However, in a previous study (Meister et al. 1998a) we measured the BRDF of a roof which had been exposed to outdoor conditions for several years. We showed that the results can be well described by assuming the BRDF of the roofing material to have a specular peak with a similar intensity as the BRDF of a new roofing tile of a similar material (for a detailed report of these measurements see (Meister et al. 1997) and (Meister et al. 1996a)).

The amount of dirty or wet surfaces in an urban area is not expected to change the shape of the BRDF considerably, except for the specular peak which will strongly increase for wet surfaces and decrease for dirty surfaces (the albedo however can change strongly).

Considering the integration of the specular peak into the urban BRDF model, the exact orientation of the surface is much more important than for a Lambertian surface. The orientation of the 'wall' and 'street' surfaces in our model (vertical resp. horizontal) is sufficiently realistic. However, roof surfaces can take a wide variety of inclinations. The street structure modeled in fig. 9.1 assumes all roof tops are *flat*, which may

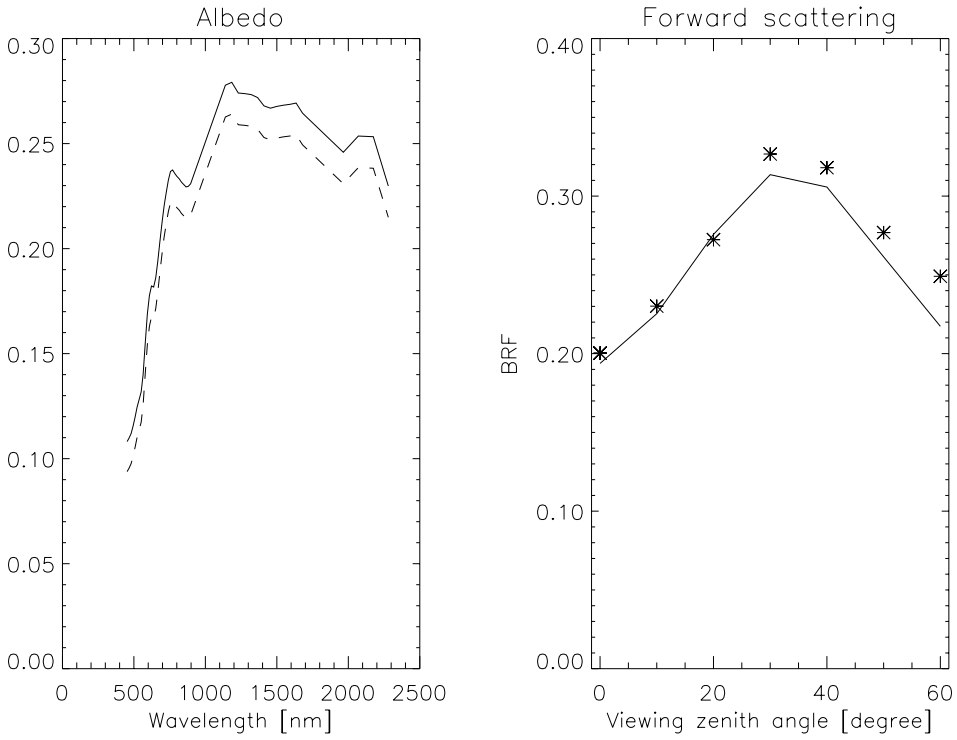

Figure 9.6: The left plot shows the albedo of the average man-made surface derived from samples of the EGO measurement campaign (cf. eq. 9.21) as a solid line, the dashed line shows the Lambertian component t_0 multiplied by π, which is equivalent to the total albedo less the albedo due to the specular peak. The parameters were determined from a fit of the Torrance-Sparrow model (eq. 5.1). The right plot shows the BRF at a wavelength of $\lambda = 660$ nm and an incident angle of $\theta_i = 30^\circ$ in the forward scattering direction. Stars show the measurements, the solid line shows the Torrance-Sparrow model.

be an acceptable first order approximation for Lambertian surfaces, but certainly not for specular surfaces. Thus we considered the inclination of roof surfaces in the following manner: The width of the specular peak is determined by the inclination angles of the reflecting surfaces. *We will assume that the distribution of the roof normals α can also be described by $P(\alpha)$ given in eq. 5.4, with an estimated average roof inclination of* 20°. This is achieved by setting the width parameter of the roof surfaces $w^{\mathrm{roof}} = 0.028$, which in turn requires that we adjust the intensity parameter t_1 in order to keep the same amount of specularly reflected albedo. Thus, for the roof surfaces, parameter t_1^{roof} has to be normalized by the ratio of albedos of the specular peak (cf. eq. 5.1):

$$t_1^{\mathrm{roof}} = t_1 \cdot \frac{A(f_r^{\mathrm{spec}}, w)}{A(f_r^{\mathrm{TS}}, w^{\mathrm{roof}})} = 0.95 * 0.14 = 0.13 \tag{9.23}$$

9.7 Modeling Results

After developing the model in the previous chapters, we can now present results from modeling an urban area. Typical values for the parameters of a street structure are $a = b = c = 0.5$ (estimation for a typical street in downtown Nuremberg, Germany, see below). This means the width of the streets is the same as the width of the houses, and the houses are as high as wide. We assume that 28 % of the area is covered by vegetation.

The results are shown as polar plots in fig. 9.7. Each plot is for a different incident zenith angle θ_i. For large θ_i, the hotspot and the specular peak are clearly separated peaks, for nadir illumination the two peaks add up to form a single peak.

Across the principal plane, the BRDF drops with increasing viewing zenith angle for $\theta_i < 45^\circ$, but it rises with increasing viewing zenith angle for $\theta_i > 45^\circ$. This behavior is caused by the vertical structures (b in fig. 9.1: the larger the viewing angle, the stronger the contribution from the vertical structure. For illumination close to nadir, the vertical structures are relatively dark (because the irradiance is proportional to the cosine of the illumination angle in the local coordinate system). Thus, for increasing viewing angle, the urban BRDF becomes darker. On the other hand, for illumination at large zenith angles, some of the vertical structures are illuminated from nadir in their local coordinate system. The effect is an increase of the urban BRDF with increasing θ_r, because the illuminated vertical structures are much brighter than the horizontal surfaces (which are illuminated at a large zenith angle and thus relatively dark).

Fig. 9.8 demonstrates the effects of the different scales considered in the model (assuming 0 % vegetation for simplicity). The solid line shows the full model, the dashed line assumes a Lambertian small scale BRDF (simply suppressing the specular peak), and the diamonds show the large scale BRDF excluding intermediate and small scale BRDF. It can be seen that the large scale effects are the dominant factor for the full model. The intermediate scale effects produce a sharper hotspot and a stronger decrease for large zenith zenith angles. The reason is that by adding the intermediate scale to the model, the amount of shadow increases (note that at $\theta_i = \theta_r, \varphi = 0^\circ$ the solid line and the diamonds coincide, because in the exact backscatter direction there is no shadow in either model). The small scale BRDF adds the specular peak in forward scattering direction (difference between solid and dashed line). It should be noted that the influence of the small scale BRDF strongly depends on wavelength and the proportion of vegetation (e.g. vegetation increases the hotspot).

Fig. 9.8 also shows the effects of skylight illumination. The crosses give BRF values calculated for the full model, assuming an *isotropic skylight irradiance*. The skylight irradiance integrated over the upper hemisphere equals 20 % of the total (direct plus diffuse) irradiance for this example, an average value measured for various *in situ* measurements in Hamburg, Germany (Meister et al. 1996a), (Meister et al. 1997) for clear sky conditions. The effects are rather small (< 6 % for viewing angles $\theta_r < 60^\circ$), thus we will not consider skylight effects in the following section. For viewing angles $> 70^\circ$ a strong increase can be seen (25 % for $\theta_i = 80^\circ, \varphi = 90^\circ$, compare crosses to solid line). Generally, skylight effects reduce the BRDF peaks (like

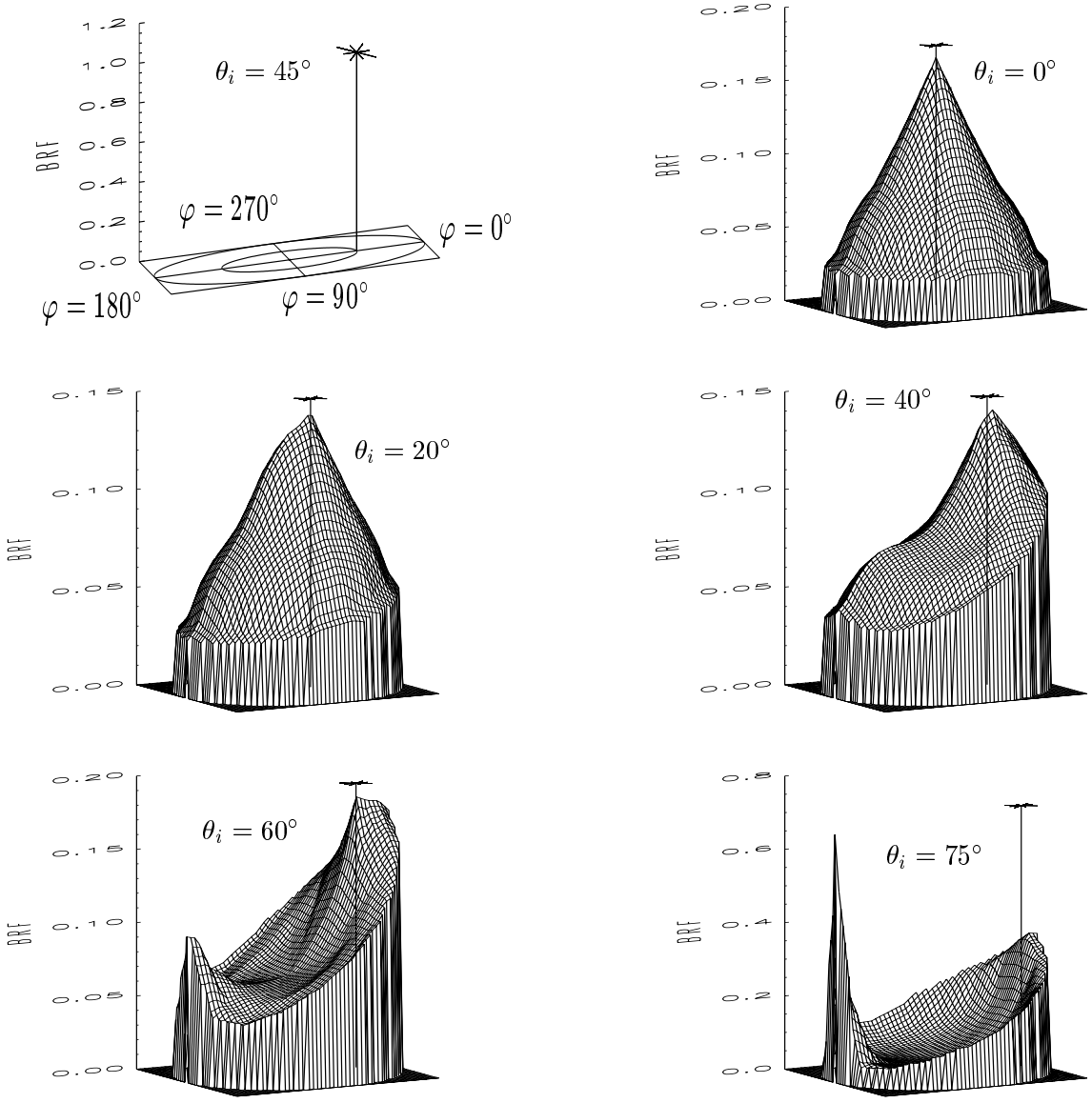

Figure 9.7: Polar plots of the urban BRDF model for $\lambda = 660$ nm, 28 % vegetation, $a = b = c = 0.5$. The plot top left explains the horizontal axes: the outer horizontal circle corresponds to $\theta_r = 90°$, the inner circle to $\theta_r = 45°$, the center to $\theta_r = 0°$. Forward scattering is to the left ($\varphi = 180°$). The incidence angle θ_i is marked by a vertical line topped by a star. The z-axis shows BRF values (dimensionless). The 5 remaining plots show the urban BRDF at $\theta_i = 0°, 20°, 40°, 60°$ and $75°$.

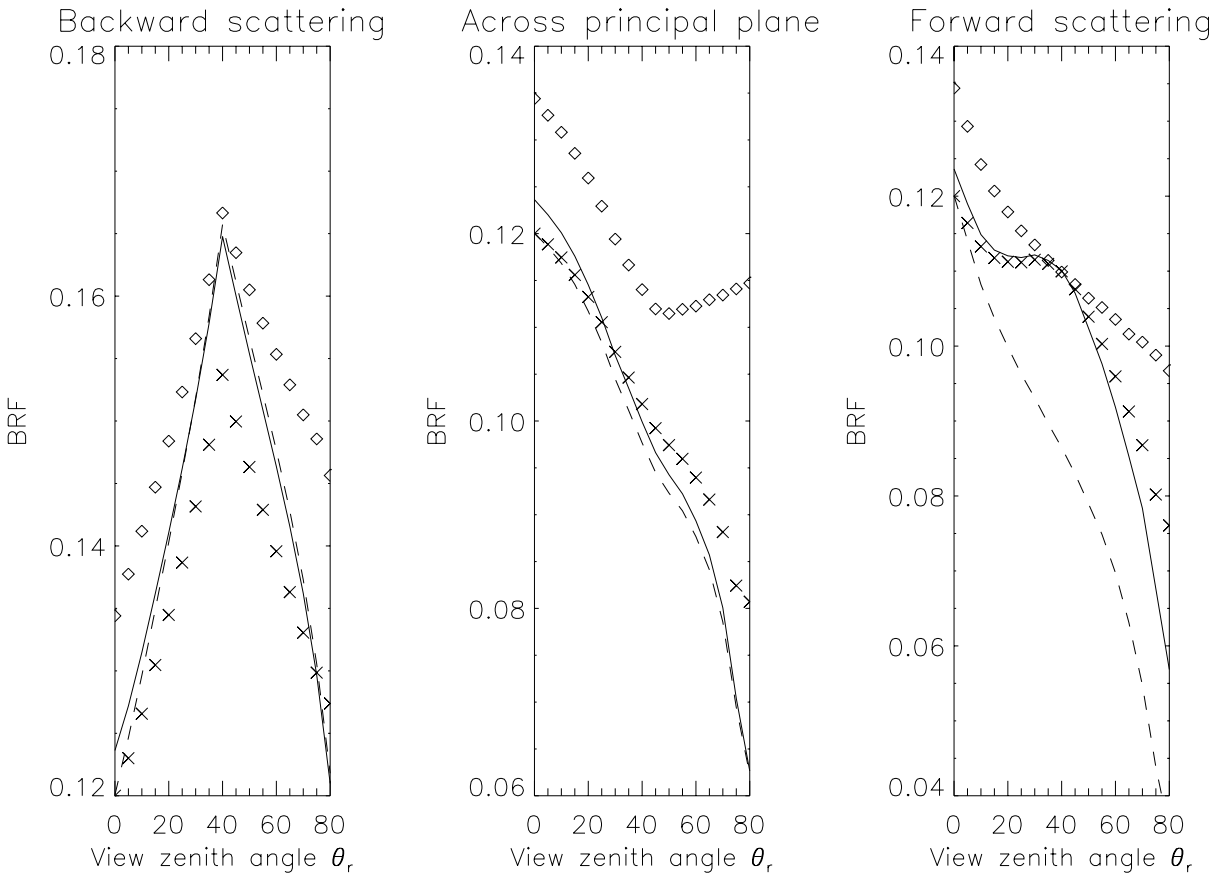

Figure 9.8: Modeled BRF values for different scales and skylight effect. Note the different scales on the y-axis. The solid line shows the full model including small scale BRDF for 0 % vegetation, the dashed line shows only the effects from large scale and intermediate scale (i.e. the specular peak of the small scale BRDF is suppressed), the diamonds show the large scale effects only. Model parameters a, b, c are the same as in fig. 9.7, incidence angle is $\theta_i = 40°$. Left plot shows backward scattering ($\varphi = 0°$), middle plot across principal plane ($\varphi = 90°$), right plot forward scattering ($\varphi = 180°$). The crosses show BRF values for the full model assuming an *isotropic* skylight (skylight irradiance = 20 % of the total irradiance). It can be seen that the intensity of the hotspot including skylight effects is decreased by about 10 %, and for larger viewing angles the BRF values including skylight effects increase strongly.

e.g. the hotspot or the specular peak) and increase the BRDF values at large viewing zenith angles.

For satellite measurements, the BRDF effects will be less pronounced than those shown in fig. 9.7. The viewing angles of most spaceborne sensors (with prominent exceptions like e.g. AVHRR) are smaller than $45°$, thus excluding a great part of the dynamic range shown in fig. 9.7. But even restricting the viewing zenith angles to $\theta_r \leq 45°$, the ratio of maximum to minimum value (called ANIX by (Sandmeier & Itten 1998)) is 1.95 for $\theta_i = 40°$ in fig. 9.7. Across principal plane ($\varphi = 90°$) effects are relatively small for $\theta_i = 40°$, our model predicts a decrease from $\theta_r = 0°$ to $\theta_r = 45°$ of about 20 % (also in fig. 9.7).

A real city is made up of street structures with a large variety of model parameters a and b (from wide streets and small buildings to high buildings and narrow streets). Thus we examined whether it is sufficient to model a city with one average street structure. Fig. 9.9 shows the BRDF of an urban area with 28 % vegetation at a wavelength of 660 nm for all possible combinations of parameters a, b varied by $\pm 50\%$ around their average value $a = b = 0.5$ ($a, b \in [0.25, 0.375, 0.5, 0.625, 0.75]$) (solid lines, 25 combinations). The BRF values from this average parameter set are marked by stars. The average BRF value (averaged over all BRF values from combinations of parameters a and b) is marked by squares. The stars and the squares are separated by less than 8 %. *We conclude that it is possible to describe the BRDF of an urban area using only the average structure parameters even if the individual parameters vary within* $\pm 50\%$.

Due to the lack of homogeneity in urban areas discussed above and in section 1, the BRDF shown in fig. 9.7 cannot be expected to model exactly the BRDF of *any* urban area. Still it is a major improvement over the Lambertian assumption.

9.8 Comparison with Airborne Data

So far very little satellite image data is available which would allow testing our model. The BRDF for an urban area extracted from POLDER data (without aerosol correction, about 6 km pixel-size) (Bicheron et al. 1999) shows a rather Lambertian BRDF in the principal plane (private communication), opposed to our model predictions. A study using AirMISR[2] data (Gerstl et al. 1999) however suggests a strong hotspot for an urban area in qualitative agreement with our model. Unfortunately, publicly available AirMISR data are corrupted by cloud cover, whereas newer data (e.g. used in (Gerstl et al. 1999)) without cloud cover are not yet publicly available. A better check will be possible as soon as data from satellites such as MODIS, MISR etc. (see introduction) will be available.

We validated the urban BRDF model with *airborne* data of high spatial resolution (nadir pixel $2.1\mathrm{m} \times 2.1\mathrm{m}$) by averaging over large areas. These averages correspond to measurements of pixels of low spatial resolution (e.g. $750\mathrm{m} \times 750\mathrm{m}$). Using high spatial resolution data has the advantage that we can determine the amount of vegetation present in the investigated area. It is also easy to exactly locate urban areas in high spatial resolution images, as well as to discriminate densely populated urban areas from less populated suburban areas.

9.8.1 Description of the Datasets

The data was taken with an airborne line scanner, the DAEDALUS AADS 1268, at a flight height of 900 m, yielding a nadir pixel size of 2.1 m × 2.1 m. 10 spectral channels cover a wavelength range from 0.46 μm to 2.16 μm. The measured radiances were converted to reflectances R (after an atmospheric correction) by using ground reflectance measurements as reference (Rothkirch et al. 1998). The maximum scan angle is $42.9°$ with 716 pixels per scan line. The images were acquired in August 1997 over Nuremberg, Germany, see fig. 9.10 for a sample. The investigated scene consists of residential, industrial and vegetated areas. Buildings usually

[2] AirMISR is a sensor similar to the MISR instrument on the Terra satellite, that was used on an high altitude aircraft for data evaluation purposes.

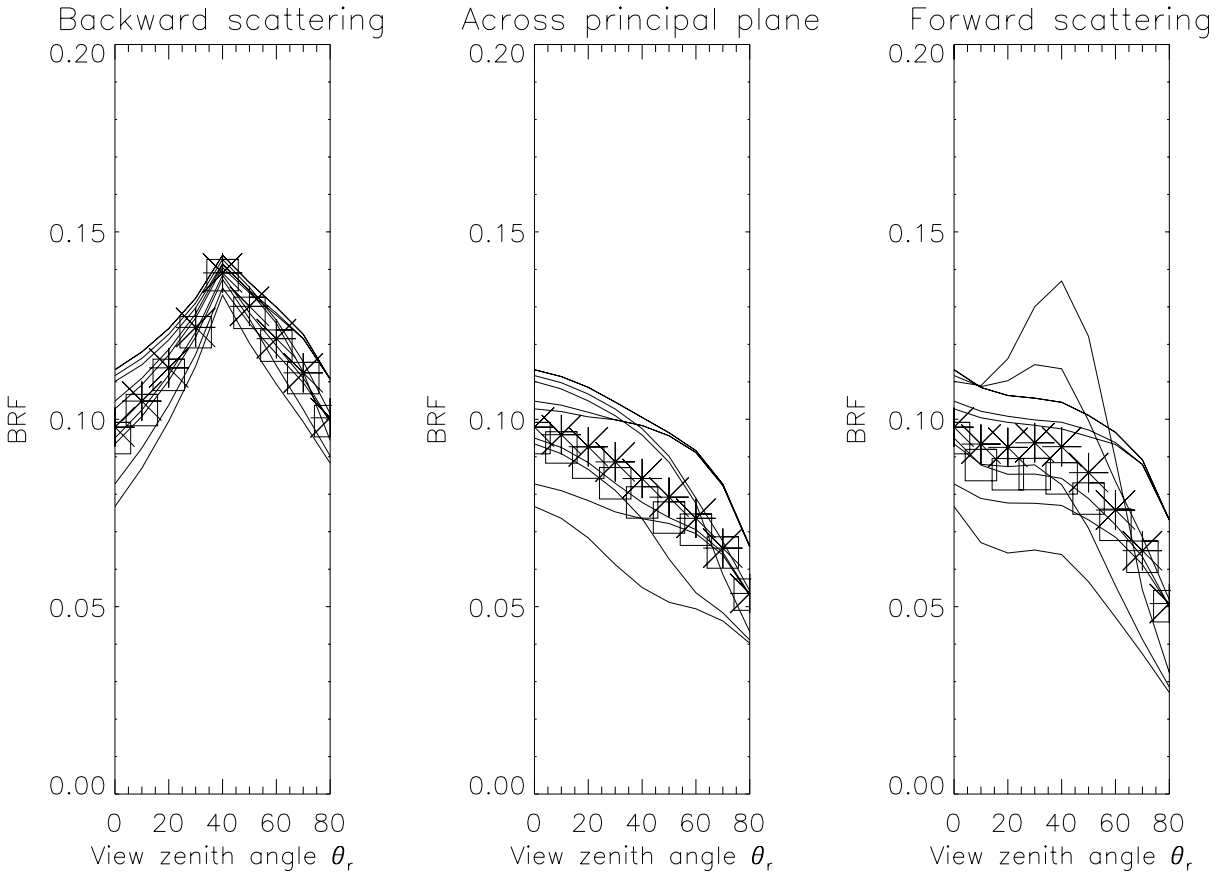

Figure 9.9: Modeled BRF values at 660 nm for an urban area with 28 % vegetation for several combinations of the structure parameters a and b (see section 9.7, only $a, b \in [0.25, 0.5, 0.75]$ are actually plotted). The stars show the BRF values of the average parameters ($a = b = 0.5$) , the squares show the average of the BRF values for all combinations $a, b \in [0.25, 0.75]$. They differ by less than 8 %. Left plot shows backward scattering ($\varphi = 0°$), middle plot shows across the principal plane ($\varphi = 90°$) and right plot shows forward scattering ($\varphi = 180°$).

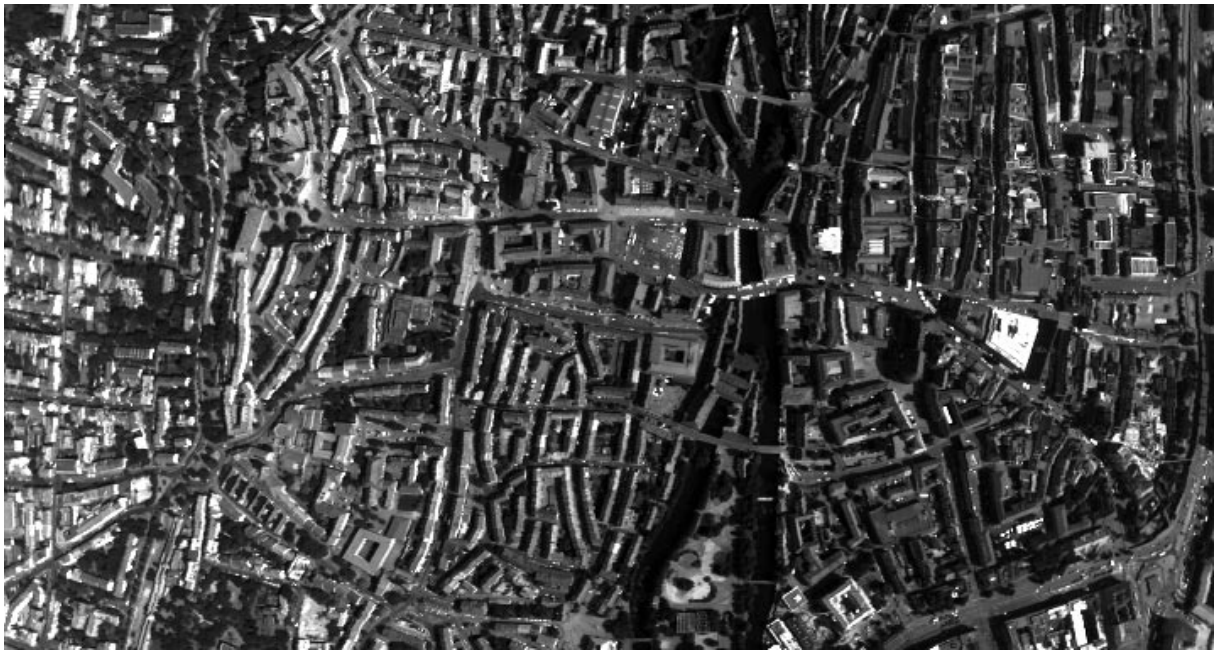

Figure 9.10: Sample of the image data (about 10% of the subset 'densely populated area') at a wavelength of 0.66 μm, histogram equalized. Flight direction is from top to bottom, scanning direction from left to right. The sun illuminates the scene from the right. The area in backscatter direction (left) is brighter than the area in forward scatter direction (right). Note that in the forward scatter direction, a few roofs contribute strongly, possibly due to specular scattering.

have less than 5 stories, the vegetated areas are dominated by deciduous trees, and grass. The sun zenith angle is 40.1°, the relative azimuth angle in backscatter direction is 25.6°, in forward scattering direction 154.4°. Care was taken to eliminate angular asymmetries of the sensor as described in chapter 8.

9.8.2 Data Processing

Two subsets from the available images were chosen. The first subset contains a densely populated urban area with a low fraction of vegetation, the second subset consists of a suburban area with a high fraction of vegetation. From the first subset, we derived two datasets: one contains only pixels with NDVI[3] lower than 0.4, the other contains all pixels. Assuming pixels with NDVI greater than 0.4 to be vegetation, we obtain 3 datasets with different proportions of vegetation:

1. Densely populated area, 0 % vegetation
2. Densely populated area, 28 % vegetation
3. Suburban area, 48 % vegetation

We projected the 716 pixels per line to a view zenith angle grid from -40° to $+40^\circ$ with an interval of 5°, yielding 17 different view zenith angles. For each view angle, we averaged each subset over its 4000 scan lines (3500 for the second subset), yielding a 'rectangular pixel' of $(\frac{716}{17} \cdot 2.1\text{m}) \times (4000 \cdot 2.1\text{m})$ for nadir viewing. This size seems to be adequate to average over the heterogeneity of this specific scene, the resulting BRDFs are quite smooth (stars in fig. 9.11). The basic assumption of our method is that the reflectance of a

[3]NDVI is calculated as $(R_{(\lambda=830nm)} - R_{(\lambda=660nm)})/(R_{(\lambda=830nm)} + R_{(\lambda=660nm)})$.

rectangular pixel is equivalent to the reflectance of a square pixel of the same area (in this case 850 m $\times$ 850 m), as long as the viewing angle is the same.

Fig. 9.12 shows the histograms of the NDVI of the subsets. Two peaks can be recognized for each subset, one centered around 0.05 corresponding to non-vegetated areas, the other one has its maximum at about 0.8 corresponding to vegetation. The NDVI threshold was chosen as 0.4 based on this histogram.

The resulting BRF values (BRF $\cong \pi \cdot$BRDF) are plotted for 3 spectral channels in fig. 9.11. The results from all 10 DAEDALUS channels are shown in (Meister et al. 1999b). The shape of the BRDF of the other channels does not vary much from the 3 channels presented here. The error of the reflectances derived from the DAEDALUS data is about 11 %, largely due to calibration uncertainties (Rothkirch et al. 1998).

The BRDF of the densely populated area excluding vegetation is plotted in the top row, including vegetation in the middle row. The bottom row shows the BRDF for the suburban area. The measured BRF values are plotted as stars. The left column shows BRF values at a wavelength of 660 nm, the middle column at 830 nm and the right column at 2160 nm. Each plot shows a strong rise in the backscatter direction ('hotspot'). This can be explained by the decreasing amount of shadow present the closer the viewing direction gets to the illumination direction. For visible light, the shape of all curves is very similar, increasing the amount of vegetation results in a negative offset because the reflectance of vegetation is lower than the average reflectance of man-made surfaces. In near infrared (NIR), the intensity of the hotspot increases if the amount of vegetation increases because the reflectance of vegetation in NIR is higher than the reflectance of man-made surfaces in NIR.

9.8.3 Model Validation

To compare our model predictions with the measured data, we plotted the results from the model (see section 9.7) into fig. 9.11 as a solid line. *The parameters a, b and c were estimated using aerial photographs of Nuremberg and the DAEDALUS data* (2.1 m nadir pixel size). We determined the amount of shadow for nadir viewing to about 20 % using the channels with wavelengths greater than 1000 nm (reflectances smaller than 0.8 % were classified as shadow). Given the sun angle of $\theta_i = 40^\circ$, the model parameter for the building height should be chosen as $b = 0.5$. Visual interpretation of the aerial photographs and supervised classification of the DAEDALUS data suggest that streets and buildings cover about the same area, thus the parameters a and c should be chosen as $a = c = 0.5$ (cf. eq. 9.1). From the aerial photographs we also deduced that the typical height of a building is about 15 m and that the typical width of a street is also 15 m, which confirms the choice of $a = b$. For simplicity, we used the same parameters for all 3 datasets (0 %, 28 % and 48 % vegetation) .

It can be seen that the overall shape is captured very well. The rise in backscatter direction is due to shadow hiding (hotspot). Remember the plots do not show exactly the principal plane, but are shifted 25° in azimuth. In the principal plane the hotspot is much stronger and a specular peak arises (cf. fig. 9.8).

In some cases the albedo of the modeled BRDF and the measured data do not agree very well, there are deviations up to 30 % (at $\lambda = 490$nm and $\lambda = 830$nm, 48 % vegetation, cf. table 9.2). The average deviation is 15 %. This means that our choice for the small scale man-made surfaces (cf. table 9.1) is different from the actual composition of the Nuremberg area and that the albedo of the grass sample (section 9.6.1) is not representative for the vegetation in Nuremberg. We do not see this as a major drawback for the urban BRDF model, because the albedos of different cities are expected to be different. Our major intention is to predict the shape of the BRDF, which is successful in the case of Nuremberg. More model validation on different urban areas is clearly needed.

To support our assumption that the major difference between model and data is due to a different albedo, we multiplied the BRDF of the man-made surface (eq. 5.1) and the vegetation (eq. 9.19) by a common factor to fit the data. (The common factor varies between 0.76 and 1.19 for the plots in fig. 9.11.) This is equivalent to multiplying the model results by this factor, because our model only considers single scattering. The result

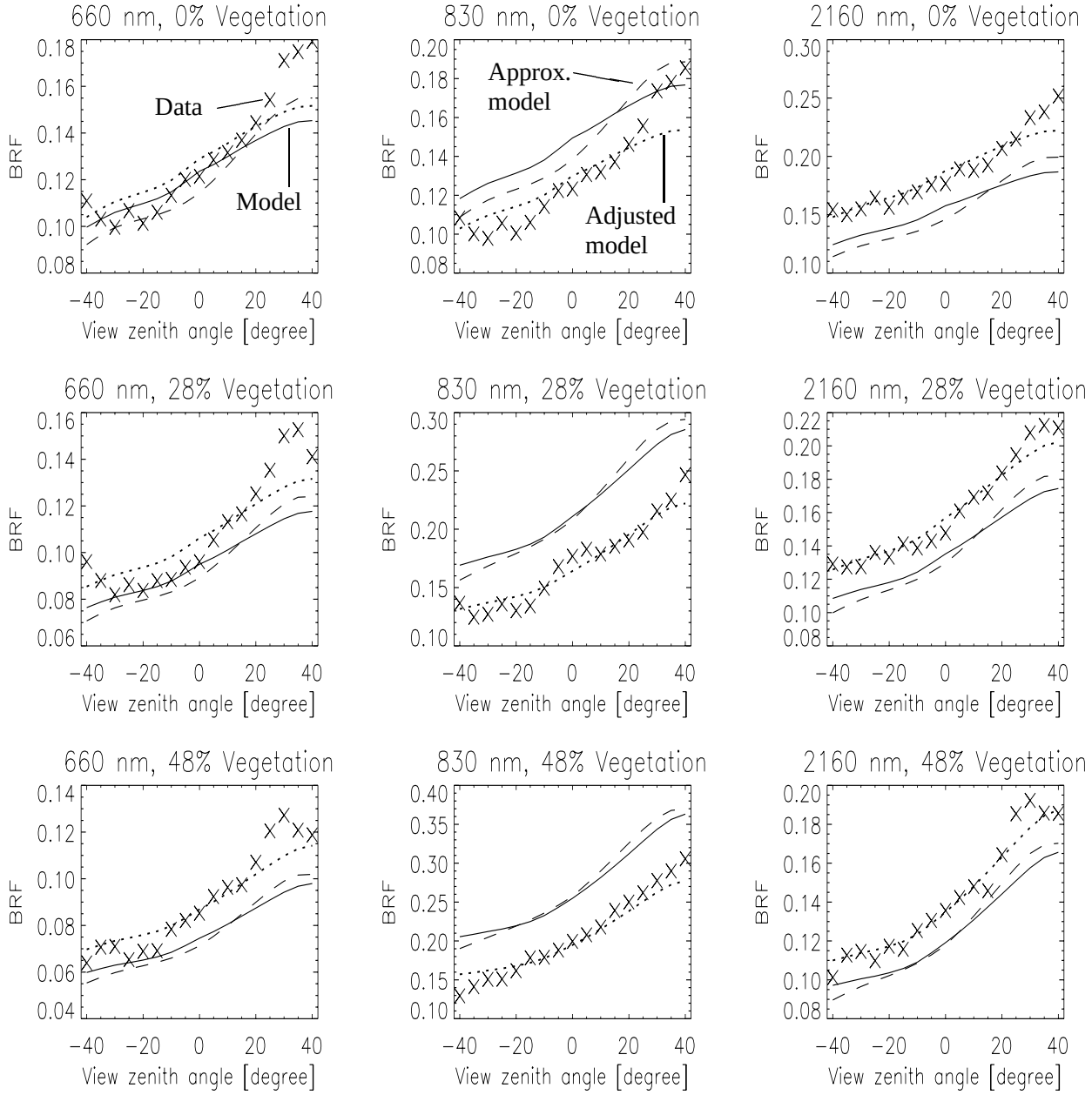

Figure 9.11: Comparison of the urban BRDF model and DAEDALUS data from Nuremberg. The BRF values are plotted versus view zenith angle. Negative view zenith angles correspond to forward scattering direction ($\varphi = 155°$), positive zenith angles to backscatter direction ($\varphi = 25°$). The sun zenith angle is $\theta_i = 40°$. Left column shows data for $\lambda = 660$nm, middle column for $\lambda = 830$nm and right column for $\lambda = 2160$nm. The top row of plots is from the dataset with 0 % vegetation, the middle row shows 28 % vegetation and the bottom row 48 % vegetation. The solid line shows the model predictions, the stars denote the DAEDALUS measurements. The dashed line shows the approximate function from eq. 9.26 fitted to the model predictions. The dotted line shows the model after adjusting for albedo, see section 9.8.3.

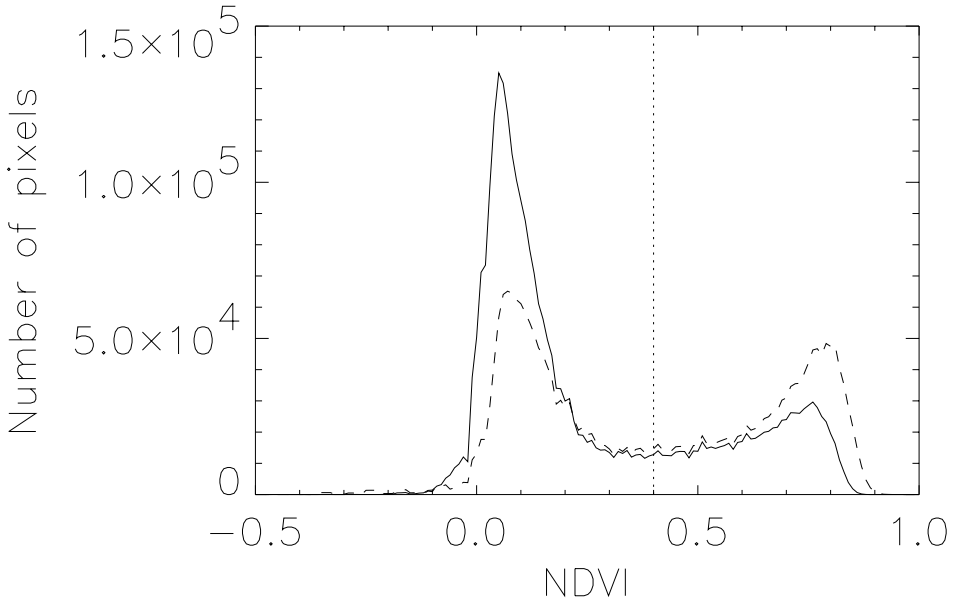

Figure 9.12: NDVI histogram of the first subset (urban area, solid line) and of the second subset (suburban area, dashed line). The dotted line shows NDVI = 0.4, pixels with a larger NDVI are considered as vegetation.

Wavelength [nm]			0 % veg.		28 % veg.		48 % veg.			
Center	Bottom	Top	DAE.	mod.	DAE.	mod.	DAE.	mod.	m.m.	grass
490	465	520	0.087	0.067	0.074	0.046	0.061	0.052	0.114	0.034
560	522	600	0.101	0.081	0.090	0.074	0.078	0.068	0.141	0.082
610	595	635	0.111	0.102	0.094	0.084	0.078	0.072	0.180	0.057
660	627	690	0.116	0.111	0.098	0.087	0.082	0.071	0.191	0.040
730	692	759	0.118	0.130	0.136	0.154	0.150	0.171	0.226	0.325
830	757	906	0.116	0.133	0.161	0.207	0.199	0.260	0.233	0.594
1680	1572	1780	0.175	0.154	0.182	0.168	0.187	0.178	0.267	0.310
2160	2055	2231	0.168	0.141	0.149	0.128	0.134	0.119	0.253	0.145

Table 9.2: Albedos of urban areas for $\theta_i = 40°$, computed with the approximate function (eq. 9.26) fitted to DAEDALUS data (DAE.) and model predictions (mod.), corresponding to the dotted resp. solid line in fig. 9.11. The first column gives the center wavelength, the second and third column show the wavelength range of the respective DAEDALUS channel where the sensitivity is at least 50 % of the maximum sensitivity. We estimate the error of the albedo of Nuremberg (DAEDALUS data) to be about 15 % (mainly due to calibration (Rothkirch et al. 1998) and model uncertainties). The last two columns show the albedo of the small scale surfaces used for modeling: man-made surface (m.m.) and grass).

is plotted as a dotted line in fig. 9.11, the agreement between stars and dotted line is generally very good. In some cases, especially at $\lambda = 660$ nm and 0 % vegetation, the model underestimates the hotspot, but generally width and intensity of the hotspot agree well.

In some cases, e.g. at $\lambda = 660$ nm and 28 % vegetation, a small rise in forward scattering direction can be seen that is not predicted by our model. One possible explanation is that the color of the asphalt on the street might be darker than the color of the walls and roofs. This would yield lower BRDF values at nadir, where the streets contribute strongly to the overall intensity. For 48 % vegetation, the rise in forward scattering direction cannot be seen, this supports our explanation because the amount of street asphalt in the scene is reduced.

For 0 % vegetation, the rise in backscatter direction in the DAEDALUS data is stronger than the rise predicted by the model, especially for 660 nm. The agreement between data and model could be improved by assuming that some man-made surfaces show a hotspot on the microstructure level, like the samples 'Asphalt' and 'Sanded roof paper' in chapter 5. Unfortunately, the samples were measured in the backscatter direction only with the SE590 sensor, which covers only the wavelength range up to 925 nm.

9.9 Approximate Analytical Function

The coding of the above model is straightforward, but tedious (the program code is available by email request[4] to the author). Furthermore the computing time is quite high due to the need for superposition of different street headings (section 9.4.6) (computing time per BRF value on a Sun Ultra II 296 MHz: 5 seconds). This is why we will give a simple, analytical approximation to our model.

It can be seen in fig. 9.7 that the basic characteristics of the modeled BRDF are the hotspot, the specular peak and the rise with large zenith angles. We will model these 3 components separately and fit their intensities (and one additional parameter) to the exact model evaluated with the parameters a, b, and c given in fig. 9.7 for 3 different amounts of vegetation. *Thus the approximate function can only be used if the average street structure is not expected to deviate strongly from the assumed values of a, b and c.* For differing amounts of vegetation the resulting parameters given in table 9.3 can be interpolated.

The hotspot will be modeled by the hotspot function derived by (Hapke 1993):

$$B(h,g) = \frac{1}{1 + (1/h) \cdot \tan(g/2)} \tag{9.24}$$

where g is the relative angle between viewing and illumination direction, see eq. 9.20. h determines the angular width of the hotspot peak. This function was developed to describe the hotspot of soils or powders based on shadow hiding. We omitted a factor $(\cos(\theta_i) + \cos(\theta_r))^{-1}$ from the original formula because this factor only applies to reflectances that are derived from radiative transfer theory. $B(h,g)$ equals 1 for the hotspot direction ($g = 0$) and decreases monotonously with g.

The specular peak will be modeled by f_r^{spec} given in eq. 5.1. The 'Geometric Attenuation Factor' G in this formula models the effects of shadowing and masking. This is similar to what is achieved by the hotspot function $B(h,g)$. We will replace G by $B(h,g)$ because shadowing and masking is dominated by the street structure. The Fresnel reflectance $F(n = 1.39, k = 0.2)$ will be approximated by $0.11 \cdot \exp(0.75 \cdot \theta_{\mathrm{i}}^2 \theta_{\mathrm{r}}^2)$ (all angles in radians). The width of the specular peak for roof surfaces is larger than for the street and wall surfaces, ($w^{\mathrm{roof}} = 0.028 \neq w = 0.095$ see section 9.6.2). For large zenith angles, the width is dominated by w^{roof}, because street and wall surfaces are mostly shadowed or hidden from view. For viewing and illumination close to nadir, both peaks are equally strong (because $a = c = 0.5$). Therefore we weight the peaks with $0.14 \cdot (0.5 + 0.5 \cdot \sin^2((\theta_i + \theta_r)/2))$ and $0.5 \cdot \cos^2((\theta_i + \theta_r)/2)$ (0.14 is the ratio of the specular

[4] meister@simbios.gsfc.nasa.gov, or nimeister0@netzero.com

Wavelength	Parameter	0 % veg.	28 % veg.	48 % veg.
660 nm	$p_1\,[\mathrm{sr}^{-1}]$	0.0603	0.0491	0.0413
	$p_2\,[\mathrm{sr}^{-1}]$	0.345	0.261	0.198
	$p_3 \cdot 100\,[\mathrm{sr}^{-1}]$	0.120	0.124	0.127
	h	0.483	0.443	0.401
830 nm	$p_1\,[\mathrm{sr}^{-1}]$	0.0739	0.1167	0.1476
	$p_2\,[\mathrm{sr}^{-1}]$	0.348	0.287	0.237
	$p_3 \cdot 100\,[\mathrm{sr}^{-1}]$	0.152	0.456	0.674
	h	0.481	0.451	0.438
2160 nm	$p_1\,[\mathrm{sr}^{-1}]$	0.0782	0.0725	0.0688
	$p_2\,[\mathrm{sr}^{-1}]$	0.348	0.281	0.229
	$p_3 \cdot 100\,[\mathrm{sr}^{-1}]$	0.163	0.228	0.276
	h	0.480	0.441	0.407

Table 9.3: Parameters of the approximate analytical function of eq. 9.26, fitted to the urban BRDF model data shown in fig. 9.11. Parameter p_3 is given multiplied by 100. Parameters describing the DAEDALUS data can be obtained by multiplying parameters p_1, p_2 and p_3 by the ratio of the albedo of the DAEDALUS data and the modeled albedo given in table 9.2. BRF values can be obtained by multiplying parameters p_1, p_2 and p_3 by π (BRF $\cong \pi\cdot$BRDF).

peak albedos, see eq. 9.23, the zenith angles are averaged in order to obey the reciprocity principle). We call the resulting specular peak $f_r^{\mathrm{spec-approx}}$:

$$f_r^{\mathrm{spec-approx}} = \frac{B(h,g)}{\cos\theta_i \cos\theta_r} \cdot \left(\frac{0.14}{2} \cdot \left(1 + \sin^2\frac{\theta_i+\theta_r}{2}\right) \cdot \mathrm{e}^{-(w^{\mathrm{roof}}\cdot\alpha)^2} + \cos^2\frac{\theta_i+\theta_r}{2} \cdot \mathrm{e}^{-(w\cdot\alpha)^2}\right) \cdot 0.11 \cdot \mathrm{e}^{0.75\cdot\theta_i^2\cdot\theta_r^2} \tag{9.25}$$

The rise with large zenith angles is produced by the vertical areas of the street structure. In eq. 9.8 it was shown that $\cos\theta_i^{VL}$ can be replaced by $\sin\theta_i$ for $\phi_i = 0°$. As in eq. 9.18 $\cos\theta_i^{VL}$ is divided by $\cos\theta_i$, this is equivalent to multiplying by $\tan\theta_i$. The same argument is valid for $\cos\theta_r^{VL}$, thus we will approximate this component by $\tan\theta_i \cdot \tan\theta_r$.

Summarizing, the approximate function has 4 parameters (p_1, p_2, p_3 and h):

$$f_r^{\mathrm{Approx}} = p_1 \cdot B(h,g) + p_2 \cdot f_r^{\mathrm{spec-approx}}(h,\theta_i,\theta_r,\varphi) + p_3 \cdot \tan\theta_i \cdot \tan\theta_r \tag{9.26}$$

The parameters were determined using a least-squares fitting procedure from the programming package IDL. A comparison between this approximate function and the exact model can be seen in fig. 9.13, where the BRF values of the exact model are plotted against the BRF values of the approximate function for 505 different combinations of angles. The BRF values were calculated for zenith angles θ_i and θ_r from $0°$ to $70°$ ($10°$ grid) and relative azimuth angles φ from $0°$ to $180°$ ($20°$ grid). The agreement between approximate function and exact model is excellent for zenith angles up to $60°$, the average deviation is 4.3 % for these angles, the maximum deviation is 19 % (for zenith angles up to $70°$ the average deviation increases to 6.1 %, with a maximum deviation of 54 %). These numbers are similar for different wavelengths resp. amounts of vegetation.

The approximate model is shown in fig. 9.11 as a dashed line, the respective coefficients are given in table 9.3.

In case a user wants to adjust the approximate model to his own urban BRDF data, we suggest to choose one set of parameters of table 9.3, selecting the most appropriate amount of vegetation and wavelength λ

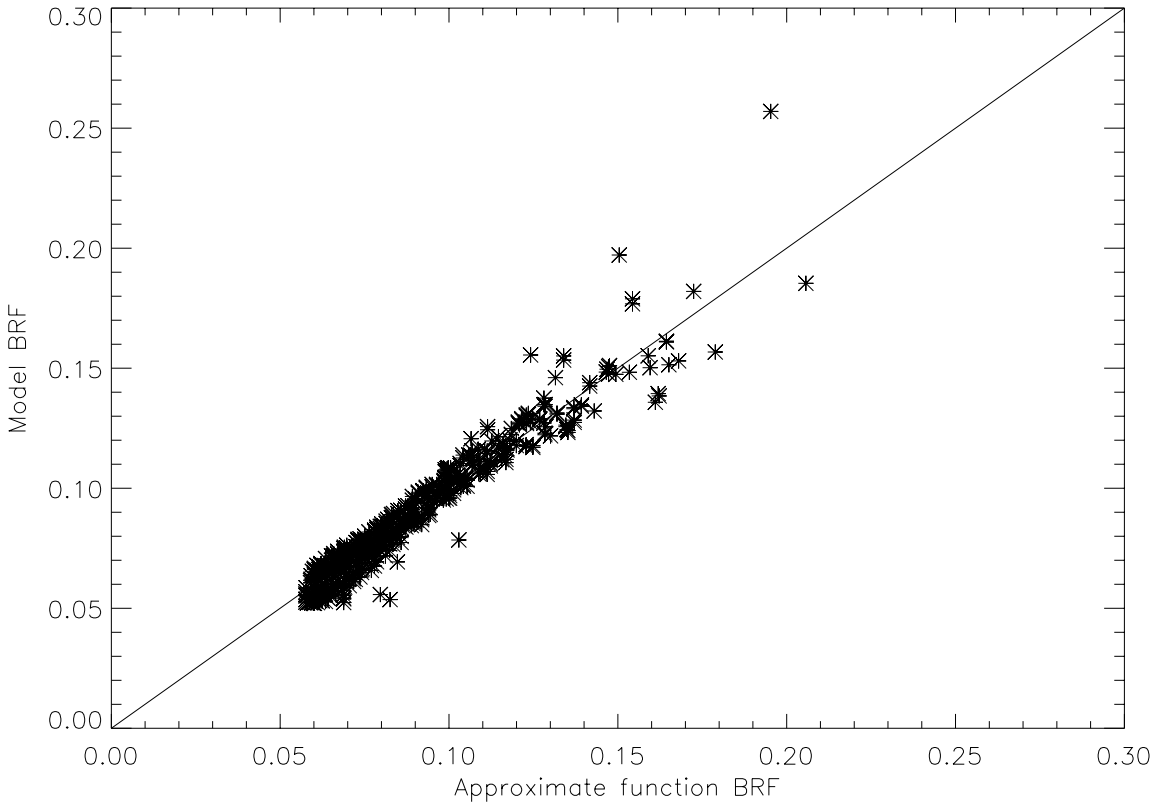

Figure 9.13: Scatterplot of BRF values of exact model (28 % vegetation, street structure parameters: $a = b = 0.5$, wavelength: $\lambda = 660$ nm) (y-axis) versus approximate model (x-axis) from eq. 9.26 using parameters from table 9.3, evaluated at $\theta_i, \theta_r \in [0°, 70°], \varphi \in [0°, 180°]$.

(660 nm for $\lambda < 700$ nm, 830 nm for the NIR, 2160 nm for $\lambda > 1000$ nm). Then parameters p_1, p_2 and p_3 should be multiplied with one common factor to fit the data. Fitting all 4 parameters independently from each other may lead to 'over-fitted' parameters if the angular sampling of the BRDF data is poor (see (Lucht & Lewis 2000)). Adjusting only one common factor makes it possible for a user to evaluate the BRDF even if the urban area was only measured at one combination of angles. This BRDF can e.g. be used for albedo determination. For an albedo determination with the approximate function, we suggest to set all the BRDF values with zenith angles $> 80°$ to their respective value at $80°$.

9.10 Sample Applications

We used the approximate function to investigate the dependence of the width of the hotspot (parameter h) on wavelength. The width of the hotspot decreases with increasing amount of vegetation, because vegetation has an intrinsic hotspot (see eq. 9.19) that adds to the hotspot caused by the street structure, whereas man-made surfaces are modeled by a Lambertian plus specular component (eq. 5.1). Although the width depends strongly on the amount of vegetation present in the scene, it stays remarkably constant over wavelength, varying in the ranges [0.48,0.50], [0.42,0.47] and [0.36,0.46] for proportions of vegetation of 0 %, 28 % and 48 % respectively for wavelengths from 490 nm to 2160 nm. This characteristic was not clear a priori, because the hotspot of the vegetation depends strongly on wavelength (Sandmeier & Itten 1999). This feature might be useful as an additional classification feature for urban areas, because many (probably most) vegetated surfaces show a wavelength dependence of the hotspot (the hotspot is usually less sharp for NIR wavelengths, because the amount of multiple scattering increases). (Sandmeier & Deering 1999) introduced the normalized

difference anisotropy index $NDAX$:

$$NDAX(\theta_i) = \frac{ANIX_{\mathrm{red}}(\theta_i) - ANIX_{\mathrm{NIR}}(\theta_i)}{ANIX_{\mathrm{red}}(\theta_i) + ANIX_{\mathrm{NIR}}(\theta_i)}, \tag{9.27}$$

where $ANIX_{\mathrm{red}}(\theta_i)$ is defined as the ratio of maximum BRF value divided by minimum BRF value, see (Sandmeier & Itten 1998). Using 660 nm as red wavelength and 830 nm as NIR wavelength, we obtain values of NDAX = -0.03, -0.03 and -0.09 from the DAEDALUS data for the 3 different datasets 0 %, 28 % and 48 % vegetation respectively. Evaluating the urban BRDF model at $\theta_i = 40^\circ$ and $\theta_r \leq 60^\circ$ we obtain NDAX = -0.01, -0.02 and 0.0 for the 3 different datasets respectively. We computed NDAX = 0.3 for grass, which is significantly higher. (Sandmeier & Deering 1999) investigated 6 different vegetation cover types, 5 of them have a NDAX of 0.3 or greater, only one (clear muskeg (fen)) has a NDAX lower than 0.1. *Thus the NDAX is a good index to support the classification of urban areas,* (i.e. to differentiate urban areas from other landcover classes). This is especially important for suburban areas like the one we investigated in the Nuremberg area (48 % vegetation), where the NDVI is 0.39 (varying between 0.33 and 0.44, depending on viewing angle) and a classification based on spectral information alone may become difficult.

We also used the approximate function to calculate the albedo by integrating eq. 9.26 over the upper hemisphere. The albedos are given in table 9.2 for an incidence angle of $\theta_i = 40^\circ$, for 3 amounts of vegetation (0 %, 28 % and 48 %) at the wavelengths of the DAEDALUS (channel 1 at 440 nm and channel 8 at 960 nm are not covered by the wavelength range of the sensors used to determine the small scale BRDF, see sections 9.6.2). The approximate function was fitted to the modeled data (see solid line in fig. 9.11) as well as to the modeled data adjusted to the albedo of the DAEDALUS data (see dotted line in fig. 9.11) using combinations of angles covering the whole upper hemisphere. The dependence of the albedo on θ_i is not strong, it is usually highest for nadir, depending on wavelength and the amount of vegetation. For $\theta_i = 60^\circ$ the albedo is on average about 10 % lower than for nadir illumination.

In general, the albedos derived from the model are lower than the albedos derived from the DAEDALUS data for wavelengths $\lambda < 700$ nm, higher in the NIR and lower for $\lambda > 1000$ nm. As discussed above, this is due to our choice of samples to model the small scale BRDF. We regard the albedos derived from the DAEDALUS data as more representative of urban albedo because our choice of samples was restricted to samples with a known BRDF.

We also provide the albedos of the man-made surface and the grass sample in the last two columns of table 9.2. They are higher than the albedos of the urban areas, because the urban structure produces shadowing and thus reduces the albedo.

Chapter 10

Summary

This study investigates the bidirectional reflectance of man-made, rough surfaces. The results are relevant for the remote sensing of urban areas and computer vision. New insight is obtained on the shape of the specular peak of rough surfaces.

In a measurement campaign at the *European Goniometric Facility* EGO, the *Bidirectional Reflectance Distribution Function* BRDF was measured for several man-made surfaces typical of urban areas (e.g. roof tiles, asphalt). The EGO consists of two rotatable quarter arcs, where different sensors or light sources can be attached. The system is programmable, which allows the effective measurement of a large number of angular combinations in a reasonable amount of time.

We evaluated the dominant error sources for laboratory BRDF measurements of man-made surfaces at the EGO. The average total error per wavelength of a single BRDF measurement varies with wavelength from 4 % to up to 14 %, depending on the spectral signature of the sample.

Measurements with a luxmeter showed that the lamp footprint is quite homogeneous for nadir illumination, but for larger incidence angles there is a rise of the intensity when approaching the lamp. This results in an error for the radiometer measurements, because the position of the center of the FOV of the detector SE590 depends on viewing angle. For samples with a constant reflectance spectrum, this is the dominant error source. We deduced the errors as a function of incidence and viewing zenith angles by comparing measurements with nadir viewing for different azimuths as well as measurements with an incidence angle of 50° for azimuths of 90° and 270°, assuming rotational symmetry of the samples. The error analysis could be improved if measurements with nadir illumination and different azimuths were available.

Comparing measurements with exactly the same illumination and viewing geometry, we determined the lamp constancy to 0.3 % and the detector noise of the SE590 to 0.2 % of the maximum value. The second error source becomes dominant for samples with a large variation in their reflected spectrum. This means that the illumination source should be chosen - whenever possible - in such a way that its maximum intensity multiplied by the sensor sensitivity is emitted at those wavelengths where the reflectance of the sample is low. For the experimental setup used in this study, this maximum is between 650 and 750 nm. The measured intensities become very low for wavelengths far away from this maximum. Demanding the instrument error to be lower than 2 % leads in our case to the exclusion of wavelengths lower than 425 nm and higher than 975 nm for the SE590. Thus we presented a general procedure to determine the appropriate wavelength range of the hyperspectral spectroradiometer SE590, which depends not only on instrument characteristics, but also on the illumination source and the samples used.

The errors of data from the detector ASDFieldspec are dominated by dark current noise. We believe that the instrument was set to its most sensitive mode. We determined the error from dark current to 20 counts, which leads to an average measurement error of 4.9 % for the samples used in this study. Both sensors are affected by problems in their upper wavelength range if the measured intensity is very high.

Two methods for calculating the irradiance are discussed. Both rely on measurements of a reference panel (in our case Spectralon). The first method assumes that the irradiance changes with viewing angle (possibly due to e.g. illumination inhomogeneities). Every measurement of the sample is divided by the measurement of the reference panel with the same angles and multiplied by the BRDF of the reference panel. The second method assumes that the irradiance changes only with illumination angle and integrates all the reflected radiances for each illumination angle. Dividing by the albedo of the reference panel yields the irradiance. The major advantage of the second method is that only the albedo, not the BRDF of the reference panel needs to be known. We chose the second method and show that the results are in better agreement with the reciprocity principle than the results from the first method.

The BRDF model of (Torrance & Sparrow 1967) (TS model) was compared to measurements of several man-made surfaces with very different roughnesses. The model can describe the measurements qualitatively very well, although the fits do not always pass a χ^2 test. Surfaces with a very large roughness show an increase in backscatter direction that can be well described by the BRDF model from (Oren & Nayar 1995). Shape and intensity of the specular peak vary less than 10 % for wavelengths from 450 nm to 700 nm, whereas the diffuse component varies strongly.

It is not possible to determine the index of refraction n and the index of absorption k using the TS model for the surfaces studied here, because the parameter for the specular intensity in the TS model allows different combinations of n and k to yield very similar Fresnel reflectances curves.

We discovered an important feature of the specular peak of rough surfaces: **we found that the width of the specular peak perpendicular to the principal plane decreases strongly with increasing illumination zenith angle, in the data as well as in the model**.

An analysis of the TS model shows that **the decrease is approximately proportional to the cosine of the illumination angle** θ_i, the deviations increase with increasing surface roughness. The proportionality to $\cos\theta_i$ of the *width perpendicular* to the principal plane is accompanied by an increase in reflectance in *intensity in* the principal plane that is $1/\cos\theta_i$ stronger than the increase for a perfectly smooth surface. Thus, these two proportionalities cancel in the calculation of the specular albedo.

Topography data is available for 8 of the samples. The vertical resolution is 0.16 μm, the horizontal resolution is 1 μm for 3-D-profiles of 1 mm $\times$ 1 mm and 1.24 μm for 2-D-profiles of 10 mm length. We derived the average surface inclination from the topography data and compared it to the average surface inclination derived from BRDF measurements. The BRDF models predict much smoother surfaces than the measured topography data by factors from 4 to 10. After smoothing over 20 μm, the deviations become smaller than 50 %.

We conclude that for the surfaces investigated in this study, which are rough on a scale comparable to the wavelength of the incoming light, the width of the specular peak cannot be predicted from our topography measurements by smoothing with one common bin size. We do not know if this is due to a lack of insight into the physical mechanisms governing the specular reflectance of rough surfaces or due to inappropriate resolution of the topography data. Maybe it is wrong to look for one common bin size because each surface could have its own characteristic facet size that determines the spatial dimension involved in the light scattering process.

The topography measurements indicate that the size of the surface patches forming the V-cavity in the TS/ON model is in the range of 20μ**m**. This result is supported by the fact that the width of the specular peak derived from BRDF measurements is relatively independent of wavelength. Because the TS and the ON model are independent of the size of the V-cavity, this result cannot be obtained from fitting either model to the BRDF measurements without the topography data.

A BRDF model for large scale urban areas (pixel-diameter $>$ 500 m) has been developed. It is derived from modeling BRDF effects on 3 scales: geometrical optics is applied to a simplified street structure, intermediate sized objects are modeled similarly. The small scale BRDF of man-made surfaces and vegetation is incorporated as well, based on the EGO measurement campaign described above and goniometer BRDF measurements of grass by (Sandmeier & Itten 1999).

The model basically depends on 5 parameters: the amount of vegetation, two geometry parameters to model the average width of the street structures and the height of buildings on the large scale and two geometry parameters to model the intermediate scale. The dominant features of the resulting BRDF are a hotspot, a specular peak and a rise for high zenith angles.

We derived large scale urban BRDF data from airborne imagery for 3 multispectral datasets for a limited set of angles. Except for the albedo, the model agrees very well with the data.

A post-flight angular calibration method of the DAEDALUS scanner had to be used to derive the data. It yielded comparable calibration factors as other calibrations studies on DAEDALUS instruments, with corrections of up to 15 %.

Our model can be used as input to calculate albedo, for atmospheric correction algorithms and global BRDF maps. Knowledge about the urban BRDF can improve classification and change detection algorithms. For users demanding speed and easy implementation, an analytical function is given that captures the dominant features very well.

An extensive validation of the model presented here will be possible as soon as satellite data with pixel-diameters of about 1 km (like MODIS, MISR, etc.) will be available. Future improvements of the urban BRDF model will have to include multiple scattering effects, a more elaborate treatment of the vegetation BRDF and varying compositions of the man-made surface BRDF. Especially relaxing the assumption that all the man-made surfaces have the same color (i.e. assigning roofs, walls and streets different albedos) can change the resulting urban BRDF considerably.

The influences on the urban BRDF from the amount of dirty or wet surfaces are not expected to change the shape of the BRDF considerably, except for the specular peak which will strongly increase for wet surfaces and decrease for dirty surfaces (the albedo however can change strongly). The DAEDALUS data of Nuremberg contain dirty surfaces, but almost no wet surfaces. The effect of varying heights of buildings is expected to be negligible.

Chapter 11

Acknowledgements

Many people contributed to this thesis, but most of all I have to thank André Rothkirch for his cooperation. Intensive discussions, support in the data acquisition in Ispra, tips on software usage, and help with several administrative procedures all played important roles in the completion of this thesis.

Prof. Hartwig Spitzer and Prof. Johann Bienlein provided valuable guidance and suggestions, spending a considerable amount of time on improving this thesis.

I greatly enjoyed the nice working atmosphere at Ispra and thank Brian Hosgood, Giovanni Andreoli and Alois Sieber from JRC, Italy for their cooperation.

Dr. Wolfgang Lucht and Prof. Alan Strahler made it possible for me to spend 3 months in the Center of Remote Sensing at Boston University prior to my PhD studies, which turned out to be an extremely important visit for me. The discussions with Wolfgang inspired the large scale urban BRDF model of this thesis.

I am indepted to Stefan Sandmeier for providing BRDF data on vegetation and fruitful suggestions.

I also thank Dr. Manfred Schröder and Volker Amman from the German Aerospace Establishment DLR (Oberpfaffenhofen) for their collaboration with my working group CENSIS.

Furthermore, I like to thank my coworkers for their support and fruitful discussions, including Ramon Franck, Niklas Rega, René Monno, Dr. Rafael Wiemker and Dr. Martin Kollewe.

Special thanks to my wife Wenge Ni and to my parents Edda and Dr. Friedrich Emil Meister, on whose loving support I could always rely.

I thank the 'Deutsche Forschungs Gemeinschaft' DFG and the University of Hamburg for their financial support.

Chapter 12

Appendix

Contents:

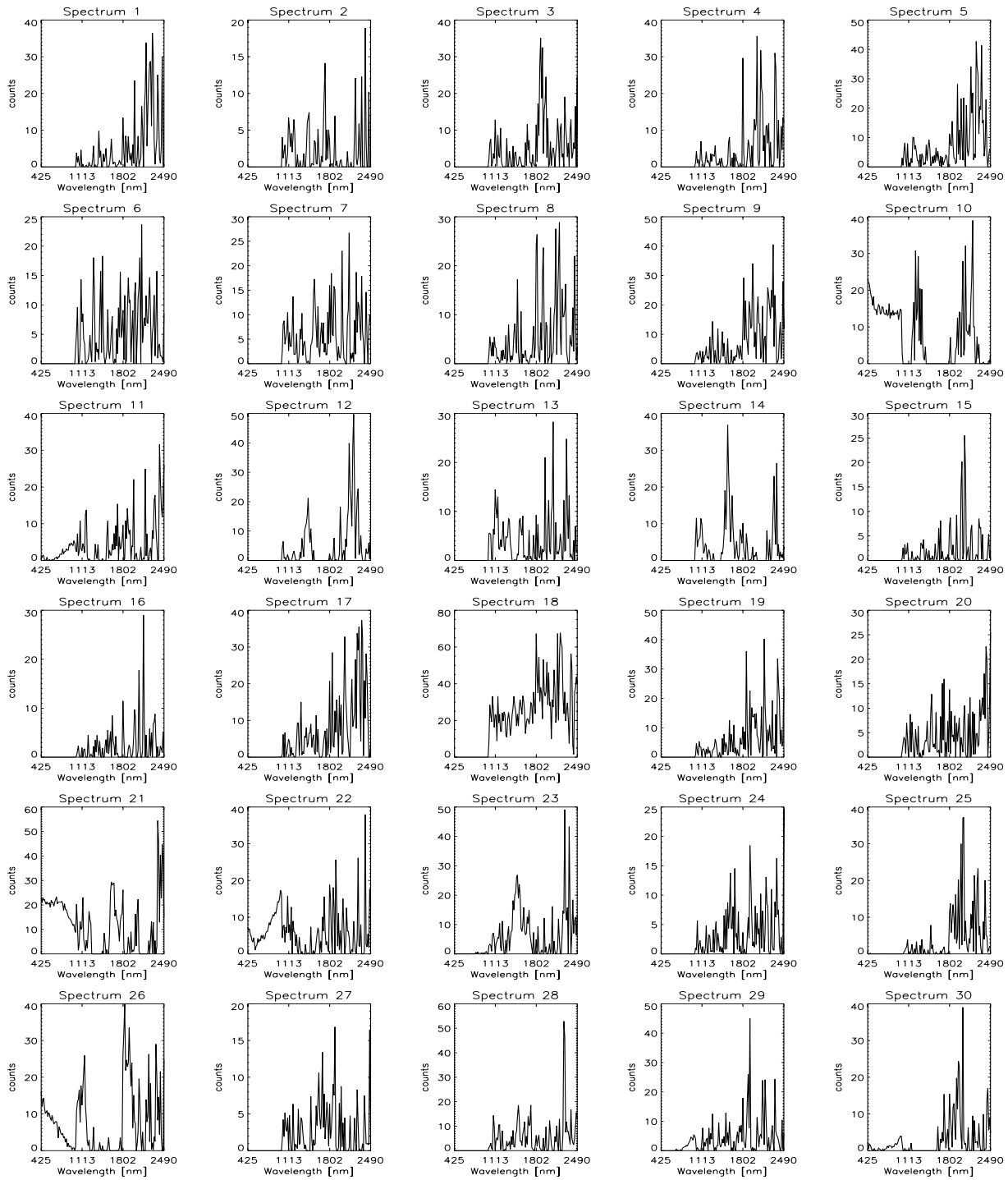

Figure 12.1: Dark current measurements of the ASD, obtained by completely covering the detector entrance. The root mean squared values are shown in fig. 4.16, page 38.

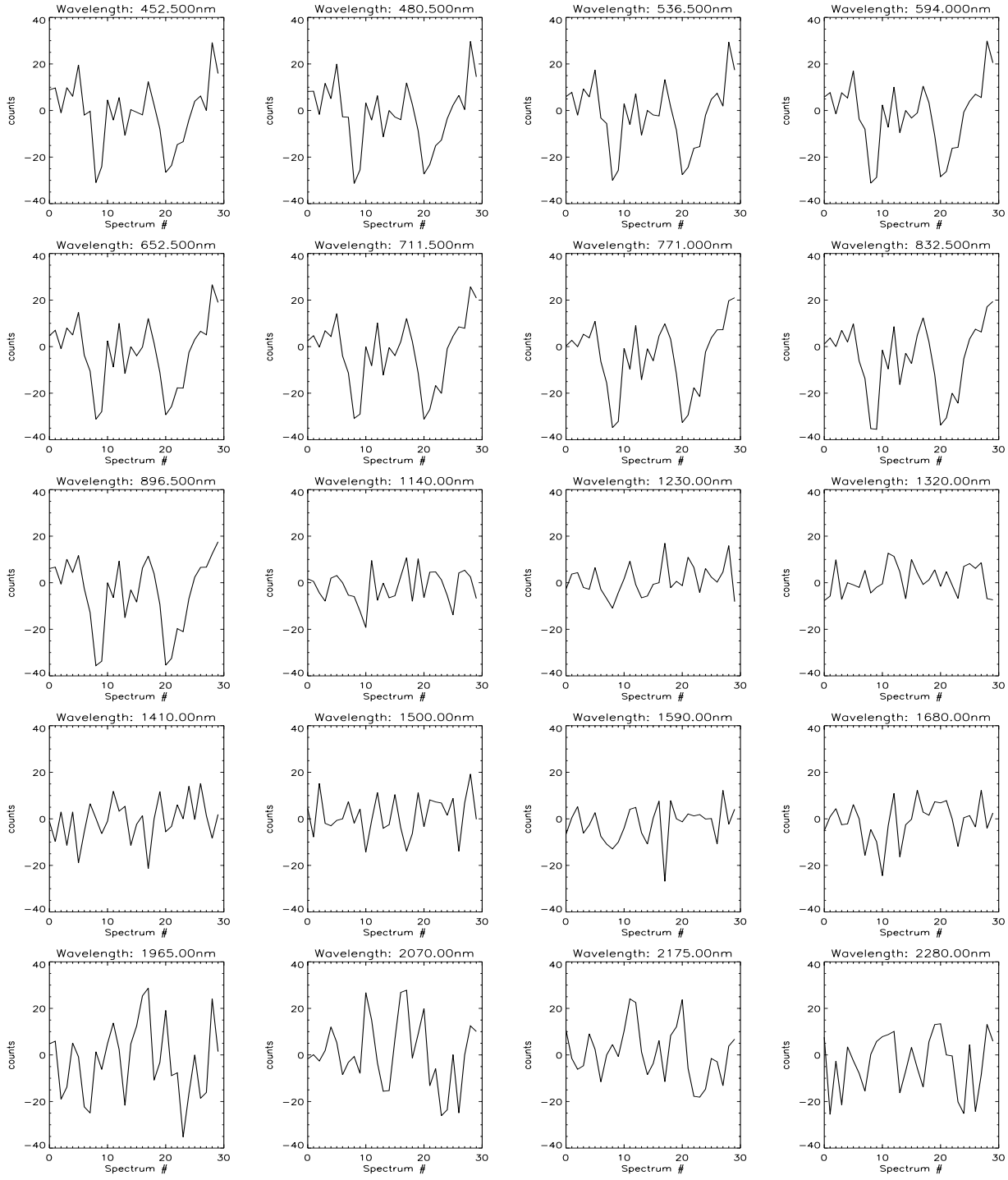

Figure 12.2: Constancy measurements of the ASD, obtained by repeated measurements of Spectralon 100 % without moving the goniometer. The plots show the measured raw data after subtraction of the median value. See fig. 4.17, page 39 for the standard deviation of these measurements, see section 4.9.2.

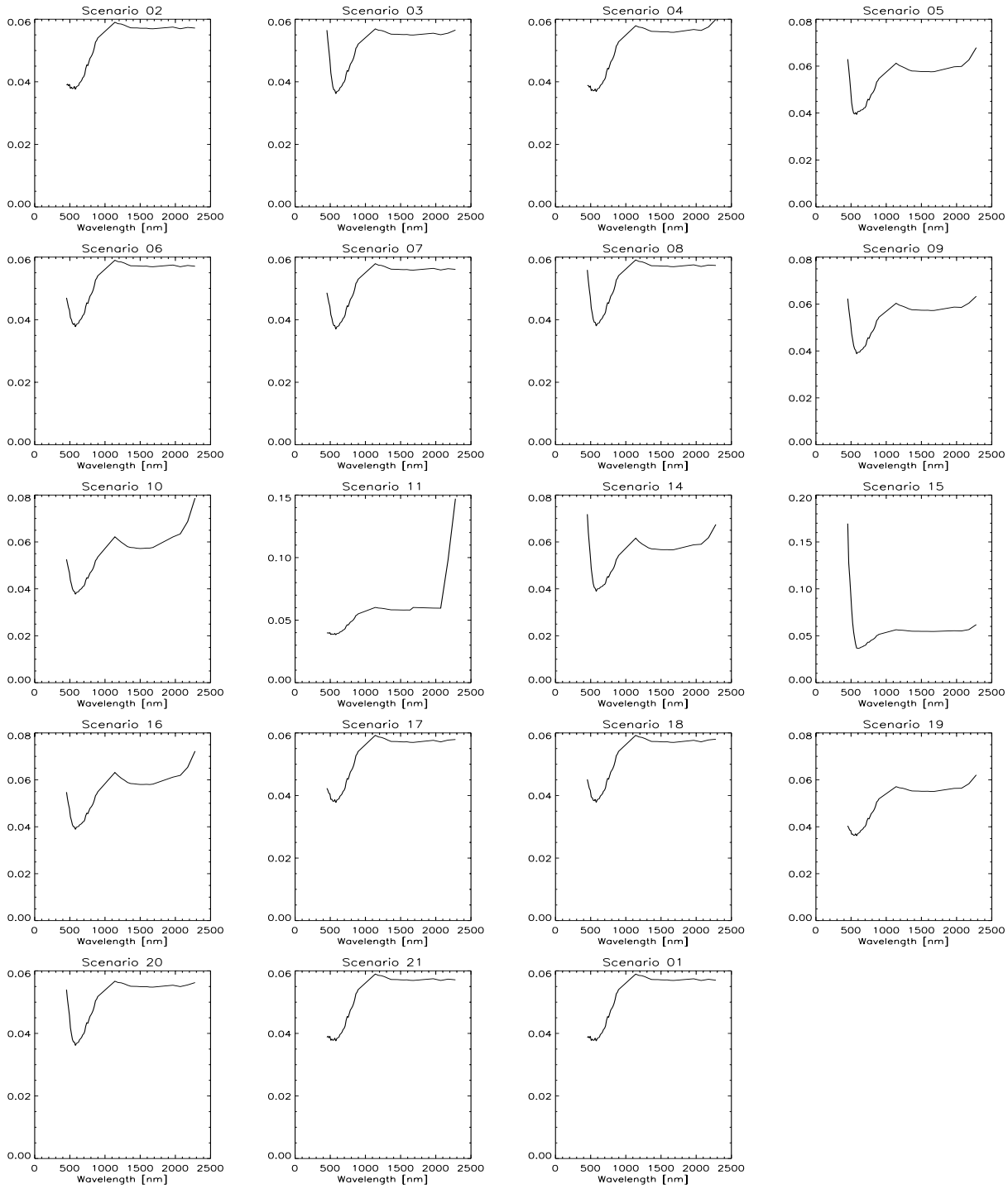

Figure 12.3: Average relative error of ASD measurements per sample as a function of wavelength, see section 4.9.2.

Sample	$t_0\,[\mathrm{sr}^{-1}]$	$t_1\,[\mathrm{sr}^{-1}]$	$w\,[\mathrm{deg}^{-1}]$	n	ρ_s	χ^2/d_f
Spectralon 0.5	0.155 ± 0.002	0.14 ± 0.12	0.032 ± 0.002	1.62 ± 1.0	0.026	1.0
Red roof tile	0.0161 ± 0.0004	0.19 ± 0.06	0.035 ± 0.001	1.83 ± 0.5	0.043	2.1
Red Aluminum	0.0144 ± 0.0002	3.39 ± 0.93	0.154 ± 0.001	1.69 ± 0.27	0.041	7.1
Blue concrete	0.0770 ± 0.0004	1.09 ± 0.27	0.084 ± 0.001	1.51 ± 0.18	0.031	1.5
Red concrete	0.0133 ± 0.0002	1.16 ± 0.23	0.081 ± 0.001	1.46 ± 0.12	0.032	3.3
Spectralon 1.0	0.3008 ± 0.0018	0.08 ± 0.27	0.044 ± 0.005	2.30 ± 9.33	0.021	0.7

Table 12.1: Parameters obtained from fitting the TS model (eq. 5.1) to the SE590 data of the respective sample at a wavelength of $\lambda = 425$ nm. The parameter k was set to 0.25. See chapter 5 for a discussion of the errors of the parameters. The error of the specular albedo ρ_s is estimated to be about 5 %. The last column shows the χ^2 value over the degrees of freedom d_f.

Sample	k_d	$k_s\,[\mathrm{sr}^{-1}]$	$k_w\,[\mathrm{rad}]$	n	ρ_s	χ^2/d_f
Sanded roof paper	0.024 ± 0.001	0.048 ± 0.04	0.593 ± 0.005	2.2 ± 1.8	0.032	0.6
Asphalt (Cadr.)	0.14 ± 0.001	0.025 ± 0.08	0.39 ± 0.02	2.6 ± 11.4	0.015	1.0

Table 12.2: Parameters obtained from fitting the ON model (eq. 5.8) to the SE590 data of the respective sample at a $\lambda = 425$ nm. The parameter k was set to 0.25. See chapter 5 for a discussion of the errors. The error of the specular albedo ρ_s is estimated to be about 5 % for the sample 'Asphalt'. The specular albedo of the sample 'Sanded roof paper' is considerably overestimated due to ignoring the black background, see page 7, propably by as much as 30 %. The last column shows the χ^2 value over the degrees of freedom d_f.

Sample	$t_0\,[\mathrm{sr}^{-1}]$	$t_1\,[\mathrm{sr}^{-1}]$	$w\,[\mathrm{deg}^{-1}]$	n	ρ_s	χ^2/d_f
Spectralon 0.5	0.162 ± 0.002	0.18 ± 0.19	0.031 ± 0.003	1.40 ± 0.8	0.020	0.6
Red roof tile	0.120 ± 0.001	0.17 ± 0.15	0.044 ± 0.002	1.75 ± 1.1	0.025	0.8
Red Aluminum	0.143 ± 0.001	2.56 ± 2.04	0.181 ± 0.002	1.98 ± 1.2	0.034	3.3
Blue concrete	0.090 ± 0.001	0.85 ± 0.36	0.085 ± 0.001	1.54 ± 0.32	0.025	0.6
Red concrete	0.103 ± 0.001	0.82 ± 0.37	0.0857 ± 0.002	1.57 ± 0.37	0.025	0.8
Spectralon 1.0	0.300 ± 0.002	0.09 ± 0.31	0.046 ± 0.008	2.02 ± 7.04	0.017	0.5

Table 12.3: Parameters obtained from fitting the TS model (eq. 5.1) to the SE590 data of the respective sample at $\lambda = 900$ nm. The parameter k was set to 0.25. See chapter 5 for a discussion of the errors of the parameters.

Sample	k_d	$k_s\,[\mathrm{sr}^{-1}]$	$k_w\,[\mathrm{rad}]$	n	ρ_s	χ^2/d_f
Sanded roof paper	0.043 ± 0.001	0.055 ± 0.06	0.671 ± 0.008	2.2 ± 2.5	0.042	0.7
Asphalt (Cadr.)	0.219 ± 0.001	0.032 ± 0.05	0.34 ± 0.04	1.7 ± 2.6	0.007	0.7

Table 12.4: Parameters obtained from fitting the ON model (eq. 5.8) to the SE590 data of the respective sample at $\lambda = 900$ nm. The parameter k was set to 0.25. See chapter 5 for a discussion of the errors.

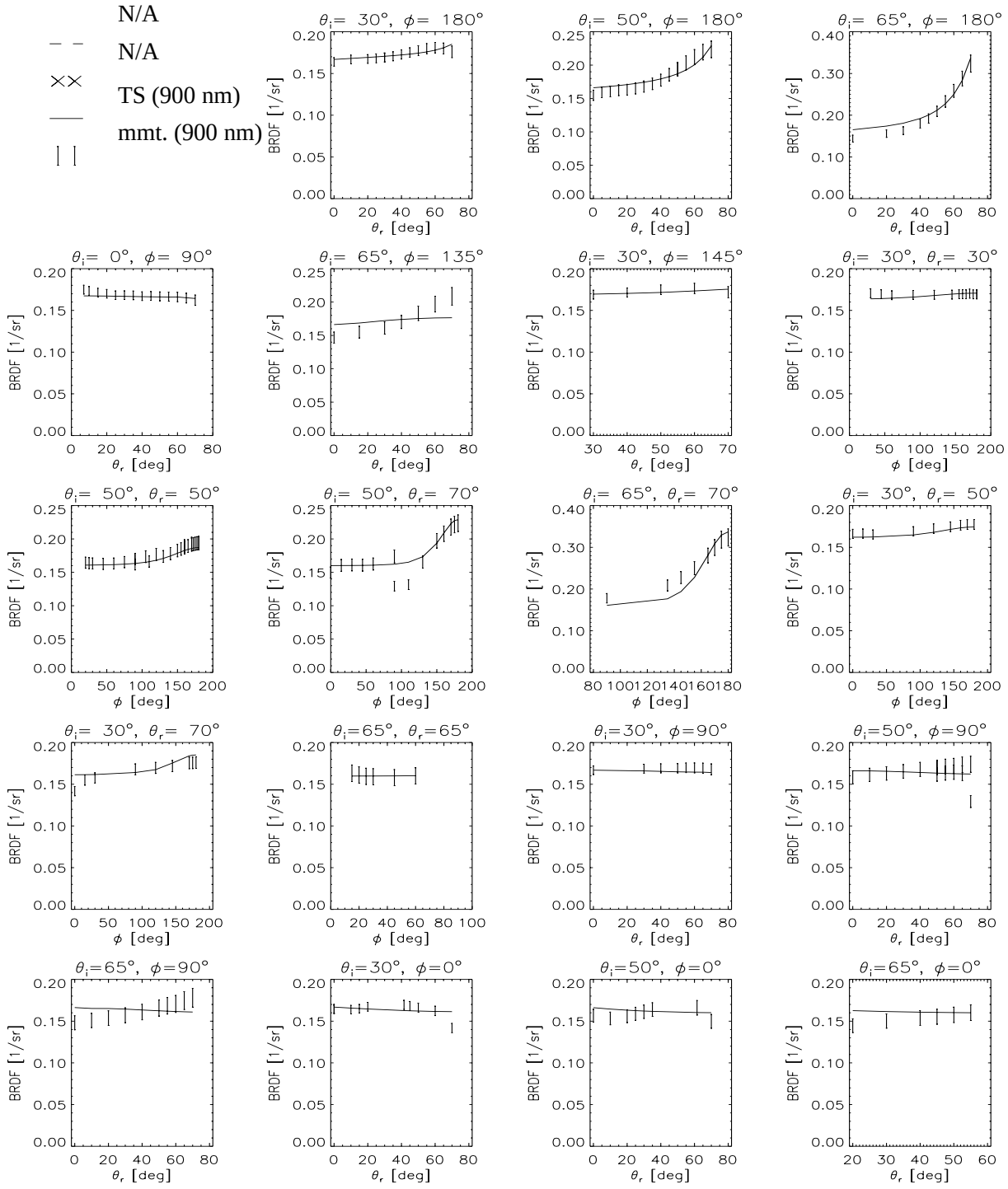

Figure 12.4: TS model fitted to BRDF measurements (mmt.) of the SE590 for Spectralon 0.5 at various angles.

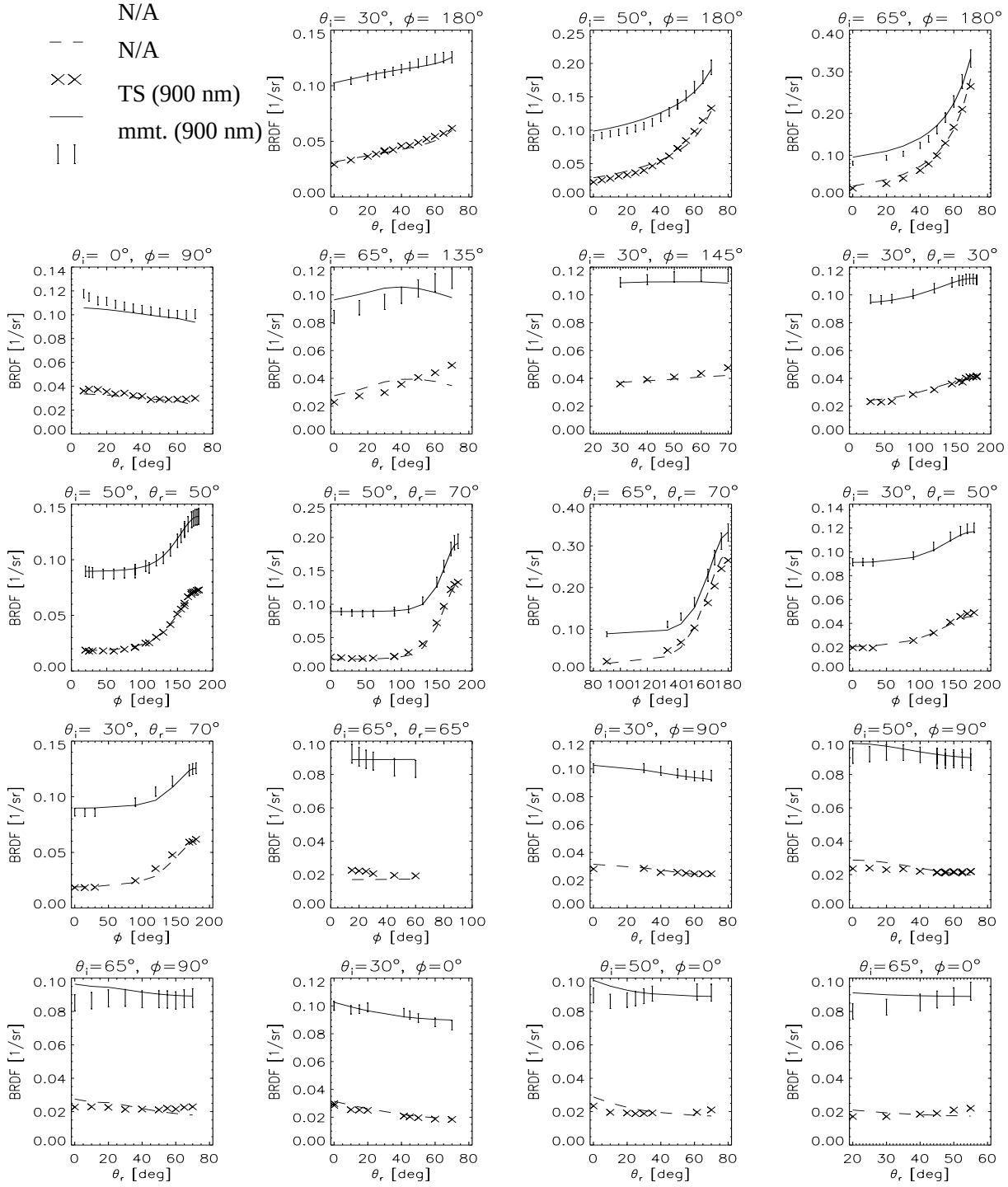

Figure 12.5: TS model fitted to BRDF measurements of the SE590 for 'red roof tile' at various angles.

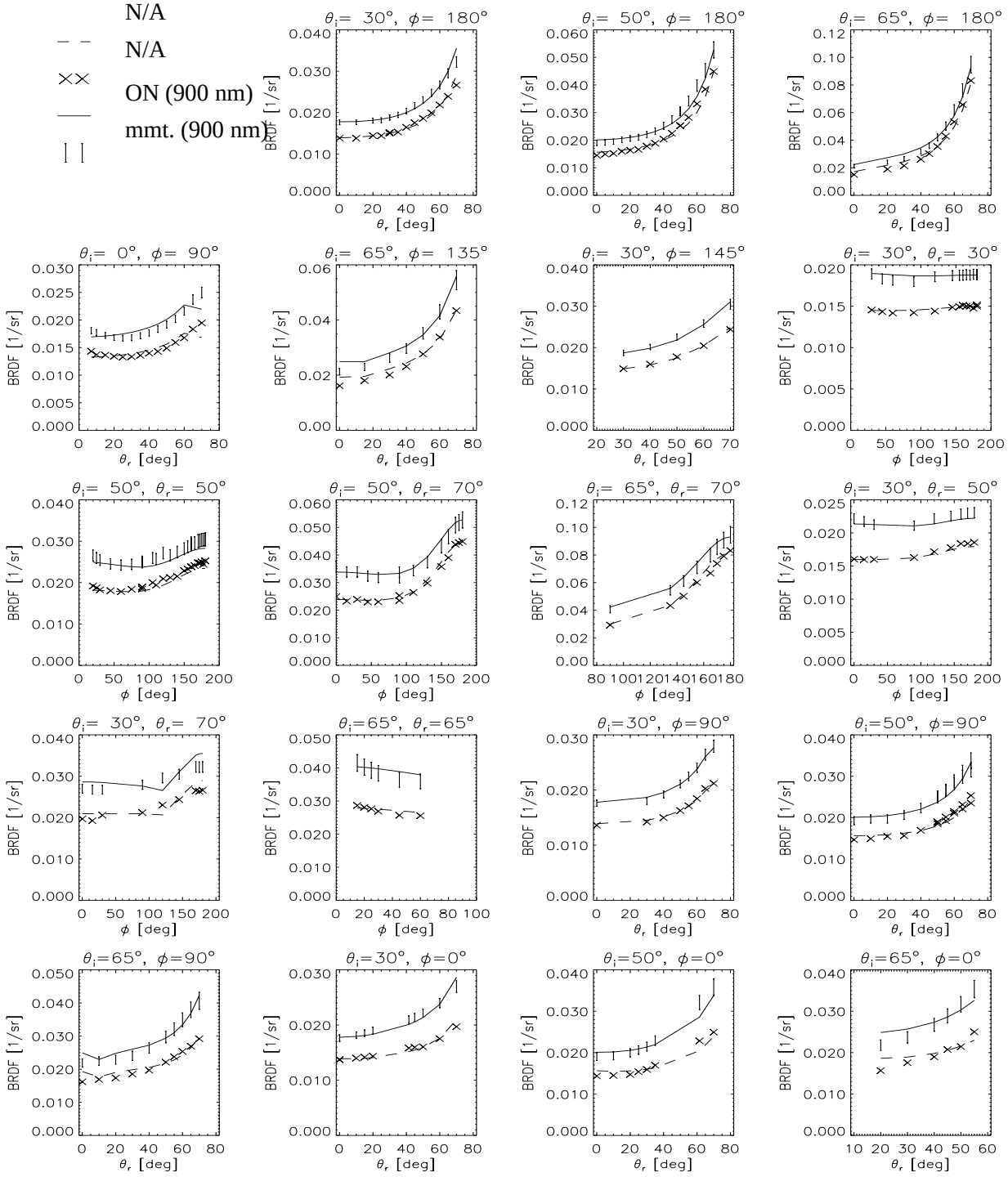

Figure 12.6: ON model fitted to BRDF measurements of the SE590 for 'sanded roof paper' at various angles.

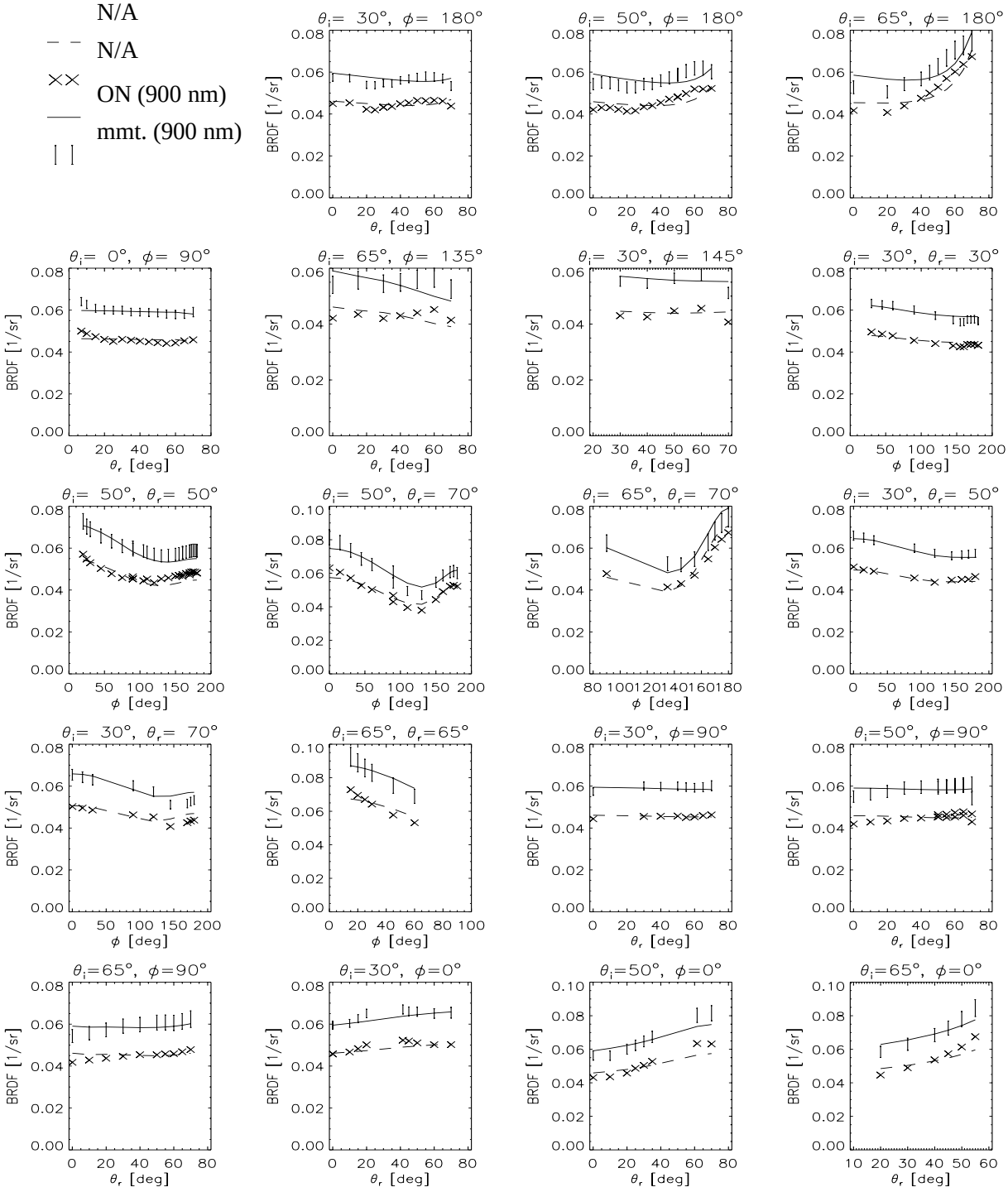

Figure 12.7: ON model fitted to BRDF measurements of the SE590 for 'asphalt' at various angles.

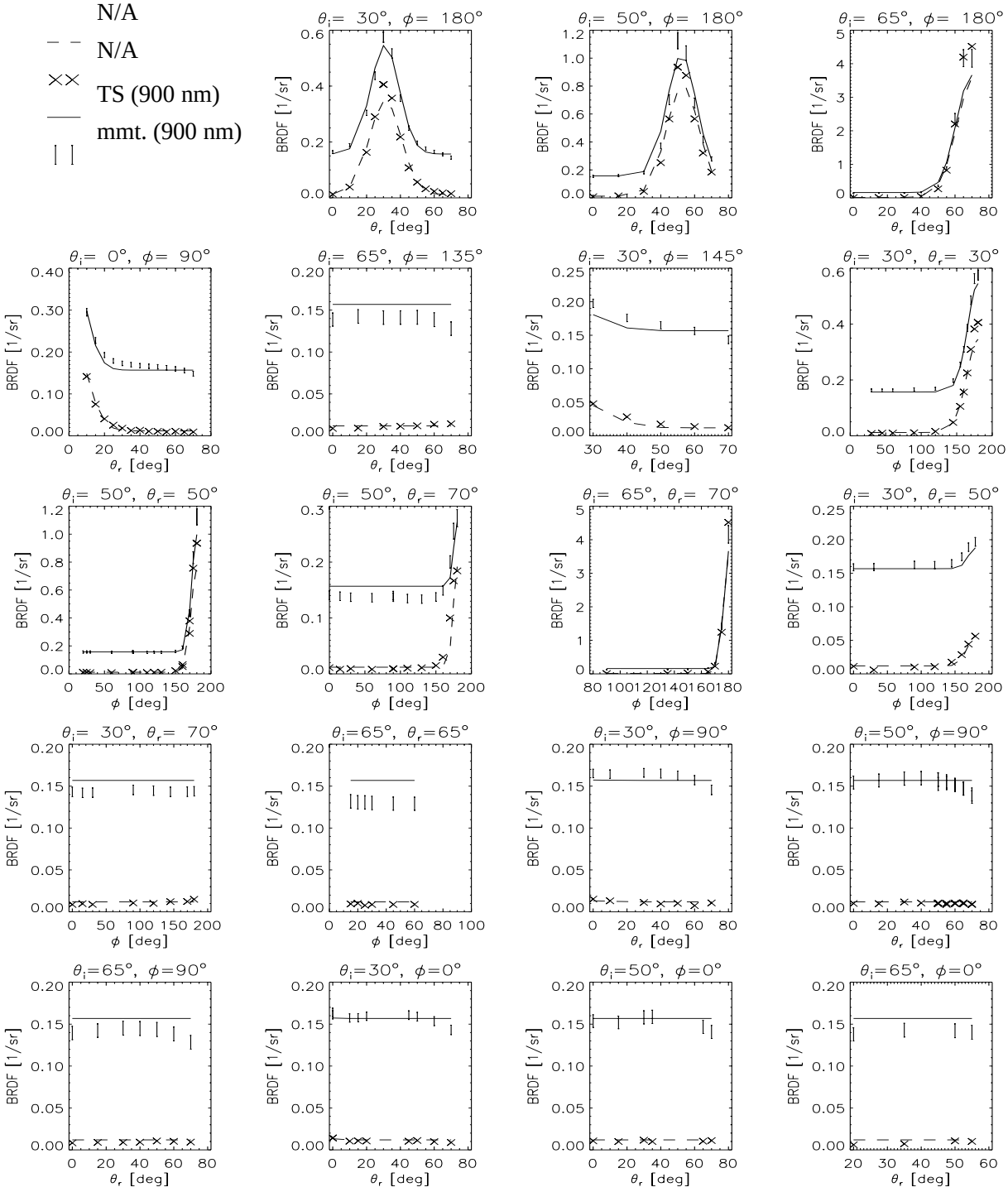

Figure 12.8: TS model fitted to BRDF measurements of the SE590 for ’aluminum’ at various angles.

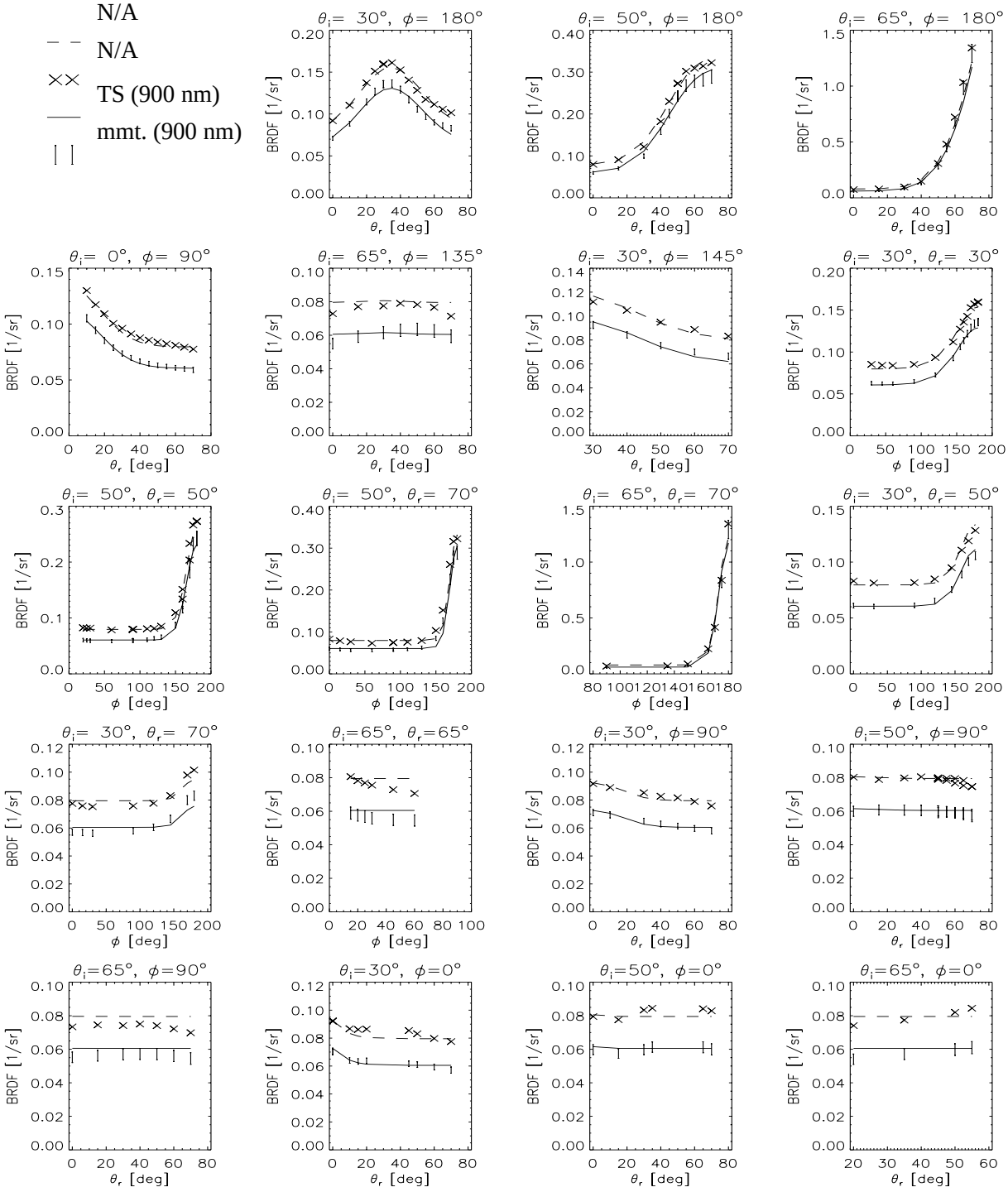

Figure 12.9: TS model fitted to BRDF measurements of the SE590 for ’blue concrete’ at various angles.

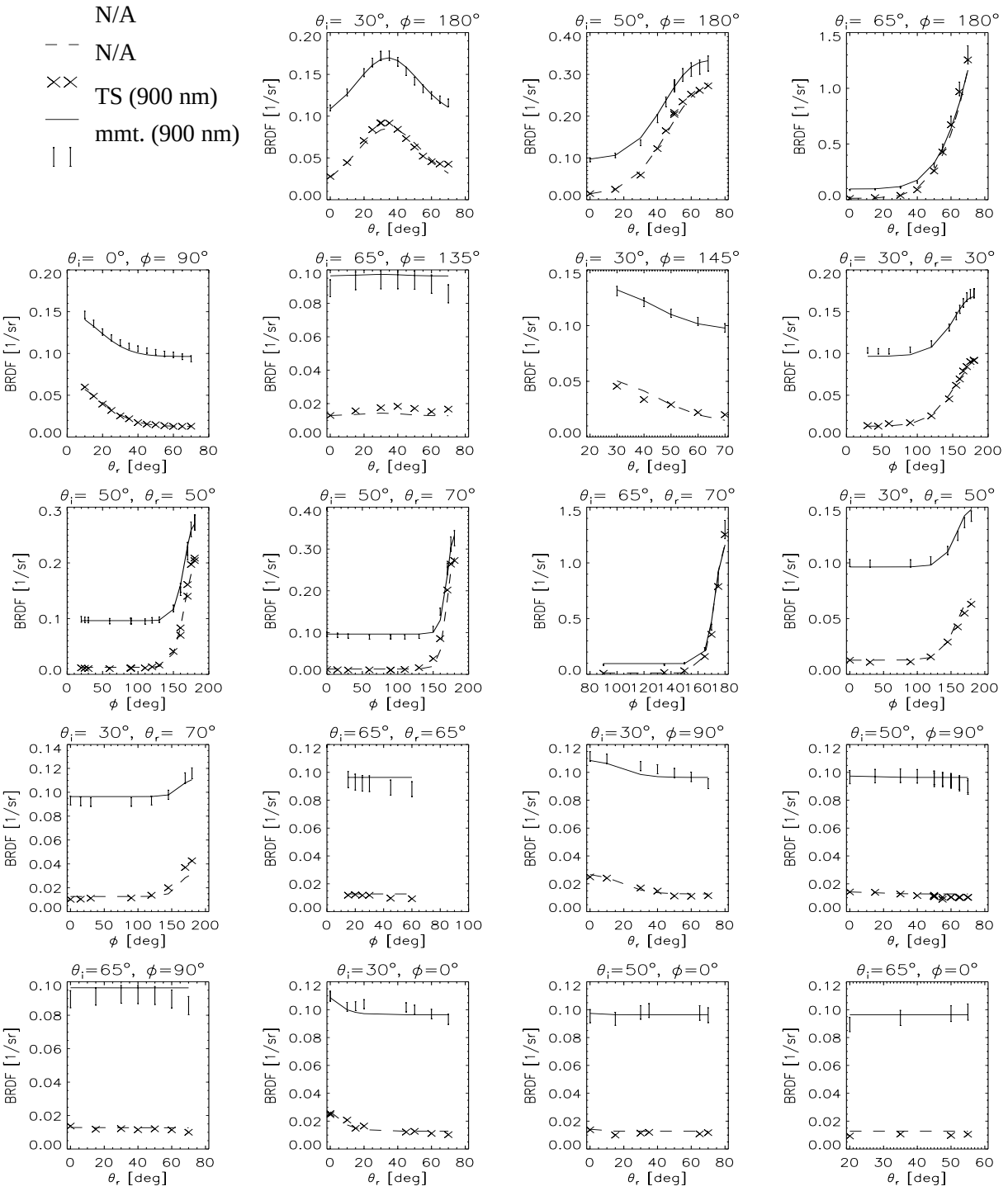

Figure 12.10: TS model fitted to BRDF measurements of the SE590 for ’red concrete’ at various angles.

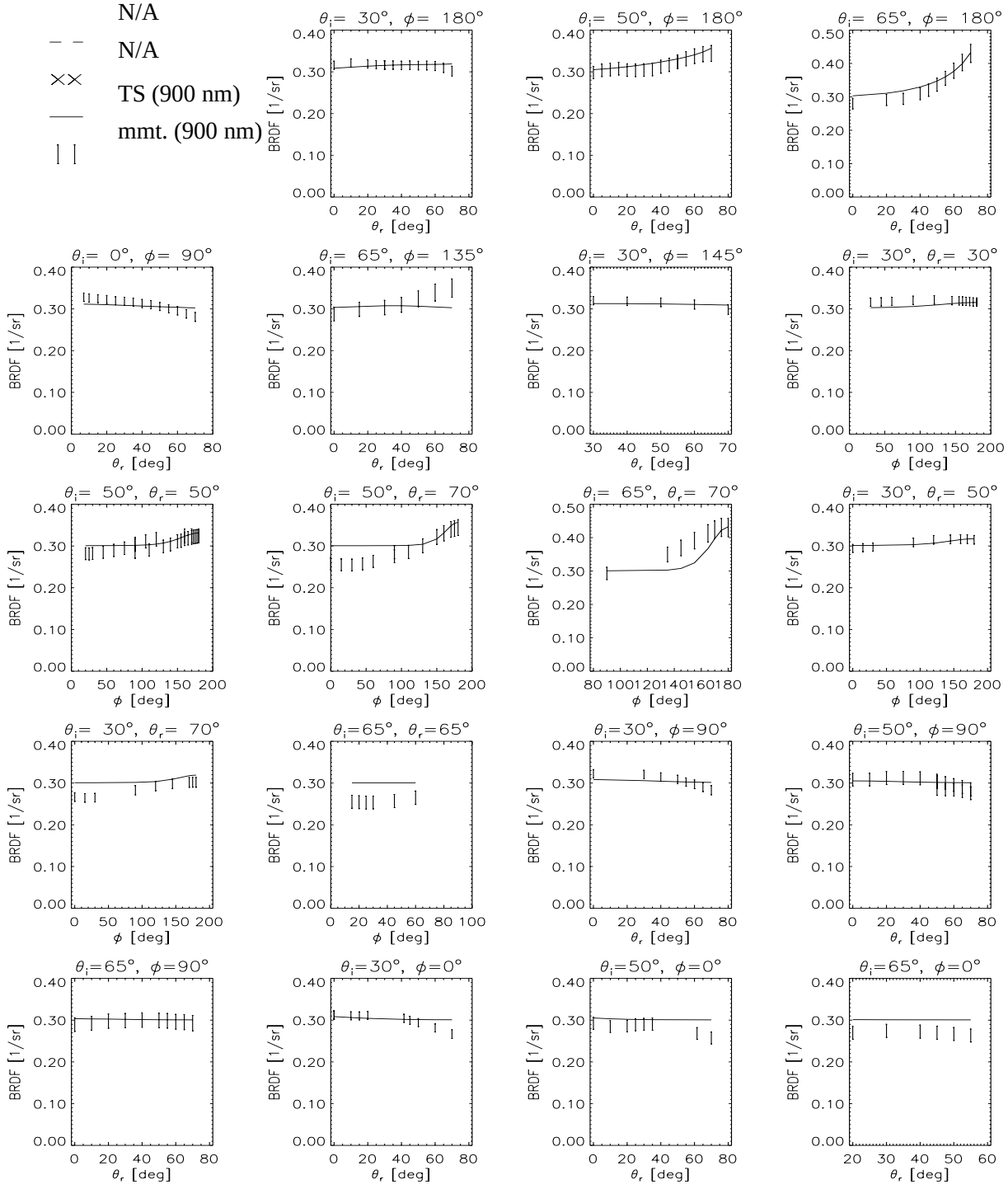

Figure 12.11: TS model fitted to BRDF measurements of the SE590 for Spectralon 1.0 at various angles.

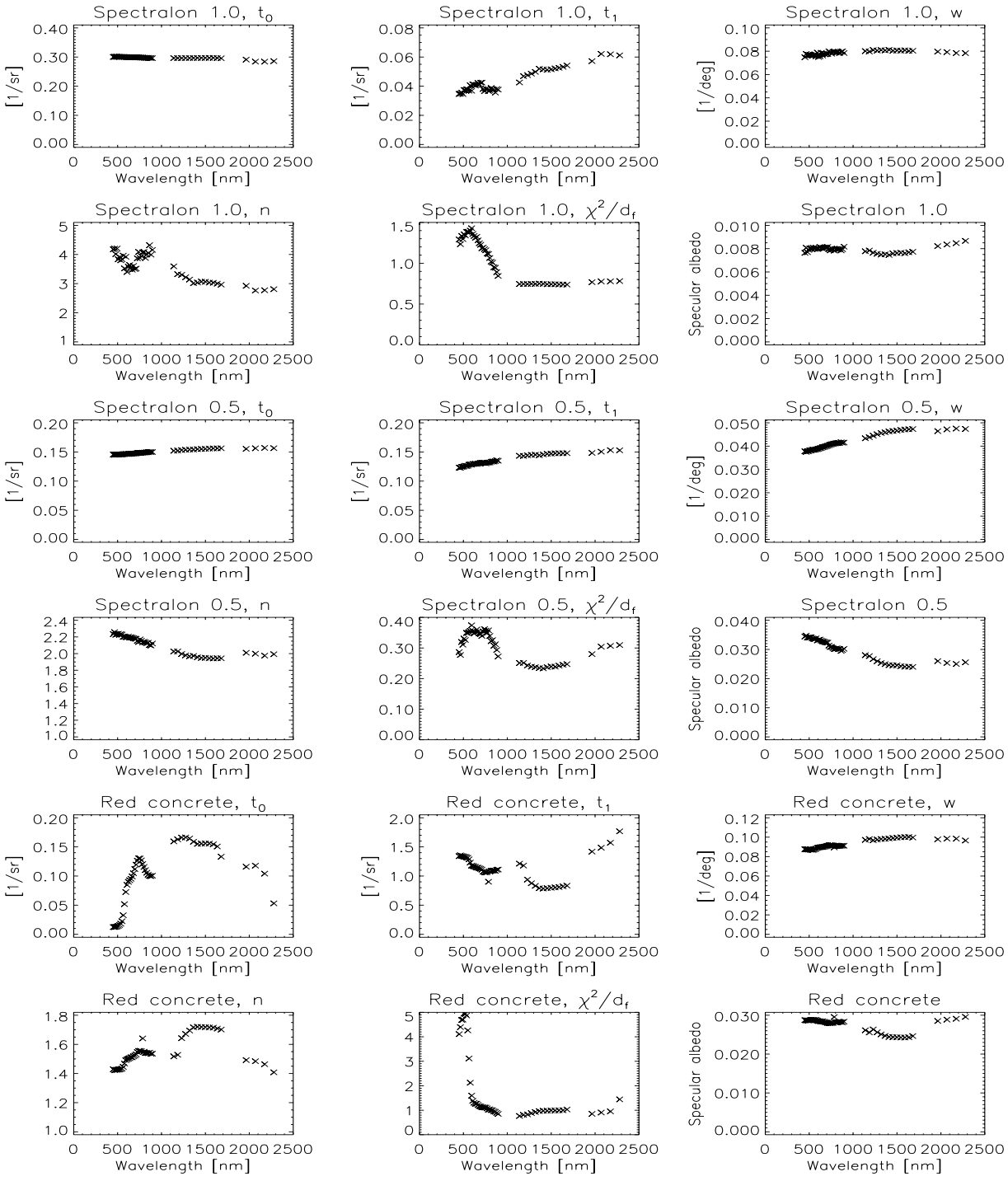

Figure 12.12: Parameters of the BRDF models fitted to the ASD measurements (1/4). t_0, t_1 and w denote parameters from the TS model. Furthermore the ratio of χ^2 over the degrees of freedom d_f and the specular albedo at $\theta_i = 30°$ is shown.

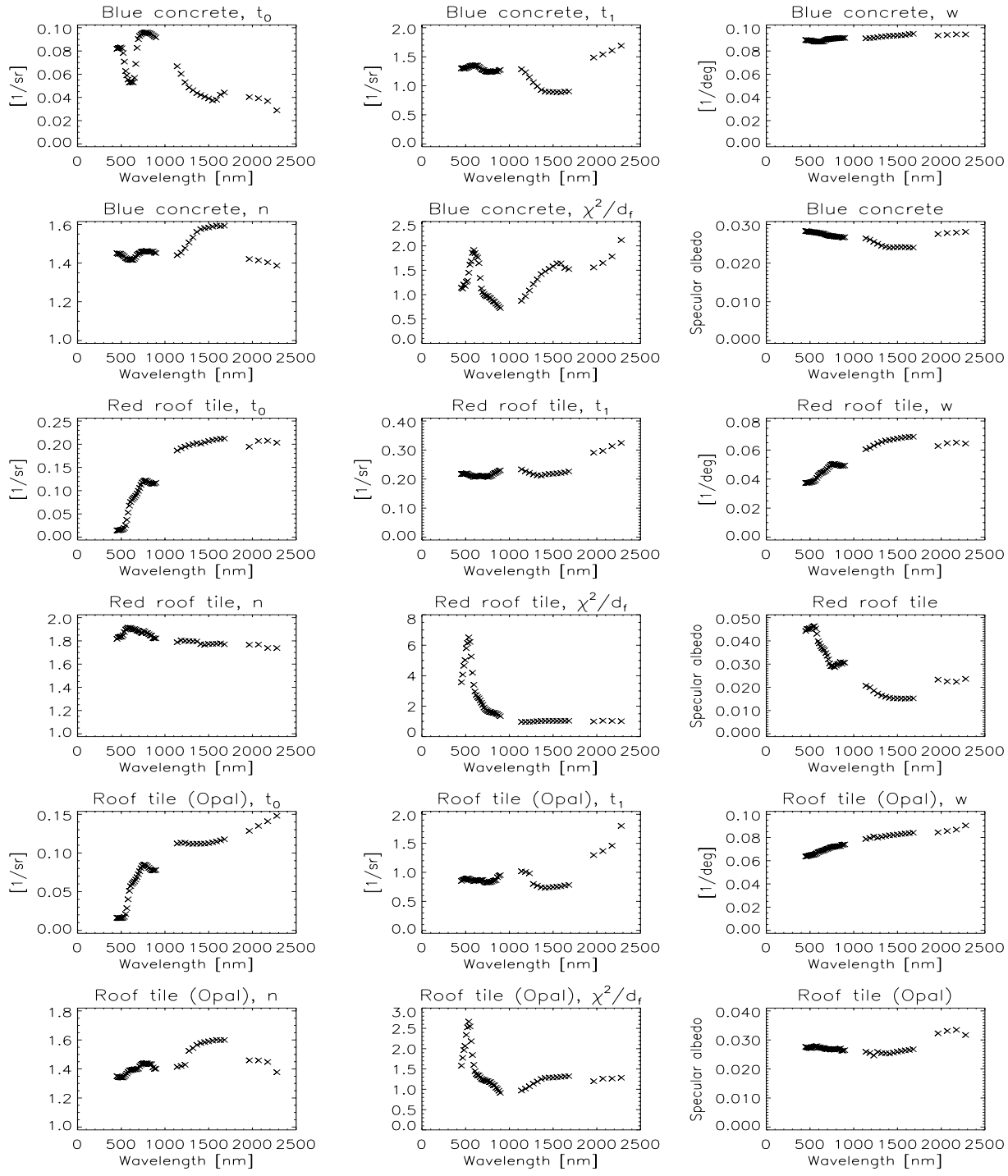

Figure 12.13: Parameters of the BRDF models fitted to the ASD measurements (2/4). t_0, t_1 and w denote parameters from the TS model. Furthermore the ratio of χ^2 over the degrees of freedom d_f and the specular albedo at $\theta_i = 30°$ is shown.

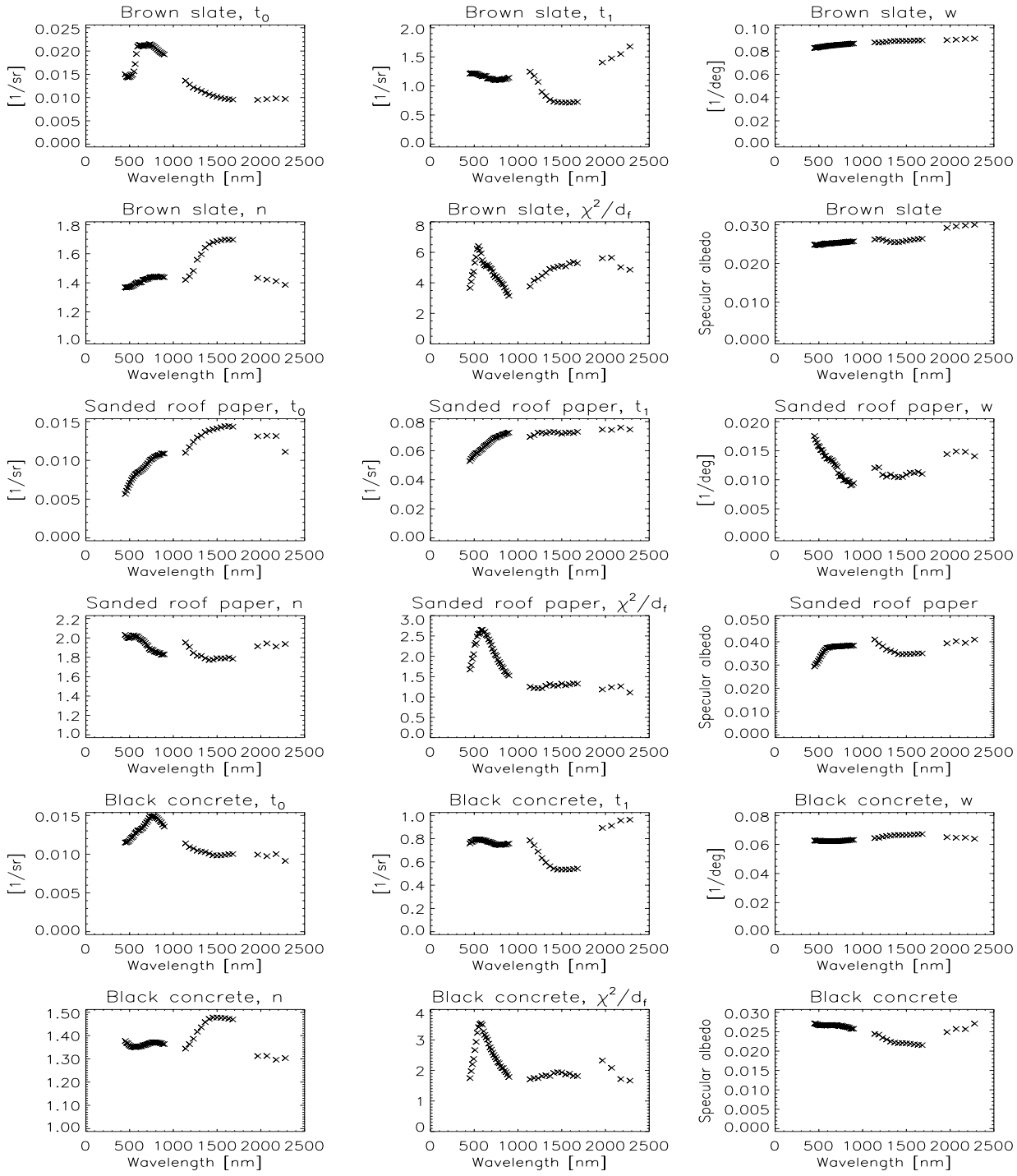

Figure 12.14: Parameters of the BRDF models fitted to the ASD measurements (3/4). t_0, t_1 and w denote parameters from the TS model. Furthermore the ratio of χ^2 over the degrees of freedom d_f and the specular albedo at $\theta_i = 30°$ is shown.

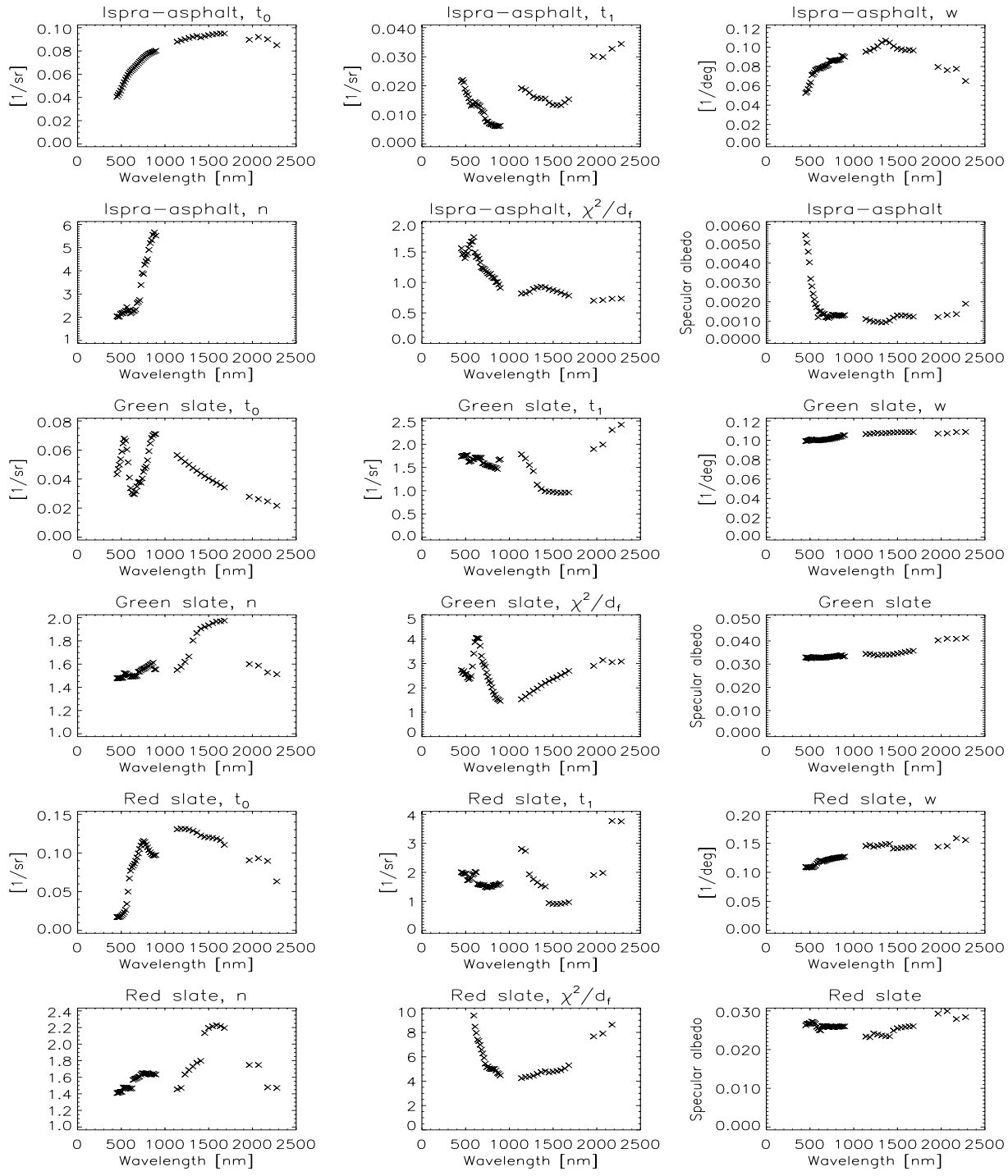

Figure 12.15: Parameters of the BRDF models fitted to the ASD measurements (4/4). t_0, t_1 and w denote parameters from the TS model. Furthermore the ratio of χ^2 over the degrees of freedom d_f and the specular albedo at $\theta_i = 30°$ is shown.

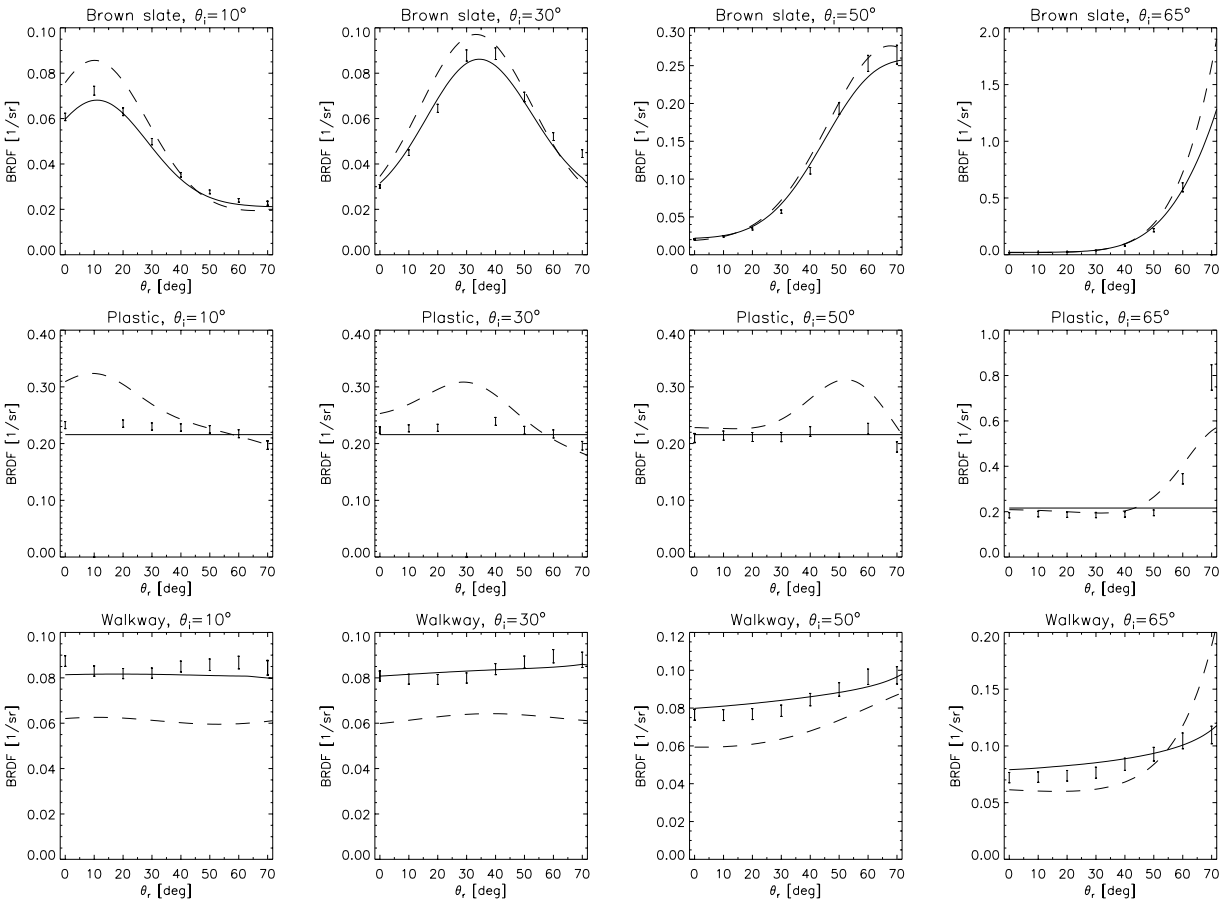

Figure 12.16: TS model (solid line) fitted to BRDF measurements of the ASD at 660 nm (error bars) and the empirical function of (Meister 1995) (dashed line) for samples 'brown slate', 'plastic' and 'walkway'.

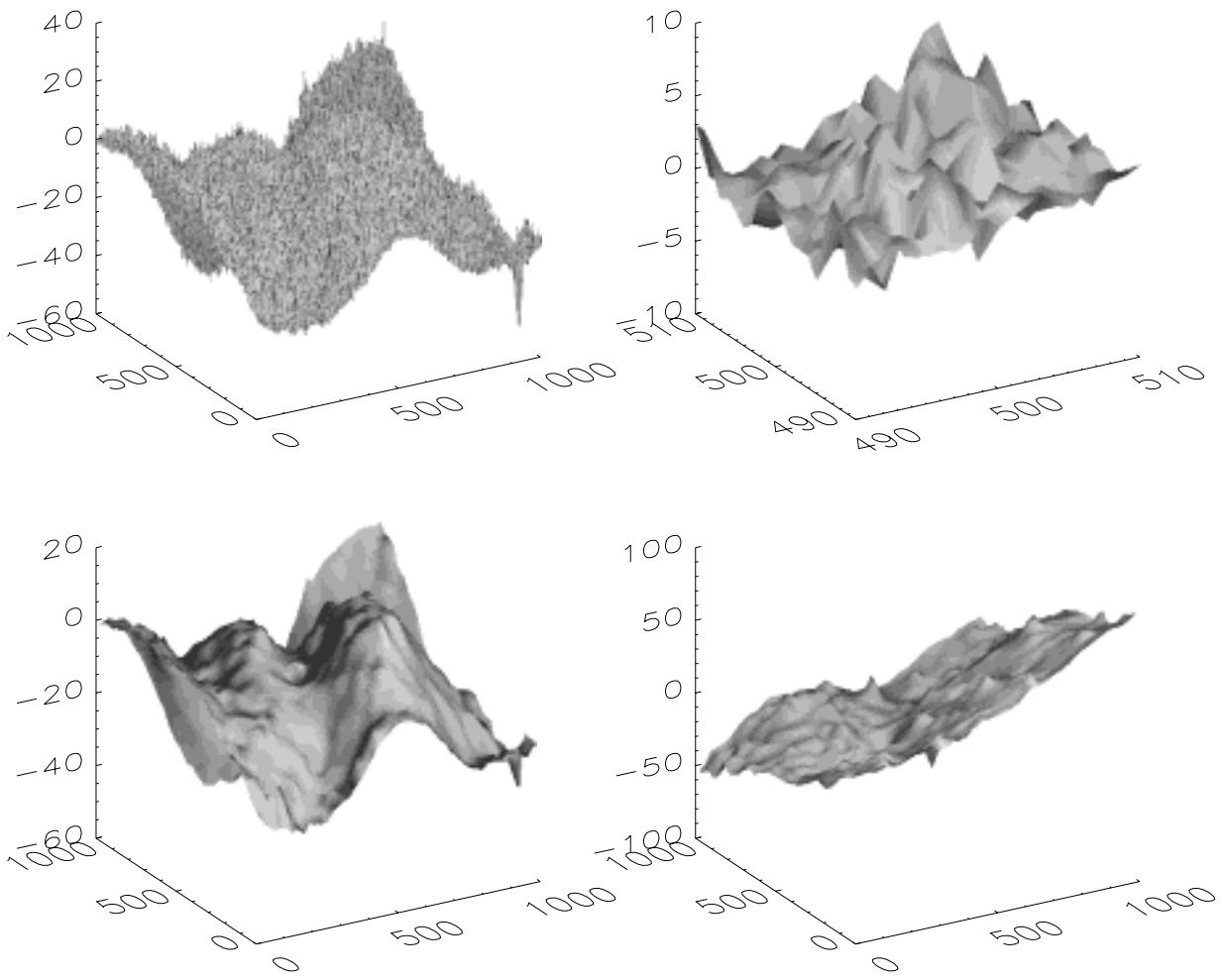

Figure 12.17: Topography data of the sample 'red concrete'. The first of the original data sets (corrected by a mean plane) of 1000 points x 1000 points is shown at top left. A subset of 20 points x 20 points taken from the center of the sampling area is shown top right. The result of averaging the original data with a bin size of 20 points times 20 points is shown on bottom left. The result after averaging for the second data set is shown bottom right. Note that only for the plot top right the vertical scale is scaled similarly to the horizontal axes. See chapter 7 for a discussion of the topography measurements.

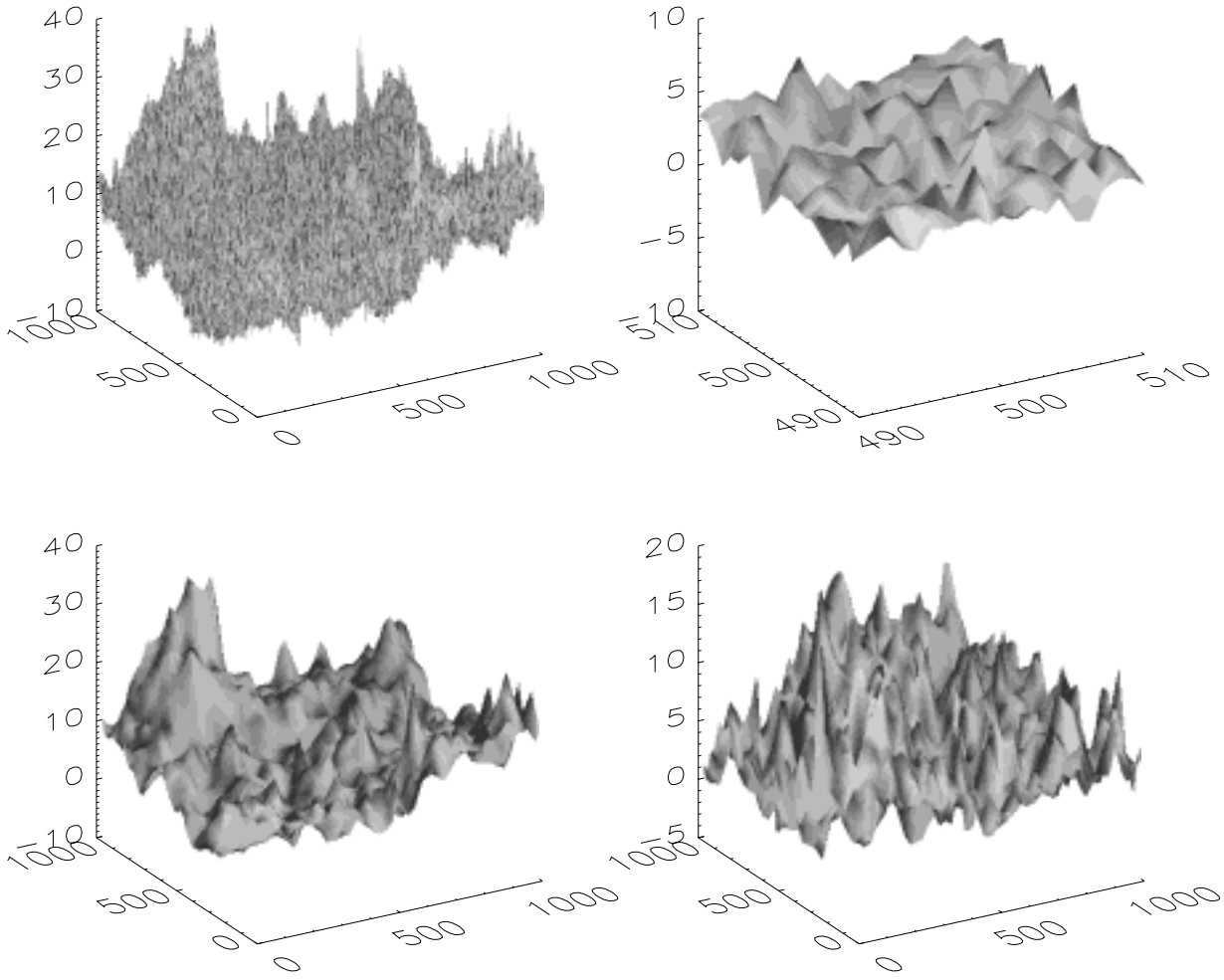

Figure 12.18: Topography data of the sample 'roof tile (Opal)'. The first of the original data sets (corrected by a mean plane) of 1000 points x 1000 points is shown at top left. A subset of 20 points x 20 points taken from the center of the sampling area is shown top right. The result of averaging the original data with a bin size of 20 points times 20 points is shown on bottom left. The result after averaging for the second data set is shown bottom right. Note that only for the plot top right the vertical scale is scaled similarly to the horizontal axes. See chapter 7 for a discussion of the topography measurements.

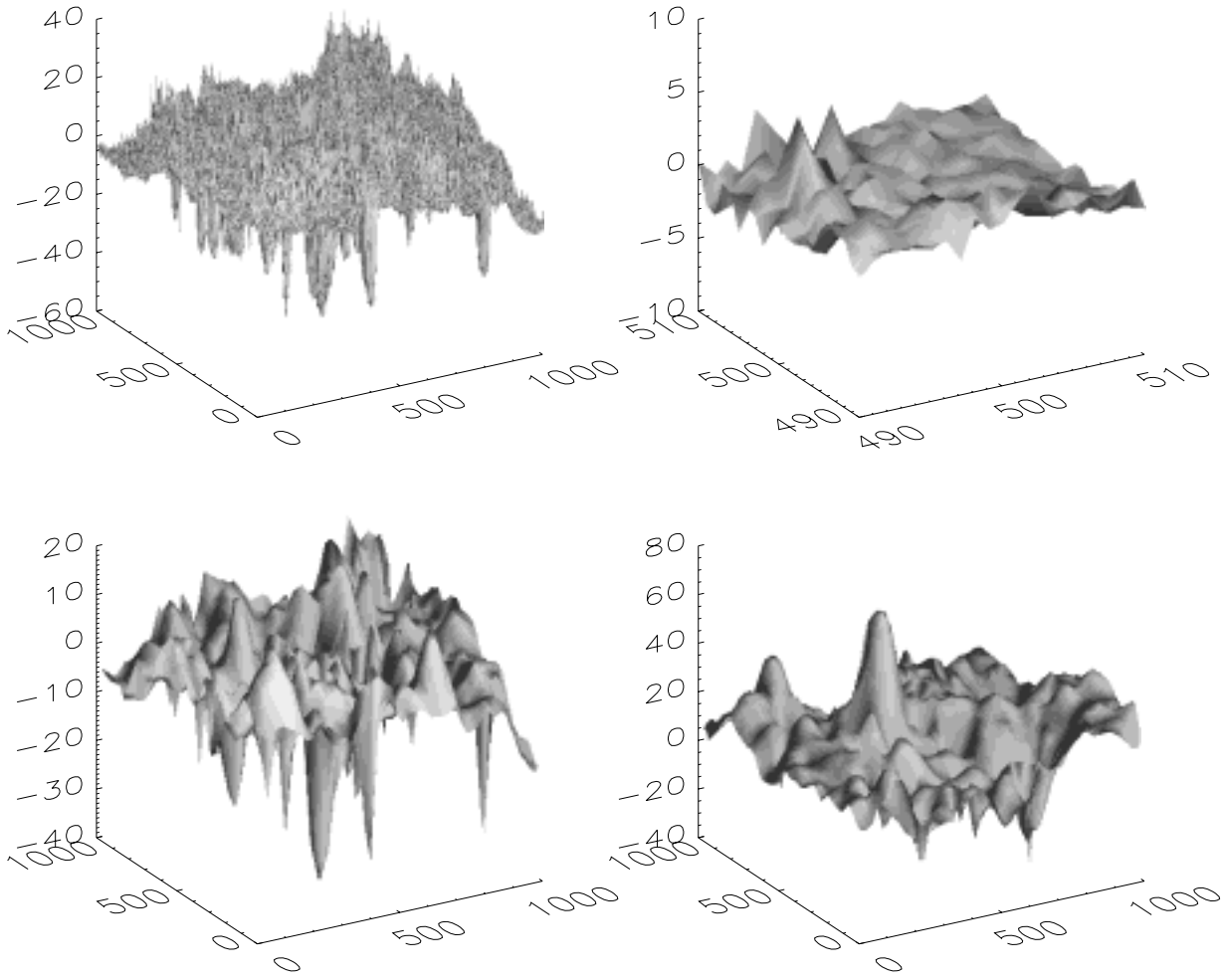

Figure 12.19: Topography data of the sample 'brown slate'. The first of the original data sets (corrected by a mean plane) of 1000 points x 1000 points is shown at top left. A subset of 20 points x 20 points taken from the center of the sampling area is shown top right. The result of averaging the original data with a bin size of 20 points times 20 points is shown on bottom left. The result after averaging for the second data set is shown bottom right. Note that only for the plot top right the vertical scale is scaled similarly to the horizontal axes. See chapter 7 for a discussion of the topography measurements.

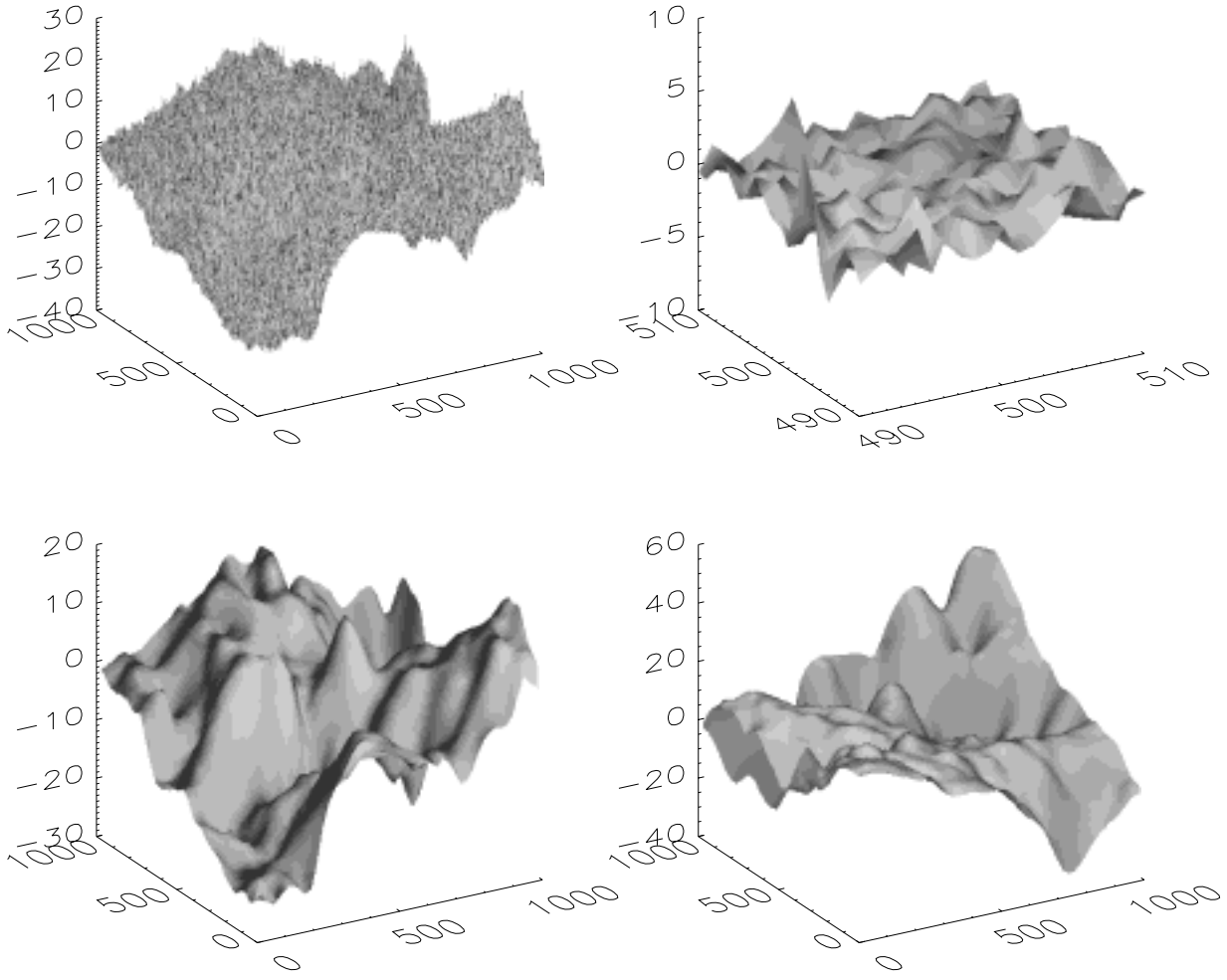

Figure 12.20: Topography data of the sample 'red slate'. The first of the original data sets (corrected by a mean plane) of 1000 points x 1000 points is shown at top left. A subset of 20 points x 20 points taken from the center of the sampling area is shown top right. The result of averaging the original data with a bin size of 20 points times 20 points is shown on bottom left. The result after averaging for the second data set is shown bottom right. The second set was rotated by $180°$ to improve the visualization. Note that only for the plot top right the vertical scale is scaled similarly to the horizontal axes. See chapter 7 for a discussion of the topography measurements.

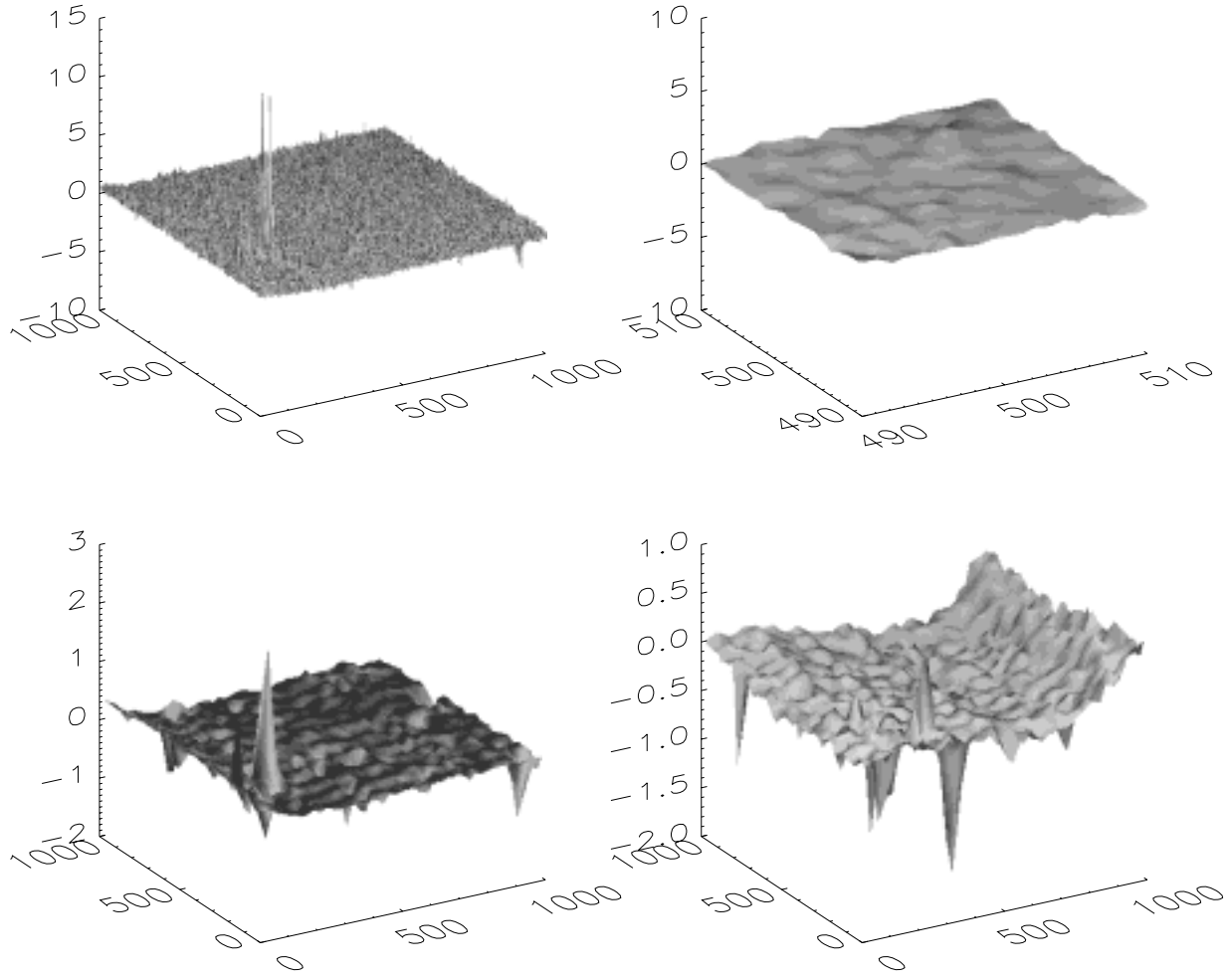

Figure 12.21: Topography data of the sample 'plastic'. The first of the original data sets (corrected by a mean plane) of 1000 points x 1000 points is shown at top left. A subset of 20 points x 20 points taken from the center of the sampling area is shown top right. The result of averaging the original data with a bin size of 20 points times 20 points is shown on bottom left. The result after averaging for the second data set is shown bottom right. The second set was rotated by $180°$ to improve the visualization. Note that only for the plot top right the vertical scale is scaled similarly to the horizontal axes. See chapter 7 for a discussion of the topography measurements.

λ [nm]	$\pi \cdot t_0$	k_0	k_1	k_2	k_3
490	0.0325	0.0076	0.00199	0.0419	0.00377
560	0.0404	0.0264	0.00600	0.0749	0.00992
610	0.0519	0.0185	0.00282	0.0559	0.00721
660	0.0568	0.0127	0.00184	0.0429	0.00446
730	0.0671	0.1799	0.02401	0.1775	0.01908
830	0.0694	0.3971	0.02887	0.2561	0.02173
1680	0.0803	0.1735	0.02472	0.1491	0.02006
2160	0.0734	0.0618	0.00982	0.0970	0.01657

Table 12.5: Parameters of the microscale BRDF for man-made surfaces and vegetation for the DAEDALUS wavelengths. The first column shows the center wavelength λ (cf. table 9.2, page 135). The second column shows the diffuse albedo of the man-made surfaces (t_0 from eq. 5.1, page 43). The remaining columns show the wavelength dependent vegetation parameters, see eq. 9.19 on page 124. The vegetation parameters independent of wavelength are given by $b_1 = 1.5, b_2 = 1.72, b_3 = 4.0, b_4 = 0.95$.

List of Figures

List of Tables

Bibliography

Anderson, G.P., F.X. Kneizys, J.H. Chetwynd, J. Wang, M.L. Hoke, L.S. Rothman, L.M. Kimball, R.A. McClatchey, E.P. Shattle, S.A. Clough, W.O. Gallery, L.W. Abreu, and J.E.A. Selby (1995). FASCODE / MODTRAN / LOWTRAN : Present / Past / Future. In *Proceedings of the 18th Annual Review Conference on Atmospheric Transmission Models, June 6–8*, 1995.

Bartsch, B., S. Bakan, and J. Fischer (1994). Remote Sensing of Water Vapour within the Solar Spectrum. In *Atmospheric Sensing and Modelling*, volume 2311, pages 197–206. SPIE, 1994.

Bartsch, B. (1996). *Fernerkundung des Wasserdampfgehalts der Atmosphäre über Land aus rückgestreuter Sonnenstrahlung*. PhD thesis, Meterologisches Institut, Universität Hamburg, 1996.

Beckmann, P. and A. Spizzichino (1963). *The Scattering of Electromagnetic Waves from Rough Surfaces*. Pergamon Press, New York, 1963.

Bezy, J.L. and G. Gourmelon (1999). The ENVISAT Medium Resolution Imaging Spectrometer (MERIS). In *Proceedings of the International Geoscience and Remote Sensing Symposium IGARSS'99, Hamburg, IEEE*, volume II, pages 1432–1434, 1999.

Bicheron, P., P. Richaume, O. Hautecoeur, and M. Leroy (1999). Retrieval of biophysical parameters at global scale by inversion of a radiative transfer model with neural network. In *Proceedings of the International Geoscience and Remote Sensing Symposium IGARSS'99, Hamburg, IEEE*, volume III, pages 1866–1868, 1999.

Brandt, S. (1992). *Datenanalyse*. BI-Wissenschaftsverlag, Mannheim, Leipzig, Wien, Zürich, 1992.

Brown, G.S. (1978). Backscattering from a Gaussian-distributed perfectly conducting rough surface. *IEEE Trans. Ant. Prop.* **AP-27**, 472–482, 1978.

CUReT (1996). Columbia Utrecht Reflectance and Texture Database. World Wide Web, http://www.cs.columbia.edu/CAVE/curet/.index.html, 1996.

Dana, K.J., S.K. Nayar, B.v. Ginneken, and J.J. Koenderink (1996). Reflectance and Texture of Real-World Surfaces. *Columbia University Technical Report CUCS-046-96, New York*, 1996.

Dana, K.J., B.v. Ginneken, S.K. Nayar, and J.J. Koenderink (1999). Reflectance and Texture of Real World Surfaces. *ACM Transactions on Graphics* **18** (1), 1–34, 1999.

Deering, D.W., T.F. Eck, and J. Otterman (1990). Bidirectional reflectance of selected desert surfaces and their three-parameter soil characterization. *Agricultural and Forest Meteorology* **52**, 71–93, 1990.

Deering, D.W., E.M. Middleton, J.R. Irons, and et al. (1992). Prairie grassland bidirectional reflectances measured by different instruments at the FIFE site. *Journal of Geophysical Research* **97(D17):18**, 18887–18903, 1992.

Diner, D., C.J. Bruegge, J.V. Martonchik, G.W. Bothwell, E.D. Danielson, V.G. Ford, L.E. Hovland, K.L. Jones, and M.L. White (1991). A multi-angle image spectroradiometer for terrestrial remote sensing with the Earth Observing System. *Int. J. Imag. Syst. Technol.* **3**, 92–107, 1991.

Diner, D., G. Asner, R. Davies, Y. Knyazikhin, J.-P. Muller, A. Nolin, B. Pinty, C. Schaaf, and J. Stroeve (1999). New directions in Earth observing: Scientific applications of multi-angle remote sensing. *Bulletin of the American Meteorological Society* **80**, 2209–2228, 1999.

Gastellu-Etchegorry, J.P., P. Guillevic, F. Zagolski, V. Demarez, V. Trichon, D. Deering, and M. Leroy (1999). Modeling BRF and Radiation Regime of Boreal and Tropical Forests: I. BRF. *Remote Sensing of Environment* **68**, 281–316, 1999.

Gerstl, S.A.W., W. Gebauer, C.C. Borel, and C. Dochitoiu (1999). Angular Signature Retrieval and Comparison with Spectral Signatures from AirMISR Data. In *Proceedings of the International Geoscience and Remote Sensing Symposium IGARSS'99, Hamburg, IEEE*, volume I, pages 404–407, 1999.

Gibbs, D.P., C.L. Betty, A.K. Fung, A.J. Blanchard, J.R. Irons, and W.L. Balsam (1993). Automated Measurement of Polarized Bidirectional Reflectance. *Remote Sensing of Environment* **43**, 97–114, 1993.

Ginneken, B.v., M. Stavridi, and J.J. Koenderink (1998). Diffuse and specular reflectance from rough surfaces. *Applied Optics* **37** (1), 130–139, 1998.

Goel, N. S. and N. Reynolds (1989). Bidirectional canopy reflectance and its relationship to vegetation characteristics. *International Journal of Remote Sensing* **10**, 107–132, 1989.

Hapke, B. W., R. M. Nelson, and W. D. Smythe (1993). The opposition effect of the moon: The contribution of coherent backscatter. *Science* **260** (23), 509–511, April 1993.

Hapke, B. (1993). *Theory of Reflectance and Emittance Spectroscopy*. Cambridge University Press, Cambridge, 1993.

Horn, B. K. P. (1986). *Robot Vision*. MIT Press / McGraw-Hill, 1986.

Hosgood, B. (1997). Results of mechanical calibration made in EGO on 10 SEP 97, technical report, EGO, SAI, JRC, Ispra, Italy, 1997.

Hu, B., W. Lucht, X. Li, and A.H. Strahler (1997). Validation of Kernel-Driven Semiempirical Models for the Surface Bidirectional Reflectance Distribution Function of Land Surfaces. *Remote Sensing of Environment* **62**, 201–214, 1997.

Jacquemoud, S., F. Baret, and J.F. Hanocq (1992). Modeling Spectral and Bidirectional Soil Reflectance. *Remote Sensing of Environment* **41**, 123–132, 1992.

James, M.E. and S.N.V. Kalluri (1994). The Pathfinder AVHRR land data set: an improved coarse resolution data set for terrestrial monitoring. *International Journal of Remote Sensing* **15**, 3347–3364, 1994.

Jupp, D.L.B. and A.H. Strahler (1991). A Hotspot Model for Leaf Canopies. *Remote Sensing of Environment* **38**, 193–210, 1991.

Kimes, D.S. (1983). Dynamics of directional reflectance factor distributions for vegetation canopies. *Applied Optics* **22** (9), 1364–1372, 1983.

Kittel, C. (1996). *Introduction to Solid State Physics*. Wiley, New York, 7th ed., 1996.

Kollewe, T. (1995). Vergleich multispektraler Flugzeugscanneraufnahmen mit Reflektanzmessungen am Boden, Diplomarbeit, Universität Hamburg, II. Institut für Experimentalphysik, CENSIS-Report 17-96, 1995.

Kraus, K. and W. Schneider (1988). *Fernerkundung, Band 1 – Physikalische Grundlagen und Aufnahmetechniken*. Ferd. Dümmlers Verlag, Bonn, 1988.

Kriebel, K. T. (1978). Measured Spectral Bidirectional Reflection Properties of Four Vegetated Surfaces. *Applied Optics* **17** (2), 253–258, 1978.

Kuga, Y. and A. Ishimaru (1984). Retroreflectance from a dense distribution of spherical particles. *Journal of the Optical Society of America* **1** (8), 831–835, 1984.

Kuusk, A. (1995). A Fast, Invertible Canopy Reflectance Model. *Remote Sensing of Environment* **51**, 342–350, 1995.

Lambert, J. H. (1760). *Photometria sive de mensura et gradibus luminus, colorum et umbrae*. Eberhard Klett, Augsburg, 1760.

Leroy, M., J. Deuze, F. Breon, O. Hautecoeur, M. Herman, J. Buriez, D. Tanre, S. Bouffies, P. Chazette, and J.L. Roujean (1997). Retrieval of atmospheric properties and surface bidirectional reflectances over land from POLDER/ADEOS. *Journal of Geophysical Research* **102**, 17023–17038, 1997.

Li, Z.H., A.K. Fung, S. Tjuatha, D.P. Gibbs, C.L. Betty, and J.R. Irons (1996). A Modeling Study of Backscattering from Soil Surfaces. *IEEE Transactions on Geoscience and Remote Sensing* **34** (1), 264–271, 1996.

Liang, S. and A. H. Strahler (1994). Retrieval of Surface BRDF from Multiangle Remotely Sensed Data. *Remote Sensing of Environment* **50**, 18–30, 1994.

Liang, S. and J.R.G. Townshend (1996a). A modified Hapke model for Soil Bidirectional Reflectance. *Remote Sensing of Environment* **55**, 1–10, 1996.

Liang, S. and J.R.G. Townshend (1996b). A parametric soil BRDF model: a four stream approximation for multiple scattering. *International Journal of Remote Sensing* **17** (7), 1303–1315, 1996.

Lucht, W. and P. Lewis (2000). Theoretical noise sensitivity of BRDF and albedo retrieval from the EOS-MODIS and MISR sensors with respect to angular sampling. *International Journal of Remote Sensing* **21** (1), 81–98, 2000.

Meister, G., R. Wiemker, J. Bienlein, and H. Spitzer (1996a). In Situ BRDF Measurements of Selected Surface Materials to Improve Analysis of Remotely Sensed Multispectral Imagery. In *Proceedings of the XVIII. Congress of the International Society for Photogrammetry and Remote Sensing ISPRS 1996, Vienna*, volume XXXI part B7 of *International Archives of Photogrammetry and Remote Sensing*, pages 493–498, 1996.

Meister, G., R. Wiemker, J. Bienlein, and H. Spitzer (1996b). In Situ BRDF Measurements of Selected Surface Materials to Improve Analysis of Remotely Sensed Multispectral Imagery. *Proc. of the 13. Congress of the Intern. Soc. for Photogrammetry and Remote Sensing ISPRS 1996, Vienna* **XXXI part B7**, 493–498, 1996.

Meister, G., A. Rothkirch R. Monno, R. Wiemker, J. Bienlein, and H. Spitzer (1997). BRDF effects in remotely sensed high resolution images of urban areas. In *Proceedings of the Joint Workshop of ISPRS WG I/1, I/3 and IV/4, Hannover, 29.IX.–2.X., Institute for Photogrammetry and Engineering Surveys, University of Hannover, 1998*, volume 17, pages 213–221, 1997.

Meister, G., A. Rothkirch, R. Wiemker, J. Bienlein, and H. Spitzer (1998a). Modeling the Directional Reflectance (BRDF) of a Corrugated Roof and Experimental Verification. In *Proceedings of the International Geoscience and Remote Sensing Symposium IGARSS'98, Seattle, IEEE*, volume III, pages 1487–1489, 1998.

Meister, G., S. Sandmeier, and W. Ni (1998b). Analyzing Hyperspectral BRDF Data of a Grass Lawn and Watercress Surface. In *Proceedings of the International Geoscience and Remote Sensing Symposium IGARSS'98, Seattle, IEEE*, volume III, pages 1246–1248, 1998.

Meister, G., R. Wiemker, R. Monno, H. Spitzer, and A. Strahler (1998c). Investigation on the Torrance-Sparrow Specular BRDF Model. In *Proceedings of the International Geoscience and Remote Sensing Symposium IGARSS'98, Seattle, IEEE*, volume IV, pages 2095–2097, 1998.

Meister, G., D. Jupp, A. Rothkirch, and H. Spitzer (1999a). Determination of the Angular Sensitivity of a Multispectral Line Scanner from Image Data. In *Proceedings of the International Geoscience and Remote Sensing Symposium IGARSS'99, Hamburg, IEEE*, volume I, pages 458–460, 1999.

Meister, G., W. Lucht, A. Rothkirch, and H. Spitzer (1999b). Large Scale Multispectral BRDF of an Urban Area. In *Proceedings of the International Geoscience and Remote Sensing Symposium IGARSS'99, Hamburg, IEEE*, volume II, pages 821–823, 1999.

Meister, G., A. Rothkirch, J. Bienlein, and H. Spitzer (1999c). BRDF Studies for Remote Sensing of Urban Areas. *Remote Sensing Reviews (accepted)*, 1999.

Meister, G., A. Rothkirch, B. Hosgood, H. Spitzer, and J. Bienlein (1999d). Error Analysis for BRDF Measurements at the European Goniometric Facility. *Remote Sensing Reviews (accepted)*, 1999.

Meister, G., A. Rothkirch, H. Spitzer, and J. Bienlein (2000). The Shape of the Specular Peak of Rough Surfaces. In *Proceedings of the XIXth Congress of the International Society for Photogrammetry and Remote Sensing (ISPRS), 16-23 July 2000, Amsterdam, ISSN 0256-1840*, volume XXXIII of *International Archives of Photogrammetry and Remote Sensing*, pages 852–860, 2000.

Meister, G. (1995). Messung der bidirektionalen Reflektanzverteilungsfunktion (BRDF) ausgewählter Oberflächen unter natürlicher Beleuchtung, diploma thesis, Universität Hamburg, II. Institut für Experimentalphysik, CENSIS-Report 18-96., 1995.

Myneni, R.B., S. Maggion, J. Iaquinta, J.L. Privette, N. Gobron, B. Pinty, D.S. Kimes, M.M. Verstaete, and D.L. Williams (1995). Optical Remote Sensing of Vegetation: Modeling, Caveats, and Algorithms. *Remote Sensing of Environment* **51**, 169–188, 1995.

Nayak, P. R. (1971). Random process model of rough surfaces. *Trans. A.S.M.E: J. Lubr. Tech* **93F**, 398–407, 1971.

Nayar, S. K., K. Ikeuchi, and T. Kanade (1991). Surface reflection: Physical and Geometrical Perspectives. *IEEE Transactions on Pattern Analysis and Machine Intelligence* **13** (7), 611–634, 1991.

Ni, W., X. Li, C.E. Woodcock, M.R. Caetano, and A.H. Strahler (1999). An Analytical Hybrid GORT Model for Bidirectional Reflectance Over Discontinuous Plant Canopies. *IEEE Transactions on Geoscience and Remote Sensing* **37** (2, part II), 987–999, 1999.

Nicodemus, F.E., J.C. Richmond, J.J. Hsia, , I.W. Ginsberg, and T. Lamperis (1977). Geometric Considerations and Nomenclature for Reflectance. Monogram 160:52, US Department of Commerce, National Bureau of Standards, 1977.

Nicodemus, F.E. (1970). Reflectance Nomenclature and Directional Reflectance and Emissivity. *Applied Optics* **9** (6), 1474–1475, 1970.

Ogilvy, J.A. (1992). *Theory of Wave Scattering from Random Rough Surfaces*. Institut of Physics Publishing, Bristol, Philadelphia, 1992.

Oren, Michael and Shree K. Nayar (1994). Seeing Beyond Lambert's Law. In Eklundh, J.-O., editor, *European Conference on Computer Vision – ECCV '94*, Heidelberg, New York, 1994, pages 269–280. Springer.

Oren, M. and S.K. Nayar (1995). Generalization of the Lambertian Model and Implications for Machine Vision. *International Journal of Computer Vision* **14**, 227–251, 1995.

Phong, B. (1975). Illumination for computer generated pictures. *Commun. ACM* **18**, 311–317, 1975.

Qin, W. and N.S. Goel (1995). An Evaluation of Hotspot Models for Vegetation Canopies. *Remote Sensing Reviews* **13**, 121–159, 1995.

Qin, W., S. Sandmeier, and S.A.W. Gerstl (1999). Use of Multiple Scattering Fraction to Estimate Leaf Area Index of Grass Canopies. In *Proceedings of the International Geoscience and Remote Sensing Symposium IGARSS'99, Hamburg, IEEE*, volume I, pages 407–409, 1999.

Rahman, H., B. Pinty, and M. M. Verstraete (1993). Coupled surface-atmosphere reflectance (CSAR) model, 2, Semiempirical surface model usable with NOAA AVHRR data. *Journal of Geophysical Research* **98**, 20791–20801, 1993.

Richter, R. (1990). A Fast Atmospheric Correction Algorithm Applied to Landsat TM Images. *International Journal of Remote Sensing* **11** (1), 159–166, 1990.

Richter, R. (1992). *Radiometrische Auslegung von Sensoren und quantitative Auswertung von Fernerkundungsdaten im optischen Spektralbereich*. PhD thesis, German Aerospace Research Establishment (DLR), Oberpfaffenhofen, 1992.

Rothkirch, A., M. Kollewe, and H. Spitzer (1998). Calibration Accuracy of Aerial Multispectral Reflectance Images and Estimation of Error Sources. In *1'st EARSel Workshop on Imaging Spectroscopy, Remote Sensing Laboratories, Zurich, CH, ISSN 2-90 885-22-0*, pages 155–163, 1998.

Rothkirch, A., G. Meister, B. Hosgood, H. Spitzer, and J. Bienlein (1999). BRDF Measurements at the EGO using a Laser Source: Equipment characteristics and estimation of error sources. *Remote Sensing Reviews (accepted)*, 1999.

Rothkirch, A., G. Meister, H. Spitzer, and J. Bienlein (2000). BRDF Measurements of Urban Surface Materials at the EGO Facility Using a Laser Source. In *Proceedings of the XIXth Congress of the International Society for Photogrammetry and Remote Sensing (ISPRS), 16-23 July 2000, Amsterdam, ISSN 0256-1840*, volume XXXIII of *International Archives of Photogrammetry and Remote Sensing*, pages 777–784, 2000.

Rothkirch, A. (1997). Feldmessung der spektralen Reflexionsfunktion (BRDF) eines Hausdaches, diploma thesis, Universität Hamburg, II. Institut für Experimentalphysik, CENSIS-REPORT-30-97, 1997.

Roujean, J. L., M. Leroy, and P. Y. Deschamps (1992). A bidirectional reflectance model of the Earth's surface for the correcion of remote sensing data. *Journal of Geophysical Research* **97**, 20455–20468, 1992.

Sandmeier, S. and D.W. Deering (1999). A New Approach to Derive Canopy Structure Information for Boreal Forests Using Spectral BRDF Data. In *Proceedings of the International Geoscience and Remote Sensing Symposium IGARSS'99, Hamburg, IEEE*, volume I, pages 410–412, 1999.

Sandmeier, S.R. and K.I. Itten (1998). Physical Mechanisms in Hyperspectral BRDF Data of Grass and Watercress. *Remote Sensing of Environment* **66**, 222–233, 1998.

Sandmeier, S. and K.I. Itten (1999). A Field Goniometer System (FIGOS) for Acquisition of Hyperspectral BRDF Data. *IEEE Transactions on Geoscience and Remote Sensing* **37** (2, part II), 978–986, 1999.

Sandmeier, S., C. Mueller, B. Hosgood, and G. Andreoli (1998). Sensitivity Analysis and Quality Assessment of Laboratory BRDF Data. *Remote Sensing of Environment* **64**, 176–191, 1998.

Sayles, R. S. and T. R. Thomas (1978). Surface topography as a non-stationary random process. *Nature* **271**, 431–434, 1978.

Schlick, C. (1994). A Survey of Shading and Reflectance Models. *Computer Graphics Forum* **13** (2), 121–131, 1994.

Smith, F.G., J.S. Accetta, and D.L. Shumaker (1993). *The Infrared and Electro–Optical Systems Handbook*, volume 2. The International Society for Optical Engineering, Washington, 1993.

Solheim, S., B. Hosgood, G. Andreoli, and J. Piironen (1996). Calibration and Characterization of Data from the European Goniometric Facility (EGO), Report EUR 17268 EN. Space Applications Institute, Joint Research Centre, Ispra, Italy, 1996.

Stavridi, M., B.v. Ginneken, and J.J. Koenderink (1997). Surface bidirectional reflection distribution function and the texture of bricks and tiles. *Applied Optics* **36** (16), 3717–3725, 1997.

Staylor, W. F. and J. T. Suttles (1986). Reflection and emission models for deserts derived from Nimbus-7 ERB scanner measurements. *J. Climate Appl. Meteorol.* **25**, 196–202, 1986.

Stout, K. J., P. J. Sullivan, W. P. Dong, E. Mainsah, N. Luo, T. Mathia, and H. Zahouani (1993). The development of methos for the characterisation of roughness in 3 dimensions, EC Contract No.3374/1/0/170/90/2, Phase II Report, Vol.1 (March 1993), 1993.

Stover, J. C. (1995). *Optical Scattering - Measurement and Analysis*. The International Society for Optical Engineering, Bellingham, Washington, 2nd edition, 1995.

Strahler, A. H. (1997). Vegetation Canopy Reflectance - recent developments and a remote sensing perspective. *Remote Sensing Reviews* **15**, 179–194, 1997.

Strugnell, N., W. Lucht, A. Hyman, and G. Meister (1998). Continental-scale albedo inferred from land cover class, field observations of typical BRDFs and AVHRR data. In *Proceedings of the International Geoscience and Remote Sensing Symposium IGARSS'98, Seattle, July 1998, IEEE*, volume II, pages 595–597, 1998.

Thomas, T. R. and R. S. Sayles (1975). Random-process analysis of the effect of waviness on thermal contact resistance. *Prog. Astronaut. Aeronaut.* **29** (3), 3–20, 1975.

Thomas, T. R. (1999). *Rough Surfaces*. Imperial College Press, London, 1999.

Torrance, K. and E. Sparrow (1967). Theory for Off-Specular Reflection from Rough Surfaces. *Journal of the Optical Society of America* **57** (9), 1105–1114, 1967.

Vermote, E.F., N.E. Saleous, C.O. Justice, Y.J. Kauffman, J.L. Privette, L. Remer, J.C. Roger, and D. Tanre (1997a). Atmospheric correction of visible to middle-infrared EOS-MODIS data over land surfaces: Background, operational algorithm and validation. *Journal of Geophysical Research* **102** (D14), 17131–17141, 1997.

Vermote, E.F., D. Tanre, J.L. Deuze, M. Herman, and J.J. Morcrett (1997b). Second Simulation of the Satellite Signal in the Solar Spectrum: An Overview. *IEEE Transactions on Geoscience and Remote Sensing* **35** (3), 675–686, May 1997.

Walthall, C. L., J. M. Norman, J. M. Welles, G. Campbell, and B. L. Blad (1985). Simple equation to approximate the bidirectional reflectance from vegetation canopies and bare soil surfaces. *Applied Optics* **24**, 383–387, 1985.

Wanner, W., X. Li, and A.H. Strahler (1995). On the derivation of kernels for kernel-driven models of bidirectional reflectance. *Journal of Geophysical Research* **100**, 21077–21090, 1995.

Wanner, W., A.H. Strahler, B. Hu, P. Lewis, J.-P. Muller, X. Li, C. Schaaf, and M.J. Barnsley (1997). Global retrieval of bidirectional reflectance and albedo over land from EOS MODIS and MISR data: Theory and algorithm. *Journal of Geophysical Research* **102**, 17143–17161, 1997.

Wiemker, R., B. Prinz, G. Meister, R. Franck, and H. Spitzer (1998). Accuracy Assessment of Vegetation Monitoring with High Spatial Resolution Satellite Imagery. In *Proceedings of the ISPRS Commission VII Symposium, ECO BP'98, WG 3, September 1–4, 1998, Budapest, International Symposium on Resource and Environmental Monitoring – Local, Regional, Global.*, 1998. In print.

Wiemker, R. (1996). Registration of Airborne Scanner Imagery Using Akima Local Quintic Polynomial Interpolation. In *Proceedings of the Second International Airborne Remote Sensing Conference and Exhibition, San Francisco*, Ann Arbor, 1996, volume III, pages 210–219. Environmental Research Institute of Michigan.

Wolff, L. B. (1994). On the Relative Brightness of Specular and Diffuse Reflection. In *Proceedings of IEEE Computer Society Conference on Computer Vision and Pattern Recognition, Seattle*, pages 369–376, 1994.

Wolff, L.B. (1996). Generalizing Lambert's Law for Smooth Surfaces. In Buxton, B. and R. Cipolla, editors, *Proceedings of the European Conference on Computer Vision, ECCV'96, Springer, Berlin*, pages 40–53, 1996.